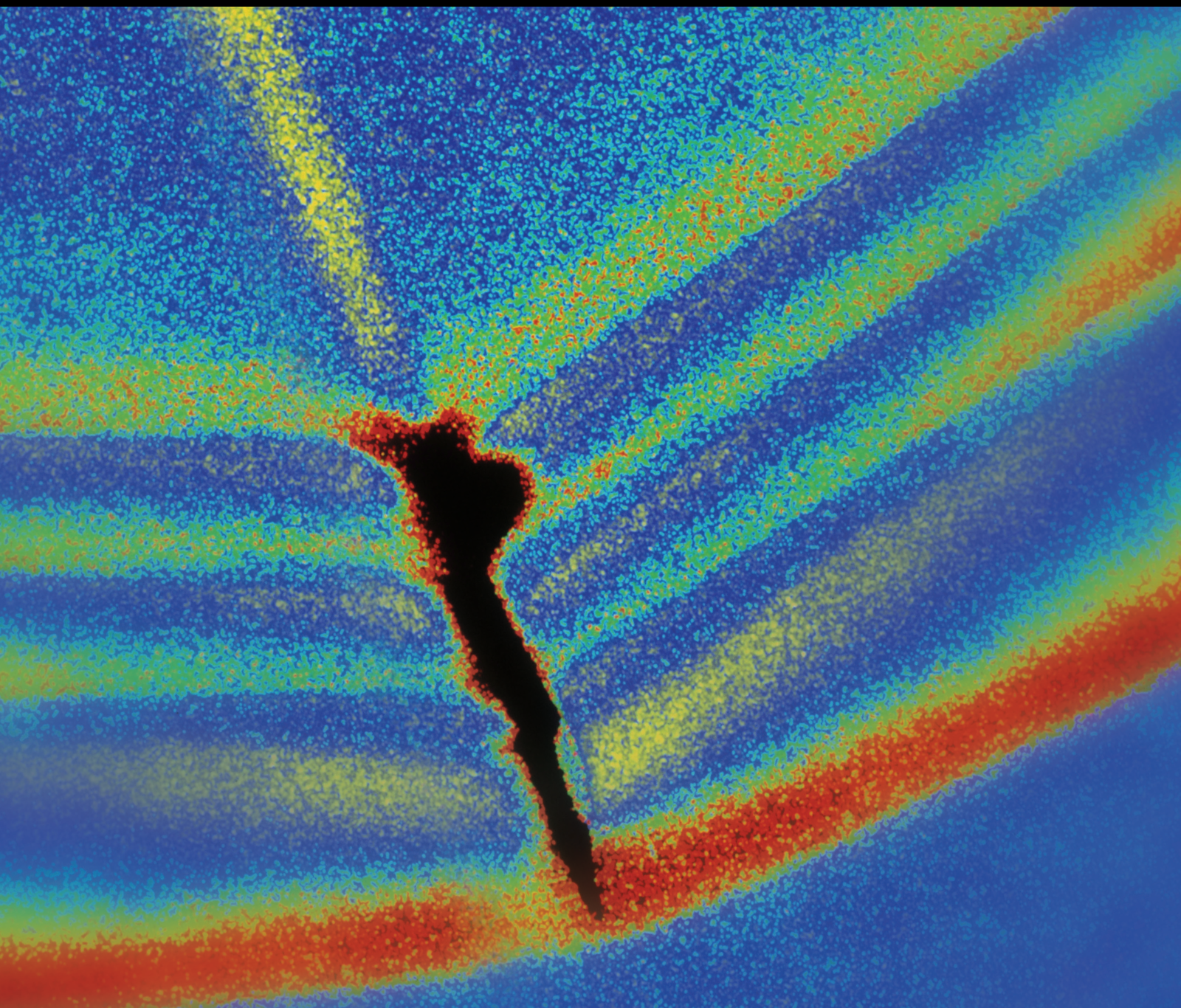


Vibration Control of Systems in Presence of Hard Nonlinearities

Guest Editors: Mario Terzo, Chia-Ming Chang, Zi-Qiang Lang,
and Salvatore Strano





Vibration Control of Systems in Presence of Hard Nonlinearities

Shock and Vibration

Vibration Control of Systems in Presence of Hard Nonlinearities

Guest Editors: Mario Terzo, Chia-Ming Chang, Zi-Qiang Lang,
and Salvatore Strano



Copyright © 2016 Hindawi Publishing Corporation. All rights reserved.

This is a special issue published in "Shock and Vibration." All articles are open access articles distributed under the Creative Commons Attribution License, which permits unrestricted use, distribution, and reproduction in any medium, provided the original work is properly cited.

Editor-in-Chief

Mehdi Ahmadian, Virginia Polytechnic Institute and State University, USA

Editorial Board

Brij N. Agrawal, USA
Marco Alfano, Italy
Farbod Alijani, Canada
Sumeet S. Aphale, UK
Mariano Artés, Spain
Hassan Askari, Canada
Matteo Aureli, USA
Ranjan Banerjee, UK
Mahmoud Bayat, Iran
José A. Becerra Villanueva, Spain
Marco Belloli, Italy
Subhamoy Bhattacharya, UK
Ivo Caliò, Italy
Antonio Carcaterra, Italy
Dumitru I. Caruntu, USA
Noel Challamel, France
Athanasios Chasalevris, UK
Peng Chen, Japan
Ashwin Chinnayya, France
Giorgio Dalpiaz, Italy
Farhang Daneshmand, Canada
Sergio De Rosa, Italy
Dario Di Maio, UK
Longjun Dong, China
Lorenzo Dozio, Italy
Mohamed El badaoui, France
Mohammad Elahinia, USA
Fiorenzo A. Fazzolari, UK

Francesco Franco, Italy
Alessandro Gasparetto, Italy
Gianluca Gatti, Italy
Anindya Ghoshal, USA
Nere Gil-Negrete, Spain
Hassan Haddadpour, Iran
M.I. Herreros, Spain
Hamid Hosseini, Japan
Ian M. Howard, Australia
Reza Jazar, Australia
Sakdirat Kaewunruen, UK
Yuri S. Karinski, Israel
Jeong-Hoi Koo, USA
Georges Kouroussis, Belgium
Mickaël Lallart, France
Kenneth J. Loh, USA
Nuno M. Maia, Portugal
Giuseppe C. Marano, Italy
Laurent Mevel, France
Emiliano Mucchi, Italy
Tony Murmu, UK
Sundararajan Natarajan, India
Toshiaki Natsuki, Japan
Miguel Neves, Portugal
Coral Ortiz, Spain
Gyuhae Park, Republic of Korea
Aleksandar Pavic, UK
Evgeny Petrov, UK

Antonina Pirrotta, Italy
Vitamor Racic, UK
Carlo Rainieri, Italy
Didier Rémond, France
Francesco Ripamonti, Italy
Salvatore Russo, Italy
Edoardo Sabbioni, Italy
Jerzy T. Sawicki, USA
Onome E. Scott-Emuakpor, USA
Vadim V. Silberschmidt, UK
Kumar V. Singh, USA
Isabelle Sochet, France
Alba Sofi, Italy
Jussi Sopanen, Finland
Stefano Sorace, Italy
Narakorn Srinil, UK
Salvatore Strano, Italy
Chao Tao, China
Mario Terzo, Italy
Tai Thai, Australia
Carlo Trigona, Italy
Federica Tubino, Italy
Nerio Tullini, Italy
Marcello Vanali, Italy
Jörg Wallaschek, Germany
Zaili L. Yang, UK
Stana Živanović, UK
Lei Zuo, USA

Contents

Vibration Control of Systems in Presence of Hard Nonlinearities

Mario Terzo, Chia-Ming Chang, Zi-Qiang Lang, and Salvatore Strano
Volume 2016, Article ID 1923574, 2 pages

Novel Distributed PZT Active Vibration Control Based on Characteristic Model for the Space Frame Structure

Hua Zhong, Yong Wang, Hanzheng Ran, Qing Wang, and Changxing Shao
Volume 2016, Article ID 5928270, 9 pages

Modelling of Hysteresis in Vibration Control Systems by means of the Bouc-Wen Model

Chia-Ming Chang, Salvatore Strano, and Mario Terzo
Volume 2016, Article ID 3424191, 14 pages

Novel Hyperbolic Homoclinic Solutions of the Helmholtz-Duffing Oscillators

Yang-Yang Chen, Shu-Hui Chen, and Wei-Wei Wang
Volume 2016, Article ID 9471423, 10 pages

A Water Hammer Protection Method for Mine Drainage System Based on Velocity Adjustment of Hydraulic Control Valve

Yanfei Kou, Jieming Yang, and Ziming Kou
Volume 2016, Article ID 2346025, 13 pages

Nonlinear Seismic Behavior of Different Boundary Conditions of Transmission Line Systems under Earthquake Loading

Li Tian and Xia Gai
Volume 2016, Article ID 6380321, 9 pages

Recent Advances in Bidirectional Modeling and Structural Control

Satyam Paul, Wen Yu, and Xiaou Li
Volume 2016, Article ID 6275307, 17 pages

Modeling and Simulation of Flexible Transmission Mechanism with Multiclearance Joints for Ultrahigh Voltage Circuit Breakers

Fangang Meng, Shijing Wu, Fan Zhang, Zenglei Zhang, Jicai Hu, and Xiaoyong Li
Volume 2015, Article ID 392328, 17 pages

Optimal Trajectory Planning and Linear Velocity Feedback Control of a Flexible Piezoelectric Manipulator for Vibration Suppression

Junqiang Lou, Yanding Wei, Guoping Li, Yiling Yang, and Fengran Xie
Volume 2015, Article ID 952708, 11 pages

Experimental and Theoretical Study on Influence of Different Charging Structures on Blasting Vibration Energy

Wenbin Gu, Zhenxiong Wang, Jianghai Chen, Jianqing Liu, and Ming Lu
Volume 2015, Article ID 248739, 11 pages

Nonlinear Dynamics Analysis of the Semiactive Suspension System with Magneto-Rheological Damper

Hailong Zhang, Enrong Wang, Fuhong Min, Ning Zhang, Chunyi Su, and Subhash Rakheja
Volume 2015, Article ID 971731, 12 pages

Editorial

Vibration Control of Systems in Presence of Hard Nonlinearities

Mario Terzo,¹ Chia-Ming Chang,² Zi-Qiang Lang,³ and Salvatore Strano¹

¹*Department of Industrial Engineering, University of Naples Federico II, 80125 Naples, Italy*

²*Department of Civil Engineering, National Taiwan University, Taipei 10617, Taiwan*

³*Department of Automatic Control and Systems Engineering, University of Sheffield, Mappin Street, Sheffield S1 3JD, UK*

Correspondence should be addressed to Mario Terzo; m.terzo@unina.it

Received 4 November 2015; Accepted 5 November 2015

Copyright © 2016 Mario Terzo et al. This is an open access article distributed under the Creative Commons Attribution License, which permits unrestricted use, distribution, and reproduction in any medium, provided the original work is properly cited.

Vibration phenomena involve a wide range of engineering systems and structures such as buildings, vehicles, aircrafts, bridges, and electronic components. Due to the undesired effects of the vibration induced motions, the vibration control is a theme on which many researchers are focusing their attention in the recent years. The main scope of the vibration control is the suppression or, at least, the attenuation of the undesirable vibrations by means of passive, semiactive, or active devices. Hard nonlinearities can be found in vibrating systems because of inherent system nonlinear properties and/or the presence of dampers, stiffness elements, and actuators which are often characterized by hysteresis, dead zone, and so forth. This special issue intends to provide an up-to-date overview of recent advances in the vibration control of systems characterized by hard nonlinearities.

In the paper “Modelling of Hysteresis in Vibration Control Systems by means of the Bouc-Wen Model” by C.-M. Chang et al., applications of the Bouc-Wen model in vibration control devices are reviewed. The paper “Novel Distributed PZT Active Vibration Control Based on Characteristic Model for the Space Frame Structure” by H. Zhong et al. presents a novel distributed PZT control strategy based on characteristic model for space frame structure. The paper “Recent Advances in Bidirectional Modeling and Structural Control” by S. Paul et al. gives an overview of building structure modeling and control under bidirectional seismic waves. In the paper “Optimal Trajectory Planning and Linear Velocity Feedback Control of a Flexible Piezoelectric Manipulator for Vibration Suppression” by J. Lou et al., an optimal trajectory planning approach is proposed and applied to a flexible piezoelectric manipulator system. The paper “Nonlinear Seismic Behavior

of Different Boundary Conditions of Transmission Line Systems under Earthquake Loading” by L. Tian and X. Gai investigates nonlinear seismic behaviors of different boundary conditions of transmission line system under earthquake loading. The paper “A Water Hammer Protection Method for Mine Drainage System Based on Velocity Adjustment of Hydraulic Control Valve” by Y. Kou et al. proposes a water hammer protection method based on velocity adjustment of hydraulic control valve to deal with the problem of valve-closing water hammer in mine drainage system. In the paper “Novel Hyperbolic Homoclinic Solutions of the Helmholtz-Duffing Oscillators” by Y.-Y. Chen, a new homoclinic solution of the Helmholtz-Duffing oscillator is presented. The paper “Modeling and Simulation of Flexible Transmission Mechanism with Multiclearance Joints for Ultrahigh Voltage Circuit Breakers” by F. Meng et al. proposes a planar rigid-flexible coupling dynamic model of high-speed multilink transmission mechanisms with clearance for ultrahigh voltage circuit breaker. In the paper “Experimental and Theoretical Study on Influence of Different Charging Structures on Blasting Vibration Energy” by W. Gu et al., a study is designed to deduce the law of different charging structures’ influence on blasting vibration energy of far region of blasting and provide reference for controlling side effects of blasting vibration and designing parameters of charging structure. The paper “Nonlinear Dynamics Analysis of the Semiactive Suspension System with Magneto-Rheological Damper” by H. Zhang et al. examines dynamical behavior of a nonlinear oscillator which models a quarter car forced by the road profile. The magneto-rheological (MR) suspension system has been

established, by employing the modified Bouc-Wen force-velocity model of magneto-rheological damper.

*Mario Terzo
Chia-Ming Chang
Zi-Qiang Lang
Salvatore Strano*

Research Article

Novel Distributed PZT Active Vibration Control Based on Characteristic Model for the Space Frame Structure

Hua Zhong,¹ Yong Wang,² Hanzheng Ran,¹ Qing Wang,¹ and Changxing Shao²

¹*Institute of Electronic Engineering, China Academy of Engineering Physics, Mianyang 621999, China*

²*Department of Automation, University of Science and Technology of China, Hefei 230027, China*

Correspondence should be addressed to Hua Zhong; huazhong@mail.ustc.edu.cn

Received 6 July 2015; Revised 19 September 2015; Accepted 21 September 2015

Academic Editor: Mario Terzo

Copyright © 2016 Hua Zhong et al. This is an open access article distributed under the Creative Commons Attribution License, which permits unrestricted use, distribution, and reproduction in any medium, provided the original work is properly cited.

A novel distributed PZT control strategy based on characteristic model is presented for space frame structure in this paper. It is a challenge to obtain the exact mechanical model for space structure, since it is a coupling MIMO plant with unknown parameters and disturbances. Thus the characteristic modeling theory is adopted to establish the needed model, which can accurately describe the dynamic characteristics of the space frame structure in real time. On basis of this model, a keep tracking controller is designed to suppress the vibration actively. It is shown that the proposed model-free method is very robust and easy to implement. To solve the complex and difficulty problem on PZT location optimization, an efficient method with modal strain energy and maximum vibration amplitude is proposed. Finally, a simulation study is conducted to investigate the effectiveness of the proposed active vibration control scheme.

1. Introduction

Space structures are usually applied in the aerospace and civil engineering such as the space boom structures [1]. Generally, since space structures are light and flexible, they are sensitive to vibration which will affect the performance of space equipment [2]. Therefore, it is necessary to suppress vibration for space structure.

Active vibration control method is a good choice for the vibration control of space structure. To achieve good vibration control performance, there are three things to be done, that is, system modelling, sensors/actuators location configuration, and control strategy design.

Space structure's model can be divided into two categories: mechanical model and identification model. The mechanical model is usually established with sophisticated finite element method [3, 4]. Additionally, it is generally used in system dynamics analysis and sensors/actuators location optimization. Nonetheless, it can not be used to design controller directly due to its complexity and inaccuracy. Due to the tremendous efforts devoted by researchers, valuable results on identification modeling for the space structure have

been obtained. Hwang presented an analytical procedure based on the Kalman filtering approach to estimate modal loads applied on a structure [5]. Hazra et al. proposed a method which integrates the blind identification with time-frequency decomposition of signals for flexible structures [6]. Schoen et al. presented an identification algorithm which utilizes modal contribution coefficients to monitor the data collection for large flexible space structures [7]. Although some aforementioned methods have been extensively used in space structure identification, there still exist several disadvantages. On the one hand, the system is inherently complicated, much less the disturbances. On the other hand, the existing results only depend on complex off-line identification methods, which is difficult to grasp the system dynamics in real time. Consequently, it is a challenge to establish the model for space structure with on-line identification method.

For active vibration control of space structure, determination of actuator locations is an important work. If locations of actuators are not proper, active vibration control may not suppress the vibration, even it can increase structure vibration. Therefore, optimization of actuators' locations has attracted many scholars to study. Chen et al. presented

a location optimization approach based on the 1st singular value perturbations of observability and controllability [8]. Xu and Jiang demonstrated an approach with the controllability and observability index of the system [4]. Zhao et al. proposed a continuous variable optimization method to solve the optimal placement of piezoelectric active bars [2]. Li and Huang presented a layered optimization strategy to address location optimization problem [9]. Though the above methods can realize location optimization actuators, the optimization process is complex. Thus, it is needed to find a simple and effective optimization method.

An active vibration controller with simple structure and strong robustness is necessary. Many scholars have devoted themselves to solving this problem. Luo et al. designed simple PD controller for vibration attenuation in Hoop truss structure [10]. Abreu et al. used a standard H_∞ robust controller to suppress structural vibrations [11]. Yang et al. presented an adaptive fuzzy sliding mode controller for vibration of a flexible rectangular plate [12]. Lin and Zheng proposed a parallel neurofuzzy control with genetic algorithm tuning for smart piezoelectric rotating truss structure [13]. de Abreu et al. designed a self-organizing fuzzy controller for vibration control of smart truss structure [1]. Mahmoodi developed a modified positive position feedback controller for vibration control [14]. Wilhelm and Rajamani applied LQR controller to realize multimodal vibration suppression [15]. Among above control strategies, simple controllers (such as PID) are with weak robustness. The complex controllers (H_∞ controller, fuzzy controller) have strong robustness, but they have difficulty in parameter tuning.

Motivated by the above discussions, a novel distributed PZT control based on characteristic model is presented. Characteristic model for space structure is established to accurately describe system's dynamics in time whose form is simple and characteristic parameters of it can contain the information of time delay or high order [16]. Additionally, a simple controller based on characteristic model called keep tracking controller with strong robustness is applied to realize vibration control. Furthermore, a novel actuators location optimization method with modal strain energy (MSE) and maximum vibration amplitude is proposed.

The remainder of the paper is organized as follows. Section 2 establishes the characteristic model for space structure. Section 3 presents the identification of characteristic parameters and control strategy. PZT location optimization is presented in Section 4. Numerical simulation is shown in Section 5. Conclusion is shown in Section 6.

2. Characteristic Modeling for Space Structure

The space frame structure is shown in Figure 1 which contains 26 nodes and 63 beam elements. Nodes 2, 3, 7, and 8 are constrained which are fixed with the floor. Structure excitation direction is z of node 10. Every node has 6 degrees of freedom (DOF). The total DOF is n . The space structure has 63 beam elements. Table 1 shows the connection information among nodes. Space structure consists of aluminum whose cross section is rectangular. Table 2 shows the top 10 natural frequencies.

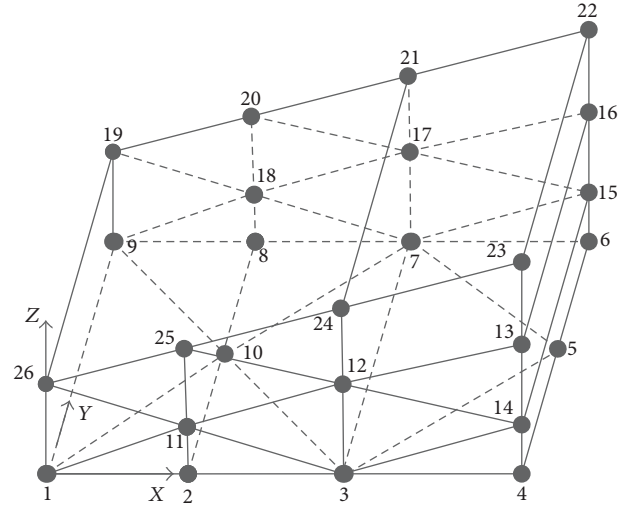


FIGURE 1: The schematic diagram of frame structure.

According to the finite element formulation, the equation of motion for any structure is given by

$$\mathbf{M}\ddot{\mathbf{X}} + \mathbf{C}\dot{\mathbf{X}} + \mathbf{K}\mathbf{X} = \mathbf{F}, \quad (1)$$

where $\mathbf{M} \in \mathbf{R}^{n \times n}$ is mass matrix, $\mathbf{C} \in \mathbf{R}^{n \times n}$ is damping matrix, $\mathbf{K} \in \mathbf{R}^{n \times n}$ is stiffness matrix, $\mathbf{F} \in \mathbf{R}^{n \times 1}$ is load force vector, and $\mathbf{X} \in \mathbf{R}^{n \times 1}$, $\dot{\mathbf{X}} \in \mathbf{R}^{n \times 1}$, and $\ddot{\mathbf{X}} \in \mathbf{R}^{n \times 1}$ are structural displacement, velocity, and acceleration vectors, respectively.

With the knowledge of space frame, parameters \mathbf{M} , \mathbf{C} , and \mathbf{K} are slow time-varying. Then, during short sampling time Δt (ms), it can be considered that \mathbf{M} , \mathbf{C} , and \mathbf{K} are time-invariant. Then the discrete form of motion equation (1) can be described as

$$\begin{aligned} \mathbf{M}\mathbf{X}(k+1) &= (2\mathbf{M} - \mathbf{C}\Delta t - \mathbf{K}\Delta t^2)\mathbf{X}(k) \\ &+ (-\mathbf{M} + \mathbf{C}\Delta t)\mathbf{X}(k-1) + \Delta t^2\mathbf{F}(k). \end{aligned} \quad (2)$$

One has the upper equation (2) as

$$\begin{aligned} \mathbf{X}(k+1) &= \mathbf{G}_1(k)\mathbf{X}(k) + \mathbf{G}_2(k)\mathbf{X}(k-1) \\ &+ \mathbf{H}_1(k)\mathbf{F}(k), \end{aligned} \quad (3)$$

where $\mathbf{G}_1(k) = 2\mathbf{I}_n - \mathbf{M}^{-1}\mathbf{C}\Delta t - \mathbf{M}^{-1}\mathbf{K}\Delta t^2$, $\mathbf{G}_2(k) = -\mathbf{I}_n + \mathbf{M}^{-1}\mathbf{C}\Delta t$, and $\mathbf{H}_1(k) = \Delta t^2\mathbf{M}^{-1}$. The expression (3) is called characteristic model; $\mathbf{G}_1(k)$, $\mathbf{G}_2(k)$, and $\mathbf{H}_1(k)$ are characteristic parameters.

When Δt is very small, the following equation holds:

$$\begin{aligned} \mathbf{G}_1(\infty) &= 2\mathbf{I}_n, \\ \mathbf{G}_2(\infty) &= -\mathbf{I}_n, \\ \mathbf{H}_1(\infty) &= \mathbf{0}_{n \times n}. \end{aligned} \quad (4)$$

Further one has the sum of characteristic parameters as

$$\mathbf{G}_1(\infty) + \mathbf{G}_2(\infty) + \mathbf{H}_1(\infty) = \mathbf{I}_n. \quad (5)$$

TABLE 1: Beam element connection information.

Beam number	Node number
1	1-2
2	2-3
3	3-4
4	4-5
5	5-6
6	6-7
7	7-8
8	8-9
9	9-1
10	9-10
11	1-10
12	2-10
13	10-8
14	10-7
15	10-3
16	3-7
17	3-5
18	5-7
19	1-26
20	25-11
21	11-2
22	24-12
23	12-3
24	23-13
25	13-14
26	14-4
27	15-6
28	16-15
29	22-16
30	17-7
31	21-17
32	18-8
33	20-18
34	19-9
35	19-26
36	26-25
37	26-11
38	1-11
39	25-24
40	25-12
41	11-12
42	11-3
43	24-23
44	24-13
45	12-13
46	12-14
47	3-14
48	23-22
49	13-16

TABLE 1: Continued.

Beam number	Node number
50	14-15
51	21-22
52	21-16
53	17-16
54	17-15
55	7-15
56	20-21
57	20-17
58	18-17
59	18-7
60	19-20
61	19-18
62	9-18
63	24-21

Assuming the output $\mathbf{X}(k)$ loops are decoupled, thus $\mathbf{G}_1(k)$ and $\mathbf{G}_2(k)$ are diagonal matrixes, which can be formulated as

$$\mathbf{G}_1(k) = \begin{bmatrix} g_{11}(k) & 0 & \cdots & 0 \\ 0 & g_{12}(k) & \cdots & 0 \\ \vdots & \vdots & \ddots & \vdots \\ 0 & 0 & \cdots & g_{1n}(k) \end{bmatrix}, \quad (6)$$

$$\mathbf{G}_2(k) = \begin{bmatrix} g_{21}(k) & 0 & \cdots & 0 \\ 0 & g_{22}(k) & \cdots & \vdots \\ \vdots & \vdots & \ddots & 0 \\ 0 & 0 & \cdots & g_{2n}(k) \end{bmatrix}.$$

The characteristic parameter $\mathbf{H}_1(k)$ can be written as

$$\mathbf{H}_1(k) = \begin{bmatrix} h_{11}(k) & h_{12}(k) & \cdots & h_{1n}(k) \\ h_{21}(k) & h_{22}(k) & \cdots & h_{2n}(k) \\ \vdots & \vdots & \ddots & \vdots \\ h_{n1}(k) & h_{n2}(k) & \cdots & h_{nn}(k) \end{bmatrix}. \quad (7)$$

According to the expression in (3) and (6)-(7), the i th characteristic model is

$$x_i(k+1) = g_{1i}(k)x_i(k) + g_{2i}(k)x_i(k-1) + \sum_{r=1}^n h_{ir}(k)F_r(k). \quad (8)$$

TABLE 2: Top 10 natural frequencies.

Order	1	2	3	4	5	6	7	8	9	10
Frequency (Hz)	10.03	15.51	18.02	22.82	25.85	27.72	29.35	31.45	42.22	42.61

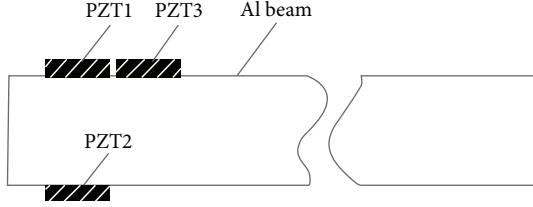


FIGURE 2: The schematic diagram of PZT structure.

Similarly, one has the characters of characteristic parameters in i th output loop as

$$\begin{aligned}
 g_{1i}(\infty) &= 2, \\
 g_{2i}(\infty) &= -1, \\
 h_{ir}(\infty) &= 0, \quad (9) \\
 g_{1i}(\infty) + g_{2i}(\infty) + \sum_{r=1}^n h_{ir}(\infty) &= 1.
 \end{aligned}$$

Because PZT with small size and light weight does not affect structure's characteristics after pasting on the structure surface, PZT is selected as sensor and actuator. Figure 2 indicates the schematic diagram of PZT structure. It is shown that a pair of PZT1 and PZT2 act as actuator and another PZT3 acts as sensor. Additionally, actuators far away PZT3 have little function on PZT3. Therefore, (8) can be simplified as

$$\begin{aligned}
 x_i(k+1) &= g_{1i}(k)x_i(k) + g_{2i}(k)x_i(k-1) \\
 &\quad + h_{ii}(k)F_i(k) = \Phi^T(k)\mathfrak{g}(k), \quad (10)
 \end{aligned}$$

where $\Phi(k) = [x_i(k) \ x_i(k-1) \ F_i(k)]^T$ and $\mathfrak{g}(k) = [g_{1i}(k) \ g_{2i}(k-1) \ h_{ii}(k)]^T$.

3. Keep Tracking Control Law

With a proper parameter estimator, the characteristic parameters can adaptively converge to true values. The general methods of parameters identification are least square method and gradient method. Compared with the least square method, gradient method has a smaller amount of calculation and it will not cause parameters to diverge with improper forgetting factors. Thus, the gradient method [16] will be used to estimate the characteristic parameters. The form is

$$\begin{aligned}
 \hat{\mathfrak{g}}(k) &= \frac{\lambda_1 \Phi(k-1) [x_i(k) - \Phi^T(k-1)\hat{\mathfrak{g}}(k-1)]}{\Phi^T(k-1)\Phi(k-1) + \lambda_2} \\
 &\quad + \hat{\mathfrak{g}}(k-1). \quad (11)
 \end{aligned}$$

The range of λ_1 and λ_2 is $0 < \lambda_1 < 1, 0 < \lambda_2 < 4$. The estimates of $g_{1i}(k)$, $g_{2i}(k)$, and $h_{ii}(k)$ in the characteristic model are $\hat{\mathfrak{g}}^T(k) = [\hat{g}_{1i}(k) \ \hat{g}_{2i}(k) \ \hat{h}_{ii}(k)]$.

To ensure the output $y(k+1)$ equals the desired reference input $r(k+1)$, the need control input should satisfy the following condition:

$$u(k) = \frac{r(k+1) - \hat{g}_{1i}(k)y(k) - \hat{g}_{2i}(k)y(k-1)}{\hat{h}_{ii}(k)}. \quad (12)$$

To avoid the fact of $\hat{h}_{ii}(0) = 0$, a slack variable λ is introduced, which could guarantee that the control input is smooth and easy to implement. Consider

$$u(k) = \frac{r(k+1) - \hat{g}_{1i}(k)y(k) - \hat{g}_{2i}(k)y(k-1)}{\lambda + \hat{h}_{ii}(k)}, \quad (13)$$

where λ is a constant. This control law is called characteristic model-based keep tracking control (CMKTC) law [16, 17]. With the control law, system can perfectly track the reference input.

4. PZT Location Optimization

Considering the complexity of traditional optimization algorithm, MSE and maximum amplitude are applied to optimize locations of PZT whose optimization process is simple.

Firstly beam elements of space structure are divided into three categories: underside beam elements $N_u = \{1, 2, \dots, 17, 18\}$, front and rear beam elements $N_{fr} = \{19, 20, \dots, 33, 34, 36, 37, \dots, 46, 47, 51, 52, \dots, 61, 62\}$, and connection beam elements between front and rear $N_c = \{35, 48, 49, 50, 63\}$. Through beams' MSE, the sensitive beams are obtained. With i th natural frequency, the j th beam's MSE [18] can be described as

$$E_{ij} = \frac{\phi_i^T \mathbf{K}_j \phi_i}{\omega_i^2}, \quad (14)$$

where ϕ_i is modal shape vector with i th natural frequency which is the i th column of \mathbf{V}_{norm} . $\mathbf{V}_{\text{norm}} = \mathbf{V}(\sqrt{\mathbf{V}^T \mathbf{M} \mathbf{V}})^{-1}$ is normalized modal matrix, where \mathbf{V} is modal matrix. \mathbf{K}_j is j th beam stiffness matrix; ω_i is i th vibration frequency.

Figures 3–6 show the first four order MSE. From the figures, sensitive beam element sets are obtained: underside sensitive beam element set $N_s = \{1, 4, 5, 9, 10, 11\}$, front and rear sensitive beam element set $N_b = \{19, 20, 23, 25, 28, 34, 36, 37\}$, and connection sensitive beam element set $N_h = \{35, 48, 49, 50, 63\}$. N_s , N_b , and N_h are the subsets of N_u , N_{fr} , and N_c , respectively.

Additionally, it is needed to select the most sensitive beam element from N_s , N_b , and N_h according to maximum

TABLE 3: z -direction maximum amplitude of beams in N_s .

Beam number	1	4	5	9	10	11
Maximum amplitude (mm)	0.0005	0.0013	0.0015	0.1422	0.3996	0.3996

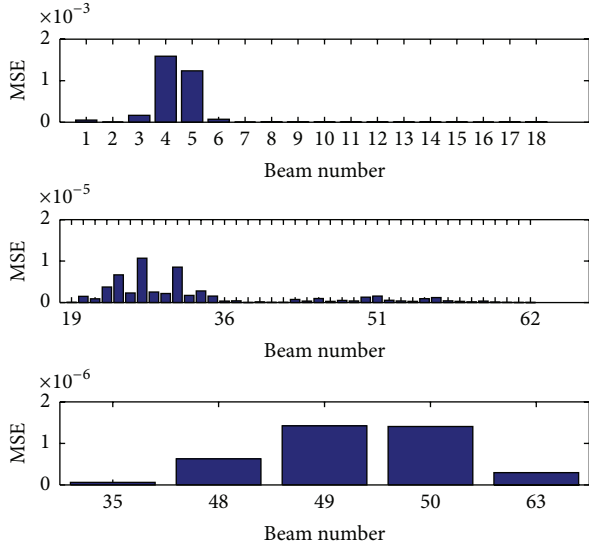


FIGURE 3: First-order MSE.

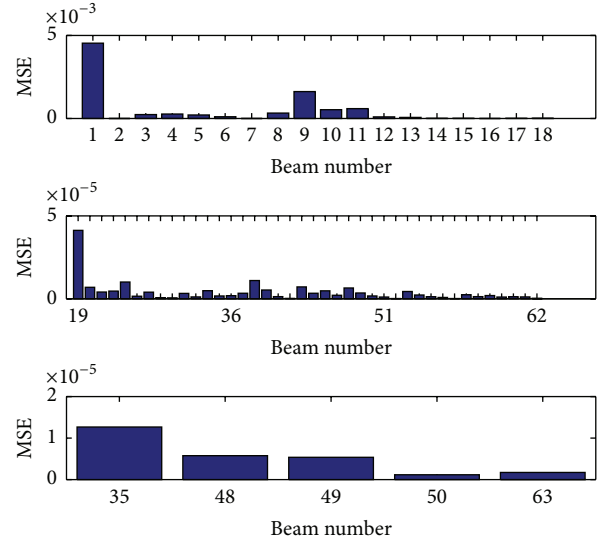


FIGURE 5: Third-order MSE.

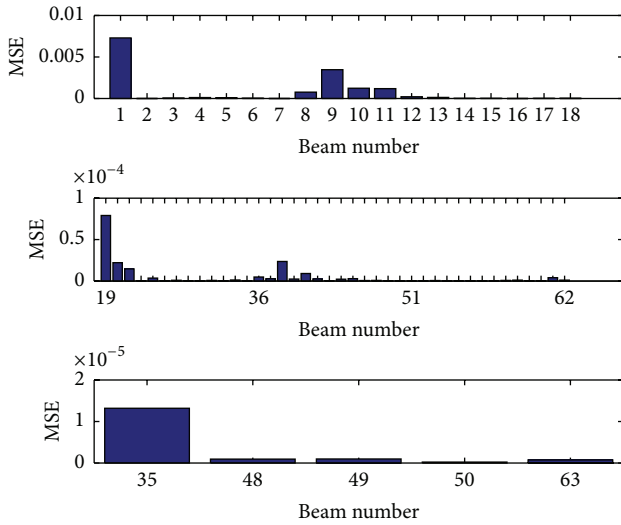


FIGURE 4: Second-order MSE.

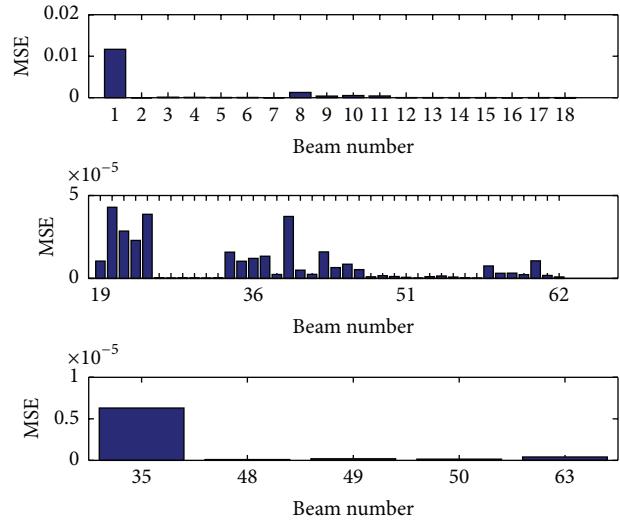


FIGURE 6: Fourth-order MSE.

amplitude. Excitation node is selected as node 10 and excitation direction is z . Excitation force $f_e = 10 \sin(2\pi ft)$, and excitation frequency f is selected as the first natural frequency 10.03 Hz. Through analysing vibration response curves of N_s , it is concluded that z -direction vibration amplitude is much larger than x and y which is considered. Similarly, analysing vibration response curves of N_b and N_h , it is shown that y -direction vibration amplitude is much larger than x and y . Thus, it is only needed to compare z -direction of the maximum amplitude for beams in N_b and N_h .

From Table 3 which shows the z -direction maximum vibration amplitude of N_s , 10th or 11th beam element is

the most sensitive beam element. In addition, compared with the other location on the 10th or 11th beam element, location approaching node 10 has larger vibration amplitude which is appropriate location for pasting PZT. Similarly, Table 4 indicates that 19th or 37th beam element is the most sensitive beam element in N_b while the 19th beam element is selected. Furthermore, considering that x -direction vibration amplitude nearing node 19 is larger than the other position on 19th beam element while y -direction vibration amplitude on any location of 19th beam element is nearly the same, so position approaching node 19 on 19th beam element is another appropriate location for pasting PZT. Lastly, 35th

TABLE 4: y -direction maximum amplitude of beams in N_b .

Beam number	19	20	23	25	28	34	36	37
Amplitude (mm)	0.1909	0.0930	0.0423	0.0713	0.0713	0.1909	0.0930	0.1909

TABLE 5: y -direction maximum amplitude of beams in N_h .

Beam number	35	48	49	50	63
Maximum amplitude (mm)	0.1909	0.1000	0.0703	0.0135	0.0714

TABLE 6: Maximum amplitude on 35th beam element.

s (m)	x (mm)	y (mm)	z (mm)
0	0.00022	0.19	0.00048
0.2	0.02	0.19	0.018
0.4	0.003	0.19	0.025
0.6	0.018	0.19	0.018
0.8	0.00018	0.19	0.00038

beam element is the most sensitive beam element in N_h from Table 5. Since any location's y -direction vibration amplitude of 35th beam element has nearly the same value, z -direction vibration amplitude is considered. Define variable s as the distance between any location on 35th beam element and node 19. Table 6 shows that the middle location with the maximum vibration amplitude is another appropriate location to paste PZT.

In a word, three optimization positions are middle position on 35th beam element (1st controller CMKTC1), location approaching node 19 on 19th beam element (2nd controller CMKTC2), and location approaching node 10 on 10th beam element (3rd controller CMKTC3).

5. Numerical Simulation

5.1. Characteristic Model Verification Simulation. To verify that characteristic model can accurately describe dynamic characters of system, with the literature [16], four forms of control input are selected as follows:

- (a) Step signal $F_i(k) = 10$.
- (b) Smooth step signal $F_i(k) = 0.97u(k-1) + 0.3$.
- (c) 10 Hz sinusoidal signal $F_i(k) = 10 \sin(20k\pi\Delta t)$.
- (d) 10 Hz square wave signal $F_i(k) = 10 \text{sign}(\sin(20k\pi\Delta t))$.

Four different control input signals are shown in Figure 7. Control input direction is z -direction of node 10; vibration displacement output direction is selected as y -direction of node 19. Output estimation error $\hat{e}(k)$ can be expressed as $\hat{e}(k) = x_i(k) - \Phi^T(k-1)\hat{\theta}(k)$. Sampling time Δt is selected as 0.001 s.

Figures 8–11 show the output estimation error with different control input. When control input is step signal or smooth step signal, output estimation error's magnitude is 10^{-7} . If control input is sinusoidal signal or square wave signal, output estimation error's magnitude is 10^{-5} . Therefore,

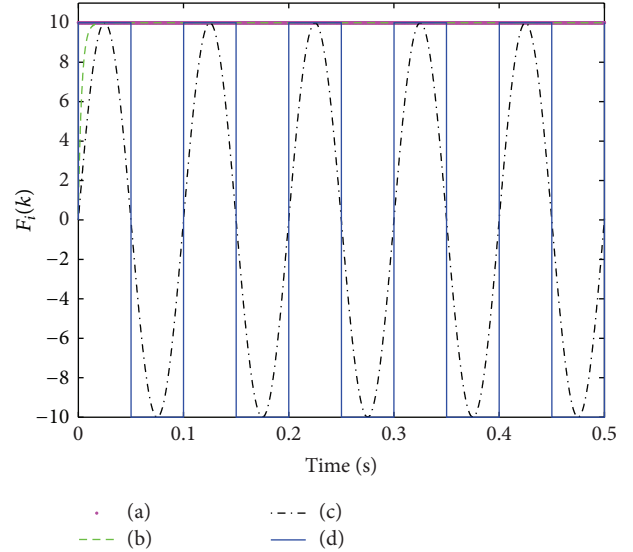


FIGURE 7: Four-control input signal.

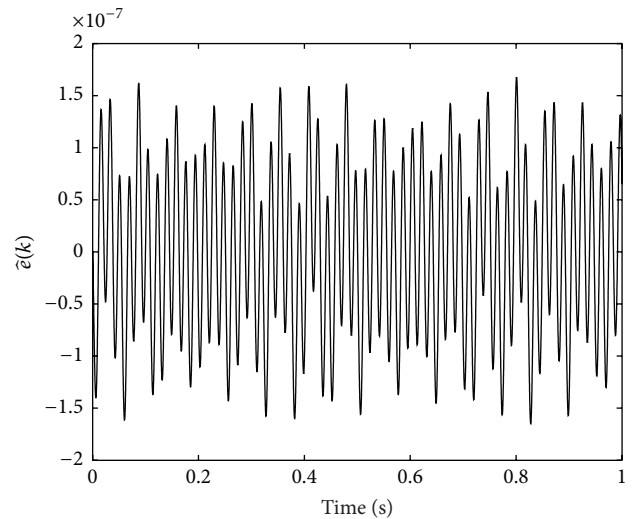


FIGURE 8: Output estimation error with (a).

output of characteristic model can approach the output of space structure. In addition, characteristic model can accurately describe space structure's dynamic characters.

5.2. Distributed PZT Vibration Simulation. Table 7 shows the related parameters of PZT and Al. With characters of characteristic parameters (9), select the initial value of

TABLE 7: Related parameters of PZT and aluminum.

	Thickness (mm)	Width (mm)	Elastic modulus (Gpa)	PSC (C/N)
PZT	1	10	8×10^{10}	5×10^{-10}
Al	5	12	7×10^{10}	—

Remark 1: PSC: Piezoelectric Strain Constant.

TABLE 8: Control parameter.

Parameter	CMKTC1	CMKTC2	CMKTC3
λ	-0.0005	-0.0005	-0.025

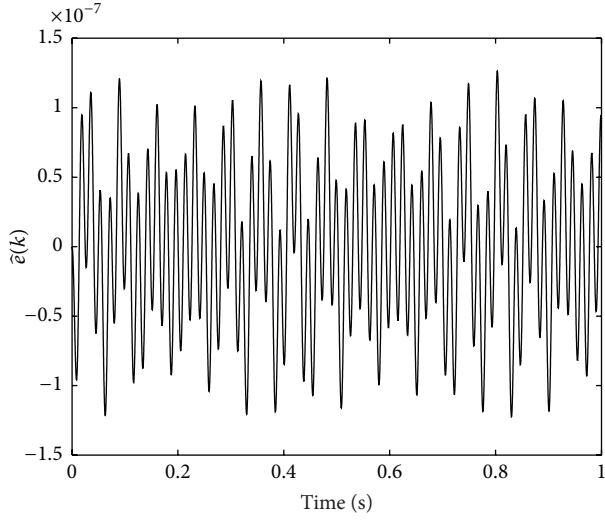


FIGURE 9: Output estimation error with (b).

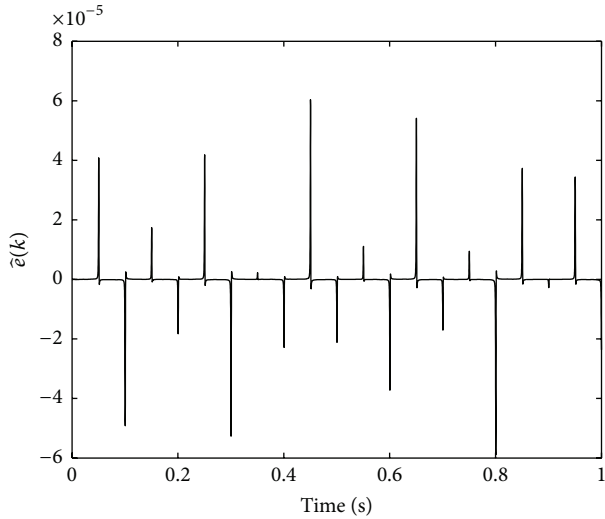


FIGURE 10: Output estimation error with (c).

characteristic parameters as $\hat{\Theta}^T(0) = [1.618 \ -0.618 \ 0.03]$. Related parameters of gradient method are $\lambda_1 = 0.8$, $\lambda_2 = 0.4$. Sampling time Δt is selected as 0.001 s. Control parameters are shown in Table 8. Excitation force $f_e = 10 \sin(2\pi ft)$; excitation frequency f is selected as the first natural frequency 10.03 Hz. Select nodes 19, 22, and 25 as observation nodes. It should be emphasized that the output feedback of CMKTC1 is y -direction displacement.

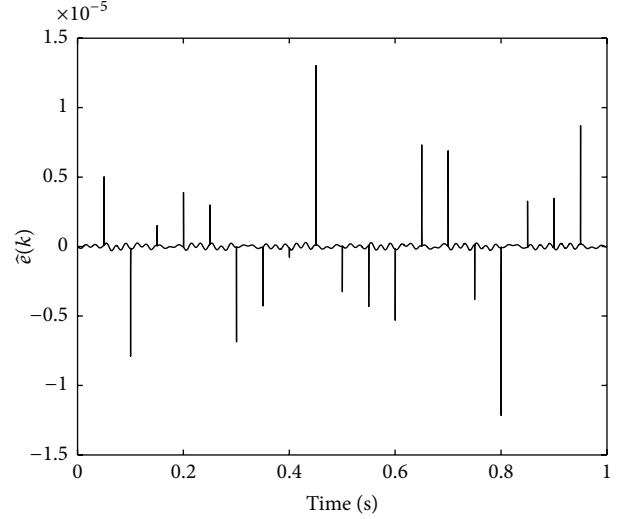


FIGURE 11: Output estimation error with (d).

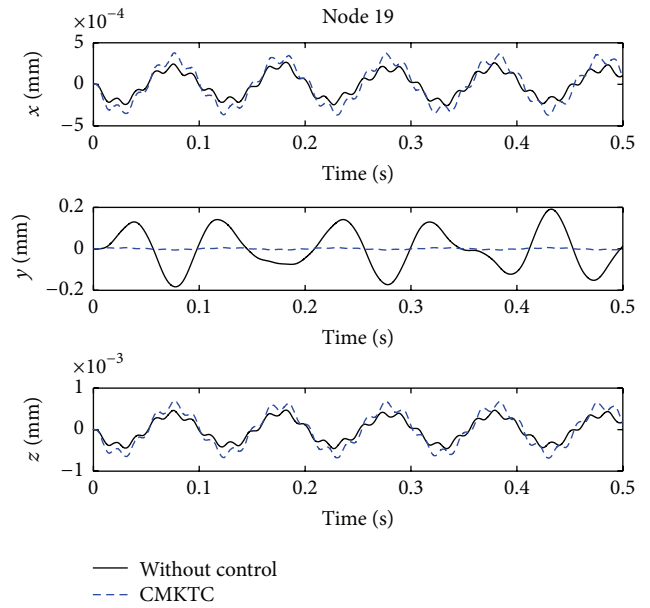


FIGURE 12: Displacement of node 19.

Figures 12–14 are the vibration displacement curves of nodes 19, 22, and 25, respectively. It is shown that y -direction vibration displacement is much larger than x or z and suppressing vibration effect of y -direction is obvious. With CMKTC, y -direction vibration displacement of nodes 19, 22, and 25 attenuates to 4×10^{-3} , 4.5×10^{-4} , and 1.8×10^{-4} , respectively, which indicates the effectiveness of distributed PZT vibration control. Control input is presented in Figure 15 which shows that control voltage is within voltage range of PZT.

TABLE 9: y -direction vibration attenuation ratio of nodes 19, 22, and 25 with different amplitude sinusoidal disturbance.

Disturbance amplitude	10	20	30	40	50	60	70	80	90	100
Node 19 (%)	96.91	96.52	96.07	95.65	95.18	94.74	94.28	93.82	93.35	92.72
Node 22 (%)	96.61	96.71	96.42	96.16	95.90	95.45	95.01	94.54	94.10	93.65
Node 25 (%)	96.36	95.27	96.47	93.73	92.00	90.33	88.60	86.90	85.20	83.50

TABLE 10: y -direction vibration attenuation ratio of nodes 19, 22, and 25 with different power-band white noise.

Noise power	0.05	0.10	0.15	0.20	0.25	0.30	0.35	0.40	0.45	0.50
Node 19 (%)	95.45	94.76	93.82	93.51	92.98	92.50	92.15	91.83	91.37	91.20
Node 22 (%)	96.24	96.34	96.21	96.21	96.21	96.21	96.19	96.18	96.16	96.15
Node 25 (%)	96.00	95.83	95.73	95.63	95.53	95.43	95.33	95.30	95.23	95.17

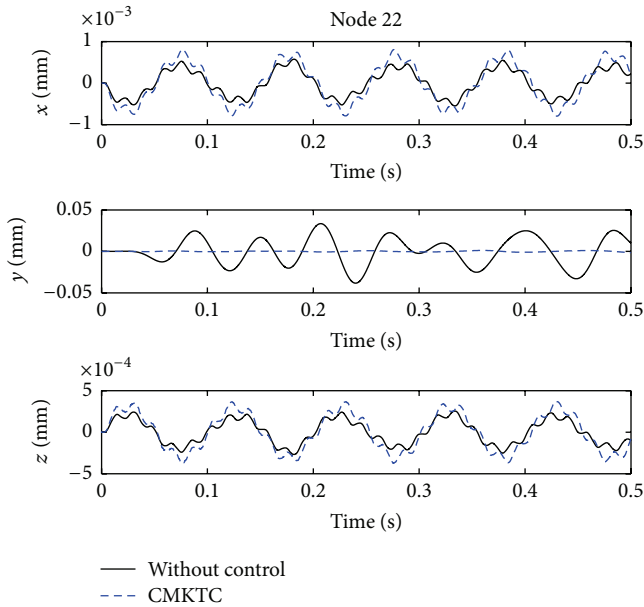


FIGURE 13: Displacement of node 22.

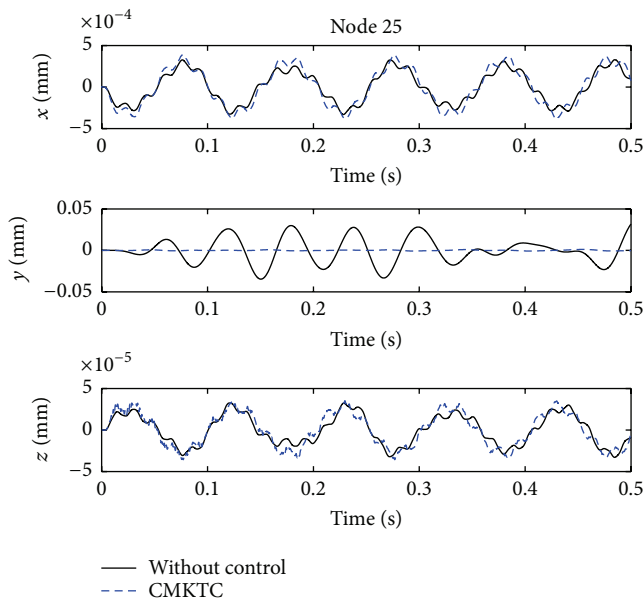


FIGURE 14: Displacement of node 25.

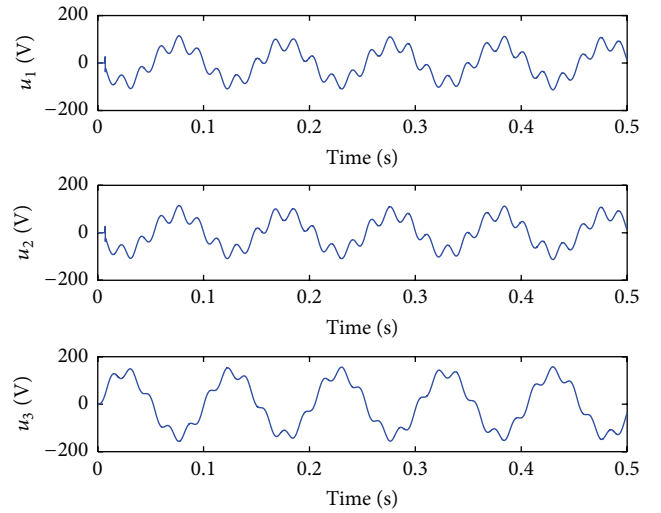


FIGURE 15: Control input.

To verify the robustness of CMKTC, the matched disturbance is added. When the sinusoidal matched disturbance $f_e = A \sin(200t)$ with different amplitude is added, Table 9 shows y -direction vibration attenuation ratio of nodes 19, 22, and 25. From the table, it is known that node 25 is more sensitive than node 19 and node 22. No matter how, sinusoidal disturbance has small effect on y -direction vibration displacement.

Considering that there exists noise in actual system, so band-white noise with different noise power is added. y -direction vibration attenuation ratio of nodes 19, 22, and 25 is presented in Table 10. The table indicates that vibration damping ratio decreases with the increase of noise power. Of course, band-white noise has small effect on system performance and CMKTC is with strong robustness.

6. Conclusion

In this paper, a novel distributed PZT control strategy based on characteristic model has been proposed. To avoid the difficulty in obtaining the mechanical model of space structure, an efficient model-free modeling approach, that is, the so-called characteristic model theory, is adopted.

Then a PZT position optimization method based on MSE and maximum vibration amplitude has been presented, in which the placement optimization of sensors and actuators is realized. Due to the established characteristic model, a simple but efficient CMKTC is designed. The power of the proposed control strategy is demonstrated on several numerical examples.

Conflict of Interests

The authors declare that there is no conflict of interests regarding the publication of this paper.

Acknowledgment

This work was supported by the National Natural Science Foundation of China (no. 61573332).

References

- [1] G. L. de Abreu, G. P. de Melo, V. Lopes, and M. J. Brennan, "Active modal damping control of a smart truss structure using a self-organizing fuzzy controller," *Journal of the Brazilian Society of Mechanical Sciences and Engineering*, vol. 37, no. 2, pp. 441–450, 2015.
- [2] G. Zhao, J. Wang, and Y. Gu, "Optimal placement of piezoelectric active bars in vibration control by topological optimization," *Acta Mechanica Sinica*, vol. 24, no. 6, pp. 699–708, 2008.
- [3] B. Jaishi and W.-X. Ren, "Structural finite element model updating using ambient vibration test results," *Journal of Structural Engineering*, vol. 131, no. 4, pp. 617–628, 2005.
- [4] B. Xu and J. S. Jiang, "Integrated optimization of structure and control for piezoelectric intelligent trusses with uncertain placement of actuators and sensors," *Computational Mechanics*, vol. 33, no. 5, pp. 406–412, 2004.
- [5] J.-S. Hwang, A. Kareem, and W.-J. Kim, "Estimation of modal loads using structural response," *Journal of Sound and Vibration*, vol. 326, no. 3-5, pp. 522–539, 2009.
- [6] B. Hazra, A. Sadhu, A. J. Roffel, and S. Narasimhan, "Hybrid time-frequency blind source separation towards ambient system identification of structures," *Computer-Aided Civil and Infrastructure Engineering*, vol. 27, no. 5, pp. 314–332, 2012.
- [7] M. P. Schoen, R. C. Hoover, S. Chinvararat, and G. M. Schoen, "System identification and robust controller design using genetic algorithms for flexible space structures," *Journal of Dynamic Systems, Measurement and Control*, vol. 131, no. 3, pp. 1–10, 2009.
- [8] S. H. Chen, Z. J. Cao, and Z. S. Liu, "A method of for the section of sensors and actuators location," *Acta Mechanica Sinica*, vol. 14, no. 4, pp. 353–362, 1998.
- [9] W. P. Li and H. Huang, "Integrated optimization of actuator placement and vibration control for piezoelectric adaptive trusses," *Journal of Sound and Vibration*, vol. 332, no. 1, pp. 17–32, 2013.
- [10] Y. Luo, M. Xu, B. Yan, and X. Zhang, "PD control for vibration attenuation in Hoop truss structure based on a novel piezoelectric bending actuator," *Journal of Sound and Vibration*, vol. 339, pp. 11–24, 2015.
- [11] G. Abreu, M. Brennan, and J. Lopes, "Robust control of an intelligent truss structure," in *Proceedings of the 10th International Conference on Recent Advances in Structural Dynamics*, Southampton, UK, July 2010.
- [12] J. Y. Yang, Z. Q. Liu, X. Cui et al., "Experimental study of adaptive fuzzy sliding mode control for vibration of a flexible rectangular plate," *International Journal of Aeronautical and Space Sciences*, vol. 16, no. 1, pp. 28–40, 2015.
- [13] J. Lin and Y. B. Zheng, "Vibration suppression control of smart piezoelectric rotating truss structure by parallel neuro-fuzzy control with genetic algorithm tuning," *Journal of Sound and Vibration*, vol. 331, no. 16, pp. 3677–3694, 2012.
- [14] S. N. Mahmoodi and M. Ahmadian, "Active vibration control with modified positive position feedback," *Journal of Dynamic Systems, Measurement and Control*, vol. 131, no. 4, 8 pages, 2009.
- [15] J. Wilhelm and R. Rajamani, "Methods for multimodal vibration suppression and energy harvesting using piezoelectric actuators," *Journal of Vibration and Acoustics*, vol. 131, no. 1, pp. 273–283, 2009.
- [16] H. X. Wu, J. Hu, and Y. C. Xie, *Characteristic Model-Based Intelligent Adaptive Control*, Science and Technology Press of China, Beijing, China, 2009.
- [17] H. X. Wu, J. Hu, and Y. C. Xie, "Characteristic model-based all-coefficient adaptive control method and its applications," *IEEE Transactions on Systems, Man and Cybernetics Part C: Applications and Reviews*, vol. 37, no. 2, pp. 213–221, 2007.
- [18] A. Preumont, "On the damping of a piezoelectric truss," in *Proceedings of the 21st International Congress of Theoretical and Applied Mechanics*, pp. 287–301, Warsaw, Poland, August 2005.

Review Article

Modelling of Hysteresis in Vibration Control Systems by means of the Bouc-Wen Model

Chia-Ming Chang,¹ Salvatore Strano,² and Mario Terzo²

¹Department of Civil Engineering, National Taiwan University, Taipei, Taiwan

²Department of Industrial Engineering, University of Naples Federico II, Naples, Italy

Correspondence should be addressed to Mario Terzo; m.terzo@unina.it

Received 24 July 2015; Revised 19 October 2015; Accepted 25 October 2015

Academic Editor: Chao Tao

Copyright © 2016 Chia-Ming Chang et al. This is an open access article distributed under the Creative Commons Attribution License, which permits unrestricted use, distribution, and reproduction in any medium, provided the original work is properly cited.

The review presents developments concerning the modelling of vibration control systems with hysteresis. In particular, the review focuses on applications of the Bouc-Wen model that describes accurate hysteretic behaviour in vibration control devices. The review consists of theoretical aspects of the Bouc-Wen model, identification procedures, and applications in vibration control.

1. Introduction

Vibration control systems are adopted for the suppression or, at least, the attenuation of undesirable vibrations that can affect systems and structures, such as buildings, vehicles, aircraft, and bridges. These systems often show nonlinear behaviour due to variable material properties, changeable geometry, and additional nonlinear devices, resulting in hysteresis phenomena. To predict system responses, many hysteretic models have been developed.

Hysteresis is a nonlinear behaviour encountered in a wide variety of processes in which the relation between input and output variables involves memory effects. The detailed physical modelling of these systems is an arduous task, and the models obtained are often too complex to be used in real-world applications [1]. For this reason, alternative models of systems with hysteresis have been proposed. These models combine some physical understanding of the hysteretic system with some black-box modelling, named “semiphysical” models.

Over the years, various semiphysical models of hysteresis have been proposed. One of the most widely adopted ones is the Bouc-Wen hysteresis model [2, 3]. The best feature of this model is its versatility; that is, through appropriate choices of model parameters, it can represent a wide variety of softening or hardening smoothly varying or nearly bilinear hysteretic behaviours.

The Bouc-Wen model has been extensively used in the current literature to mathematically describe components and devices with hysteretic behaviours. Thus, the objective of this literature review is to provide engineers and researchers with an overview of the work that addresses the modelling of vibration control systems by means of the Bouc-Wen model. This review is divided into three major parts: Section 2 focuses on the mathematical and physical properties of the Bouc-Wen model, whereas Section 3 focuses on identification of the Bouc-Wen model parameters. Section 4 provides results concerning several vibration control case studies in which the effectiveness of the Bouc-Wen model, for the accurate description of hysteresis, is verified.

2. Mathematical Properties of the Bouc-Wen Model

In this section, a description of the mathematical formulation of the Bouc-Wen model is presented.

Consider, as an example, the equation of motion of a single-degree-of-freedom (SDOF) mechanical system:

$$m\ddot{u}(t) + c\dot{u}(t) + F(t) = f(t), \quad (1)$$

where m is the mass, $u(t)$ is the displacement, c is the linear viscous coefficient, $F(t)$ is the restoring force, and $f(t)$ is the

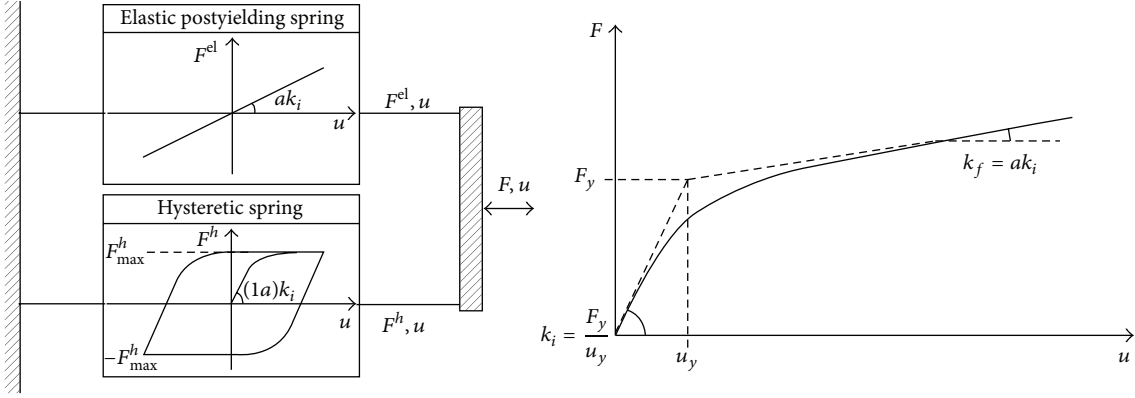


FIGURE 1: Bouc-Wen model [4].

excitation force; the overdot indicates derivative with respect to time.

The restoring force $F(t)$, based on the Bouc-Wen model, is

$$F(t) = a \frac{F_y}{u_y} u(t) + (1-a) F_y z(t), \quad (2)$$

where $a := k_f/k_i$ is the ratio of postyield stiffness k_f to preyield stiffness $k_i := F_y/u_y$, F_y is the yield force, u_y is the yield displacement, and $z(t)$ is a nonobservable dimensionless hysteretic variable that obeys the following nonlinear differential equation with zero initial condition ($z(0) = 0$):

$$\dot{z}(t) = \dot{u}(t) \{A - [\gamma + \beta \operatorname{sgn}(\dot{u}(t) z(t))] |z(t)|^n\}. \quad (3)$$

The coefficients A , β , γ , and n are dimensionless quantities that control the behaviour of the model and $\operatorname{sgn}(\cdot)$ is the signum function. For small values of the positive exponential parameter n the transition from elastic to postelastic branch is smooth, whereas for large values the transition becomes abrupt, approaching that of a bilinear model. The parameters β and γ control the size and shape of the hysteretic loop. The notation varies from paper to paper and very often the places of β and γ are exchanged.

From (2) it follows that the restoring force $F(t)$ can be divided into an elastic and a hysteretic part as follows:

$$F^{\text{el}}(t) = a \frac{F_y}{u_y} u(t) = ak_i u(t) = k_f u(t), \quad (4)$$

$$F^h(t) = (1-a) k_i z(t).$$

Thus, the model can be visualized as two springs connected in parallel [4] (Figure 1).

The parameters of the Bouc-Wen model have the following criteria:

$$\begin{aligned} a &\in [0, 1], \\ k_i &> 0, \\ k_f &> 0, \\ c &> 0, \\ A &> 0, \\ n &> 1, \\ \beta &> 0, \\ \gamma &\in [-\beta, \beta]. \end{aligned} \quad (5)$$

In [23], it has been proved that the parameters of the Bouc-Wen model are functionally redundant, and indeed multiple parameter vectors can produce an identical response under a given excitation. This redundancy can be then removed by fixing parameter A to unity [23].

Constantinou and Adnane [24] suggested the constraint $A/(\beta+\gamma) = 1$ in order to reduce the total number of unknown parameters to six: γ , n , a , F_y , u_y , and c .

In [25], an asymmetrical Bouc-Wen model has been obtained adjusting the velocity as

$$\dot{u}(t) \leftarrow (\dot{u}(t) - \operatorname{sgn}(u(t))), \quad (6)$$

where μ is the scale factor for the adjustment.

Modification of the Bouc-Wen model presented in [26–28] included strength, stiffness, and pinching degradation effects, by means of suitable degradation functions:

$$\begin{aligned} \dot{z}(t) = & \frac{h(z(t))}{\eta(\varepsilon)} \dot{u}(t) \{A(\varepsilon) \\ & - \nu(\varepsilon) [\beta \operatorname{sgn}(\dot{u}(t)) |z(t)|^{n-1} z(t) + \gamma |z(t)|^n]\}, \end{aligned} \quad (7)$$

where ε is the absorbed hysteretic energy and the functions $\nu(\varepsilon)$, $\eta(\varepsilon)$, and $h(z)$ are associated with strength, stiffness, and

pinching degradation effects, respectively. $\nu(\varepsilon)$, $A(\varepsilon)$, and $\eta(\varepsilon)$ are linearly increasing functions defined as

$$\begin{aligned}\nu(\varepsilon) &= \nu_0 + \delta_\nu \varepsilon(t), \\ A(\varepsilon) &= A_0 - \delta_A \varepsilon(t), \\ \eta(\varepsilon) &= \eta_0 + \delta_\eta \varepsilon(t).\end{aligned}\quad (8)$$

The pinching function $h(z)$ is

$$h(z) = 1 - \varsigma_1(\varepsilon) \exp\left(-\frac{(z(t) \operatorname{sgn}(\dot{u}) - qz_u)^2}{(\varsigma_2(\varepsilon))^2}\right), \quad (9)$$

where

$$\begin{aligned}\varsigma_1(\varepsilon) &= (1 - \exp(-p\varepsilon(t))) \varsigma, \\ \varsigma_2(\varepsilon) &= (\psi_0 + \delta_\psi \varepsilon(t)) (\lambda + \varsigma_1(\varepsilon)),\end{aligned}\quad (10)$$

and z_u is the ultimate value of z , given by

$$z_u = \sqrt[n]{\frac{1}{\nu(\beta + \gamma)}}. \quad (11)$$

The additional model parameters are $\delta_\nu > 0$, $\delta_A > 0$, $\delta_\eta > 0$, ν_0 , A_0 , η_0 , ψ_0 , δ_ψ , λ , p , and ς . When $\delta_\nu = 0$, $\delta_\eta = 0$, or $h(z) = 1$, respectively, no strength degradation, stiffness degradation, or pinching effect is considered in the model.

It is important to note that a Bouc-Wen model could present a good match with the real data for a specific input, while it could not necessarily keep significant physical properties for different exciting inputs. On the basis of this consideration, the physical and mathematical properties of the Bouc-Wen model are comprehensively discussed in [1] and it has been found that if the system parameters respect the constraints

$$\begin{aligned}n &\geq 1, \\ u_y &> 0, \\ A &> 0, \\ \beta + \gamma &> 0, \\ \beta - \gamma &\geq 0,\end{aligned}\quad (12)$$

then the model is valid independently of the exciting input. When (12) are satisfied, (3) can be expressed in a normalized form.

Defining the parameters

$$\begin{aligned}\rho &= \frac{A}{u_y z_0} > 0, \\ \sigma &= \frac{\beta}{\beta + \gamma} \geq \frac{1}{2}, \\ z_0 &= \sqrt[n]{\frac{A}{\beta + \gamma}},\end{aligned}\quad (13)$$

it follows

$$\begin{aligned}\dot{w}(t) &= \rho \dot{u}(t) \left\{ 1 + |w(t)|^n \sigma \left[1 - \operatorname{sgn}(\dot{u}(t) w(t)) - \frac{1}{\sigma} \right] \right\}\end{aligned}\quad (14)$$

with

$$w(t) = \frac{z(t)}{z_0}. \quad (15)$$

In [29], it is demonstrated that $w(t)$ is bounded in the range $[-1, 1]$.

Substituting (14) and (15) in (2), it follows

$$F(t) = k_f u(t) + k_w w(t), \quad (16)$$

where

$$k_w = (1 - a) F_y z_0 > 0. \quad (17)$$

Consequently, the unknown parameters of the normalized form of the Bouc-Wen model are ρ , σ , n , k_f , and k_w with the following constraints:

$$\begin{aligned}\rho &> 0, \\ \sigma &\geq \frac{1}{2}, \\ n &\geq 1, \\ k_f &> 0, \\ k_w &> 0.\end{aligned}\quad (18)$$

The model parameters can be determined by system identification techniques, using experimental input and output data.

3. Bouc-Wen Model Parameter Identification

The identification of the Bouc-Wen model parameters is performed by adopting an identification algorithm that compares model output signals and those measured, for the same input signals, in order to determine the unknown model parameters. Nonlinearity of the Bouc-Wen model introduces the complexity for parameter identification. Several methods, based on different approaches, have been then proposed. In this section, an overview of different identification algorithms is presented.

An iterative least-squares procedure, based on a modified Gauss-Newton approach, was presented in [5]. Identification was carried out to estimate the parameters of an extended Bouc-Wen model that accounts for strength and stiffness degradation in accordance with [26]. The system identification procedure is shown in Figure 2.

In [30], a vibration control system composed of a magnetorheological damper in series with a magnetorheological elastomer was presented. The Bouc-Wen model was adopted to reproduce the hysteresis of the magnetorheological damper, and the parameters were identified using a least-squares method.

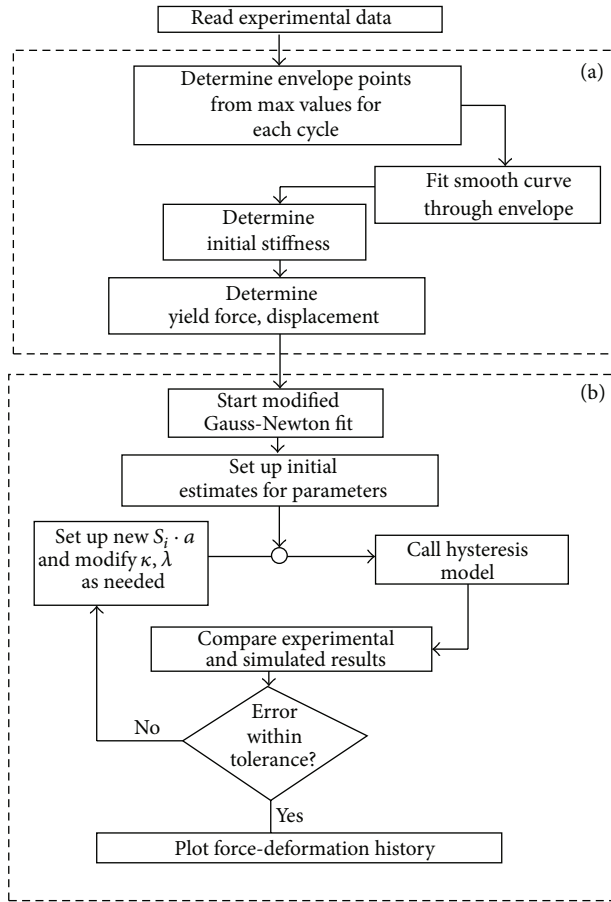


FIGURE 2: Flow diagram for complete identification process [5].

On-line parameter identification of the Bouc-Wen model has also drawn a lot of attention to researchers. Studies in [31, 32] presented an on-line identification method using a least-squares adaptive law. Another study in [33] employed an adaptive on-line identification methodology with a variable trace method to adjust the adaptation gain matrix. In [34], a linear parameterized estimator was established for the on-line estimation of the hysteretic Bouc-Wen model with unknown coefficients (including the parameter n). In [35], an adaptive on-line identification algorithm was proposed for parametric and nonparametric identification of structural models and was applied to a generalized Bouc-Wen model. The proposed identification methodology was a recursive least-squares algorithm that required only acceleration measurements.

In addition to the least-squares regression method, a genetic based identification algorithm was proposed in [36]. The reproduction procedure adopts the roulette wheel selection and the method of crossover and uniform mutation [37].

To account for asymmetric behaviour, a modified Bouc-Wen model [6] was adopted for modelling a PZT actuator. A modified particle swarm optimization algorithm [38] was proposed in order to identify and optimize the model parameters (see Figure 3). The fitness function in Figure 3 is evaluated as the root-mean-square error between the actual measured displacement and the model output.

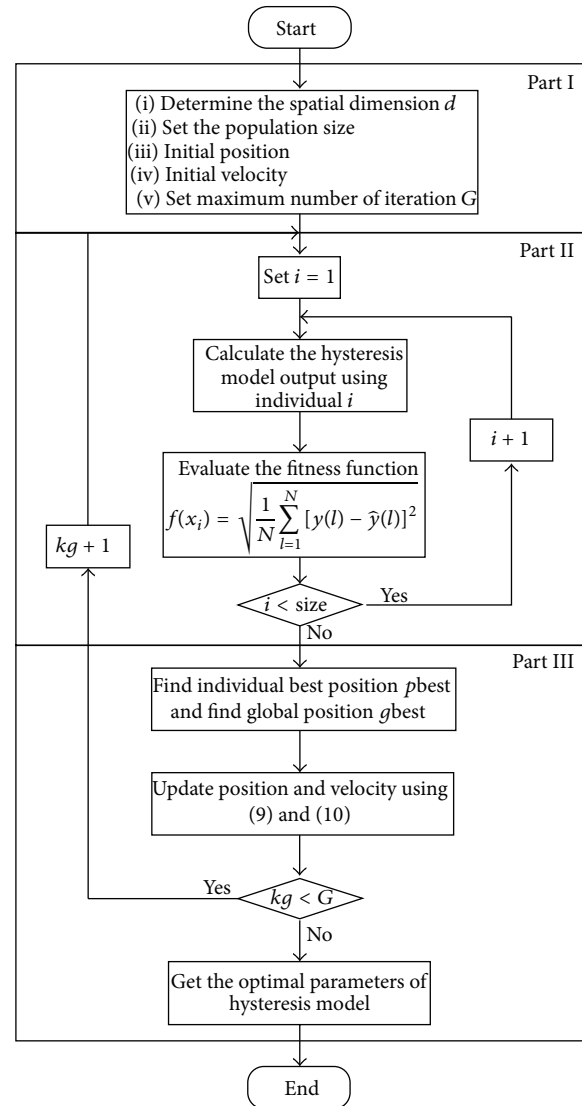


FIGURE 3: Flowchart of the identification hysteretic model parameters [6].

The particle swarm optimization was also adopted in [39] to identify the parameters of Bouc-Wen model. In this study, the identified model was used to describe the dynamics of a large-scale magnetorheological damper for seismic hazard mitigation.

Gauss-Newton iterations were used as a method of estimating the parameters of hysteretic system with slip on the basis of input-output data [40]. Reference [41] proposed a frequency domain parametric identification method of nonlinear hysteretic isolators. In [42, 43], an identification method for the normalized Bouc-Wen model was developed. Using the analytical description of the hysteresis loop developed in [29], an algorithm was proposed along with its analytical proof. It consisted in exciting the Bouc-Wen model with two periodic signals with a loading-unloading shape (wave periodic) which gives rise asymptotically to a hysteretic periodic response. The obtained two limit cycles

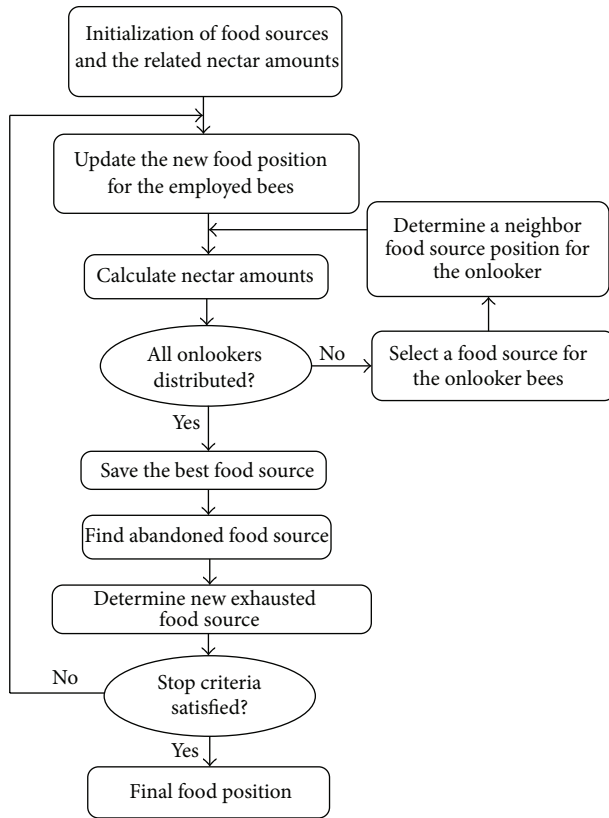


FIGURE 4: Flowchart of the parameter identification algorithm presented in [7].

were then used as an input to exactly determine the unknown parameters.

The limit cycle approach was also adopted in [10] to identify the parameters of the Bouc-Wen model adopted to reproduce the hysteresis of a wire-cable vibration isolator. In [44], the limit cycle approach was adopted to identify the parameters of a large-scale magnetorheological fluid damper model.

Another optimization method based on artificial bee colony algorithm [7, 45] was developed to determine the optimum parameters of Bouc-Wen hysteretic systems. The proposed flowchart is shown in Figure 4.

In [46, 47], a constrained nonlinear optimization was exploited in parametric identification. In [48], the Bouc-Wen nonlinear hysteresis term was approximated by a power series expansion of suitable basis functions, and then the coefficients of the functions were determined using the standard least-squares method.

Bouc-Wen model parameters could be also identified with procedures based on nonlinear filtering, using, for example, the extended Kalman filter (EKF) or the unscented Kalman filter (UKF). Yang and Ma [49] proposed a constrained EKF with a global weighted iteration strategy, which was effective in estimating all the parameters of the Bouc-Wen model of hysteresis. Zhang et al. [50] also applied the EKF for the identification of hysteretic systems that exhibit

degradation and pinching; all the parameters of the BW-model were identified without problem.

In [51–53], the UKF was used for the identification of nondegrading and degrading hysteretic systems. The identification results show that the UKF is well suited for the identification of complicated nonlinear systems and that this methodology can yield accurate estimates of the parameters of the Bouc-Wen models. The results also show that the UKF outperforms the EKF with regard to computational efficiency and robustness to measurement noise levels.

4. Vibration Control System Modelling Using the Bouc-Wen Model

The main scope of the vibration control is the suppression or, at least, the attenuation of undesirable vibrations that can affect systems and structures, such as buildings, vehicles, aircraft, and bridges. Vibration control is typically realized using passive, semiactive, or active [54–58] systems, and considerable hysteretic behaviours can be found in each of these.

Passive vibration control, such as the passive base isolation, is one solution that has proven effective for enhancing structural performance against seismic events. The main concept behind passive base isolation is to increase the structure flexibility, thus avoiding potentially dangerous seismic ground motions [59–62]. Base isolation bearings have been installed in many buildings for seismic protection [63]; however, large base displacements resulting from the increased flexibility of the passive isolation system can potentially exceed the prescribed limit of structural designs under severe seismic excitations [64–66].

Semiactive vibration control consists of a passive isolation system combined with a controllable semiactive device [67–71]. Semiactive vibration control is one control technique that consumes less power to change the features of the isolation system, but no mechanical energy is introduced into the structural system. Differently from passive control techniques, semiactive control systems have higher variability due to the different capabilities of energy dissipation from the control devices when the power levels are changed, such as variable stiffness and/or damping values.

Active vibration control is another control technique which uses the energy generated from the active control devices, supplied by means of an external power source, to improve the vibrational system performance. The mitigation of the vibration phenomena is based on the employment of suitable actuators that transmit mechanical energy to the structure and, in recent years, a great number of studies have been accomplished on active vibration control of flexible structures using piezoelectric actuators. Among the several kinds of actuation systems, piezoelectric ceramic materials have received much diffusion in the active vibration control because of their mechanical simplicity, small volume, light weight, large useful bandwidth, efficient conversion between electrical energy and mechanical energy, and easy integration with various metallic and composite structures [72].



FIGURE 5: Isolator prototype [8].

4.1. Passive Systems. The Bouc-Wen model has been widely adopted for the numerical modelling of passive hysteretic control devices. In this section, an overview of various components for different applications is presented.

Passive seismic isolators aim to reduce the earthquake input energy to the structure to keep linear structural vibration. Many devices are strongly nonlinear, showing different hysteretic behaviours. In this context, the Bouc-Wen model has been used extensively for its intrinsic ability in describing the behaviour of a wide range of real-world passive seismic isolators.

In [8], a prototype seismic isolator, composed of a wire rope spring and a ball transfer unit, was proposed as shown in Figure 5. The nonlinear behaviour of the restoring force was represented by the Bouc-Wen model.

The Bouc-Wen model was used in [73] to model the dissipated energy by the wire rope isolators for seismic protection of equipment in buildings. In [9, 10], modified Bouc-Wen models were adopted to numerically reproduce hardening behaviours [9] (see Figure 6) or asymmetrical hysteresis cycles [10] (see Figure 7) of wire rope isolators.

A combined energy dissipation system was presented in [11]. As shown in Figure 8, a lead rubber damper (LRD) and its parallel connection with an oil damper (OD) were used in the braces of a structural frame. The restoring force characteristic of the LRD was then simulated by the Bouc-Wen hysteretic model.

In [12], the Bouc-Wen model was employed to mathematically represent two different elastomeric seismic isolators (see Figure 9), characterized by different characteristics because of the elastomeric layers and reinforcements (in the following indicated with “IUT_a” and “IUT_b,” resp.). The experimental and simulated hysteresis cycles for IUT_a and IUT_b were demonstrated in Figures 10(a) and 10(b), respectively.

In [74], the Bouc-Wen model was utilized to mathematically model a frictional behaviour of Teflon sliding bearings for a base isolation application. The study in [13] facilitated the Bouc-Wen model to describe the behaviour of hysteretic dampers that interconnect two adjacent structures subjected to seismic excitation as shown in Figure 11.

Effectiveness of dissipative passive devices used as connections between two structures was investigated [75]. An analytical model for the response of a reinforced concrete

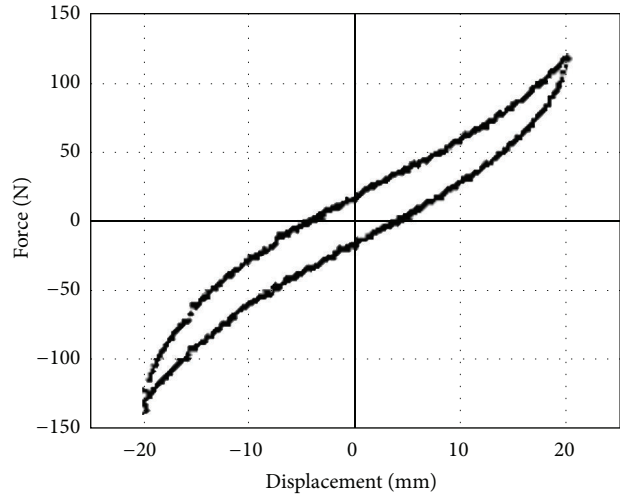


FIGURE 6: Hysteresis cycle with hardening [9].

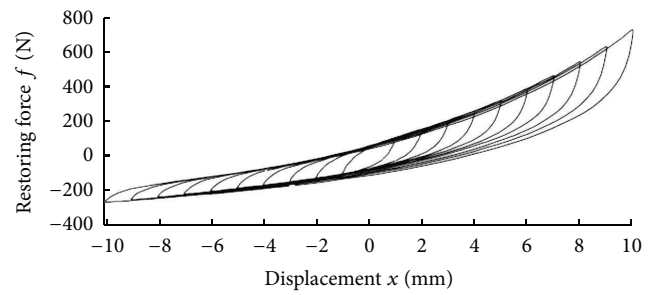


FIGURE 7: Asymmetrical cycles for tension-compression loading of a wire rope isolator [10].

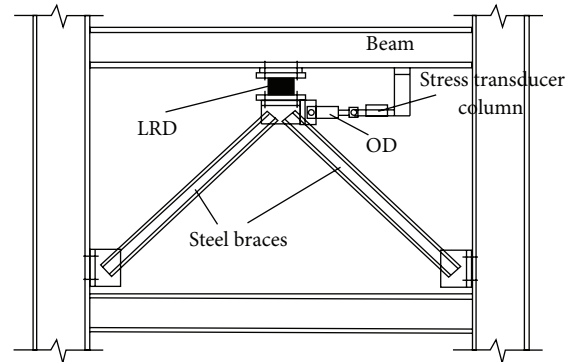


FIGURE 8: The configuration of the combined energy dissipation system in a frame [11].

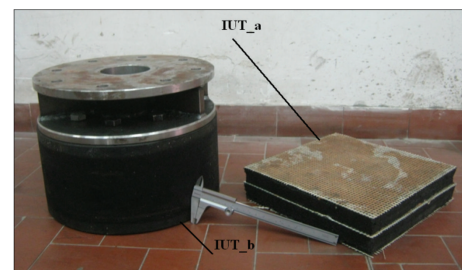


FIGURE 9: Seismic isolators presented in [12].

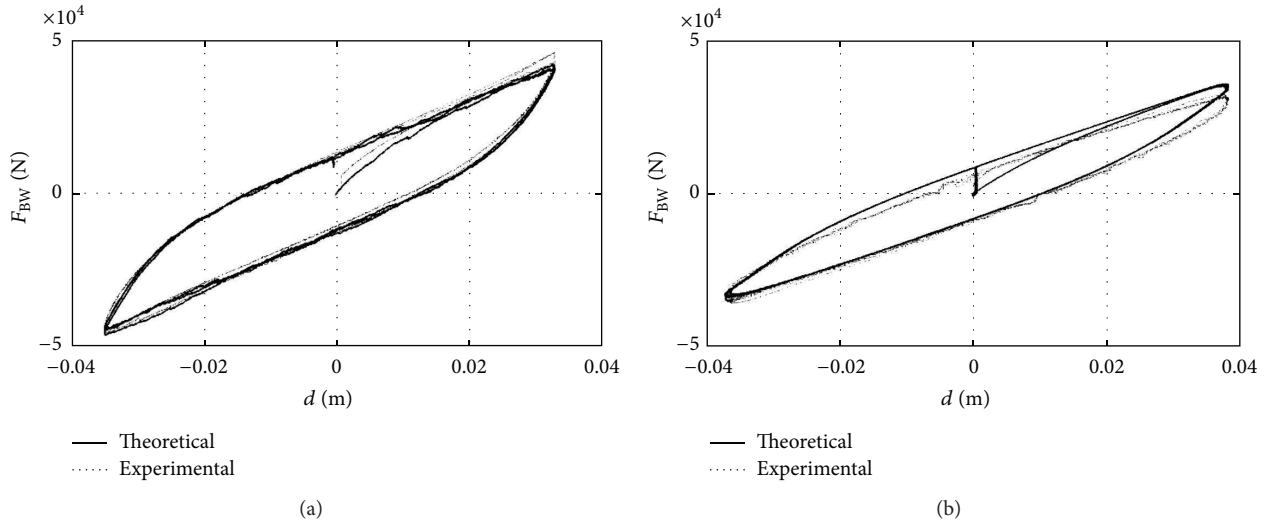


FIGURE 10: Experimental and simulated hysteretic cycles: (a) IUT_a; (b) IUT_b [12].

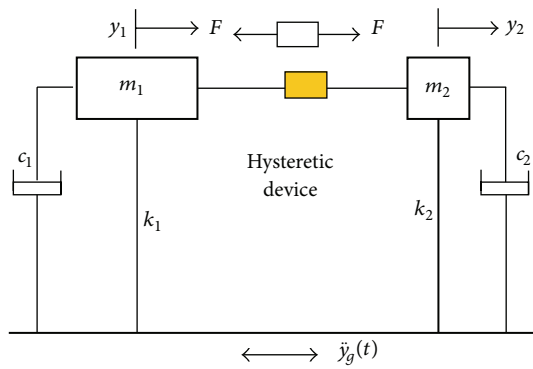


FIGURE 11: Schematic of the hysteretic device that interconnects two adjacent structures [13].

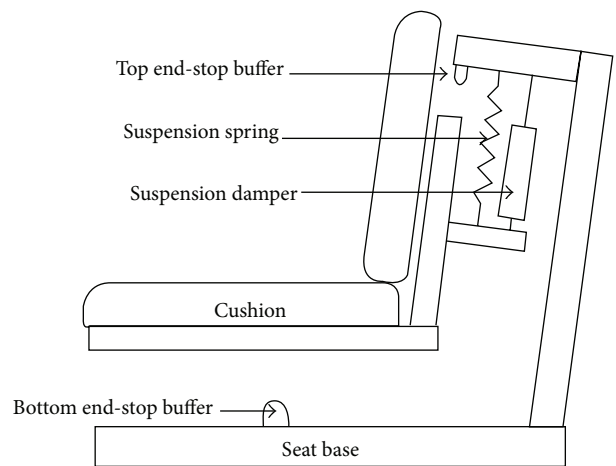


FIGURE 12: Schematic of the industrial truck seat [14].

panel with friction energy dampers was presented. The modelling of the hysteretic device was developed using an extended Bouc-Wen model. In [14], the study verified that the Bouc-Wen model well predicted the responses of suspension seats of the off-road machines to transient inputs as shown in Figure 12. The Bouc-Wen model used in [14] is shown schematically in Figure 13. The Bouc-Wen coefficients were obtained by minimizing the difference between the predicted and measured acceleration of a load supported in the seat. The measured hysteresis force-deflection cycles for the bottom buffers are shown in Figure 14. The study in [14] concluded that the Bouc-Wen model can provide a useful simulation of an existing seat.

4.2. Semiactive Systems. The magnetorheological (MR) fluids consist of suspensions of micron-sized ferrous particles immersed in a carrier fluid; their rheological behaviour can be changed by means of an applied magnetic field.

Researchers have used the controllable variation in yield stress to develop various smart devices [76–79]. In recent years, magnetorheological dampers have been widely studied as a controllable engineering component because of their continuously controllable mechanical properties and rapid response [80]. As shown in Figure 15, MR dampers can operate under three different fluid working modes [15]: shear [81, 82], flow [83–85], and squeeze [86–89]. The shear mode occurs when one wall of a gap translates or rotates relative to the other wall. In the shear mode, the fluid is sheared parallel to the walls. The flow mode occurs when two walls of a gap are fixed, as in a valve system, and the fluid flows through the gap and along the longitudinal axis of the walls. The squeeze mode occurs when the walls move toward each other, squeezing out the fluid. The fluid in the squeeze mode flows orthogonally to the direction of wall motion. According to the motion of the

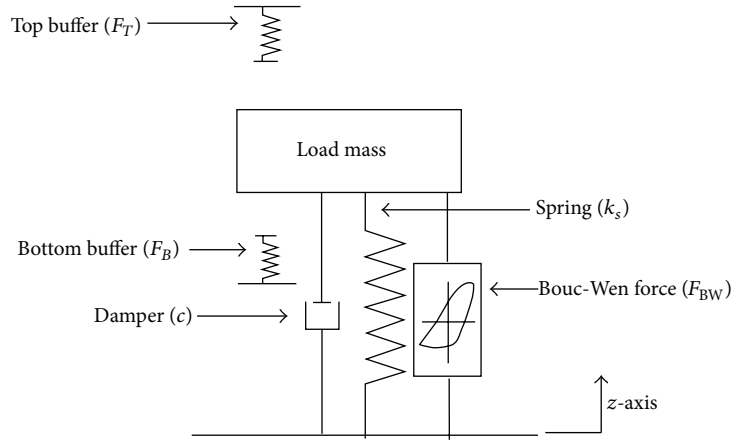


FIGURE 13: Schematic of the Bouc-Wen model [14].

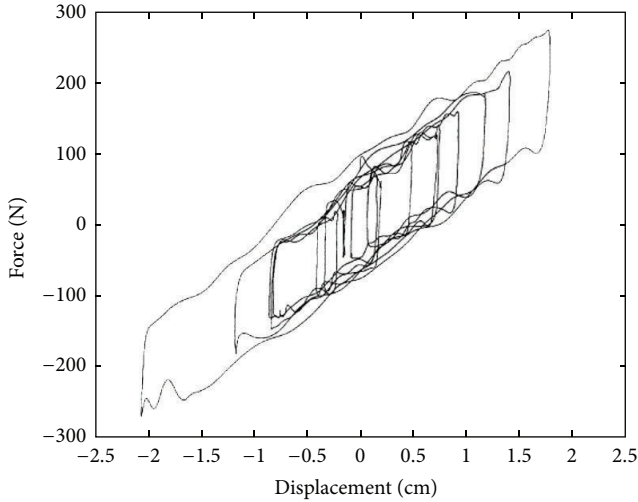


FIGURE 14: Force-displacement diagram—industrial truck seat exposed to random excitation [14].

constitutive elements, MR dampers can be categorized as linear MR dampers [16] (see Figure 16) and rotary MR dampers.

The modelling of MR dampers represents an important role to accurately describe their behaviours. A validated dynamic model allows executing several fundamental steps such as performance prediction, design, numerical simulations, and control synthesis. To this end, it is important to highlight the hysteretic phenomenon that occurs in these devices. Indeed, as it can be observed from experimental data in Figure 17, a hysteretic loop appears in the force-velocity diagram.

Several approaches have been established to model the MR dampers, and among these, the parametric approach drew considerable attention to researchers. The parametric models were developed using the schematization of the device as a combination of different physical elements, and

a typical example was constituted by the Bouc-Wen hysteresis operator-based dynamic model [20, 90–93].

The Bouc-Wen model has been extensively applied to simulate the hysteresis loops since it possesses the force-displacement and force-velocity behaviour of the MR dampers. In the following, the most widely adopted approaches will be presented. Spencer Jr. et al. [15, 17] employed the Bouc-Wen hysteretic operator to represent the hysteretic behaviour of MR dampers, and the schematic of the proposed simple Bouc-Wen model for MR dampers is shown in Figure 18 [15, 17]. The damping force in this system is given by

$$F = c_0 \dot{x} + k_0 (x - x_0) + \alpha z, \quad (19)$$

where c_0 and k_0 are the viscous damping and stiffness, respectively; x_0 represents an initial displacement due to the presence of an accumulator; z is the evolutionary variable governed by (3). By adjusting the parameter values α , β , γ , and n , the force-velocity relationship is characterized.

Later, Spencer Jr. et al. [15, 17] proposed a modified Bouc-Wen model to predict the behaviour of MR dampers over a wide range of inputs as shown in Figure 19. The model is given by the following equations:

$$F = c_1 \dot{y} + k_1 (x - x_0), \quad (20)$$

where

$$\dot{y} = \frac{1}{c_0 + c_1} [\alpha z + c_0 \dot{x} + k_0 (x - y)], \quad (21)$$

$$\dot{z} = -\gamma |\dot{x} - \dot{y}| |z|^{n-1} z - \beta (\dot{x} - \dot{y}) |z|^n + A (\dot{x} - \dot{y}),$$

and k_1 is the accumulator stiffness; c_0 and c_1 are the viscous damping observed at large and low velocities, respectively; k_0 is the stiffness at large velocities; x_0 is the term that accounts for the presence of an accumulator. The scale and shape of the hysteresis loop can be adjusted by γ , β , A , and n .

To model the behaviour of the shear mode MR damper (see Figure 20(a)), a Bouc-Wen hysteresis operator-based

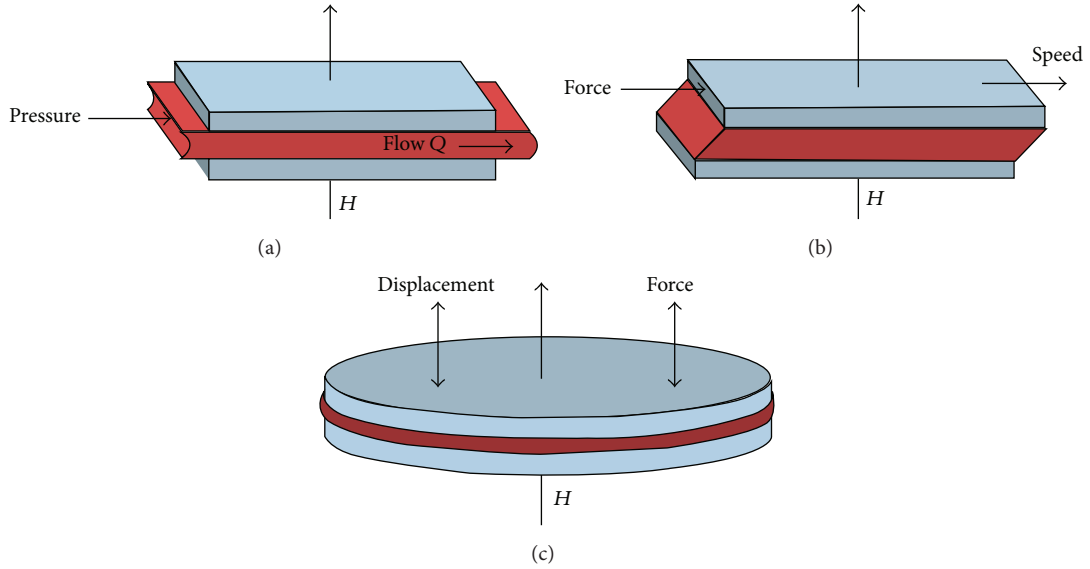


FIGURE 15: MR fluid operational modes [15]: (a) the flow mode, (b) the direct shear mode, and (c) the squeeze mode.

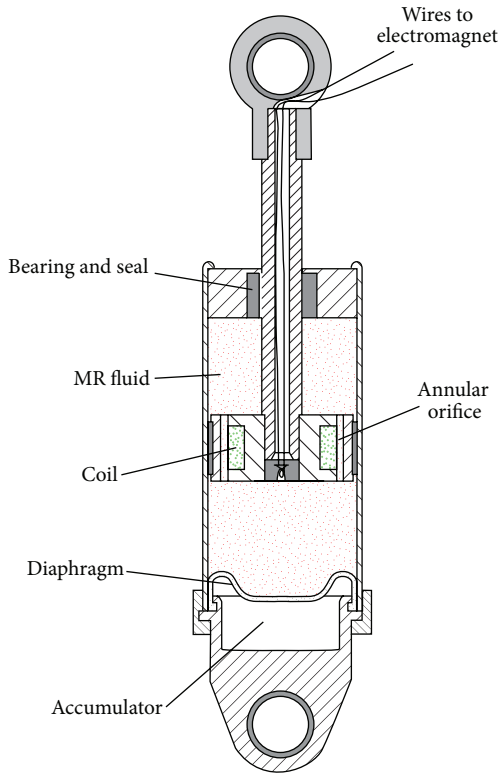


FIGURE 16: Typical scheme of a linear MR damper [16].

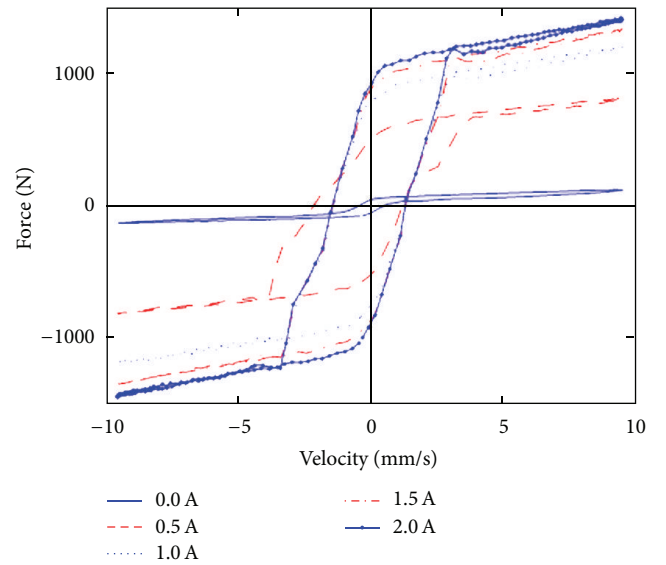


FIGURE 17: The damping force versus velocity [16].

dynamic model, as shown in Figure 20(b), was proposed [18, 19]. The equation governing the damping force is given by

$$F = c_0 \dot{x} + \alpha z, \quad (22)$$

where z is the evolutionary variable given by (3). The Bouc-Wen model in Figure 21 was developed for large-scale MR dampers [20], and the damper force is given by

$$F = m\ddot{x} + c_0(\dot{x})\dot{x} + k_0x + \alpha z + f_0. \quad (23)$$

In (23), m is the equivalent mass; k_0 is the accumulator stiffness; f_0 is the damper friction force; z is the evolutionary variable governed by (3). $c_0(\dot{x})$ is given by

$$c_0(\dot{x}) = a_1 e^{-(a_2|\dot{x}|)^p}, \quad (24)$$

where a_1 , a_2 , and p are positive constants.

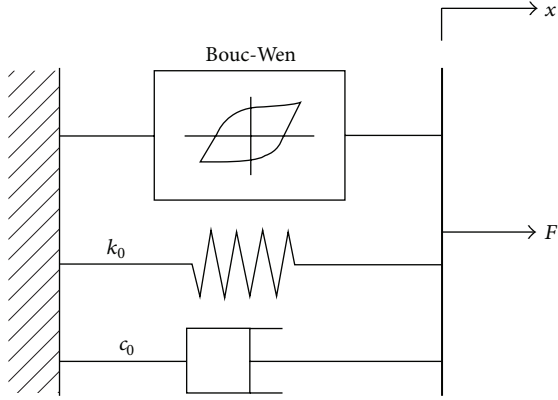


FIGURE 18: Simple Bouc-Wen model for MR dampers [15, 17].

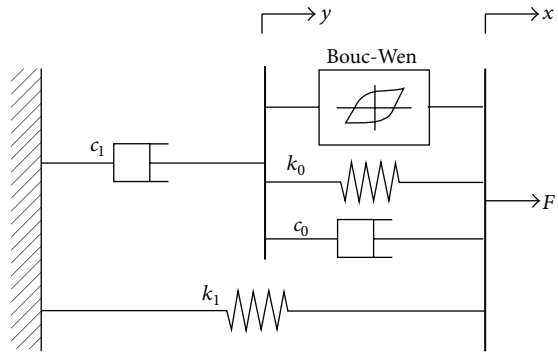


FIGURE 19: Modified Bouc-Wen model for MR dampers [15, 17].

4.3. Active Systems. Piezoelectric actuators (PEAs) represent a functional tool in the field of the active vibration control and, in the recent years, extensive researches have been conducted for modelling and control. PEAs utilize the converse piezoelectric effect of piezoelectric materials to generate displacement and force. Indeed, a piece of piezoelectric material will be mechanically strained if subject to an electric field (by placing it into the electric field or applying voltages to its surfaces).

The hysteresis nonlinearity constitutes one of the principal key issues to be solved in PEAs and its modelling is of fundamental importance for their control. In PEAs, hysteresis exists in both the electric field- (voltage-) polarization relationship and the electric field- (voltage-) strain (deformation or displacement) relationship (Figure 22), with the latter being mostly of concern in micro- and nanopositioning systems, and it is caused by the nonlinearities in the converse piezoelectric effect of the unit cells and the switching and movement of domain walls [21, 94].

The hysteresis trajectory of a PEA can be treated as being composed of three types of components: (1) the major loop which is the hysteresis loop that spans the whole input (voltage) range, (2) the minor loops which are the hysteresis

loops that only span portions of the input range, and (3) the initial ascending curve. As hysteresis is the major nonlinearity of PEAs and possesses detrimental effects on the positioning accuracy and stability margins of feedback control systems [95], compensation of hysteresis has always been a major concern in modelling and control of PEAs.

In [96], a PEA was modelled by means of the Bouc-Wen model and a PID control was applied. The dynamic relationship governing the actuator is given by

$$m\ddot{x} + c\dot{x} + k_a x = k_b k_x u + k_b k_w w, \quad (25)$$

where w is the evolutionary variable governed by (14); m is the equivalent mass; c is the damping coefficient; k_a and k_b are elastic constants; x is the actuator displacement; k_x and k_w are constant gains; n , ρ , and σ are the Bouc-Wen model parameters.

A Bouc-Wen based approach was introduced in [22] to compensate the hysteresis of piezoelectric actuators (see Figure 23) via a feedforward control. Indeed, feedback controllers for small systems, such as micro/nanoactuators, are strongly limited by the difficulty integrating the sensor. According to the multiplicative-inverse structure, the proposed compensator scheme was adapted to hysteresis with an advantage that no more computation was required for the compensator.

The hysteresis compensation is established using the following relationship:

$$U = \frac{1}{d_p} (y_r + H(U)) \quad (26)$$

U being the applied electrical voltage; d_p the piezoelectric coefficient; y_r the target displacement of the actuator; $H(U)$ a nonlinear operator due to the Bouc-Wen model. Equation (26) is used as a compensator that employs y_r as an input and U as an output with respect to the scheme in Figure 24.

To linearize the hysteresis behaviour of stack piezoelectric ceramic actuators, the feedforward linearization method, based on the Bouc-Wen model, and the hybrid linearization method, combining the feedforward method and PI feedback loop, were proposed and explored in [97]. The rapid control prototypes of the linearization controllers were established and tested, and the results showed that both the feedforward and hybrid linearization methods can linearize the hysteresis behaviour. Meanwhile, PEAs can exhibit an asymmetric hysteretic behaviour so that a modified Bouc-Wen model was proposed in [6] by introducing an input bias and an asymmetric factor into the standard Bouc-Wen hysteresis model.

5. Conclusion

This review reported the literature related to the utilization of the Bouc-Wen model for modelling hysterical behaviours of several vibration control systems. The review was organized into three sections that address specific issues: mathematical property of the Bouc-Wen model, identification of the model parameters, and applications of the Bouc-Wen model for

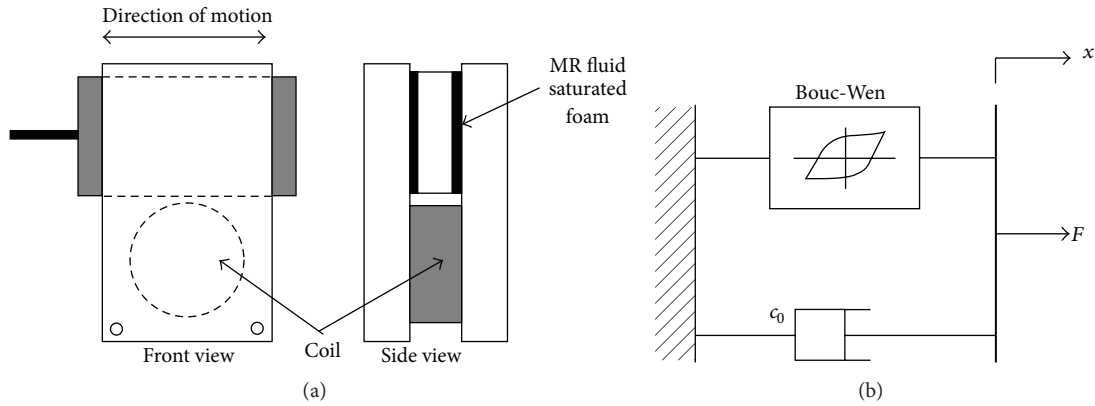


FIGURE 20: (a) Schematic diagram of shear mode MR damper; (b) mechanical model of the parallel plate MR damper [15, 18, 19].

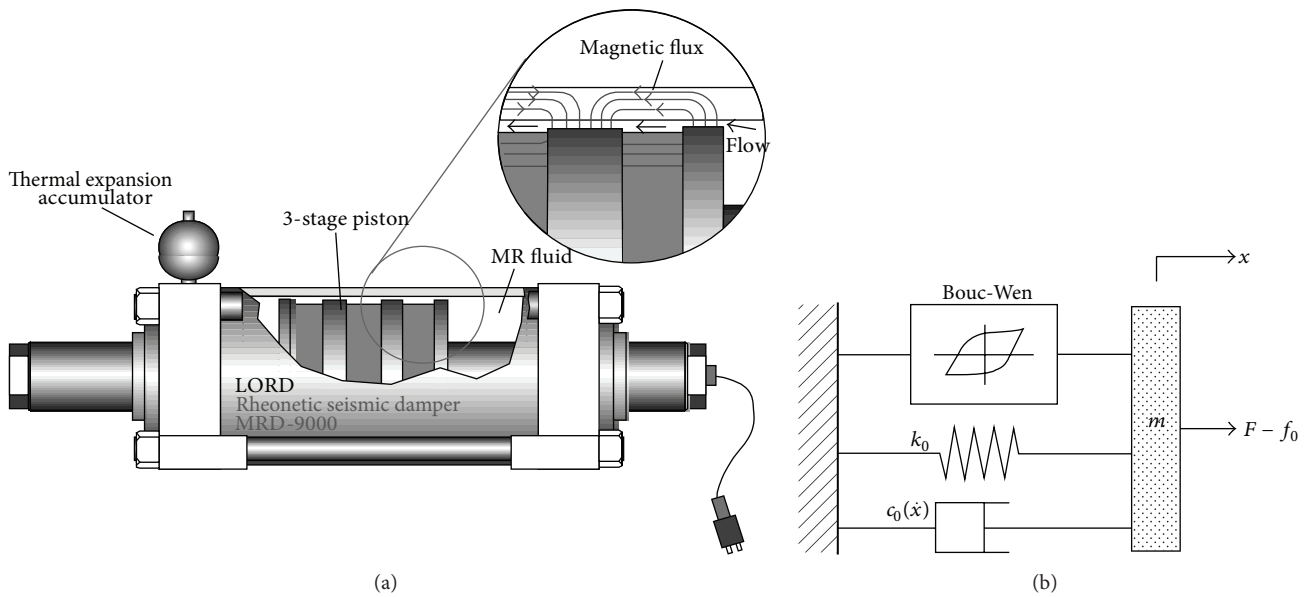


FIGURE 21: (a) Schematic of large-scale magnetorheological fluid damper; (b) Bouc-Wen model for large-scale MR dampers [15, 20].

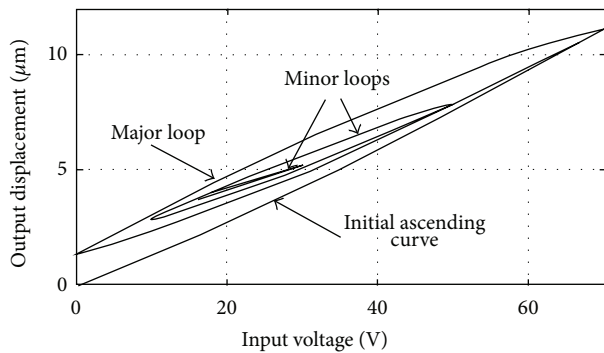


FIGURE 22: Hysteresis of a PEA [21].

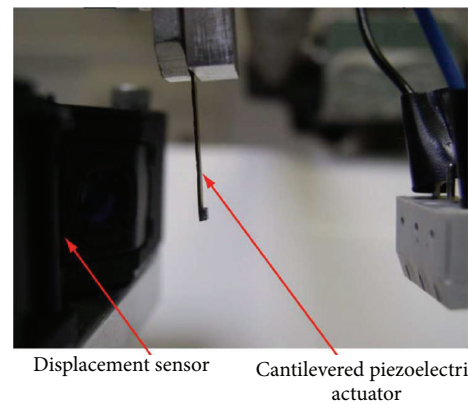


FIGURE 23: Photography of the piezoelectric actuator [22].

the dynamical description of different types of vibration control systems. Section 2 described the theoretical basis of the Bouc-Wen model, its first formulation, and its successive

modifications. Section 3 presented different approaches used for the identification of the Bouc-Wen model parameters.

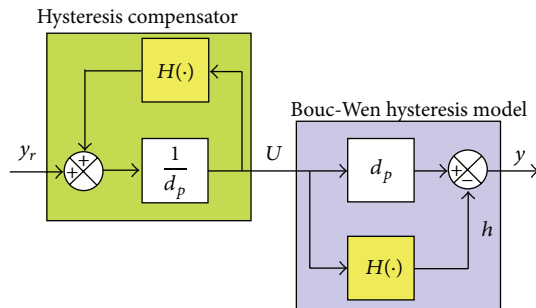


FIGURE 24: Bouc-Wen based compensator [22].

Section 4 provided several applications of the Bouc-Wen model for the modelling of devices extensively used in vibration control. Each section has presented what, from the authors' point of view, are the main contributions for the specific issue.

Conflict of Interests

The authors declare that there is no conflict of interests regarding the publication of this paper.

References

- [1] M. Ismail, F. Ikhrouane, and J. Rodellar, "The hysteresis Bouc-Wen model, a survey," *Archives of Computational Methods in Engineering*, vol. 16, no. 2, pp. 161–188, 2009.
- [2] R. Bouc, "Modèle mathématique d'hystérésis," *Acustica*, vol. 21, pp. 16–25, 1971.
- [3] Y. K. Wen, "Method of random vibration of hysteretic systems," *Journal of the Engineering Mechanics Division*, vol. 102, no. 2, pp. 249–263, 1976.
- [4] A. E. Charalampakis and V. K. Koumousis, "Identification of Bouc-Wen hysteretic systems by a hybrid evolutionary algorithm," *Journal of Sound and Vibration*, vol. 314, no. 3–5, pp. 571–585, 2008.
- [5] S. K. Kunnath, J. B. Mander, and L. Fang, "Parameter identification for degrading and pinched hysteretic structural concrete systems," *Engineering Structures*, vol. 19, no. 3, pp. 224–232, 1997.
- [6] H. Qin, N. Bu, W. Chen, and Z. Yin, "An asymmetric hysteresis model and parameter identification method for piezoelectric actuator," *Mathematical Problems in Engineering*, vol. 2014, Article ID 932974, 14 pages, 2014.
- [7] S. Talatahari, M. Nouri, and F. Tadbiri, "Optimization of skeletal structures using artificial bee colony algorithm," *International Journal of Optimization in Civil Engineering*, vol. 2, no. 4, pp. 557–571, 2012.
- [8] S. Pagano and S. Strano, "Wire rope springs for passive vibration control of a light steel structure," *WSEAS Transactions on Applied and Theoretical Mechanics*, vol. 8, no. 3, pp. 212–221, 2013.
- [9] G. Di Massa, S. Pagano, E. Rocca, and S. Strano, "Sensitive equipments on WRS-BTU isolators," *Meccanica*, vol. 48, no. 7, pp. 1777–1790, 2013.
- [10] H.-X. Wang, X.-S. Gong, F. Pan, and X.-J. Dang, "Experimental investigations on the dynamic behaviour of O-type wire-cable vibration isolators," *Shock and Vibration*, vol. 2015, Article ID 869325, 12 pages, 2015.
- [11] X. Lu and Q. Zhou, "Dynamic analysis method of a combined energy dissipation system and its experimental verification," *Earthquake Engineering & Structural Dynamics*, vol. 31, no. 6, pp. 1251–1265, 2002.
- [12] S. Strano and M. Terzo, "A first order model based control of a hydraulic seismic isolator test rig," *Engineering Letters*, vol. 21, no. 2, pp. 52–60, 2013.
- [13] M. Basili and M. De Angelis, "Optimal passive control of adjacent structures interconnected with nonlinear hysteretic devices," *Journal of Sound and Vibration*, vol. 301, no. 1–2, pp. 106–125, 2007.
- [14] T. P. Gunston, J. Rebelle, and M. J. Griffin, "A comparison of two methods of simulating seat suspension dynamic performance," *Journal of Sound and Vibration*, vol. 278, no. 1–2, pp. 117–134, 2004.
- [15] D. H. Wang and W. H. Liao, "Magnetorheological fluid dampers: a review of parametric modelling," *Smart Materials and Structures*, vol. 20, no. 2, Article ID 023001, 2011.
- [16] S. J. Dyke, B. F. Spencer Jr., M. K. Sain, and J. D. Carlson, "An experimental study of MR dampers for seismic protection," *Smart Materials and Structures*, vol. 7, no. 5, pp. 693–703, 1998.
- [17] B. F. Spencer Jr., S. J. Dyke, M. K. Sain, and J. D. Carlson, "Phenomenological model for magnetorheological dampers," *Journal of Engineering Mechanics*, vol. 123, no. 3, pp. 230–238, 1997.
- [18] L. M. Jansen and S. J. Dyke, "Semiactive control strategies for MR dampers: comparative study," *Journal of Engineering Mechanics*, vol. 126, no. 8, pp. 795–803, 2000.
- [19] F. Yi, S. J. Dyke, J. M. Caicedo, and J. D. Carlson, "Experimental verification of multi-input seismic control strategies for smart dampers," *Journal of Engineering Mechanics*, vol. 127, no. 11, pp. 1152–1164, 2001.
- [20] G. Yang, B. F. Spencer Jr., H.-J. Jung, and J. D. Carlson, "Dynamic modeling of large-scale magnetorheological damper systems for civil engineering applications," *Journal of Engineering Mechanics*, vol. 130, no. 9, pp. 1107–1114, 2004.
- [21] P. Jingyang and C. Xiongbiao, "A survey of modeling and control of piezoelectric actuators," *Modern Mechanical Engineering*, vol. 3, no. 1, pp. 1–20, 2013.
- [22] M. Rakotondrabe, "Bouc-Wen modeling and inverse multiplicative structure to compensate hysteresis nonlinearity in piezoelectric actuators," *IEEE Transactions on Automation Science and Engineering*, vol. 8, no. 2, pp. 428–431, 2011.
- [23] F. Ma, H. Zhang, A. Bockstedte, G. C. Foliente, and P. Paevere, "Parameter analysis of the differential model of hysteresis," *Journal of Applied Mechanics*, vol. 71, no. 3, pp. 342–349, 2004.
- [24] M. C. Constantinou and M. A. Adnane, "Dynamics of soil-base-isolated structure systems: evaluation of two models for yielding systems," Report to NSAF, Department of Civil Engineering, Drexel University, Philadelphia, Pa, USA, 1987.
- [25] N. M. Kwok, Q. P. Ha, M. T. Nguyen, J. Li, and B. Samali, "Bouc-Wen model parameter identification for a MR fluid damper using computationally efficient GA," *ISA Transactions*, vol. 46, no. 2, pp. 167–179, 2007.
- [26] T. T. Baber and Y. K. Wen, "Random vibration of hysteretic degrading systems," *Journal of Engineering Mechanics*, vol. 107, no. 6, pp. 1069–1087, 1981.
- [27] T. T. Baber and M. N. Noori, "Random vibration of degrading pinching systems," *Journal of Engineering Mechanics*, vol. 111, no. 8, pp. 1010–1026, 1985.

- [28] T. T. Baber and M. N. Noori, "Modeling general hysteresis behavior and random vibration application," *Journal of Vibration, Acoustics, Stress, and Reliability in Design*, vol. 108, no. 4, pp. 411–420, 1986.
- [29] F. Ikhouane and J. Rodellar, "On the hysteretic Bouc-Wen model. Part I: forced limit cycle characterization," *Nonlinear Dynamics*, vol. 42, no. 1, pp. 63–78, 2005.
- [30] W. Zhu and X.-T. Rui, "Semiactive vibration control using a magnetorheological damper and a magnetorheological elastomer based on the bouc-wen model," *Shock and Vibration*, vol. 2014, Article ID 405421, 10 pages, 2014.
- [31] A. G. Chassiakos, S. F. Masri, A. W. Smyth, and T. K. Caughey, "On-line identification of hysteretic systems," *Journal of Applied Mechanics*, vol. 65, no. 1, pp. 194–203, 1998.
- [32] A. W. Smyth, S. F. Masri, A. G. Chassiakos, and T. K. Caughey, "Online parametric identification of MDOF nonlinear hysteretic systems," *Journal of Engineering Mechanics*, vol. 125, no. 2, pp. 133–142, 1999.
- [33] J.-W. Lin, R. Betti, A. W. Smyth, and R. W. Longman, "On-line identification of non-linear hysteretic structural systems using a variable trace approach," *Earthquake Engineering and Structural Dynamics*, vol. 30, no. 9, pp. 1279–1303, 2001.
- [34] C.-H. Loh, L. Y. Wu, and P. Y. Lin, "Displacement control of isolated structures with semi-active control devices," *Journal of Structural Control*, vol. 10, no. 2, pp. 77–100, 2003.
- [35] J.-W. Lin and R. Betti, "On-line identification and damage detection in non-linear structural systems using a variable forgetting factor approach," *Earthquake Engineering & Structural Dynamics*, vol. 33, no. 4, pp. 419–444, 2004.
- [36] J.-L. Ha, Y.-S. Kung, R.-F. Fung, and S.-C. Hsien, "A comparison of fitness functions for the identification of a piezoelectric hysteretic actuator based on the real-coded genetic algorithm," *Sensors and Actuators A: Physical*, vol. 132, no. 2, pp. 643–650, 2006.
- [37] R. L. Haupt and S. E. Haupt, *Practical Genetic Algorithms*, John Wiley & Sons, New York, NY, USA, 1998.
- [38] J. Kennedy and R. Eberhart, "Particle swarm optimization," in *Proceedings of the IEEE International Conference on Neural Networks*, pp. 1942–1948, December 1995.
- [39] Y. Chae, J. M. Ricles, and R. Sause, "Modeling of a large-scale magneto-rheological damper for seismic hazard mitigation. Part I: passive mode," *Earthquake Engineering and Structural Dynamics*, vol. 42, no. 5, pp. 669–685, 2013.
- [40] S. J. Li, H. Yu, and Y. Suzuki, "Identification of non-linear hysteretic systems with slip," *Computers & Structures*, vol. 82, no. 2-3, pp. 157–165, 2004.
- [41] Y. Q. Ni, J. M. Ko, and C. W. Wong, "Identification of non-linear hysteretic isolators from periodic vibration tests," *Journal of Sound and Vibration*, vol. 217, no. 4, pp. 737–756, 1998.
- [42] F. Ikhouane and O. Gomis-Bellmunt, "A limit cycle approach for the parametric identification of hysteretic systems," *Systems & Control Letters*, vol. 57, no. 8, pp. 663–669, 2008.
- [43] F. Ikhouane and J. Rodellar, "On the hysteretic Bouc-Wen model. Part II: robust parametric identification," *Nonlinear Dynamics*, vol. 42, no. 1, pp. 79–95, 2005.
- [44] A. Rodríguez, N. Iwata, F. Ikhouane, and J. Rodellar, "Model identification of a large-scale magnetorheological fluid damper," *Smart Materials and Structures*, vol. 18, no. 1, Article ID 015010, 2009.
- [45] S. Talatahari, H. Mohagheg, K. Najafi, and A. Manafzadeh, "Solving parameter identification of nonlinear problems by artificial bee colony algorithm," *Mathematical Problems in Engineering*, vol. 2014, Article ID 479197, 6 pages, 2014.
- [46] P.-Q. Xia, "An inverse model of MR damper using optimal neural network and system identification," *Journal of Sound and Vibration*, vol. 266, no. 5, pp. 1009–1023, 2003.
- [47] D. H. Wang and W. H. Liao, "Modeling and control of magnetorheological fluid dampers using neural networks," *Smart Materials and Structures*, vol. 14, no. 1, pp. 111–126, 2005.
- [48] S. F. Masri, J. P. Caffrey, T. K. Caughey, A. W. Smyth, and A. G. Chassiakos, "Identification of the state equation in complex non-linear systems," *International Journal of Non-Linear Mechanics*, vol. 39, no. 7, pp. 1111–1127, 2004.
- [49] Y. Yang and F. Ma, "Constrained Kalman filter for nonlinear structural identification," *Journal of Vibration and Control*, vol. 9, no. 12, pp. 1343–1357, 2003.
- [50] H. Zhang, G. C. Foliente, Y. Yang, and F. Ma, "Parameter identification of inelastic structures under dynamic loads," *Earthquake Engineering and Structural Dynamics*, vol. 31, no. 5, pp. 1113–1130, 2002.
- [51] E. N. Chatzi and A. W. Smyth, "The unscented Kalman filter and particle filter methods for nonlinear structural system identification with non-collocated heterogeneous sensing," *Structural Control and Health Monitoring*, vol. 16, no. 1, pp. 99–123, 2009.
- [52] E. N. Chatzi, A. W. Smyth, and S. F. Masri, "Experimental application of on-line parametric identification for nonlinear hysteretic systems with model uncertainty," *Structural Safety*, vol. 32, no. 5, pp. 326–337, 2010.
- [53] Z. Xie and J. Feng, "Real-time nonlinear structural system identification via iterated unscented Kalman filter," *Mechanical Systems and Signal Processing*, vol. 28, pp. 309–322, 2012.
- [54] R. I. Skinner, W. H. Robinson, and G. H. McVerry, *An Introduction to Seismic Isolation*, Wiley, Chichester, UK, 1993.
- [55] F. Naeim and J. M. Kelly, *Design of Seismic Isolated Structures: From Theory to Practice*, Wiley, Chichester, UK, 1999.
- [56] H. Yoshioka, J. C. Ramallo, and B. F. Spencer Jr., "'Smart' base isolation strategies employing magnetorheological dampers," *Journal of Engineering Mechanics*, vol. 128, no. 5, pp. 540–551, 2002.
- [57] C.-M. Chang and B. F. Spencer Jr., "Active base isolation of buildings subjected to seismic excitations," *Earthquake Engineering and Structural Dynamics*, vol. 39, no. 13, pp. 1493–1512, 2010.
- [58] J. Fei, "Active vibration control of flexible steel cantilever beam using piezoelectric actuators," in *Proceedings of the 37th Southeastern Symposium on System Theory (SST '05)*, pp. 35–39, IEEE, March 2004.
- [59] J. M. Kelly, G. Leitmann, and A. G. Soldatos, "Robust control of base-isolated structures under earthquake excitation," *Journal of Optimization Theory and Applications*, vol. 53, no. 2, pp. 159–180, 1987.
- [60] S. Strano and M. Terzo, "A multi-purpose seismic test rig control via a sliding mode approach," *Structural Control and Health Monitoring*, vol. 21, no. 8, pp. 1193–1207, 2014.
- [61] A. Calabrese, G. Serino, S. Strano, and M. Terzo, "Experimental investigation of a low-cost elastomeric anti-seismic device using recycled rubber," *Meccanica*, vol. 50, no. 9, pp. 2201–2218, 2015.
- [62] J. C. Ramallo, E. A. Johnson, and B. F. Spencer Jr., "'Smart' base isolation systems," *Journal of Engineering Mechanics*, vol. 128, no. 10, pp. 1088–1099, 2002.
- [63] I. Buckle, S. Nagarajaiah, and K. Ferrell, "Stability of elastomeric isolation bearings: experimental study," *Journal of Structural Engineering*, vol. 128, no. 1, pp. 3–11, 2002.

- [64] J. M. Kelly, "The role of damping in seismic isolation," *Earthquake Engineering and Structural Dynamics*, vol. 28, no. 3, pp. 3–20, 1999.
- [65] S. Nagarajaiah and K. Ferrell, "Stability of elastomeric seismic isolation bearings," *Journal of Structural Engineering*, vol. 125, no. 9, pp. 946–954, 1999.
- [66] B. F. Spencer Jr., E. A. Johnson, and J. C. Ramallo, "Smart isolation for seismic control," *JSME International Journal, Series C: Mechanical Systems, Machine Elements and Manufacturing*, vol. 43, no. 3, pp. 704–711, 2000.
- [67] N. Makris, "Rigidity-plasticity-viscosity: can electrorheological dampers protect base-isolated structures from near-source earthquakes," *Earthquake Engineering & Structural Dynamics*, vol. 26, no. 5, pp. 571–591, 1997.
- [68] S. Nagarajaiah, S. Sahasrabudhe, and R. Iyer, "Seismic response of sliding isolated bridges with MR dampers," in *Proceedings of the American Control Conference*, vol. 6, pp. 4437–4441, Chicago, Ill, USA, June 2000.
- [69] D. Shook, P.-Y. Lin, T.-K. Lin, and P. N. Roschke, "A comparative study in the semi-active control of isolated structures," *Smart Materials and Structures*, vol. 16, no. 4, pp. 1433–1446, 2007.
- [70] S. Sahasrabudhe, S. Nagarajaiah, and C. Hard, "Experimental study of sliding isolated buildings with smart dampers subjected to near-source ground motions," in *Proceedings of the ASCE 14th Engineering Mechanics Conference (EM '00)*, Austin, Tex, USA, 2000.
- [71] J. Zhang, L. He, E. Wang, and R. Gao, "A LQR controller design for active vibration control of flexible structures," in *Proceedings of the Pacific-Asia Workshop on Computational Intelligence and Industrial Application (PACIIA '08)*, pp. 127–132, IEEE, Wuhan, China, December 2008.
- [72] APC International, *Piezoelectric Ceramics: Principles and Applications*, APC International, 2011.
- [73] G. F. Demetriades, M. C. Constantinou, and A. M. Reinhorn, "Study of wire rope systems for seismic protection of equipment in buildings," *Engineering Structures*, vol. 15, no. 5, pp. 321–334, 1993.
- [74] M. Constantinou, A. Mokha, and A. Reinhorn, "Teflon bearings in base isolation II. Modeling," *Journal of Structural Engineering*, vol. 116, no. 2, pp. 455–474, 1990.
- [75] M. Sasaki and E. P. Popov, "Seismic energy dissipators for RC panels: analytical studies," *Journal of Engineering Mechanics*, vol. 127, no. 8, pp. 835–843, 2001.
- [76] A. Lanzotti, M. Russo, R. Russo, F. Renno, and M. Terzo, "A physical prototype of an automotive magnetorheological differential," in *Proceedings of the World Congress on Engineering (WCE 2013)*, vol. 3 of *Lecture Notes in Engineering and Computer Science*, pp. 2131–2135, 2013.
- [77] A. Lanzotti, F. Renno, M. Russo, R. Russo, and M. Terzo, "Design and development of an automotive magnetorheological semi-active differential," *Mechatronics*, vol. 24, no. 5, pp. 426–435, 2014.
- [78] K. Karakoc, E. J. Park, and A. Suleman, "Design considerations for an automotive magnetorheological brake," *Mechatronics*, vol. 18, no. 8, pp. 434–447, 2008.
- [79] B. M. Kavlicoglu, N. C. Kavlicoglu, Y. Liu et al., "Response time and performance of a high-torque magneto-rheological fluid limited slip differential clutch," *Smart Materials and Structures*, vol. 16, no. 1, pp. 149–159, 2007.
- [80] N. M. Wereley, J. U. Cho, Y. T. Choi, and S. B. Choi, "Magnetorheological dampers in shear mode," *Smart Materials and Structures*, vol. 17, no. 1, Article ID 015022, 2008.
- [81] Z. Lou, R. D. Ervin, F. E. Filisko, and C. B. Winkler, "An electrorheologically controlled semi-active landing gear," SAE Technical Paper Series 931403, SAE International, 1993.
- [82] Z. Lou, R. D. Ervin, and F. E. Filisko, "Preliminary parametric study of electrorheological dampers," *Journal of Fluids Engineering, Transactions of the ASME*, vol. 116, no. 3, pp. 570–576, 1994.
- [83] N. M. Wereley and L. Pang, "Nondimensional analysis of semi-active electrorheological and magnetorheological dampers using approximate parallel plate models," *Smart Materials and Structures*, vol. 7, no. 5, pp. 732–743, 1998.
- [84] Y.-T. Choi and N. M. Wereley, "Comparative analysis of the time response of electrorheological and magnetorheological dampers using nondimensional parameters," *Journal of Intelligent Material Systems and Structures*, vol. 13, no. 7-8, pp. 443–451, 2002.
- [85] N. M. Wereley, J. Lindler, N. Rosenfeld, and Y.-T. Choi, "Biviscous damping behavior in electrorheological shock absorbers," *Smart Materials and Structures*, vol. 13, no. 4, pp. 743–752, 2004.
- [86] R. Stanway, J. L. Sproston, and N. G. Stevens, "Non-linear modelling of an electro-rheological vibration damper," *Journal of Electrostatics*, vol. 20, no. 2, pp. 167–184, 1987.
- [87] E. W. Williams, S. G. Rigby, J. L. Sproston, and R. Stanway, "Electrorheological fluids applied to an automotive engine mount," *Journal of Non-Newtonian Fluid Mechanics*, vol. 47, pp. 221–238, 1993.
- [88] N. D. Sims, R. Stanway, A. R. Johnson, and J. S. Yang, "Vibration isolation using a magnetorheological damper in the squeeze-flow mode," in *Smart Structures and Materials: Smart Structures and Integrated Systems*, vol. 3668 of *Proceedings of SPIE*, pp. 520–527, Newport Beach, Calif, USA, June 1999.
- [89] Y. K. Ahn, J.-Y. Ha, Y.-H. Kim et al., "Dynamic characteristics of squeeze-type mount using magnetorheological fluid," *Proceedings of the Institution of Mechanical Engineers Part K: Journal of Multi-body Dynamics*, vol. 219, no. 1, pp. 27–34, 2005.
- [90] A. Dominguez, R. Sedaghati, and I. Stiharu, "Modelling the hysteresis phenomenon of magnetorheological dampers," *Smart Materials and Structures*, vol. 13, no. 6, pp. 1351–1361, 2004.
- [91] A. Dominguez, R. Sedaghati, and I. Stiharu, "A new dynamic hysteresis model for magnetorheological dampers," *Smart Materials and Structures*, vol. 15, no. 5, pp. 1179–1189, 2006.
- [92] A. Dominguez, R. Sedaghati, and I. Stiharu, "Semi-active vibration control of adaptive structures using magnetorheological dampers," *AIAA Journal*, vol. 44, no. 7, pp. 1563–1571, 2006.
- [93] A. Dominguez, R. Sedaghati, and I. Stiharu, "Modeling and application of MR dampers in semi-adaptive structures," *Computers and Structures*, vol. 86, no. 3–5, pp. 407–415, 2008.
- [94] I. Mayergoyz and G. Bertotti, Eds., *The Science of Hysteresis*, vol. 3, Elsevier, St. Louis, Mo, USA, 2005.
- [95] J. A. Main and E. Garcia, "Piezoelectric stack actuators and control system design: strategies and pitfalls," *Journal of Guidance, Control, and Dynamics*, vol. 20, no. 3, pp. 479–485, 1997.
- [96] O. Gomis-Bellmunt, F. Ikhouane, and D. Montesinos-Miracle, "Control of Bouc-Wen hysteretic systems: application to a piezoelectric actuator," in *Proceedings of the 13th International Power Electronics and Motion Control Conference (EPE-PEMC '08)*, pp. 1670–1675, Poznan, Poland, September 2008.
- [97] D. H. Wang, W. Zhu, and Q. Yang, "Linearization of stack piezoelectric ceramic actuators based on Bouc-Wen Model," *Journal of Intelligent Material Systems and Structures*, vol. 22, no. 5, pp. 401–413, 2011.

Research Article

Novel Hyperbolic Homoclinic Solutions of the Helmholtz-Duffing Oscillators

Yang-Yang Chen,¹ Shu-Hui Chen,² and Wei-Wei Wang²

¹Key Laboratory of Vibration Control and Structural Safety, Guangzhou University, Guangzhou 510405, China

²Department of Applied Mechanics and Engineering, Sun Yat-sen University, Guangzhou 510275, China

Correspondence should be addressed to Yang-Yang Chen; yychen@gzhu.edu.cn

Received 28 May 2015; Revised 23 August 2015; Accepted 26 August 2015

Academic Editor: Chia-Ming Chang

Copyright © 2016 Yang-Yang Chen et al. This is an open access article distributed under the Creative Commons Attribution License, which permits unrestricted use, distribution, and reproduction in any medium, provided the original work is properly cited.

The exact and explicit homoclinic solution of the undamped Helmholtz-Duffing oscillator is derived by a presented hyperbolic function balance procedure. The homoclinic solution of the self-excited Helmholtz-Duffing oscillator can also be obtained by an extended hyperbolic perturbation method. The application of the present homoclinic solutions to the chaos prediction of the nonautonomous Helmholtz-Duffing oscillator is performed. Effectiveness and advantage of the present solutions are shown by comparisons.

1. Introduction

It has been widely accepted that homoclinic solutions play a fundamental role in global bifurcations and chaos predictions of dynamical systems [1, 2]. For instance, the experimental study of certain magnetic pendulum verified the homoclinic solutions as the precursors to chaotic vibration [3]. Some occurrences of homoclinic solutions can be regarded as the criterion from single well chaos to cross well chaos motion of oscillators [4], or as the onsets of chaotic vibrations of asymmetric nonconservative oscillators [5]. Homoclinic solutions were also adopted in bifurcation and chaotic vibration controls for beam structures [6, 7]. Another typical application of homoclinic solutions aims at solitary wave studies. For instance, a proper homoclinic solution can govern the solitary roll waves down an open inclined channel [8], or optical solitary waves propagating in fibers [9, 10]. The association between the singular solitary waves and homoclinic solutions can be interpreted based on phase plane analysis [11].

Because of their importance in nonlinear systems, many homoclinic solutions have been derived in the past few decades. Such works include but are not limited to the following: Xu et al. [12] proposed the perturbation-incremental method for homoclinic solutions; Chan et al. [13] applied the perturbation-incremental method to study the stability and

the homoclinic bifurcations of limit cycles; Belhaq et al. [14] analytically developed criteria for predicting homoclinic connection of limit cycle. Mikhlin and Manucharyan [15] and Manucharyan and Mikhlin [16] applied the Padé and quasi-Padé approximants for homo- and heteroclinic solutions. Y. Y. Chen and S. H. Chen [17] and Chen et al. [18] developed perturbation techniques by hyperbolic functions for homoclinic solutions of strongly nonlinear oscillators. Cao et al. [19] improved the perturbation-incremental homoclinic solutions for strongly nonlinear oscillators. Recently, Li et al. [20] improved the perturbation method based on harmonic functions to derive homoclinic solutions of Helmholtz-Duffing oscillators.

Nevertheless, to the best of our knowledge, the completely analytical, exact, and explicit homoclinic solution of the strongly nonlinear Helmholtz-Duffing oscillators has not yet been derived, in spite of the wide application of its equation for many engineering problems such as ship dynamics, oscillation of the human ear drum, oscillations of one-dimensional structural system with an initial curvature, some electrical circuits, microperforated panel absorber, and heavy symmetric gyroscope [21–29]. It should be pointed out that the previous typical solutions [14–18] become invalid for such mix-parity systems. Even for the conservative Helmholtz-Duffing oscillator, solutions by the perturbation methods [12,

13, 19, 20] based on generalized harmonic functions can only be obtained implicitly, in which the infinite time domain of a homoclinic motion has to be transformed into a finite period of the harmonic. Moreover, for strongly nonlinear oscillators, as the perturbation-incremental method [12, 13, 19] consists of perturbation procedure with the incremental harmonic balance method, their solutions are always expressed by harmonic functions with numerical coefficients. That means such implicit solutions are semianalytical and seminumerical and cumbersome for practical application.

This paper aims to present new homoclinic solutions of the Helmholtz-Duffing oscillators. The completely analytical, exact, and explicit homoclinic solution of the conservative Helmholtz-Duffing oscillator will be derived by a hyperbolic function balance procedure. Then the homoclinic solution of the self-excited Helmholtz-Duffing oscillator will also be obtained by an extended hyperbolic perturbation method. The application of the present solutions to the chaos prediction of the nonautonomous Helmholtz-Duffing oscillator is performed. The preference of the present solution will be illustrated by comparison.

2. The Explicit and Exact Homoclinic Solution of the Undamped Helmholtz-Duffing Oscillator

Consider the homoclinic solution of the undamped Helmholtz-Duffing equation

$$\ddot{x} + c_1 x + c_2 x^2 + c_3 x^3 = 0. \quad (1)$$

If $c_2 = 0$, (1) becomes the classical Duffing equation, which possesses a homoclinic solution with $c_1 < 0$ and $c_3 > 0$. Such homoclinic solution of classical Duffing equation has been discussed in detail in [17], in which the solution can be written as

$$x_0 = \pm \sqrt{\frac{-2c_1}{c_3}} \operatorname{sech} \sqrt{-c_1} t. \quad (2)$$

If $c_3 = 0$, (1) becomes the classical Helmholtz equation, which possesses a homoclinic solution. Such homoclinic solution of classical Helmholtz equation has been discussed in detail in [18], in which the solution can be written as

$$x_0 = \frac{3|c_1|}{2c_2} \operatorname{sech}^2 \frac{\sqrt{|c_1|}}{2} t - \frac{(|c_1| + c_1)}{2c_2}, \quad (3)$$

Noting the relationship as below,

$$\operatorname{sech}^2 \frac{\sqrt{|c_1|}}{2} t = \frac{1}{\cosh^2 \left(\frac{\sqrt{|c_1|}}{2} t \right)} = \frac{2}{1 + \cosh \sqrt{|c_1|} t}. \quad (4)$$

we can rewrite (2) and (3), respectively; that is,

$$x_0 = \frac{3|c_1|}{c_2} \frac{1}{\left(1 + \cosh \sqrt{|c_1|} t\right)} - \frac{(|c_1| + c_1)}{2c_2}, \quad (5)$$

$$x_0 = \pm \sqrt{\frac{-2c_1}{c_3}} \frac{1}{\cosh \sqrt{|c_1|} t}.$$

Here, to find a proper trial solution form for (1), we can observe the two special cases above. It can be seen that the two expressions above are similar, because they have the common form expressed as

$$x_0 = \frac{a_0}{b + \cosh \omega_0 t} + u, \quad (6)$$

in which, when $c_3 = 0$, the constants of (6) are $a_0 = 3|c_1|/c_2$, $b = 1$, $\omega_0 = \sqrt{c_1}$, and $u = -(|c_1| + c_1) / 2c_2$. While when $c_2 = 0$, $c_1 < 0$, and $c_3 > 0$, the constants of (6) are $a_0 = \pm \sqrt{-2c_1/c_3}$, $b = 0$, $\omega_0 = \sqrt{c_1}$, and $u = 0$.

Thus, the time derivative of (6) is

$$\dot{x}_0 = -\frac{a_0 \omega_0 \sinh \omega_0 t}{(b + \cosh \omega_0 t)^2}. \quad (7)$$

Note that $(u, 0)$ is the homoclinic point. For $c_2 \neq 0$ and $c_3 \neq 0$, we adopt (6) as a trial solution for the homoclinic solution of (1) and try to determine all its constants by substituting (6) into (1); that is,

$$\begin{aligned} & \left[(b + \cosh \omega_0 t)^{-3} (c_1 a_0 b^2 + c_1 b^3 u + c_2 b^3 u^2 + c_2 a_0^2 b \right. \\ & \quad + 2c_2 a_0 b^2 u + c_3 b^3 u^3 + c_3 a_0^2 + 3c_3 a_0 b^2 u^2 + 3c_3 a_0^2 b u \\ & \quad - 2a_0 \omega_0^2) + (b + \cosh \omega_0 t)^{-2} (2c_1 a_0 b + 3c_1 b^2 u \\ & \quad + c_2 a_0^2 + 4c_2 a_0 b u + 3c_2 b^2 u^2 + 3c_3 a_0^2 u + 6c_3 a_0 b u^2 \\ & \quad + 3c_3 b^2 u^3 - a_0 b \omega_0^2) + (b + \cosh \omega_0 t)^{-1} (c_1 a_0 \\ & \quad + 3c_1 b u + 2c_2 a_0 u + 3c_2 b u^2 + 3c_3 a_0 u^2 + 3c_3 b u^3 \\ & \quad \left. + a_0 \omega_0^2) + (c_1 u + c_2 u^2 + c_3 u^3) \right] = 0. \end{aligned} \quad (8)$$

In order to balance (8) for all time t , we equate coefficients of like powers of the hyperbolic function term $(b + \cosh \omega_0 t)$ and get the following nonlinear algebraic equations:

$$c_1 a_0 b^2 + c_1 b^3 u + c_2 b^3 u^2 + c_2 a_0^2 b + 2c_2 a_0 b^2 u + c_3 b^3 u^3 \quad (9)$$

$$+ c_3 a_0^2 + 3c_3 a_0 b^2 u^2 + 3c_3 a_0^2 b u - 2a_0 \omega_0^2 = 0,$$

$$2c_1 a_0 b + 3c_1 b^2 u + c_2 a_0^2 + 4c_2 a_0 b u + 3c_2 b^2 u^2 + 3c_3 a_0^2 u \quad (10)$$

$$+ 6c_3 a_0 b u^2 + 3c_3 b^2 u^3 - a_0 b \omega_0^2 = 0,$$

$$c_1 a_0 + 3c_1 b u + 2c_2 a_0 u + 3c_2 b u^2 + 3c_3 a_0 u^2 + 3c_3 b u^3 \quad (11)$$

$$+ a_0 \omega_0^2 = 0,$$

$$c_1 u + c_2 u^2 + c_3 u^3 = 0. \quad (12)$$

From (12),

$$u = 0, \quad (13)$$

or

$$u = \frac{-c_2 \pm \sqrt{c_2^2 - 4c_1c_3}}{2c_3}. \quad (14)$$

The left hand side of (12) can be regarded as the restoring force of the oscillator with $x = u$. In other words, (12) means that the displacement derivative of the potential energy curve at $x = u$ is zero. Furthermore, we have to make sure that the potential energy curve at $x = u$ is not concave. Thus, the displacement derivative of the restoring force at $x = u$ will not be positive; that is,

$$\left. \frac{d}{dx} (c_1x + c_2x^2 + c_3x^3) \right|_{x=u} = c_1 + 2c_2u + 3c_3x^2 \leq 0. \quad (15)$$

Therefore, u can be determined by (13)–(15) and then, (9)–(11) can be discussed, respectively, in the two cases as follows.

Case 1 ($u = 0$). Equations (9)–(11) can be rewritten as below

$$\begin{aligned} c_1b^2 + c_2a_0b + c_3a_0^2 - 2\omega_0^2 &= 0, \\ 2c_1b + c_2a_0 - b\omega_0^2 &= 0, \\ c_1 + \omega_0^2 &= 0, \end{aligned} \quad (16)$$

by which one can obtain

$$\begin{aligned} \omega_0 &= \sqrt{-c_1}, \\ a_0 &= \pm \frac{3\sqrt{2}c_1}{\sqrt{2c_2^2 - 9c_1c_3}}, \\ b &= \mp \frac{\sqrt{2}c_2}{\sqrt{2c_2^2 - 9c_1c_3}}. \end{aligned} \quad (17)$$

Case 2 ($u = (-c_2 \pm \sqrt{c_2^2 - 4c_1c_3})/2c_3$). As a_0 and u are nonzero, multiplying (12) by $-b^2(b + a_0/u)$ and then adding it to (9) yield

$$c_2a_0b + c_2b^2u + c_3a_0^2 + 3c_3a_0bu + 2c_3b^2u^2 - 2\omega_0^2 = 0. \quad (18)$$

Multiplying (12) by $-b(3b + 2a_0/u)$ and then adding it to (10), the latter becomes

$$c_2a + 2c_2bu + 3c_3au + 4c_3bu^2 - b\omega_0^2 = 0. \quad (19)$$

Multiplying (12) by $(-3b + a_0/u)$ and then adding it to (11), we also get

$$c_2u + 2c_3u^2 + \omega_0^2 = 0. \quad (20)$$

Thus from (18)–(20),

$$\begin{aligned} \omega_0 &= \sqrt{-u(c_2 + 2c_3u)}, \\ a_0 &= \pm \frac{3\sqrt{2}u(c_2 + 2c_3u)}{\sqrt{c_2(2c_2 + 3c_3u)}}, \\ b &= \mp \frac{\sqrt{2}(c_2 + 3c_3u)}{\sqrt{c_2(2c_2 + 3c_3u)}}. \end{aligned} \quad (21)$$

Furthermore, noting that, for the homoclinic solution, the potential energy values at $t = 0$ and at $t = \pm\infty$ should be equal, we have

$$\begin{aligned} \frac{1}{2}c_1u^2 + \frac{1}{3}c_2u^3 + \frac{1}{4}c_3u^4 \\ = \frac{1}{2}c_1\left(\frac{a_0}{b+1} + u\right)^2 + \frac{1}{3}c_2\left(\frac{a_0}{b+1} + u\right)^3 + \frac{1}{4}c_3\left(\frac{a_0}{b+1} + u\right)^4, \end{aligned} \quad (22)$$

by which the final values of a_0 , b , and ω_0 expressed by (17) or (21) can be selected.

Example 1. Here we apply the method for equation

$$\ddot{x} - x - 3x^2 + x^3 = 0, \quad (23)$$

which is a case of (1) with $c_1 = -1$, $c_2 = -3$, and $c_3 = 1$. From (14), (21), and (22), we can determine all the constants and get the homoclinic solution as

$$x = \frac{-1}{1 \pm \sqrt{3/2} \cosh t}, \quad (24)$$

$$\dot{x} = \frac{\sinh t}{\pm \sqrt{2/3} + 2 \cosh t \pm \sqrt{3/2} \cosh^2 t}. \quad (25)$$

The time histories and the phase portraits of the solutions by different methods are shown in Figures 1 and 2, respectively. It can be seen from the figures that the present method yields accurate and explicit solutions in both the figures, while the generalized harmonic function perturbation method can only provide valid solution in Figure 2. The reason is that based on harmonic functions [12, 13, 19, 20] the homoclinic solutions can only be expressed implicitly by the nonlinear time scale they adopted and be investigated only in phase planes. Such implicit solutions are too abstract or cumbersome to use in some practical problems. Therefore, the present explicit solutions in respect to time t are more applicable.

3. Perturbation Homoclinic Solution of the Self-Excited Helmholtz-Duffing Oscillator

Consider the homoclinic solution of the self-excited Helmholtz equation

$$\ddot{x} + c_1x + c_2x^2 + c_3x^3 = \varepsilon f(\mu, x, \dot{x}), \quad (26)$$

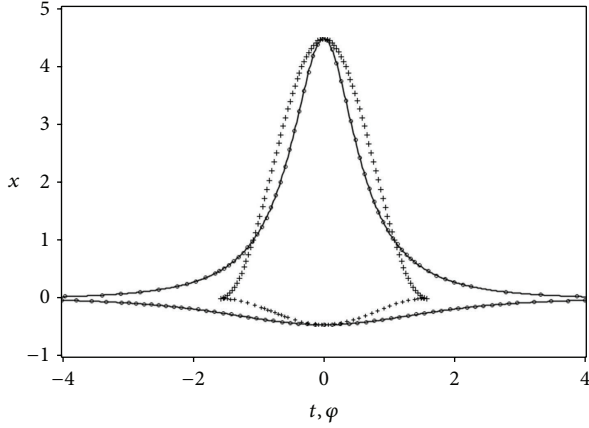


FIGURE 1: Time histories for homoclinic solutions of (23): — AUTO numerical method [30, 31]; $\circ \circ$ present method; +++ generalized harmonic function perturbation method [20].

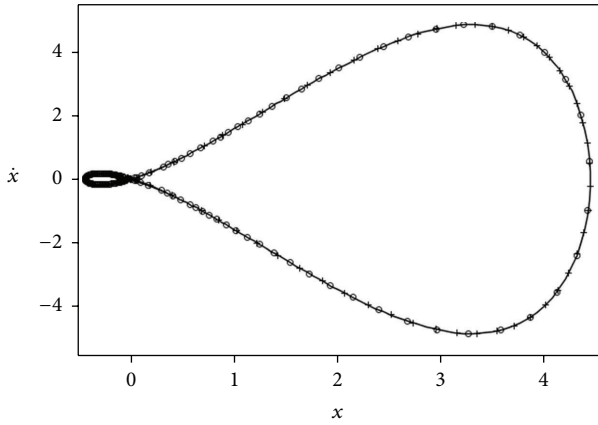


FIGURE 2: Phase portrait for homoclinic solutions x of (23): — AUTO numerical method [30, 31]; $\circ \circ$ present method; +++ generalized harmonic function perturbation method [20].

where μ denotes constants. We assume the homoclinic solution of (26) can still be expressed in the similar form of (6); that is,

$$x = \frac{a}{b + \cosh \tau} + u; \quad (27)$$

however, the amplitude a and the nonlinear time scale τ will depend upon the perturbation parameter ε . Thus a and ω , respectively, can be expanded in the powers of ε ; that is,

$$a = a_0 + \varepsilon a_1 + \dots = \sum_{n=0}^{\infty} \varepsilon^n a_n, \quad (28)$$

$$\frac{d\tau}{dt} = \omega(\tau) = \omega_0 + \varepsilon \omega_1(\tau) + \dots = \sum_{n=0}^{\infty} \varepsilon^n \omega_n(\tau). \quad (29)$$

Then (27) can be rewritten as

$$x = x_0 + \varepsilon x_1 + \dots = \sum_{n=0}^{\infty} \varepsilon^n x_n, \quad (30)$$

where

$$x_n = \frac{a_n}{b + \cosh \tau}. \quad (31)$$

Then

$$\frac{dx_n}{d\tau} = x_n' = -\frac{a_n \sinh \tau}{(b + \cosh \tau)^2}. \quad (32)$$

After substituting (29) and (30) into (26), equating coefficients of like powers of ε yields the following equations:

$$\varepsilon^0 : \omega_0^2 x_0'' + c_1 x_0 + c_2 x_0^2 + c_3 x_0^3 = 0, \quad (33)$$

$$\varepsilon^1 : \omega_0^2 x_1'' + \omega_0 \frac{d}{d\tau} (\omega_1 x_0') + \omega_1 \frac{d}{d\tau} (\omega_0 x_0') + (c_1 + 2c_2 x_0 + 3c_3 x_0^2) x_1 = f(\mu, x_0, \omega_0 x_0'), \quad (34)$$

\vdots

Then solutions x_0, x_1, \dots can be determined by solving linear equations (33), (34), \dots one by one. It can be seen that (33) is obtained from (1) via the transformation in (29). Therefore, the homoclinic solution of (33) can be given by (6). Multiplying (34) by x_0' and integrating it from τ_0 to τ , we obtain

$$\begin{aligned} \omega_0 \omega_1 x_0'^2 \Big|_{\tau_0}^{\tau} &= I(\tau) - I(\tau_0) - \omega_0^2 x_0' x_1' \Big|_{\tau_0}^{\tau} \\ &\quad - x_1 (c_1 x_0 + c_2 x_0^2 + c_3 x_0^3) \Big|_{\tau_0}^{\tau}, \end{aligned} \quad (35)$$

where

$$I(\tau) = \int_0^{\tau} x_0' f(\mu, x_0, \omega_0 x_0') d\tau. \quad (36)$$

Noting the properties of hyperbolic functions, we have

$$x_0(0) = \frac{a_0}{(b+1)} + u, \quad (37a)$$

$$x_0(\pm\infty) = u, \quad (37b)$$

$$x_1(0) = \frac{a_1}{(b+1)}, \quad (37c)$$

$$\begin{aligned} x_1(\pm\infty) &= x_0'(0) = x_0'(\pm\infty) = x_1'(0) = x_1'(\pm\infty) \\ &= 0. \end{aligned} \quad (37d)$$

Thus letting $\tau_0 = -\infty$ and $\tau = +\infty$ in (35), we derive

$$\int_{-\infty}^{+\infty} x_0' f(\mu, x_0, \omega_0 x_0') d\tau = I(+\infty) - I(-\infty) = 0. \quad (38)$$

Equation (38), which can also be derived by the classical Melnikov method, represents the critical condition under which the homoclinic bifurcation occurs. In other words, there exists a homoclinic solution once all the constants in (26) satisfy (38). Letting $\tau_0 = 0$ and $\tau = +\infty$ in (35) gives

$$a_1 = \frac{-(b+1)I(+\infty)}{c_1(a_0/(b+1)+u) + c_2(a_0/(b+1)+u)^2 + c_3(a_0/(b+1)+u)^3}. \quad (39)$$

Furthermore, substituting $\tau_0 = 0$ into (35) yields

$$\begin{aligned} \omega_1 = \frac{1}{\omega_0 x_0'^2} & \left\{ I(\tau) - \omega_0^2 x_0' x_1' - x_1 (c_1 x_0 + c_2 x_0^2 \right. \\ & + c_3 x_0^3) + \left(\frac{a_1}{b+1} \right) \left[c_1 \left(\frac{a_0}{b+1} + u \right) \right. \\ & \left. \left. + c_2 \left(\frac{a_0}{b+1} + u \right)^2 + c_3 \left(\frac{a_0}{b+1} + u \right)^3 \right] \right\}. \end{aligned} \quad (40)$$

The three equations above allow μ_c , a_1 , and ω_1 to be determined one by one. As an illustration, here we consider

$$f(\mu, x_0, \omega_0 x_0') = \omega_0 x_0' (\mu_0 + \mu_1 x_0 + \mu_2 x_0^2), \quad (41)$$

in which μ_0 , μ_1 , and μ_2 are constants. Noting (41), and substituting (6) and (7) into (36), the latter becomes

$$\begin{aligned} I(\tau) = \frac{a_0^2 \omega_0}{(b^2-1)^2} & \left\{ \frac{(-b\mu_0 + \beta\mu_1 + \gamma\mu_2)}{\sqrt{b^2-1}} \right. \\ & \cdot \operatorname{arctanh} \left(\sqrt{\frac{b-1}{b+1}} \tanh \left(\frac{\tau}{2} \right) \right) \\ & + \frac{\sinh(\tau)}{6(\cosh(\tau)+b)^3} \left[\mu_0 \sum_{i=0}^2 A_i \cosh^i(\tau) \right. \\ & + \frac{\mu_1}{4(b^2-1)(\cosh(\tau)+b)} \sum_{i=0}^3 B_i \cosh^i(\tau) \\ & \left. \left. + \frac{\mu_2}{20(b^2-1)^2(\cosh(\tau)+b)^2} \sum_{i=0}^4 D_i \cosh^i(\tau) \right] \right\}, \end{aligned} \quad (42)$$

where the expressions of the constants β , γ , A_i , B_i , and D_i are listed in Appendix. Noting that, in (41), x_0 is an even function and x_0' is an odd function with respect to τ , (38) can be rewritten as

$$I(+\infty) = 0. \quad (43)$$

Thus substituting (42) into (43), one derives

$$\begin{aligned} \mu_0 A_2 + \frac{\mu_1 B_3}{4(b^2-1)} + \frac{\mu_2 D_4}{20(b^2-1)^2} \\ + \frac{6(-b\mu_0 + \beta\mu_1 + \gamma\mu_2)}{\sqrt{b^2-1}} \operatorname{arctanh} \left(\sqrt{\frac{b-1}{b+1}} \right) \\ = 0. \end{aligned} \quad (44)$$

Equation (44) is the condition under which homoclinic bifurcation occurs. Substituting (43) into (39) gives

$$a_1 = 0. \quad (45)$$

Then (40) can be rewritten as

$$\begin{aligned} \omega_1(\tau) = \frac{(\cosh(\tau)+b)^4}{(b^2-1)^2 \sinh^2(\tau)} & \left\{ \frac{(-b\mu_0 + \beta\mu_1 + \gamma\mu_2)}{\sqrt{b^2-1}} \right. \\ & \cdot \operatorname{arctanh} \left(\sqrt{\frac{b-1}{b+1}} \tanh \left(\frac{\tau}{2} \right) \right) \\ & + \frac{\sinh(\tau)}{6(\cosh(\tau)+b)^3} \left[\mu_c \sum_{i=0}^2 A_i \cosh^i(\tau) \right. \\ & + \frac{\mu_1}{4(b^2-1)(\cosh(\tau)+b)} \sum_{i=0}^3 B_i \cosh^i(\tau) \\ & \left. \left. + \frac{\mu_2}{20(b^2-1)^2(\cosh(\tau)+b)^2} \sum_{i=0}^4 D_i \cosh^i(\tau) \right] \right\}. \end{aligned} \quad (46)$$

Finally, the expression for homoclinic solution can be expressed by

$$\begin{aligned} x &= \frac{a_0}{b + \cosh \tau} + u + O(\varepsilon^2), \\ \dot{x} &= -\frac{[\omega_0 + \varepsilon \omega_1(\tau)] a_0 \sinh \tau}{(b + \cosh \tau)^2} + O(\varepsilon^2). \end{aligned} \quad (47)$$

It can be seen that once c_2 or c_3 becomes zero, the present procedures can be reduced to the methods and solutions presented in [17] or in [18].

Example 2. Consider the equation

$$\ddot{x} + x - x^2 - 2x^3 = (\mu_0 - 2x + 9x^2) \dot{x}, \quad (48)$$

which is a generalized Helmholtz-Duffing-Van der Pol equation with $c_1 = 1$, $c_2 = -1$, $c_3 = -2$, $\varepsilon = 1$, $\mu_1 = -2$, and $\mu_2 = 9$. Here μ_0 is the classical damping coefficient which is considered as the bifurcation parameter. A limit cycle motion can break up by homoclinic bifurcation at a critical value of the damping coefficient. From (14), (15), (21), and (22), we have $u = 0.5$, $\omega_0 = 1/\sqrt{2}$, $a_0 = -9/\sqrt{10}$, and $b = 4\sqrt{2}/\sqrt{5}$.

From (44), the homoclinic bifurcation value of the damping coefficient μ_0 is

$$\mu_0 = \frac{-1}{120} \cdot \frac{22625\sqrt{6} \operatorname{arctanh}\left(3\sqrt{3}/(4\sqrt{2} + \sqrt{5})\right) - 44478}{20\sqrt{6} \operatorname{arctanh}\left(3\sqrt{3}/(4\sqrt{2} + \sqrt{5})\right) - 63} \quad (49)$$

$$= -0.241.$$

Then from (46) and (47), the homoclinic solution can be obtained as below,

$$x = \frac{-9}{8 + \sqrt{10} \cosh \tau} + \frac{1}{2}, \quad (50)$$

$$\dot{x} = \frac{45\sqrt{5} \left[\sqrt{3/2} + \omega_1(\tau) \right] \sinh \tau}{\sqrt{2} (4\sqrt{10} + 5 \cosh \tau)^2},$$

where

$$\begin{aligned} \omega_1(\tau) = & -250\sqrt{3} \sinh^3 \tau (2032\sqrt{2} + 392\sqrt{5} \cosh \tau \\ & + 49\sqrt{2} \cosh^2 \tau) \operatorname{arctanh}\left(\frac{3\sqrt{3}}{4\sqrt{2} + \sqrt{5}}\right) \\ & + 98\sqrt{3} (8192\sqrt{5} + 25600\sqrt{2} \cosh \tau \\ & + 12800\sqrt{5} \cosh^2 \tau + 8000\sqrt{2} \cosh^3 \tau \\ & + 1000\sqrt{5} \cosh^4 \tau + 125\sqrt{2} \cosh^5 \tau) \\ & \cdot \operatorname{arctanh}\left(\frac{3\sqrt{3}}{4\sqrt{2} + \sqrt{5}} \tanh \frac{\tau}{2}\right) + 63 \sinh \tau \\ & \cdot (-39400 \\ & - 14238\sqrt{10} \cosh \tau - 2040 \cosh^2 \tau \\ & + 175\sqrt{10} \cosh^3 \tau). \end{aligned} \quad (51)$$

The time history diagrams and the phase portraits of the solutions by different methods are shown in Figures 3 and 4, respectively. It can be seen from the figures that the present method still shows preference in the comparison. By the numerical method, the homoclinic bifurcation point can be found at $\mu_c = -0.239$, which are very close to those predicted by the present method.

4. Application to the Chaos Prediction of the Nonautonomous Helmholtz-Duffing Oscillator

Consider the nonautonomous Helmholtz-Duffing equation

$$\ddot{x} + c_1 \dot{x} + c_2 x^2 + c_3 x^3 = \varepsilon (\mu_0 \dot{x} + F \cos \Omega t), \quad (52)$$

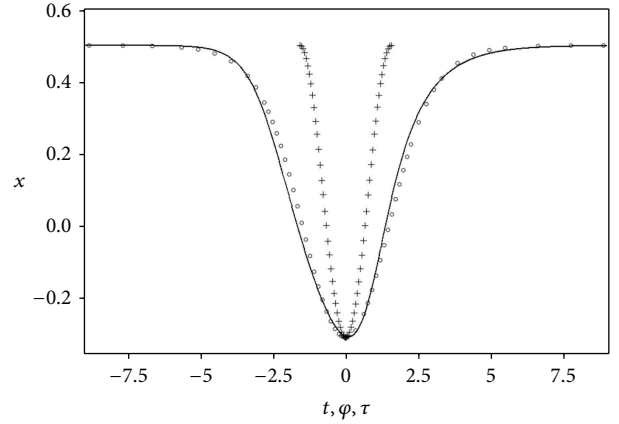


FIGURE 3: Time histories for homoclinic solutions of (48): — AUTO numerical method [30, 31]; ○ ○ ○ present method; +++ generalized harmonic function perturbation method [20].

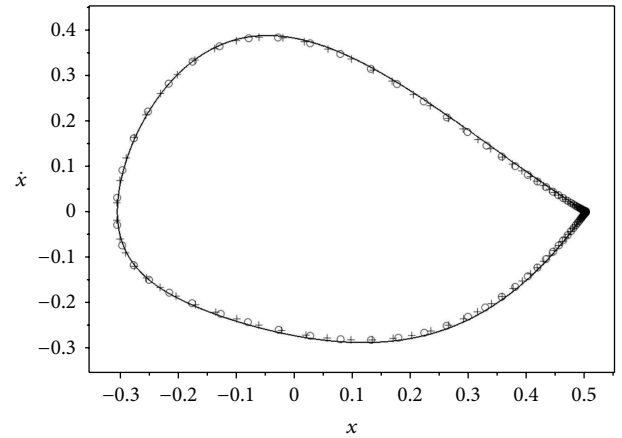


FIGURE 4: Phase portrait for homoclinic solutions of (48): — AUTO numerical method [30, 31]; ○ ○ ○ present method; +++ generalized harmonic function perturbation method [20].

where $F \cos \Omega t$ is the external harmonic excitation with the amplitude F and the frequency Ω . According to the Melnikov method [1, 2], the Melnikov function of (52) can be written as

$$\begin{aligned} M(\theta) = & \int_{-\infty}^{+\infty} \left[\dot{x}_0, c_1 x_0 + c_2 x_0^2 + c_3 x_0^3 \right]^T \\ & \wedge [0, \mu_0 \dot{x}_0 + F \sin \Omega(t + \theta)]^T d\theta \quad (53) \\ = & \mu_0 \int_{-\infty}^{+\infty} \dot{x}_0^2 dt - F \sin(\Omega\theta) \int_{-\infty}^{+\infty} \dot{x}_0 \sin(\Omega t) dt, \end{aligned}$$

where x_0 is the solution presented in (6) and \wedge denotes the vector cross product. Then the chaotic response of the system may occur if there exists a simple zero point of $M(\theta)$. Thus, we substitute (7) into (53), and let $M(\theta) = 0$; the latter yields

$$M(\theta) = F \sin \Omega\theta + \frac{I}{J} = 0, \quad (54)$$

where

$$I = \frac{a_0^2 \omega_0}{(b^2 - 1)^2} \left[\frac{-b\mu_0}{\sqrt{b^2 - 1}} \cdot \operatorname{arctanh} \left(\sqrt{\frac{b-1}{b+1}} \tanh \frac{\omega_0 t}{2} \right) + \frac{\sinh \omega_0 t}{6 (\cosh \omega_0 t + b)^3} \mu_0 \sum_{i=0}^2 A_i \cosh^i \omega_0 t \right], \quad (55)$$

$$J = a_0 \omega_0 \int_{-\infty}^{+\infty} \frac{\sinh \omega_0 t \sin \Omega t}{(b + \cosh \omega_0 t)^2} dt.$$

Therefore, from (54) it can be seen that $M(\theta)$ possesses simple zero points if

$$F > F_c = \left| \frac{I}{J} \right|, \quad (56)$$

by which the onset of chaos can be evaluated with the threshold value F_c .

Furthermore, if we rewrite (52) as

$$\ddot{x} + c_1 \dot{x} + c_2 x^2 + c_3 x^3 - \varepsilon \mu_0 \dot{x} = \varepsilon F \cos \Omega t, \quad (57)$$

and consider using the homoclinic solution expressed in (47) for Melnikov function, then we can derive

$$M(\theta) = \int_{-\infty}^{+\infty} [\dot{x}_0, c_1 x_0 + c_2 x_0^2 + c_3 x_0^3]^T \wedge [0, F \sin \Omega(t + \theta)]^T d\theta \quad (58)$$

$$= F \int_{-\infty}^{+\infty} \dot{x} \cos \Omega(t + \theta) dt$$

instead. Note that \dot{x} is odd function of t . For any real value of F , there exists $\theta = 2k\pi$, where k can be any integer number, to satisfy $M(\theta) = 0$. That means the condition for chaos prediction becomes less restricted than that presented with the exact homoclinic solution of conservative system. Comparing (58) and (53) we can see that the difference is caused by omitting of the damping term $\mu_0 \dot{x}$ in the Melnikov function calculation. In essence, the Melnikov method is based on approximation theory and, according to the method, it should be better to arrange all the perturbation terms at the right hand side of the equation to take them into account in the Melnikov function calculation. In other words, if we get the homoclinic solutions with perturbation method firstly and then implement the Melnikov function, we probably get a less restricted condition, because actually we conduct the perturbation approximations twice.

It is worth pointing out that as the present solutions by hyperbolic functions are explicit in respect to the real time t , they are more applicable to the Melnikov method for chaos prediction than those derived implicitly by generalized harmonic functions [12, 13, 19, 20]. In particular, it should also

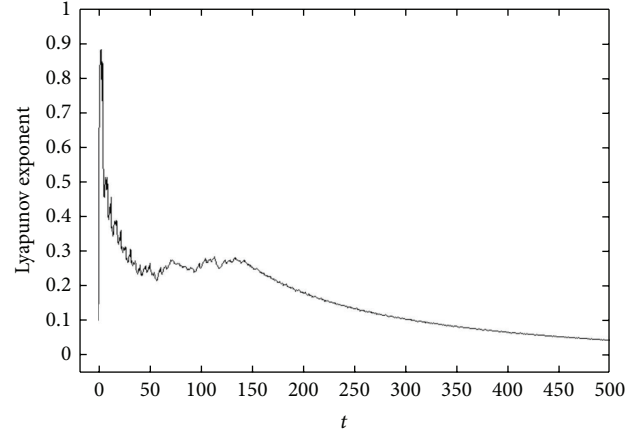


FIGURE 5: Lyapunov exponent diagram of (59) with $F = 3$.

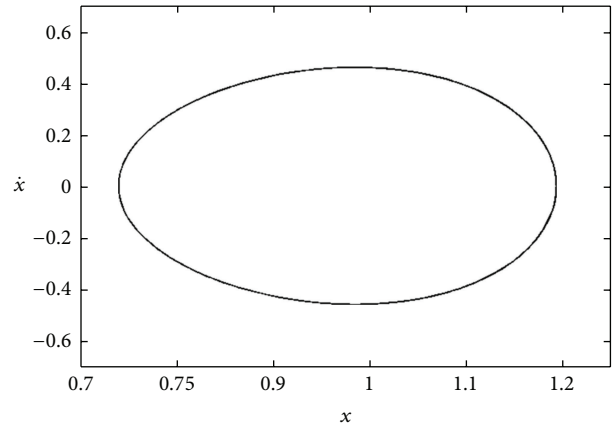


FIGURE 6: Limit cycle of (59) with $F = 3$.

be pointed out that the Melnikov method is only regarded as one of the conditions for chaotic prediction. At present, a chaotic motion should still be evaluated more thoroughly with qualitative theory and numerical method. Below are two examples which satisfy the Melnikov condition but with different characters of chaotic motions.

Example 3. Consider the equation

$$\ddot{x} - x - x^2 + 2x^3 = 0.1(-\dot{x} + F \cos 2t), \quad (59)$$

which is the case of (52) with $c_1 = -1$, $c_2 = -1$, $c_3 = 2$, $\varepsilon = 0.1$, $\mu_0 = -1$, and $\Omega = 2$. From (17), (55), and (56) we can derive that $F_c = 1.43$ when $a_0 = 0.94868$ and $F_c = 1.11$ when $a_0 = -0.94868$. Therefore it can be estimated that chaotic motion may happen if $F > 1.43$. The numerical results of homoclinic bifurcation by AUTO numerical method [30, 31] show that, with $F = 3$, the Lyapunov exponent value shows chaos behavior from $t = 0$ to about $t = 145$ and then converts to 0 gradually. That means the chaotic motion possesses dissipative chaos property. The Lyapunov exponent diagram is shown in Figure 5. The Lyapunov exponent value converts to less than 0.01 after $t = 1000$. The phase portrait of the system after $t = 1000$ is shown in Figure 6, which shows that the motion converts to a limit cycle.

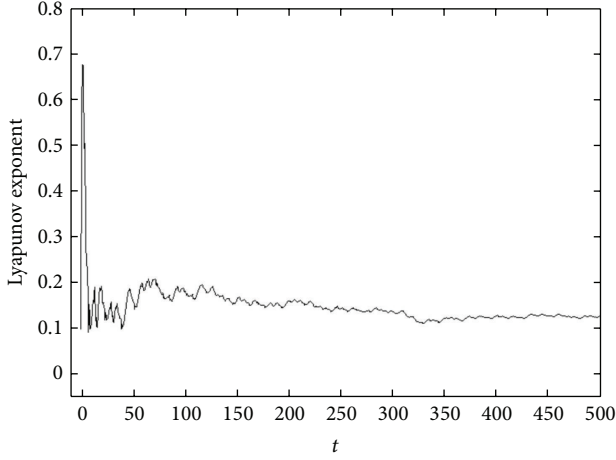


FIGURE 7: Lyapunov exponent diagram of (60) with $F = 2.90$.

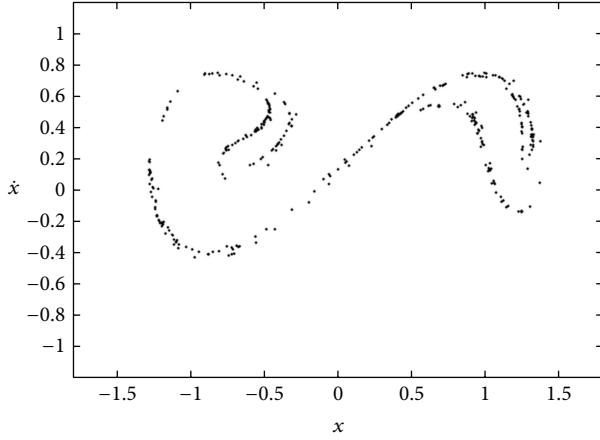


FIGURE 8: Strange attractor of (60) with $F = 2.90$.

Example 4. Consider the equation

$$\ddot{x} - x - 0.05x^2 + x^3 = 0.1(-2.5\dot{x} + F \cos t), \quad (60)$$

which is the case of (52) with $c_1 = -1$, $c_2 = -0.05$, $c_3 = 1$, $\varepsilon = 0.1$, $\mu_0 = -2.5$, and $\Omega = 1$. From (17), (55), and (56) we can derive that $F_c = 1.94$ when $a_0 = 1.4138$ and $F_c = 1.82$ when $a_0 = -1.4138$. Therefore it can be estimated that chaotic motion may happen if $F > 1.94$. The numerical results of homoclinic bifurcation by AUTO numerical method [30, 31] show that the Lyapunov exponent value stays more than 0 when $F = 2.90$. The Lyapunov exponent diagram is shown in Figure 7. The Poincaré projection of the system from $t = 500$ to $t = 5000$ is shown in Figure 8. In the figure, the fractal character of a strange attractor can be observed, which supports the prediction of chaotic motion.

5. Conclusions

The present procedures are efficient for constructing homoclinic solutions of the Helmholtz-Duffing oscillator. The exact and explicit homoclinic solution of the undamped Helmholtz-Duffing oscillator is derived by a hyperbolic function balance procedure. The homoclinic solution of the self-excited system is then obtained by the extension of the hyperbolic perturbation procedure. The application to the chaos prediction of the nonautonomous Helmholtz-Duffing oscillator can also be conducted.

Appendix

Consider

$$\beta = \frac{-4b^3u - 4a_0b^2 + 4bu - a_0}{4(b^2 - 1)},$$

$$\gamma = \frac{-4b^5u^2 - 8a_0b^4u - 4a_0^2b^3 + 8b^3u^2 + 6a_0b^2u - 3a_0^2b - 4bu^2 + 2a_0u}{4(b^2 - 1)^2},$$

$$A_0 = 5b^2 - 2,$$

$$A_1 = 3b(b^2 + 1),$$

$$A_2 = b^2 + 2,$$

$$B_0 = 20b^5u + 28a_0b^4 - 28b^3u - 19a_0b^2 + 8bu + 6a_0,$$

$$B_1 = 12b^6u + 12a_0b^5 + 20b^4u + 37a_0b^3 - 40b^2u - 4a_0b,$$

$$B_2 = 16b^5u + 8a_0b^4 + 4b^3u + 40a_0b^2 - 20bu - 3a_0,$$

$$B_3 = 4b^4u + 2a_0b^3 + 4b^2u + 13a_0b - 8u,$$

$$D_0 = 100b^8u^2 + 280a_0b^7u + 180a_0^2b^6 - 240b^6u^2 - 470a_0b^5u - 149a_0^2b^4 + 180b^4u^2 + 250a_0b^3u + 98a_0^2b^2 - 40b^2u^2 - 60a_0bu - 24a_0^2,$$

$$D_1 = 60b^9u^2 + 120a_0b^8u + 60a_0^2b^7 + 140b^7u^2 + 530a_0b^6u + 375a_0^2b^5 - 540b^5u^2 - 880a_0b^4u - 25a_0^2b^3 + 420b^3u^2 + 290a_0b^2u + 10a_0^2b - 80bu^2 - 60a_0u,$$

$$D_2 = 140b^8u^2 + 200a_0b^7u + 60a_0^2b^6 - 20b^6u^2 + 570a_0b^5u + 563a_0^2b^4 - 420b^4u^2 - 840a_0b^3u - a_0^2b^2 + 340b^2u^2 + 70a_0bu + 8a_0^2 - 40u^2,$$

$$D_3 = 100b^7u^2 + 100a_0b^6u + 30a_0^2b^5 - 60b^5u^2 + 430a_0b^4u + 355a_0^2b^3 - 180b^3u^2 - 560a_0b^2u + 35a_0^2b + 140bu^2 + 30a_0u,$$

$$D_4 = 20b^6u^2 + 20a_0b^5u + 6a_0^2b^4 + 110a_0b^3u + 83a_0^2b^2 - 60b^2u^2 - 130a_0bu + 16a_0^2 + 40u^2.$$

(A.1)

Conflict of Interests

The authors hereby declare that there is no conflict of interests regarding the publication of this paper.

Acknowledgments

The financial supports from the National Basic Research Program of China (2011CB013606), the National Natural Science Foundations of China (91315301-07, 11102045), and the National Plan for Science and Technology Support of China (2012BAJ07B02) are gratefully acknowledged.

References

- [1] A. H. Nayfeh and B. Balachandran, *Applied Nonlinear Dynamics: Analytical, Computational, and Experimental Method*, Wiley-Interscience, New York, NY, USA, 1995.
- [2] J. Guckenheimer and P. Holmes, *Nonlinear Oscillations, Dynamical Systems, and Bifurcation of Vector Field*, Springer, New York, NY, USA, 2002.
- [3] F. C. Moon, J. Cusumano, and P. J. Holmes, "Evidence for homoclinic orbits as a precursor to chaos in a magnetic pendulum," *Physica D: Nonlinear Phenomena*, vol. 24, no. 1-3, pp. 383-390, 1987.
- [4] A. L. Katz and E. H. Dowell, "From single well chaos to cross well chaos: a detailed explanation in terms of manifold intersections," *International Journal of Bifurcation and Chaos*, vol. 4, no. 4, pp. 933-941, 1994.
- [5] J. J. Feng, Q. C. Zhang, and W. Wang, "Chaos of several typical asymmetric systems," *Chaos, Solitons & Fractals*, vol. 45, no. 7, pp. 950-958, 2012.
- [6] S. Lenci, G. Menditto, and A. M. Tarantino, "Homoclinic and heteroclinic bifurcations in the non-linear dynamics of a beam resting on an elastic substrate," *International Journal of Non-Linear Mechanics*, vol. 34, no. 4, pp. 615-632, 1999.
- [7] S. Lenci and G. Rega, "Control of the homoclinic bifurcation in buckled beams: infinite dimensional vs reduced order modeling," *International Journal of Non-Linear Mechanics*, vol. 43, no. 6, pp. 474-489, 2008.
- [8] J. H. Merkin and D. J. Needham, "On infinite period bifurcations with an application to roll waves," *Acta Mechanica*, vol. 60, no. 1-2, pp. 1-16, 1986.
- [9] I. M. Uzunov, "Description of the suppression of the soliton self-frequency shift by bandwidth-limited amplification," *Physical Review E*, vol. 82, Article ID 066603, 8 pages, 2010.
- [10] I. M. Uzunov and T. N. Arabadzchiev, "Suppression of the soliton self-frequency shift and compression in the presence of bandwidth-limited amplification," *Physical Review E*, vol. 84, no. 2, Article ID 026607, 9 pages, 2011.
- [11] Q. Bi, "Singular solitary waves associated with homoclinic orbits," *Physics Letters A*, vol. 352, no. 3, pp. 227-232, 2006.
- [12] Z. Xu, H. S. Y. Chan, and K. W. Chung, "Separatrices and limit cycles of strongly nonlinear oscillators by the perturbation-incremental method," *Nonlinear Dynamics*, vol. 11, no. 3, pp. 213-233, 1996.
- [13] H. S. Y. Chan, K. W. Chung, and Z. Xu, "Stability and bifurcations of limit cycles by the perturbation-incremental method," *Journal of Sound and Vibration*, vol. 206, no. 4, pp. 589-604, 1997.
- [14] M. Belhaq, B. Fiedler, and F. Lakrad, "Homoclinic connections in strongly self-excited nonlinear oscillators: the Melnikov function and the elliptic Lindstedt-Poincaré method," *Nonlinear Dynamics*, vol. 23, no. 1, pp. 67-86, 2000.
- [15] Y. V. Mikhlin and G. V. Manucharyan, "Construction of homoclinic and heteroclinic trajectories in mechanical systems with several equilibrium positions," *Chaos, Solitons and Fractals*, vol. 16, no. 2, pp. 299-309, 2003.
- [16] G. V. Manucharyan and Y. V. Mikhlin, "The construction of homo- and heteroclinic orbits in non-linear systems," *Journal of Applied Mathematics and Mechanics*, vol. 69, pp. 42-52, 2005.
- [17] Y. Y. Chen and S. H. Chen, "Homoclinic and heteroclinic solutions of cubic strongly nonlinear autonomous oscillators by the hyperbolic perturbation method," *Nonlinear Dynamics*, vol. 58, no. 1-2, pp. 417-429, 2009.
- [18] S. H. Chen, Y. Y. Chen, and K. Y. Sze, "A hyperbolic perturbation method for determining homoclinic solution of certain strongly nonlinear autonomous oscillators," *Journal of Sound and Vibration*, vol. 322, no. 1-2, pp. 381-392, 2009.
- [19] Y. Y. Cao, K. W. Chung, and J. Xu, "A novel construction of homoclinic and heteroclinic orbits in nonlinear oscillators by a perturbation-incremental method," *Nonlinear Dynamics*, vol. 64, no. 3, pp. 221-236, 2011.
- [20] Z. B. Li, J. S. Tang, and P. Cai, "A generalized harmonic function perturbation method for determining limit cycles and homoclinic orbits of Helmholtz-Duffing oscillator," *Journal of Sound and Vibration*, vol. 332, no. 21, pp. 5508-5522, 2013.
- [21] S. H. Chen and Y. K. Cheung, "A modified Lindstedt-Poincaré method for a strongly nonlinear system with quadratic and

- cubic nonlinearities,” *Shock and Vibration*, vol. 3, no. 4, pp. 279–285, 1996.
- [22] A. Y. T. Leung and Z. Guo, “Homotopy perturbation for conservative Helmholtz-Duffing oscillators,” *Journal of Sound and Vibration*, vol. 325, no. 1-2, pp. 287–296, 2009.
- [23] Z. Guo and A. Y. T. Leung, “The iterative homotopy harmonic balance method for conservative Helmholtz-Duffing oscillators,” *Applied Mathematics and Computation*, vol. 215, no. 9, pp. 3163–3169, 2010.
- [24] H. Askari, Z. Saadatnia, D. Younesian, A. Yildirim, and M. Kalami-Yazdi, “Approximate periodic solutions for the Helmholtz-Duffing equation,” *Computers and Mathematics with Applications*, vol. 62, no. 10, pp. 3894–3901, 2011.
- [25] A. Elías-Zúñiga, “Exact solution of the quadratic mixed-parity Helmholtz-Duffing oscillator,” *Applied Mathematics and Computation*, vol. 218, no. 14, pp. 7590–7594, 2012.
- [26] A. Elías-Zúñiga, “Analytical solution of the damped Helmholtz-Duffing equation,” *Applied Mathematics Letters*, vol. 25, no. 12, pp. 2349–2353, 2012.
- [27] K.-E. Thylwe, “Exact quenching phenomenon of undamped driven Helmholtz and Duffing oscillators,” *Journal of Sound and Vibration*, vol. 161, no. 2, pp. 203–211, 1993.
- [28] Y. Y. Lee, X. Guo, and E. W. M. Lee, “Effect of the large amplitude vibration of a finite flexible micro-perforated panel absorber on sound absorption,” *International Journal of Nonlinear Sciences and Numerical Simulation*, vol. 8, no. 1, pp. 41–44, 2007.
- [29] S. K. Lai, J. Harrington, Y. Xiang, and K. W. Chow, “Accurate analytical perturbation approach for large amplitude vibration of functionally graded beams,” *International Journal of Non-Linear Mechanics*, vol. 47, no. 5, pp. 473–480, 2012.
- [30] E. J. Doedel, H. B. Keller, and J.-P. Kernévez, “Numerical analysis and control of bifurcation problems (I): bifurcation in finite dimensions,” *International Journal of Bifurcation and Chaos*, vol. 1, no. 3, pp. 493–520, 1991.
- [31] E. J. Doedel, H. B. Keller, and J.-P. Kernévez, “Numerical analysis and control of bifurcation problems. (II): bifurcation in infinite dimensions,” *International Journal of Bifurcation and Chaos in Applied Sciences and Engineering*, vol. 1, no. 4, pp. 745–772, 1991.

Research Article

A Water Hammer Protection Method for Mine Drainage System Based on Velocity Adjustment of Hydraulic Control Valve

Yanfei Kou,^{1,2} Jieming Yang,^{1,2} and Ziming Kou³

¹Research Institute of Machinery and Electronics, Taiyuan University of Technology, Taiyuan 030024, China

²Key Laboratory of Advanced Transducers & Intelligent Control System, Ministry of Education, Taiyuan University of Technology, Taiyuan 030024, China

³Taiyuan University of Technology College of Mechanical Engineering, Mine Fluid Control Engineering Research Center (Laboratory) in Shanxi Province, Taiyuan 030024, China

Correspondence should be addressed to Jieming Yang; jmyang666@163.com

Received 3 June 2015; Accepted 28 September 2015

Academic Editor: Mario Terzo

Copyright © 2016 Yanfei Kou et al. This is an open access article distributed under the Creative Commons Attribution License, which permits unrestricted use, distribution, and reproduction in any medium, provided the original work is properly cited.

Water hammer analysis is a fundamental work of pipeline systems design process for water distribution networks. The main characteristics for mine drainage system are the limited space and high cost of equipment and pipeline changing. In order to solve the protection problem of valve-closing water hammer for mine drainage system, a water hammer protection method for mine drainage system based on velocity adjustment of HCV (Hydraulic Control Valve) is proposed in this paper. The mathematic model of water hammer fluctuations is established based on the characteristic line method. Then, boundary conditions of water hammer controlling for mine drainage system are determined and its simplex model is established. The optimization adjustment strategy is solved from the mathematic model of multistage valve-closing. Taking a mine drainage system as an example, compared results between simulations and experiments show that the proposed method and the optimized valve-closing strategy are effective.

1. Introduction

Mine drainage system is an important part in the safety production of coal mine [1]. Due to the limited space and the high cost of equipment changing, water hammer is a common phenomenon in mine drainage system and its harm is inestimable [2, 3]. The minor injuries of water hammer can cause severe shock or even pipes breaking, and the major injuries can cause equipment damaging, pumping station flooding, or even injuries to underground staff. There are several traditional water hammer protection methods such as installing vacuum valves, exhaust valve, and pressure tank. However, when these water hammer protection methods are used to mine drainage system, the original piping arrangement has to be changed because additional equipment is needed. It is unenforceable to do this in this limited mine space and the cost is too high. In this situation, controlling the time and velocity of valve-closing is an effective means to protect water hammer in mine drainage system. A water hammer is easily to be formed in pipeline if the valve-closing

is fast. On the contrary, the capability of pumps is inefficient if the valve-closing is too slow because pumps in mine drainage system are centrifugal. This inefficient operation has damage for pumps, because power provided by pumps is converted into heat. Therefore, it is important for us to research the critical valve-closing velocity for Hydraulic Control Valve (HCV). Researches of theoretical system and engineering applications for water hammer protection of pipeline fluid delivery areas are increasingly improved [4–6]. But it is still a difficult problem in mine drainage system because of the limited mine space [7, 8].

At present, the theories and methods of water hammer and its protection means become more and more mature. In summary, researches about this problem are mainly in three aspects: hydraulic transient modeling, the calculation, and protection methods of water hammer.

(1) *Hydraulic Transient Modeling*. For the research on hydraulic transient, from the mathematical derivation of the 18th century to the graphical analysis of the mid-20th

century and to the current computer digital simulation, scholars have already made a lot of research results. The major achievements are getting the relationship between multiphase and multicomponent transient flow equations, water hammer equations, and the control equations, such as Joukowski equation [9]. Based on the transient flow simulation theory, Colombo et al. [10] proposed an aqueducts fault detection technology, Lee et al. [11] proposed the pipe network leak and deterioration over time detection technology by the time domain reflectometry (TDR), Arbon et al. [12] proposed pipeline corrosion and blockage detection technology, Gong et al. [13] proposed a detection technology for pipe friction, wall thickness, velocity, position, and the length of the pipes, and Ferrante et al. [14] presented a leak detection method with coupling wavelet analysis and a Lagrangian model techniques. Meniconi et al. [15] presented a pipe system diagnosis method with the small amplitude sharp pressure waves.

(2) *The Calculation Methods of Hydraulic Transient for Water Hammer.* The calculation methods of hydraulic transient for water hammer include arithmetic method, graphic method, and numerical method.

(i) *Arithmetic Method.* Before the 1930s, the hydraulic transient calculation of water hammer used Allievi equations mostly [16]. Allievi equations can be called Arithmetic method which is used to solve the problems of water hammer that with simple boundary conditions and its workload is very large.

(ii) *Graphic Method.* Graphic method is developed in 1930s to 1960s. Bergeron, Parmakian, and so forth [17] are committed to develop this method. Boundary conditions and the process of water hammer fluctuation are expressed through coordinate graphics of H and V according to this method. Due to the graphics, it is simple and intuitive for the hydraulic transient calculation of water hammer. However, the accuracy is not high because this method is restricted by calculating means and assumptions.

(iii) *Numerical Method.* From 1960s, some numerical methods appeared that can be aided by computers, such as Characteristic (MOC) [18], Wave Characteristic Method (WCM) [19], Implicit Method [20, 21], and Finite Element Method (FEM) [22, 23]. The WCM can solve water hammer problems of complex piping systems and boundary conditions. It is the most common method because of the high accuracy and computing. The Implicit Method divides pipeline into several segments and solves equations of the entire pipeline system simultaneously in each segment. The advantage of Implicit Method can be described in a way that a longer segment is selected and the number of calculations is reduced. However, there is more time needed for calculation in large and complex pipeline network system [24]. FEM with flexibility is used in pipe network system which have complex boundary conditions. However, it has a limitation in solving hydraulic transient problems.

(3) *Water Hammer Protection.* Prevention and controlling means for water hammer are researched with the development of their theory and calculation. Wylie [25–27] has researched several protective devices for water hammer, such as air valves, check valves, pressure tank, and surge tank. Lee [28] and Stephenson [29] discussed the performances of air valves in water hammer protection. However, these researches have not given a quantitative calculation for the problem of water hammer protection.

This paper proposed a water hammer protection method based on velocity adjustment of HCV to deal with the problem of valve-closing water hammer in mine drainage system. The mathematic model of water hammer fluctuations is founded based on MOC according to the hydraulic transient. Then, boundary conditions of water hammer controlling for mine drainage system are determined and the simplex model is established. Finally, the optimization adjustment strategy is solved with simulation and experiment.

The remainder of this paper is organized as follows. Section 2 provides the mathematic model of the propagation and superposition model for water hammer fluctuations. Section 3 provides an optimization method to determine the adjustment strategy for HCV. Section 4 presents a case study. Concluding remarks are offered in the last section of this paper.

2. The Process of Water Hammer Fluctuations

2.1. Mathematic Model

(1) *Foundation Equations.* The momentum equations of transient flow can be expressed as

$$-\frac{1}{g} \frac{\partial V}{\partial t} = \frac{\partial H}{\partial x} + \frac{f}{D} \frac{V^2}{2g} + \frac{\partial}{\partial x} \left(\frac{V^2}{2g} \right), \quad (1)$$

where V is longitudinal mean velocity, H is pressure head, f is friction factor, D is diameter of pipeline, g is gravitational acceleration, x is propagation distance along pipe, and t is time.

The left of the equation represents the time-varying inertia force in a unit volume. In the right, the first item represents the pressure in a unit volume of fluid. The second item is friction loss pressure in a unit length of pipe, and the third item is pressure of transient flow.

The continuity equation is used to describe transient flow and it can be expressed as follows:

$$\frac{\partial H}{\partial t} + V \frac{\partial H}{\partial x} + \frac{a^2}{g} \frac{\partial V}{\partial x} - V \sin \theta = 0, \quad (2)$$

where a is propagation speed of water hammer wave and θ is the angle between the axis of pipe and the horizontal line.

(2) *The Process of Water Hammer Fluctuations.* Pressures that are caused by friction loss and transient flow velocity are ignored. Furthermore, $V \ll a$ is considered for continuity

equations. Then, the foundation equations can be simplified as

$$\begin{aligned} \frac{\partial H}{\partial x} + \frac{1}{g} \frac{\partial V}{\partial t} &= 0, \\ \frac{\partial H}{\partial t} + \frac{a^2}{g} \frac{\partial V}{\partial x} &= 0. \end{aligned} \quad (3)$$

The second-order partial differential equations about $H(x, t)$ and $V(x, t)$ are obtained through the partial derivative and are taken for variables x and t in (3). Therefore, the momentum equations for water hammer wave in pipeline drainage system are expressed as

$$\begin{aligned} \frac{\partial H^2}{\partial x^2} &= \frac{1}{a^2} \frac{\partial H^2}{\partial t^2}, \\ \frac{\partial V^2}{\partial x^2} &= \frac{1}{a^2} \frac{\partial V^2}{\partial t^2}. \end{aligned} \quad (4)$$

The functions $F(x, t)$ and $f(x, t)$ are introduced along with characteristic lines $dx = \pm dt$. Then, the general solution of (4) can be described as

$$\begin{aligned} H - H_0 &= F\left(t - \frac{x}{a}\right) + f\left(t + \frac{x}{a}\right), \\ V - V_0 &= -\frac{g}{a} \left[F\left(t - \frac{x}{a}\right) - f\left(t + \frac{x}{a}\right) \right], \end{aligned} \quad (5)$$

where H_0 is the initial pressure head, V_0 is the initial flow velocity, and $F(x, t)$ and $f(x, t)$ are direct and reflection fluctuation functions.

2.2. Propagation and Superposition Model of Water Hammer Wave Based on Characteristic Line Method. Pumps and valves are the generating sources of water hammer wave in hydraulic transition process of pipeline fluid delivery system. These two kinds of water hammer wave start at the same time and propagation directions are superimposed. The superposition leads to strengthening of fluctuations for water hammer. In order to control the water hammer pressure effectively, the superposition effects of water hammer wave need to be weakened as much as possible.

The fundamental equations of water hammer can be rewritten as

$$\begin{aligned} L_1 &= g \frac{\partial H}{\partial t} + V \frac{\partial V}{\partial x} + \frac{\partial V}{\partial t} + \frac{fV|V|}{2D} = 0, \\ L_2 &= \frac{\partial H}{\partial t} + V \frac{\partial V}{\partial x} + \frac{a^2}{g} \frac{\partial V}{\partial x} - V \sin \theta = 0. \end{aligned} \quad (6)$$

These equations are combined linearly using an unknown multiplier λ . Let $L = L_1 + \lambda L_2$ be the linear combination. The coefficient λ can be determined by

$$\lambda = \pm \frac{g}{a}. \quad (7)$$

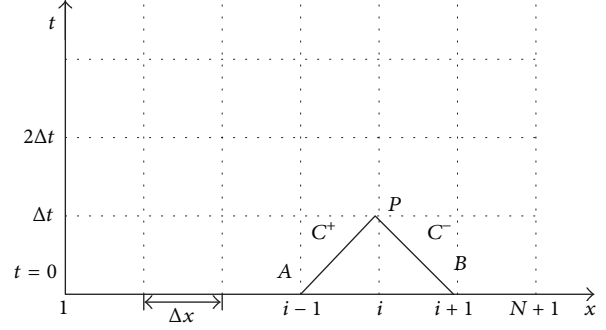


FIGURE 1: Characteristic line grid for water hammer calculation.

In the constraint of characteristic line equation $dx/dt = V \pm a$, (6) converts to ordinary differential equation as follows:

$$\begin{aligned} C^+ &\begin{cases} \frac{dH}{dt} + \frac{a}{g} \frac{dV}{dt} - V \sin \theta + \frac{faV|V|}{2gD} = 0 \\ \frac{dx}{dt} = V + a, \end{cases} \\ C^- &\begin{cases} \frac{dH}{dt} - \frac{a}{g} \frac{dV}{dt} - V \sin \theta - \frac{faV|V|}{2gD} = 0 \\ \frac{dx}{dt} = V - a. \end{cases} \end{aligned} \quad (8)$$

V and $V \sin \theta$ are negligible when $V \ll a$ and the tilt angle of pipeline is less than 25° . The average flow velocity V is replaced by flow Q . The characteristic equations are changed into

$$\begin{aligned} C^+ &\begin{cases} \frac{dH}{dt} + \frac{a}{gA} \frac{dQ}{dt} + \frac{faQ|Q|}{2gDA^2} = 0 \\ \frac{dx}{dt} = +a, \end{cases} \\ C^- &\begin{cases} -\frac{dH}{dt} + \frac{a}{gA} \frac{dQ}{dt} + \frac{faQ|Q|}{2gDA^2} = 0 \\ \frac{dx}{dt} = -a, \end{cases} \end{aligned} \quad (9)$$

where C^+ is the characteristic line of forward wave in x -axis, C^- is the characteristic line of reflected wave in x -axis, and A is cross-sectional area of pipe.

The integral operation and differential conversion are introduced to (9). The discrete characteristic equations of water hammer are obtained as follows. Equation (10) and the characteristic line grid are shown in Figure 1:

$$\begin{aligned} H_P - H_A + \frac{a}{gA} (Q_P - Q_A) + \frac{f\Delta x Q_A |Q_A|}{2gDA^2} &= 0, \\ H_P - H_B + \frac{a}{gA} (Q_P - Q_B) + \frac{f\Delta x Q_B |Q_B|}{2gDA^2} &= 0. \end{aligned} \quad (10)$$

By solving the above equations, transient variables H_P and Q_P in the node i of the pipe over the time Δt are expressed as

$$\begin{aligned} H_P &= \frac{(C_P + C_M)}{2}, \\ Q_P &= \frac{(C_P - H_P)}{B}, \end{aligned} \quad (11)$$

where $B = a/gA$.

Consider

$$\begin{aligned} C_P &= H_A + BQ_A - \frac{f\Delta x}{2gDA^2}Q_A|Q_A|, \\ C_M &= H_B - BQ_A - \frac{f\Delta x}{2gDA^2}Q_B|Q_B|. \end{aligned} \quad (12)$$

The initial condition of water hammer is that of a steady flow, C_P and C_M in (11) are known, and the parameters on each time step can be solved.

Hydraulic characteristics of HCV can be described through loss coefficient ξ and capacity coefficient C . Consider

$$\begin{aligned} Q_f &= \frac{A}{\sqrt{\xi}}\sqrt{2g\Delta H_f}, \\ Q_f &= C\sqrt{\Delta H_f}, \end{aligned} \quad (13)$$

where A is cross-sectional area of the upstream of HCV and ΔH_f is the pressure difference of HCV in upper and lower.

Let $\tau = (C/C_0)(\tau = \sqrt{\xi_0/\xi})$ be the relative opening displacement of HCV. The dimensionless flow through HCV can be described as

$$q_f = \frac{Q_f}{Q_{f0}} = \tau\sqrt{\Delta h_f}, \quad (14)$$

where Δh_f is pressure difference on HCV. It can be solved as $\Delta H_f/\Delta H_{f0}$. The subscript "0" represents HCV being open completely.

3. Optimization Method for Velocity Adjustment of HCV

3.1. Boundary Conditions. Boundary conditions for pump of outlet are shown in Figure 2. If the inlet loss of pump is ignored, the inlet of pool, pump, and HCV can be combined and dealt with as a boundary of characteristic line in foundational equations of water hammer.

The equilibrium condition for water head is established in this boundary. It can be described as

$$H_f + H - H_l = H_p, \quad (15)$$

where H_f is the depth of pool inlet, H is the work lift of the pump, H_l is the transient resistance loss of HCV, and H_p is the pressure head of HCV outlet.

We take the balance equations of water head which in the characteristic line C^- and inertia equations of pump unit

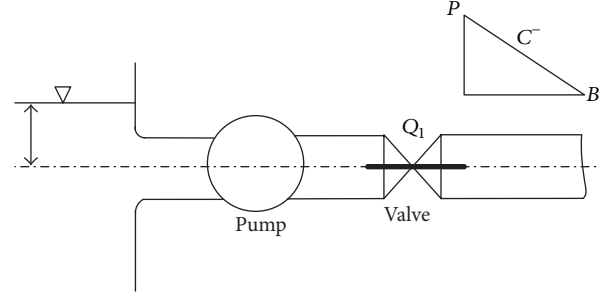


FIGURE 2: Boundary conditions of pump outlet.

together. And then the boundary conditions can be expressed as follows based on the characteristic lines of pumps:

$$\begin{aligned} x &= \pi + \arctan \frac{q}{\alpha}, \\ WH(x) &= \frac{h}{\alpha^2 + q^2}, \\ WB(x) &= \frac{\beta}{\alpha^2 + q^2}, \end{aligned} \quad (16)$$

where the pump-lift is $h = H/H_R$. The flow of pump is $q = Q/Q_R$. The rotational speed is $\alpha = n/n_R$. The torque is $\beta = T/T_R$. The subscript represents rated working conditions. Then, (16) is generated as follows:

$$\begin{aligned} F_1 &= H_j - C_M - BQ_Rq + H_R(\alpha^2 + q^2)WH(x) \\ &\quad - \frac{H_{f0}q|q|}{\tau^2} = 0, \\ F_2 &= (\alpha^2 + q^2)WB(x) + \beta_0 - K_1(\alpha_0 - \alpha) = 0, \end{aligned} \quad (17)$$

where $K_1 = 2Kn_R/T_R$; $K = \pi GD^2/120g$; and GD^2 is rotational inertia. α_0 and β_0 are rotational speed and torque in the initial state. Then, (17) can be rewritten as follows when variables α and q are introduced:

$$\begin{aligned} F_1 + F_{1q}\Delta q + F_{1\alpha}\Delta\alpha &= 0, \\ F_2 + F_{2q}\Delta q + F_{2\alpha}\Delta\alpha &= 0. \end{aligned} \quad (18)$$

The problem is solved as follows:

$$\begin{aligned} \alpha^{(k+1)} &= \alpha^{(k)} + \Delta\alpha, \\ q^{(k+1)} &= q^{(k)} + \Delta q, \end{aligned} \quad (19)$$

in which $\Delta\alpha$ and Δq are solved through (18).

The iterative errors should meet (19). Consider

$$|\Delta\alpha| + |\Delta q| \leq \varepsilon \quad (\varepsilon = 0.0002). \quad (20)$$

3.2. Optimization Method of HCV Adjustment. The boundary conditions of multistage valve-closing are introduced in the characteristic line calculation of water hammer for which

the best procedure for multistage valve-closing is considered. The displacement of valve-closing at any time can be determined through linear procedure in multistage valve closure.

Through a large number of practical tests, the valve closure with a uniform or uniform variable speed is found to have a small influence on the water hammer in the front 2/3 of valve-closing stroke, while there is a large influence on the later 1/3 of valve-closing stroke. Therefore, the valve closure process is divided into multistage. By doing so, the

uniform and uniform variable speeds are both introduced to valve closure process. In the following section we will discuss uniform or uniform variable speed calculation method in valve closure process.

Assuming that the times of valve-closing in multi-stage are $T_1, T_2, \dots, T_i, \dots, T_n$, the corresponding displacements of valve-closing are $s_1, s_2, \dots, s_i, \dots, s_n$. Then, the displacements of valve-closing at any time t are determined as follows:

$$s_i = \begin{cases} \frac{s_1}{T_1} & t \leq T_1, \text{ The 1st stage of valve-closing} \\ s_1 + \frac{s_2}{T_2} (t - T_1) & T_1 \leq t \leq T_1 + T_2, \text{ The 2nd stage of valve-closing} \\ s_1 + s_2 + \dots + s_{i-1} + \frac{s_i}{T_i} (t - T_{i-1}) & T_1 + T_2 + \dots + T_{i-1} \leq t \leq T_1 + T_2 + \dots + T_i, \text{ The } i \text{ stage of valve-closing} \\ s_1 + s_2 + \dots + s_i + \dots + \frac{s_n}{T_n} (t - T_{n-1}) & T_1 + T_2 + \dots + T_i + \dots + T_{n-1} \leq t \leq T_1 + T_2 + \dots + T_i + \dots + T_n, \text{ The } n \text{ stage of valve-closing} \\ s_1 + s_2 + \dots + s_i + s_n = S & t > T_1 + T_2 + \dots + T_i + T_n, \text{ valve-closing is completed,} \end{cases} \quad (21)$$

where s_i is displacement of valve-closing at t and S is the total stroke of valve-closing.

For the valve-closing displacement s_i at any time t , we can calculate the dimensionless opening degree τ using (21) through linear interpolation according to equidistant Δs_i and its input value:

$$\begin{aligned} \tau &= \tau(i) + \frac{u^{(k)}}{2} [\tau(i+1) - k\tau(i)] \tau(i) \\ &+ \frac{u^{(k-1)}}{2} [\tau(i+1) - (k-1)\tau(i)] + \dots \\ &+ \frac{u^2}{2} [\tau(i+1) - 2\tau(i)] \\ &+ \frac{u}{2} [\tau(i+1) - \tau(i)], \\ u &= \frac{s_i - s_0}{\Delta s_i} - 1. \end{aligned} \quad (22)$$

In the scope of velocity adjustment for HCV, the velocity, displacement, and time of valve-closing have various combinations. This paper adopts a multistage adjustment strategy according to simulation results of water hammer.

The valve closure time for the first stage is equal or close to the time of the flow of pump that is zero. The valve closure time for the following stages is one in four of the previous stage. Consequently, the initial valve closure procedure is determined. Then, search computing is taken to determine the optimization valve closure procedure.

4. Case Study and Experiment

4.1. Working Conditions. The mine with normal water quality was considered. The water normal inflow was $50 \text{ m}^3/\text{h}$ and the maximum inflow was $250 \text{ m}^3/\text{h}$. Water was discharged into

ground by two drain pipes of which the specifications were $D273 \times 12$, respectively (one was used and another was spare). The pipes in this existing and antiquated mine drainage system were seamless steel pipe. The allowed pressure was lower at 6.4 MPa. The wellhead elevation was 997.991 m and the borehole inclination was 20° . There were three multistage centrifugal pumps and two HCVs were used in Figure 3. And the specification of pumps was MD280-65 \times 6 ($Q = 280 \text{ m}^3/\text{h}$, $H = 390 \text{ m}$). One pump was used and others were maintenance when the mine was with a normal inflow, or two pumps were used and one was spare when the mine was with a maximum inflow.

The automatic drainage system was chosen in this mine. Check valves were installed in pump outlet. There are HCVs in pipeline shown in Figure 3(a) where the stroke was 220 mm with the structure of HCV shown in Figure 4. During normal pump stopping, HCVs were closed first, and then pumps were stopped. The water hammer phenomenon was significant in drains pipeline during this process. Therefore, we should take some measures to prevent the water hammer phenomenon.

4.2. Simulations. An algorithm was developed using commercial simulation software Fluent6.3 based on the water hammer theory described in Section 2. The acceleration, amplitude, pipeline pressure, and valve closure displacement were obtained in the cases of uniform and uniform variable speed through transient simulation for water hammer. The correctness of simulation and the proposed theory were then verified against experimental results. We simulated the valve-closing in single-stage with a constant velocity and in multistage with a variable velocity based on the proposed theory.

(1) *The Simulation of Valve-Closing in Single-Stage with a Constant Velocity.* The velocity $v = 0.01 \text{ m/s}$ of valve-closing in single-stage was determined through repeated simulation.

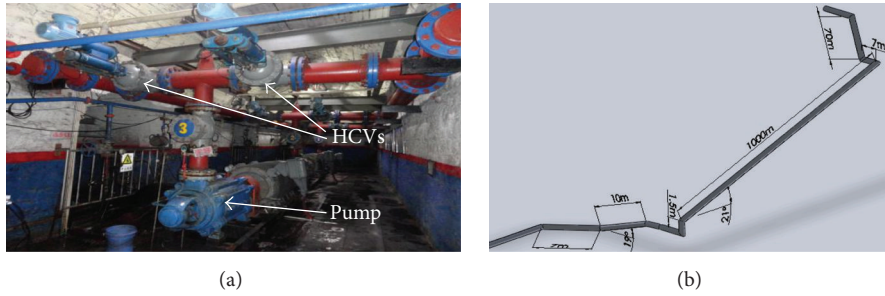
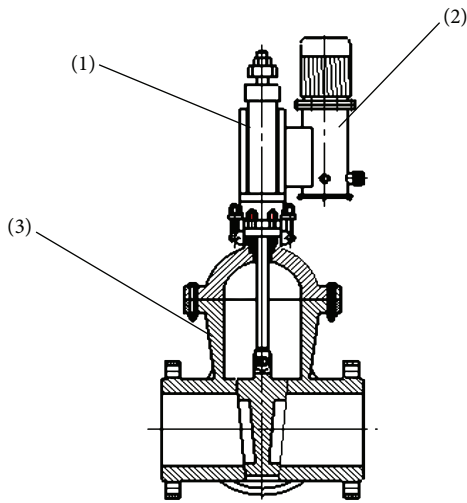


FIGURE 3: Diagram of drain pipes.



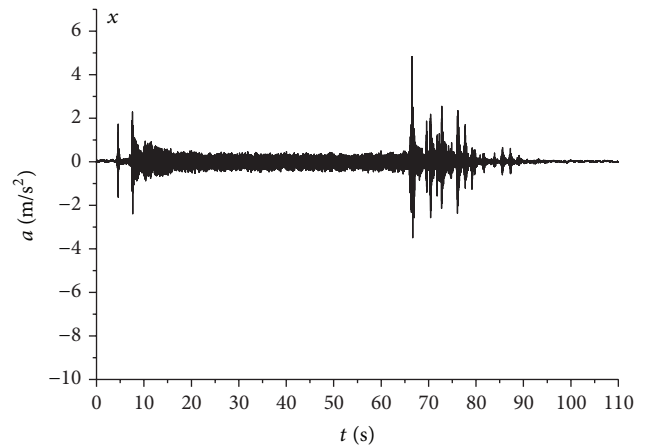
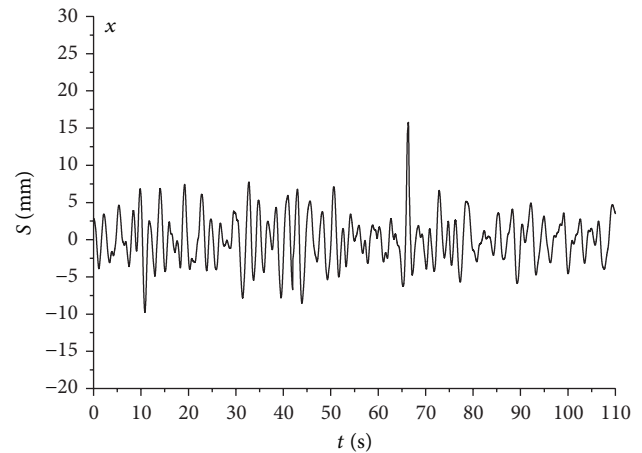
- (1) Hydraulic system
- (2) Explosion-proof motors
- (3) Valve body

FIGURE 4: Structure diagram of HCV.

Then, times of equipment in this situation were obtained using (20) to (21) as shown in Table 1.

The simulation results of valve-closing parameters in single-stage with 0.01 m/s are shown in Figures 5–12.

For Figures 5–12, the static pressure of pipeline was at 3.06 MPa for pump stopping. After the vacuum was completed, the pump was started and HCV was open with a constant velocity. At this moment, pipeline pressure was increased along with the valve-opening displacement of HCV. Then, pressure fluctuations appeared. The valve-opening displacement of HCV was 42.6 mm and the maximum pressure was 3.84 MPa when $t = 12.148$ s. After this moment, the pressure was steady. The valve-opening displacement of HCV was 70.2 mm and the maximum pressure was 3.25 MPa when $t = 15.244$ s. The drainage system pressure reached a steady state along with the increasing of valve-opening displacement. The pressure of pipeline began to drop when $t = 62.436$ s and valve-closing displacement was 53.4 mm. Water hammer phenomenon appeared when $t = 67.211$ s. When $t = 70.6$ s, the maximum boost of water hammer was $\Delta H = 152$ m and the pressure of pipeline at this moment

FIGURE 5: Acceleration in x .FIGURE 6: Amplitude in x .

was 4.77 Mpa. It is 1.47 times the normal discharge pressure (3.25 MPa) and the pressure increased by 50% suddenly. The acceleration and amplitude of pipeline in directions of x , y , and z were changed significantly when water hammer occurred. Maximum acceleration in directions of x , y , and z was 4.83 m/s², 6.46 m/s², and 5.45 m/s² and the maximum amplitude was 15.8 mm, 25.8 mm, and 15.3 mm, respectively. Additionally, the total stroke of HCV was assumed to be S . Valve-closing with rapid and constant velocity were taken

TABLE 1: Times of equipment in single-stage valve-closing.

Equipment actions	Pump start	Valve-opening	Full open	Valve-closing	Valve closed	Water hammer finished	Total times
Times t (s)	4.128	7.883	31.590	46.007	67.934	110.500	21.927

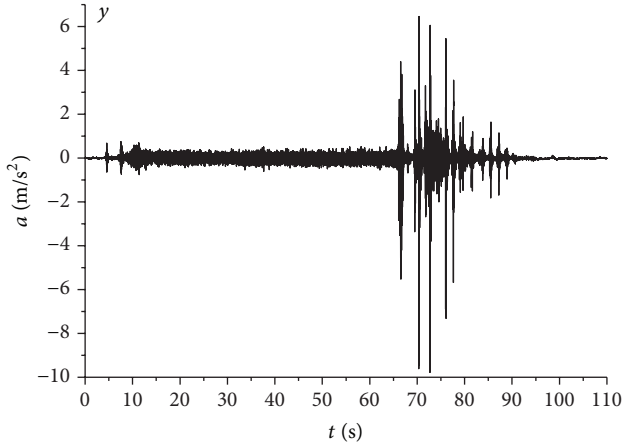


FIGURE 7: Acceleration in y .

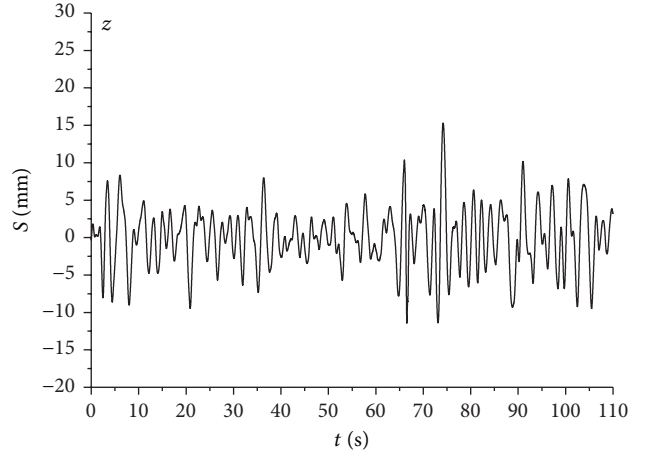


FIGURE 10: Amplitude in z .

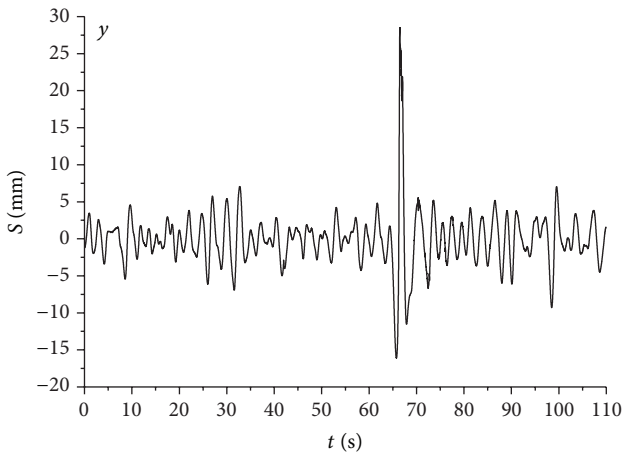


FIGURE 8: Amplitude in y .

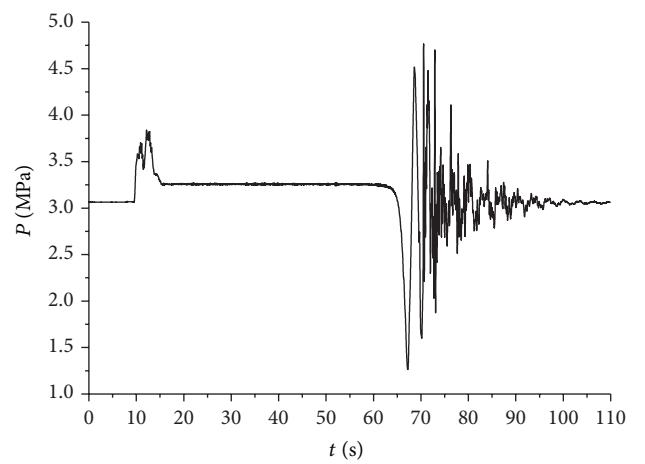


FIGURE 11: Pressure in pipeline.

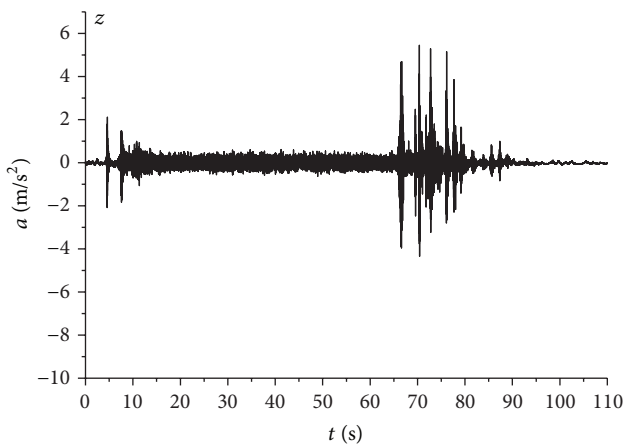


FIGURE 9: Acceleration in z .

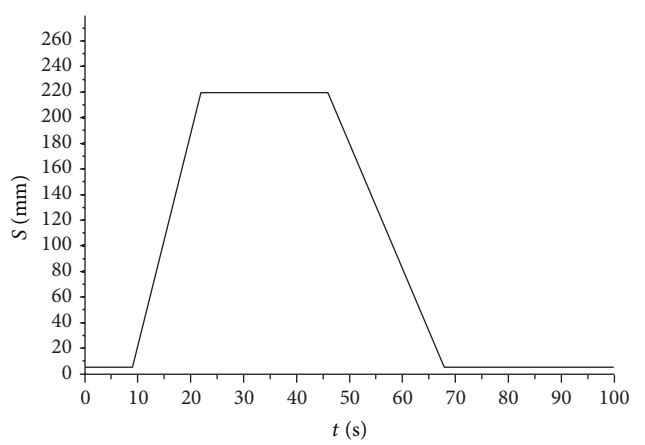
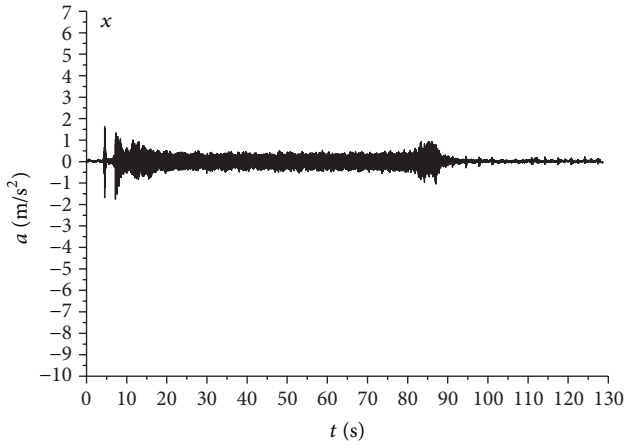
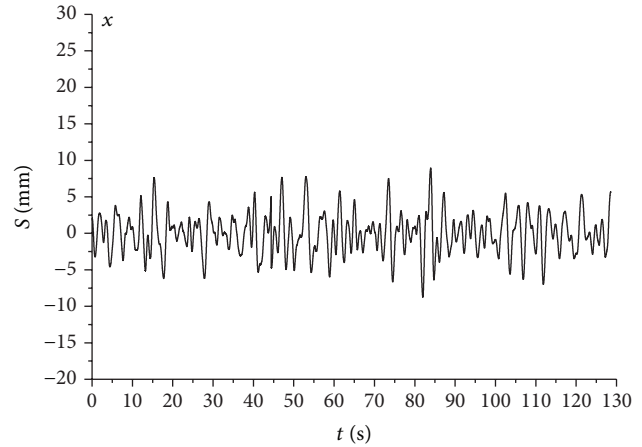


FIGURE 12: Amplitude of HCV.

FIGURE 13: Acceleration in x .FIGURE 14: Amplitude in x .

in the former $2S/3$ and a variable velocity was taken in the latter $S/3$ according to the simulation results of valve-closing water hammer. Due to the velocity of valve-closing that has a large impact on water hammer parameters, it is an effective approach to protect water hammer by choosing a reasonable velocity for valve-closing.

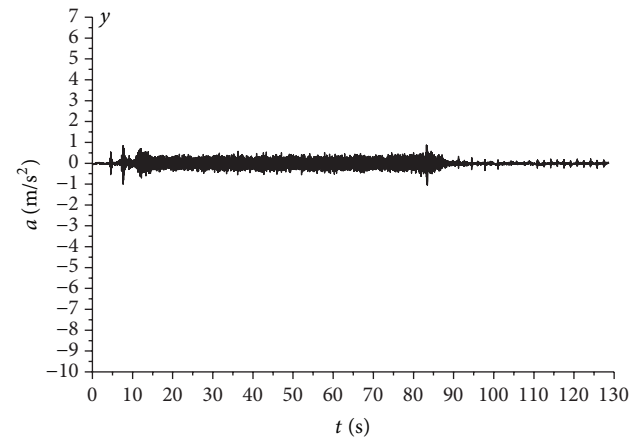
The allowed pressure of pipe is lower and its value was 6.4 MPa. However, the pressure of pipeline reached 4.8 MPa in the case of 22 s valve-closing from the above analysis. This value is near to the allowed pressure of pipe with the pressure being not high, and the water hammer phenomenon was not significant compared with other mine drainage systems. In order to reduce the pressure of pipeline to protection pipeline, it is necessary to develop water hammer protection.

(2) *The Simulation of Valve-Closing in Multistage with a Variable Velocity.* The optimization strategy of valve-closing adjustment for HCV is generated using boundary conditions according to optimization method of valve-closing adjustment that is proposed in this paper. It is a multistage valve-closing with a variable velocity. In the front $2/3$ of valve-closing stroke, the velocity is constant and its value is 0.01 m/s. In the later $1/3$ of valve-closing stroke, the velocity is a variable (the deceleration is constant) and the initial value is 0.01 m/s. The total time of valve-closing is 43.823 s. Times of equipment in multistage valve-closing are shown in Table 2.

The simulation results of valve-closing parameters in multistage are shown in Figures 13–20.

The pipeline pressuring, acceleration, and amplitude in the directions of x , y , and z are significantly reduced in multistage valve-closing with a variable velocity. Valve-closing with a constant velocity is started at 46.007 s, and valve-closing with a variable velocity is started at 60.6 s. The HCVs are closed and pumps are stopped at 89.83 s. In this process, the maximum pressure of water hammer is 3.49 MPa. No effect of water hammer occurred under this situation.

4.3. Experiments. The experimental devices include multifunction data acquisition instrument, vibration sensor, pressure sensors, and cable displacement encoder. Multifunction

FIGURE 15: Acceleration in y .

data acquisition instrument has 16 channels and its acquisition frequency is 102.4 kHz. Data of acceleration, amplitude, flow, pressure, and displacement of valve-closing were acquired by this multifunction data acquisition instrument. Vibration sensor was used to measure piping vibration under the influence of water hammer. It was disposed along with the x , y , and z direction of the pipe. Pressure sensors were used to measure pipeline pressure. Its measurement accuracy and range are 0–10 MPa and ± 0.5 FS. Cable displacement encoder was used to posit the displacement of valve-closing. The arrangement diagram of sensors and flow chart of pumps are shown in Figures 21 and 22.

HCVs control system was designed in this experiment which is shown in Figure 23. Sensors were used to collect signals of pressure and acceleration in pipeline. PLC unit was used to analyze pipeline pressure and vibration for water hammer on the basis of pressure and acceleration signals. An expected running speed was given to HCVs. And then, voltage, current, power, and fault protection information of pumps, pressure, flow, temperature, vacuum, and HCVs status information were monitored at real time. These multi-parameter data were integrated using of fuzzy control theory with calculus and control strategy. The HCVs control system

TABLE 2: Times of equipment in multistage valve-closing.

Equipment actions	Pump start	Valve-opening	Full open	Valve-closing	Valve closed	Water hammer finished	Total times
Times t (s)	4.128	8.5	39.504	46.007	89.830	128.816	43.823

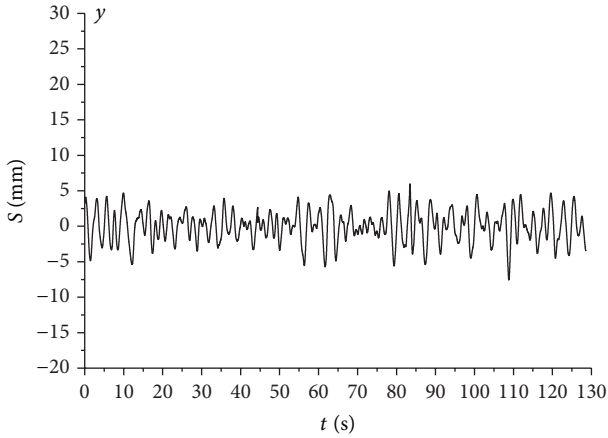


FIGURE 16: Amplitude in y .

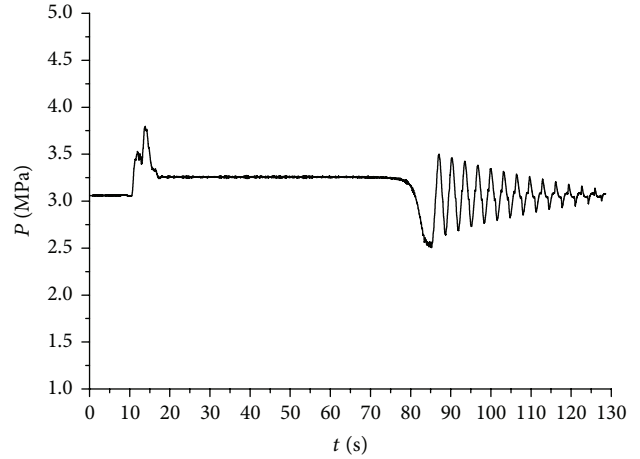


FIGURE 19: Pressure in pipeline.

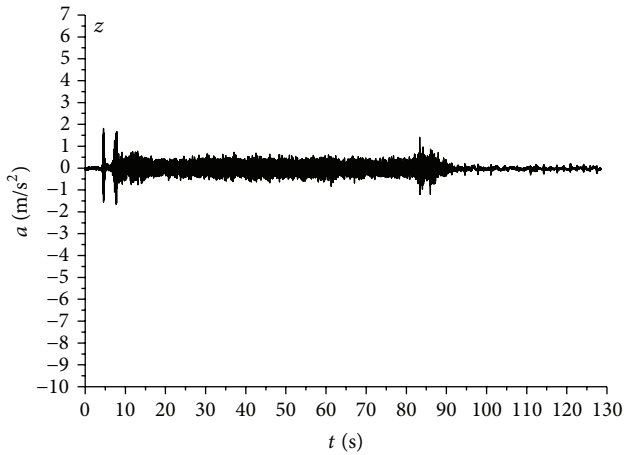


FIGURE 17: Acceleration in z .

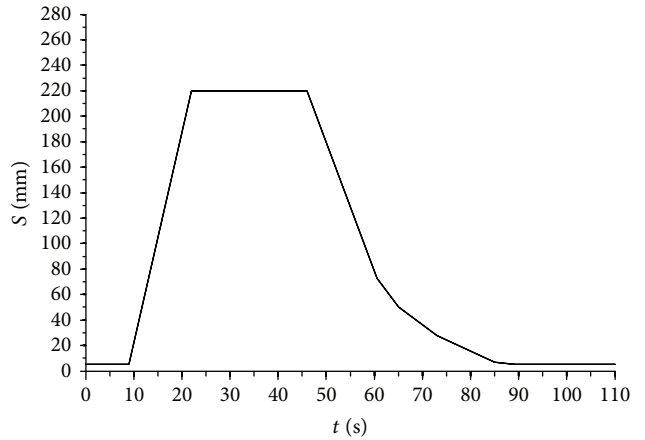


FIGURE 20: Displacement of HCV.

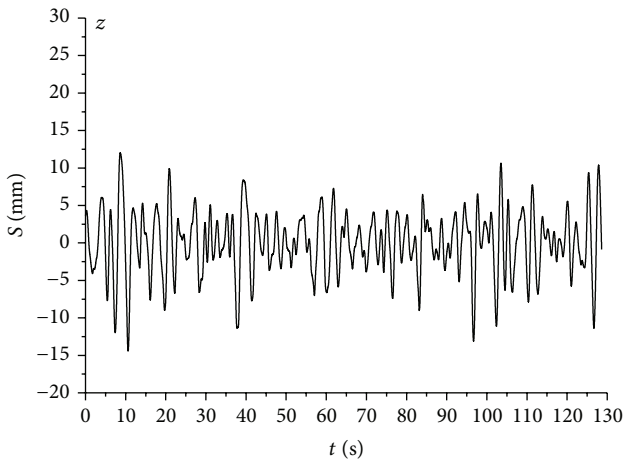


FIGURE 18: Amplitude in z .

can control starting and stopping of pumps automatically and can monitor the signals in system running process timely.

For the total stroke of valve S , the experimental conditions are as follows. In the front $2/3$ of the stroke, the velocity was constant and its value was 0.01 m/s. In the later $1/3$, the velocity is variable (the deceleration is constant) and the initial value was 0.01 m/s. The full valve-closing times were 44 s. Measured values of water hammer parameters in multistage are shown in Table 3.

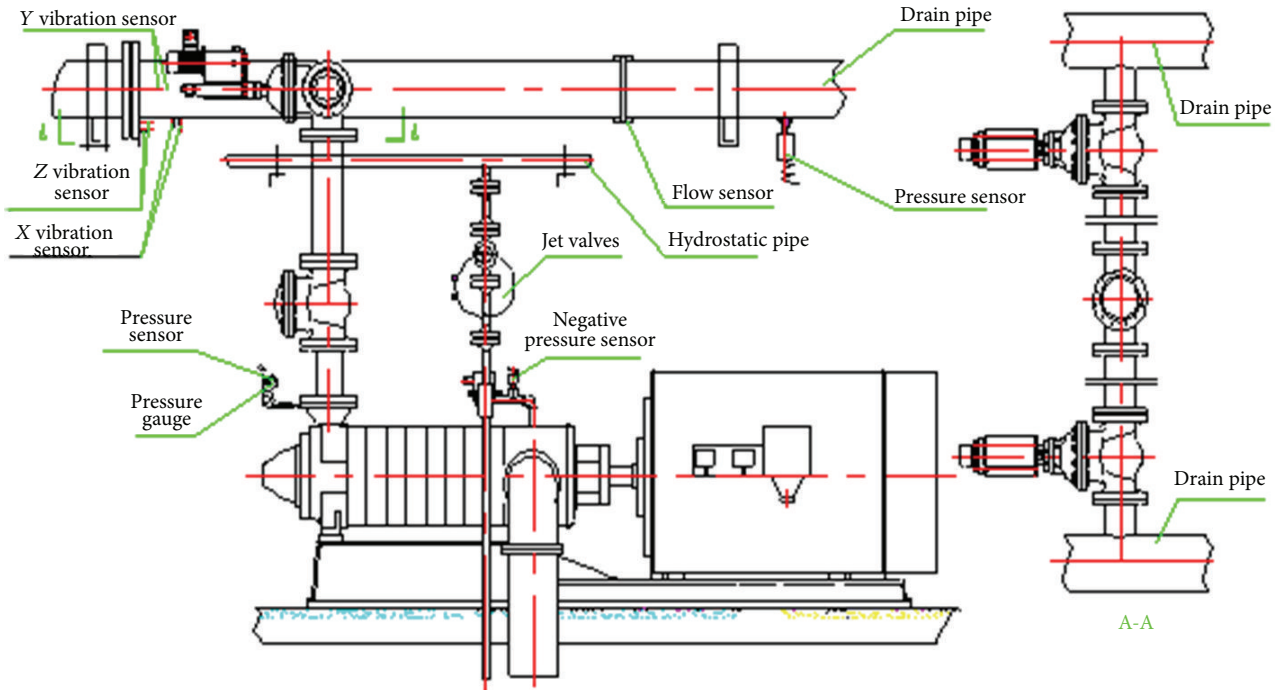


FIGURE 21: Arrangement diagram of sensors.

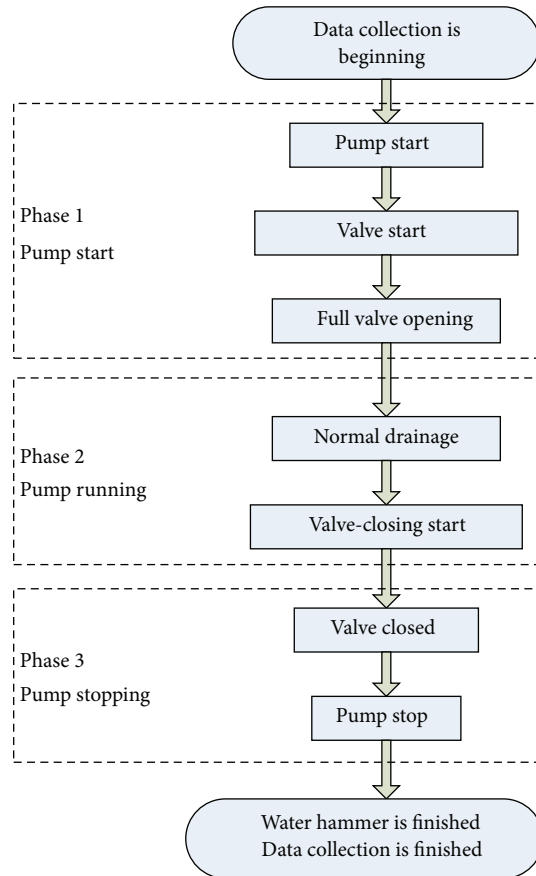


FIGURE 22: The flow chart of test for pumps.

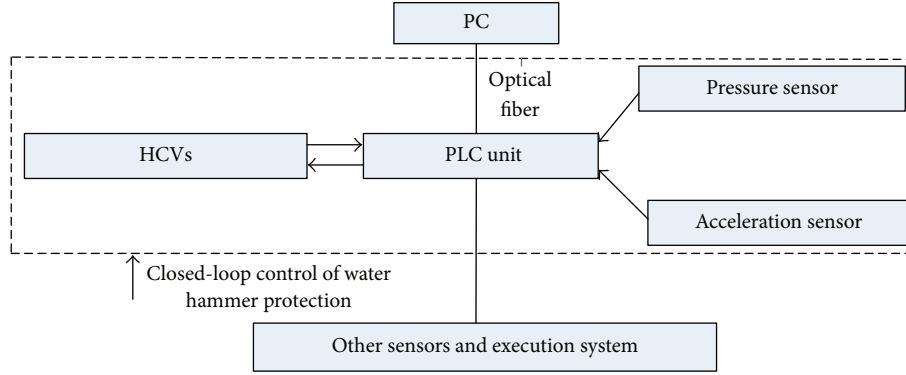


FIGURE 23: Composition of HCVs control system.

TABLE 3: Measured values of water hammer parameters.

Measured parameters	Acceleration (m/s^2)			Displacement (mm)			Pressure P (Mpa)
	$a(x)$	$a(y)$	$a(z)$	$S(x)$	$S(y)$	$S(z)$	
Valve-closing times (s)							
22	4.8308	6.4582	5.4457	15.7662	28.5192	15.3051	4.5865
25	4.8207	6.4581	5.4453	15.7515	28.5139	15.3012	4.5564
28	4.7986	6.3215	5.4394	15.7495	28.4632	15.2036	4.4952
31	4.5689	6.1265	5.2563	13.6938	26.8576	13.0369	4.4678
33	4.5389	6.1063	5.1935	13.5963	24.6985	12.6325	4.4612
36	4.3236	5.9638	5.0632	12.6985	23.8965	11.7652	4.2675
39	1.7231	1.1023	1.6352	9.2514	6.3656	11.3251	3.5615
42	1.7016	1.0363	1.5426	9.0356	6.1563	10.9968	3.5423
44	1.6987	0.8692	1.4112	8.9482	5.9354	10.6432	3.5006
48	1.6886	0.8629	1.4003	8.9235	5.9139	10.6365	3.5006

5. Results and Discussion

The reliability and effectiveness are illustrated through the comparison between the results of simulation and experiment.

(1) *Results of Valve-Closing in Single-Stage with a Constant Velocity and in Multistage with a Variable Velocity Are Compared.* Pipeline pressures and displacements of valve-opening under these two conditions are shown in Figures 24 and 25, respectively. The red curves represent the variations in single-stage with a constant velocity while the black curves represent the variations for multistage with a variable velocity.

Figures 24 and 25 show a significant water hammer effect in single-stage valve-closing with a constant velocity, and the valve-closing time is shorter (22 s). On the other hand, water hammer phenomenon was found to be considerably improved for multistage valve-closing condition with a variable velocity and the valve-closing time was extended (44 s). It shows that valve-closing in multistage with a variable velocity can control the water hammer phenomenon effective in mine drainage system.

(2) *Results of the Simulation and Experiment Are Also Compared.* Results for valve-closing with a variable velocity are shown in Table 4.

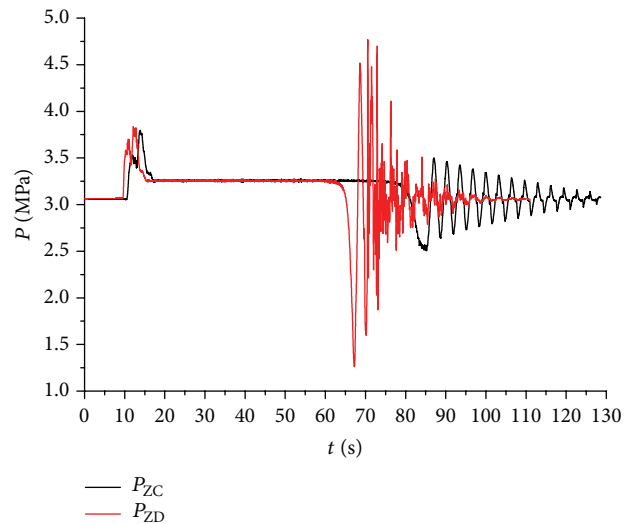


FIGURE 24: Pressure in pipeline.

It can be seen from Table 4 that the simulation for valve-closing with a variable velocity shows good agreement with the experiment. The errors between simulation and experiment are less than 5%. Therefore, the valve-closing in

TABLE 4: Results comparison of simulation and experiment.

Parameters	Max acceleration (m/s^2)			Max displacement (mm)			Max pressure
	$a(x)$	$a(y)$	$a(z)$	$S(x)$	$S(y)$	$S(z)$	P (Mpa)
Simulation	4.5830	6.2672	5.2341	16.5122	27.3335	14.8726	4.5798
Experiment	4.8308	6.4582	5.4457	15.7660	28.5192	15.3051	4.5867
Errors	4.6%	2.9%	3.9%	4.7%	4.2%	2.8%	0.2%
Simulation	1.6876	0.8446	1.3651	8.6395	5.6689	10.4653	3.4901
Experiment	1.6987	0.8692	1.4112	8.9482	5.9354	10.6432	3.5006
Errors	0.7%	2.8%	3.3%	3.4%	4.4%	1.7%	0.3%

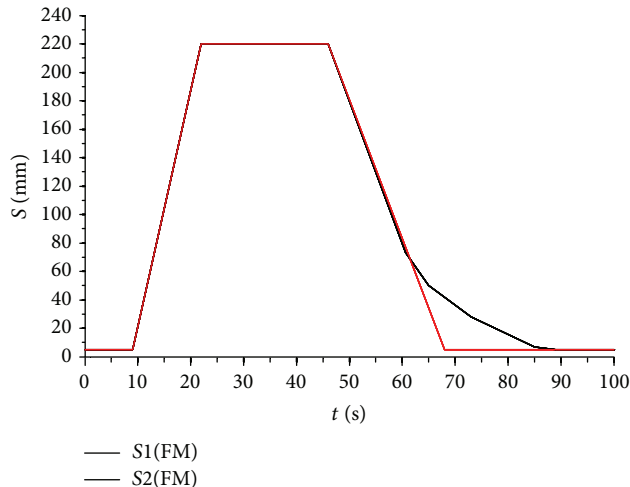


FIGURE 25: Displacement of HCV.

multistage with a variable velocity can reduce the impact from water hammer in mine drainage system.

6. Conclusions and Future Work

Limited space and high cost of equipment changing are the main characteristics for mine drainage system. For the problem of valve-closing water hammer protection in mine drainage system, this paper proposed a protection method based on velocity adjustment of HCVs. The mathematic model of valve-closing water hammer is established based on fundamental equations. The strategy of valve-closing in multistage with a variable velocity is obtained by velocity adjustment strategy of HCVs, and it is effective in protecting the valve-closing water hammer without change piping arrangement or addition equipment. The results of simulations and experiments in different adjustment velocity are compared. We obtained that the water hammer phenomenon is not obvious with valve-closing velocity in the front 2/3 of its stroke, and it is very seriously within the later 1/3. Therefore, we take a two-stage valve-closing strategy. In the first stage, the velocity is constant and its value is 0.01 m/s. In the second stage, the velocity is variable (the deceleration is constant) and the initial value is 0.01 m/s.

Extending errors in the theoretical wave speed have an important influence on prediction of the closure rate

before a water hammer occurs in the actual pipeline. A very challenging mathematical task is variable. This is beyond the scope of this paper and may be considered as a future work.

Conflict of Interests

The authors declare that there is no conflict of interests regarding the publication of this paper.

Acknowledgment

This work was supported by the National 12.5 Technology Support Program of China under Grant no. SQ2012BAJY3504.

References

- [1] M. Sun, X.-R. Ru, and L.-F. Zhai, "In-situ fabrication of supported iron oxides from synthetic acid mine drainage: high catalytic activities and good stabilities towards electro-Fenton reaction," *Applied Catalysis B: Environmental*, vol. 165, pp. 103–110, 2015.
- [2] A. Kaliaatka, M. Vaišnoras, and M. Valinčius, "Modelling of valve induced water hammer phenomena in a district heating system," *Computers & Fluids*, vol. 94, pp. 30–36, 2014.
- [3] N. Jeong, D. Chi, and J. Yoon, "Analytic estimation of the impact pressure in a beam-tube due to water-hammer effect," *Journal of Nuclear Science and Technology*, vol. 50, no. 12, pp. 1139–1149, 2013.
- [4] W. S. Yi, J. Jiang, D. D. Li, G. Lan, and Z. Zhao, "Pump-stopping water hammer simulation based on RELAP5," *IOP Conference Series: Materials Science and Engineering*, vol. 52, no. 7, Article ID 072009, 2013.
- [5] Q. W. Yong, M. Jiang, and Y. Tang, "Study on liquid pipeline water hammer and protective device with gas concentration," *Advanced Materials Research*, vol. 616–618, pp. 774–777, 2013.
- [6] J. Zhang, J. Gao, M. Diao, W. Wu, T. Wang, and S. Qi, "A case study on risk assessment of long distance water supply system," *Procedia Engineering*, vol. 70, pp. 1762–1771, 2014.
- [7] K. I. M. Sang-Gyun, L. E. E. Kye-Bock, and K. I. M. Kyung-Yup, "Water hammer in the pump-rising pipeline system with an air chamber," *Journal of Hydrodynamics, Series B*, vol. 26, no. 6, pp. 960–964, 2015.
- [8] M. A. Bouaziz, M. A. Guidara, C. Schmitt, E. Hadj-Taïeb, and Z. Azari, "Water hammer effects on a gray cast iron water network after adding pumps," *Engineering Failure Analysis*, vol. 44, pp. 1–16, 2014.

- [9] M. S. Ghidaoui, M. Zhao, D. A. McInnis, and D. H. Axworthy, "A review of water hammer theory and practice," *Applied Mechanics Reviews*, vol. 58, no. 1–6, pp. 49–76, 2005.
- [10] A. F. Colombo, P. Lee, and B. W. Karney, "A selective literature review of transient-based leak detection methods," *Journal of Hydro-Environment Research*, vol. 2, no. 4, pp. 212–227, 2009.
- [11] P. J. Lee, M. F. Lambert, A. R. Simpson, J. P. Vítkovský, and D. Misiunas, "Leak location in single pipelines using transient reflections," *Australian Journal of Water Resources*, vol. 11, no. 1, pp. 53–65, 2007.
- [12] N. S. Arbon, M. F. Lambert, A. R. Simpson, and M. L. Stephens, "Field test investigations into distributed fault modeling in water distribution systems using transient testing," in *Proceedings of the World Environmental and Water Resources Congress*, Tampa, Fla, USA, May 2007.
- [13] J. Gong, A. R. Simpson, M. F. Lambert, A. C. Zecchin, Y.-I. Kim, and A. S. Tijsseling, "Detection of distributed deterioration in single pipes using transient reflections," *Journal of Pipeline Systems Engineering and Practice*, vol. 4, no. 1, pp. 32–40, 2013.
- [14] M. Ferrante, B. Brunone, and S. Meniconi, "Leak detection in branched pipe systems coupling wavelet analysis and a Lagrangian model," *Journal of Water Supply: Research and Technology*, vol. 58, no. 2, pp. 95–106, 2009.
- [15] S. Meniconi, B. Brunone, and M. Ferrante, "Water-hammer pressure waves interaction at cross-section changes in series in viscoelastic pipes," *Journal of Fluids and Structures*, vol. 33, pp. 44–58, 2012.
- [16] W. H. Hager, "Swiss contributions to water hammer theory," *Journal of Hydraulic Research*, vol. 39, no. 1, pp. 3–7, 2001.
- [17] M. S. Ghidaoui and B. W. Karney, "Modified transformation and integration of 1D wave equations," *Journal of Hydraulic Engineering*, vol. 121, no. 10, pp. 758–760, 1995.
- [18] A. Adamkowski and M. Lewandowski, "Cavitation characteristics of shutoff valves in numerical modeling of transients in pipelines with column separation," *Journal of Hydraulic Engineering*, vol. 141, no. 2, 2015.
- [19] E. Yao, G. Kember, and D. Hansen, "Analysis of water hammer attenuation in applications with varying valve closure times," *Journal of Engineering Mechanics*, vol. 141, no. 1, Article ID 04014107, 2014.
- [20] R. Korbar, Z. Virag, and M. Šavar, "Truncated method of characteristics for quasi-two-dimensional water hammer model," *Journal of Hydraulic Engineering*, vol. 140, no. 6, Article ID 04014013, 2014.
- [21] M. Rohani and M. H. Afshar, "Simulation of transient flow caused by pump failure: point-implicit method of characteristics," *Annals of Nuclear Energy*, vol. 37, no. 12, pp. 1742–1750, 2010.
- [22] A. Triki, "Multiple-grid finite element solution of the shallow water equations: water hammer phenomenon," *Computers & Fluids*, vol. 90, pp. 65–71, 2014.
- [23] A. Keramat, A. S. Tijsseling, Q. Hou, and A. Ahmadi, "Fluid-structure interaction with pipe-wall viscoelasticity during water hammer," *Journal of Fluids and Structures*, vol. 28, pp. 434–455, 2012.
- [24] S.-G. Kim, K.-B. Lee, and K.-Y. Kim, "Water hammer in the pump-rising pipeline system with an air chamber," *Journal of Hydrodynamics*, vol. 26, no. 6, pp. 960–964, 2014.
- [25] E. B. Wylie and V. L. Streeter, *Fluid Transients*, McGraw-Hill, New York, NY, USA, 1978.
- [26] W. Wan, W. Huang, and C. Li, "Sensitivity analysis for the resistance on the performance of a pressure vessel for water hammer protection," *Journal of Pressure Vessel Technology—Transactions of the ASME*, vol. 136, no. 1, Article ID 011303, 2014.
- [27] G. De Martino, F. De Paola, N. Fontana, and M. Giugni, "Discussion of 'simple guide for design of air vessels for water hammer protection of pumping lines' by D. Stephenson," *Journal of Hydraulic Engineering*, vol. 130, no. 3, pp. 273–275, 2004.
- [28] T. S. Lee, "Air influence on hydraulic transients on fluid system with air valves," *Journal of Fluids Engineering*, vol. 121, no. 3, pp. 646–650, 1999.
- [29] D. Stephenson, "Effects of air valves and pipework on water hammer pressures," *Journal of Transportation Engineering*, vol. 123, no. 2, pp. 101–106, 1997.

Research Article

Nonlinear Seismic Behavior of Different Boundary Conditions of Transmission Line Systems under Earthquake Loading

Li Tian and Xia Gai

School of Civil Engineering, Shandong University, Jinan, Shandong 250061, China

Correspondence should be addressed to Li Tian; tianli@sdu.edu.cn

Received 9 June 2015; Revised 24 September 2015; Accepted 30 September 2015

Academic Editor: Mario Terzo

Copyright © 2016 L. Tian and X. Gai. This is an open access article distributed under the Creative Commons Attribution License, which permits unrestricted use, distribution, and reproduction in any medium, provided the original work is properly cited.

Nonlinear seismic behaviors of different boundary conditions of transmission line system under earthquake loading are investigated in this paper. The transmission lines are modeled by cable element accounting for the nonlinearity of the cable. For the suspension type, three towers and two span lines with spring model (Model 1) and three towers and four span lines' model (Model 2) are established, respectively. For the tension type, three towers and two span lines' model (Model 3) and three towers and four span lines' model (Model 4) are created, respectively. The frequencies of the transmission towers and transmission lines of the suspension type and tension type are calculated, respectively. The responses of the suspension type and tension type are investigated using nonlinear time history analysis method, respectively. The results show that the responses of the transmission tower and transmission line of the two models of the suspension type are slightly different. However, the responses of transmission tower and transmission line of the two models of the tension type are significantly different. Therefore, in order to obtain accurate results, a reasonable model should be considered. The results could provide a reference for the seismic analysis of the transmission tower-line system.

1. Introduction

Transmission line is an important facility and a continuous structure which is made up of transmission towers and transmission lines [1]. Its failure may lead to the outage of power supply [2]. However, there are no code provisions for seismic design of transmission tower-line coupled system [3, 4]. Owing to the interaction of adjacent towers, transmission tower-line system is a complex space towers and lines coupled system, so its accurate calculation is difficult and complex [5]. It is unrealistic to assume that the transmission tower-line system is safe to go through earthquakes without adequate analysis. When the transmission tower-line system is located in strong earthquake zone, the response of the structure under seismic loading may be larger than that of wind load and ice load. There are several recent cases of damage to transmission tower-line system during earthquakes. During the 1994 Northridge earthquakes, 85 cables were damaged when they fell off their towers and two transmission towers collapsed due to high earthquake [6]. In the 1999 CHI-CHI earthquake, transmission towers and lines were damaged

most severely, and a lot of lines were broken and some towers collapsed [7, 8]. During the 2008 Wenchuan earthquake, Sichuan electric network was severely damaged [9]. Some transmission lines were ruptured during the 2013 Lushan earthquake. Therefore, seismic action may govern the design of transmission tower-line system in high-intensity earthquake zones.

Researchers have done some analysis on the response of transmission tower-line system under seismic excitation in the past decades. Li et al. [10, 11] have completed a number of studies on the seismic response of transmission towers and have verified that the effect of lines in seismic design should not be neglected. Suzuki et al. [12] applied the frequency response method as the seismic response analysis to investigate characteristics of towers concerned with overhead wires. Ghobarah et al. [13] investigated the effects of multisupport excitations on the response of overhead power transmission lines. Li et al. [14] presented the mechanical model of soil-pile-structure interaction of transmission tower-cable system in in-plane and derived the corresponding equations of motion. Lei and Chien [15] studied the dynamic behavior

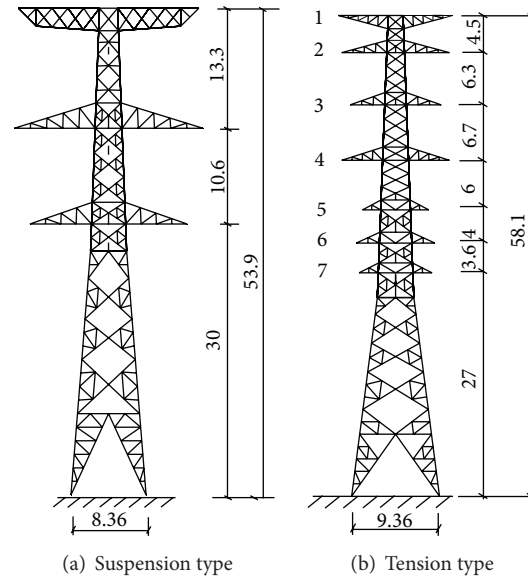


FIGURE 1: Transmission tower model (m).

of a group of transmission towers linked together through electrical wires and subjected to a strong ground motion. Bai et al. [16] investigated the response of a transmission tower-line system at a canyon site to spatially varying ground motions. The results showed that the effect of ground motion spatial variations should be incorporated in seismic analysis of the transmission tower-line system. Wang et al. [17] researched the progressive collapse analysis of a transmission tower-line system under earthquake. The results indicated that the proposed procedure can provide collapse mode and vulnerable points for use in seismic performance and retrofit evaluation of structure. Wu et al. [18] compared the seismic response of a large crossing transmission tower-line system subjected to near-fault pulse-like ground motions and ordinary ground motions. Tian et al. [19] analyzed the effects of boundary conditions, ground motion spatial variations, the incident angle of the seismic wave, coherency loss, and wave travel on the responses of the tension type of the transmission tower-line system, respectively. The comparisons of the longitudinal response of the two models are obtained only, but the comparisons of the transverse and vertical responses of the two models are not researched. Transmission tower-line system is different from general civil engineering structures. The most notable feature is that it contains complex mechanical properties of transmission lines, and the geometric nonlinearities of transmission lines are very significant. So the reasonable model of transmission tower-line system is very important. However, there are little studies about the boundary conditions of the transmission line system under seismic excitation. Not to mention the boundary conditions analysis of the system under multicomponent multisupport seismic excitations.

Nonlinear seismic behavior of different boundary conditions of transmission line systems under nonuniform seismic excitations is studied in this paper. The transmission towers are modeled by beam elements, while the transmission line

is modeled by cable elements that account for the nonlinear geometry of the transmission lines. The frequencies of transmission towers and lines of the suspension type and tension type are calculated according to dynamic characteristic analysis, respectively. The responses of the suspension type and tension type of the transmission tower-line system under multicomponent and multisupport seismic excitations are performed using nonlinear time history analysis method, respectively. The results could provide a reference for seismic analysis of the transmission tower-line system.

2. Structural Model

Figure 1 shows the transmission tower models. Two different types of transmission towers are selected: (a) suspension type and (b) tension type. The height of the suspension type tower and tension type tower is 53.9 m and 58.1 m, respectively. The structural members of the two types of towers are made of angle steel with the elastic modulus of 206 GPa. Based on real projects, three-dimensional finite element tower-line systems are established using SAP2000 software. The connections of members are rigid, and it has been approved that the numerical results of transmission tower using beam element are close to the test results [20], so the beam elements are selected for the simulation of the transmission towers.

To consider the effect of the other part of the transmission line, the boundary condition of the system should be simulated. To compare the responses with different boundary conditions, different models are established. Figure 2 shows the suspension type transmission tower-line system models. Three towers and two span lines with spring model (Model 1) and three towers and four span lines' model (Model 2) are established, respectively. The stiffness constants of the springs are defined by the adjacent transmission lines. The tension type transmission tower-line system models are shown in

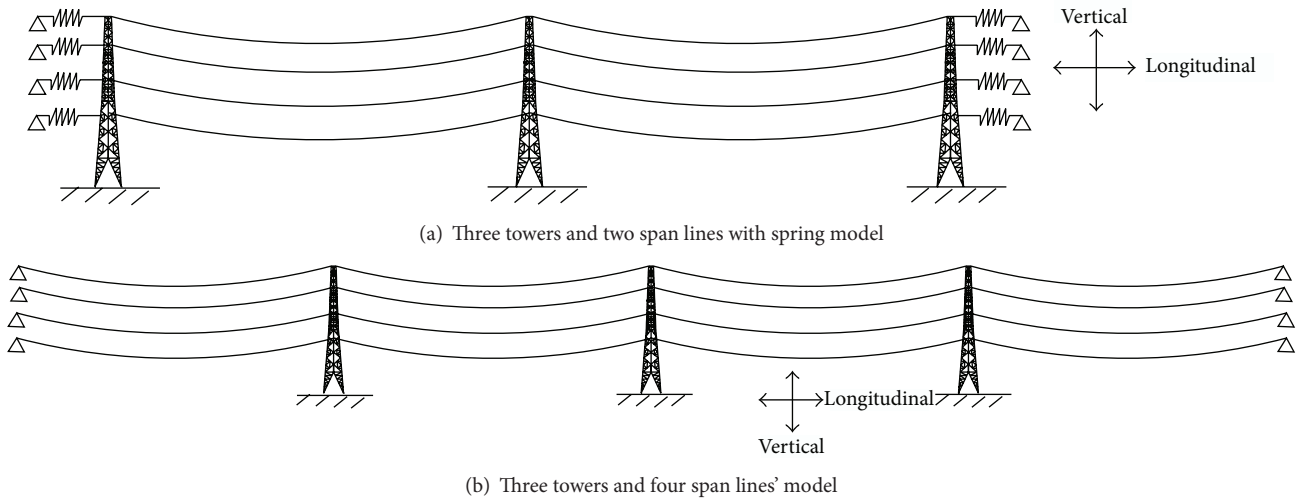


FIGURE 2: Suspension type transmission tower-line system models.

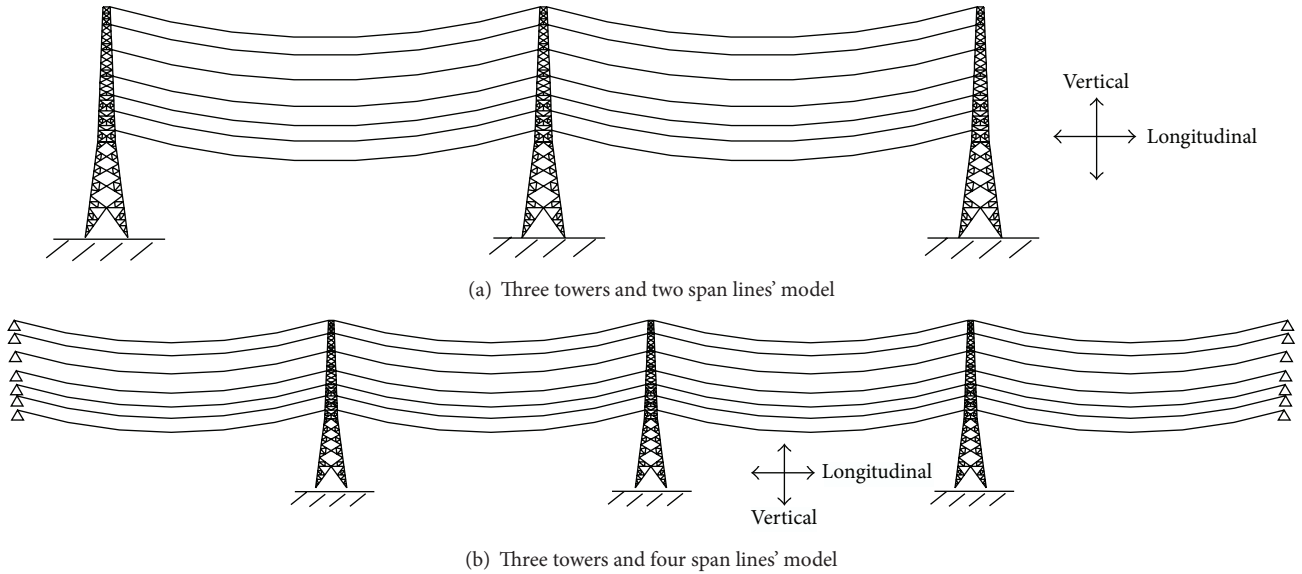


FIGURE 3: Tension type transmission tower-line system models.

Figure 3. Three towers and two span lines' model (Model 3) and three towers and four span lines' model (Model 4) are created, respectively.

For the suspension type transmission tower, the types of ground line and conductor are LGJ-95/55 and LGJ-400/35, respectively. The ground line and conductor properties of the suspension type are shown in Table 1. The upper two cables of every span are ground lines and lower six cables of every span are four bundled conductors. For the tension type transmission tower, the types of ground line and conductor are JLB40-150, LGJ-400/35, and LGJ-240/30, respectively. Ground line and conductor properties of tension type are listed in Table 2. The upper two cables of every span are ground lines and lower twelve cables of every span are two bundled conductors.

TABLE 1: Ground line and conductor properties of the suspension type.

Type	Ground line	Conductor
	LGJ-95/55	LGJ-400/35
Outside diameter (m)	$16.00E-3$	$26.82E-3$
Area (m^2)	$152.81E-6$	$425.2E-6$
Young's modulus (MPa)	105000	65000
Poisson's ratio	0.3	0.3
Density (Kg/m^3)	4559.3	3172.3

The spans to adjacent towers of suspension and tension types are all 400 m. The base points of the transmission tower are fixed to the ground. The connections between

TABLE 2: Ground line and conductor properties of the tension type.

Type	Ground line		Conductor
	JLB40-150	LGJ-400/35	LGJ-240/30
Outside diameter (m)	$15.75E-3$	$26.82E-3$	$21.60E-3$
Area (m ²)	$148.0E-6$	$425.2E-6$	$275.9E-6$
Young's modulus (MPa)	103600	65000	73000
Poisson's ratio	0.3	0.3	0.3
Density (Kg/m ³)	4705.2	3172.3	3341.7

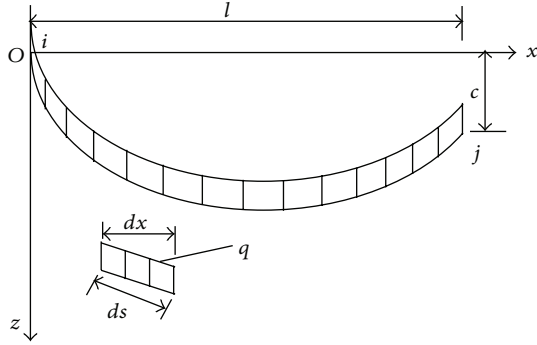


FIGURE 4: Coordinates of a single cable under self-weight.

transmission towers and lines of the suspension type and tension type are hinged by suspension and tension insulators, respectively. The bar element is used to simulate insulator.

The initial axial force and large deformation effect of cable are taken into consideration. Under self-weight, the cable spatial configuration is a catenary. Based on the coordinate system illustrated in Figure 4, the mathematical expression used to define the initial geometry of the cable profile is given in the following form [21]:

$$z = \frac{H}{q} \left| \cosh(\alpha) - \cosh \left| \frac{2\beta x}{l} - \alpha \right| \right|, \quad (1)$$

where $\alpha = \sinh^{-1} |\beta(c/l) / \sin(\beta)| + \beta$, $\beta = ql/2H$, in which H represents initial horizontal tension which can be obtained from a preliminary static analysis and q denotes uniformly distributed gravity loads along the transmission line.

3. The Selection of Seismic Wave and Analytical Method

3.1. The Selection of Seismic Wave. El Centro wave (May 19, 1940) is selected in this paper. The seismic waves include two horizontal components and one vertical component. The NS, WE, and vertical components of the seismic wave coincide with the longitudinal, transverse, and vertical directions of the transmission tower-line system, respectively. The peak ground acceleration is adjusted to 0.4g, and the increases of the peak accelerations of the other two directions of seismic wave are equal proportions. Longitudinally extended structure such as transmission tower-line system is often multisupported, and the effect of wave travel is considered with apparent velocity 1000 m/s.

3.2. Analytical Method. n -degree-of-freedom linear system subjected to m support motions can be written in the matrix form [22, 23]:

$$\begin{bmatrix} \mathbf{M}_{aa} & \mathbf{M}_{ab} \\ \mathbf{M}_{ba} & \mathbf{M}_{bb} \end{bmatrix} \begin{Bmatrix} \dot{\mathbf{x}}_a \\ \dot{\mathbf{x}}_b \end{Bmatrix} + \begin{bmatrix} \mathbf{C}_{aa} & \mathbf{C}_{ab} \\ \mathbf{C}_{ba} & \mathbf{C}_{bb} \end{bmatrix} \begin{Bmatrix} \dot{\mathbf{x}}_a \\ \dot{\mathbf{x}}_b \end{Bmatrix} + \begin{bmatrix} \mathbf{K}_{aa} & \mathbf{K}_{ab} \\ \mathbf{K}_{ba} & \mathbf{K}_{bb} \end{bmatrix} \begin{Bmatrix} \mathbf{x}_a \\ \mathbf{x}_b \end{Bmatrix} = \begin{Bmatrix} 0 \\ \mathbf{P}_b(t) \end{Bmatrix}, \quad (2)$$

where $\mathbf{x}_a = [\mathbf{x}_{a1}, \dots, \mathbf{x}_{an}]^T$ is the n -vector of displacements at the unconstrained degrees of freedom. $\mathbf{x}_b = [\mathbf{x}_{b1}, \dots, \mathbf{x}_{bm}]^T$ is the m -vector of prescribed support displacements. \mathbf{M}_{aa} , \mathbf{C}_{aa} , and \mathbf{K}_{aa} are the $n \times n$ mass, damping, and stiffness matrices associated with the unconstrained degrees of freedom, respectively. \mathbf{M}_{bb} , \mathbf{C}_{bb} , and \mathbf{K}_{bb} are the $m \times m$ matrices associated with the supported degrees of freedom. \mathbf{M}_{ab} , \mathbf{C}_{ab} , and \mathbf{K}_{ab} are the $n \times m$ coupling matrices associated with both sets of degrees of freedom, and $\mathbf{P}_b(t)$ is the m -vector of the reacting forces at the support degrees of freedom.

The equation defining the response degrees of freedom "a" is given by

$$\mathbf{M}_{aa}\ddot{\mathbf{x}}_a + \mathbf{C}_{aa}\dot{\mathbf{x}}_a + \mathbf{K}_{aa}\mathbf{x}_a = -\mathbf{M}_{ab}\ddot{\mathbf{x}}_b - \mathbf{C}_{ab}\dot{\mathbf{x}}_b - \mathbf{K}_{ab}\mathbf{x}_b. \quad (3)$$

The solution of (3) depends on how the earthquake motion is defined in the right-hand side of the equation. Equation (3) is the equation of motion for the absolute displacement. Assuming that the mass matrix is diagonal and \mathbf{C}_{ab} is neglected, (3) can be expressed as

$$\mathbf{M}_{aa}\ddot{\mathbf{x}}_a + \mathbf{C}_{aa}\dot{\mathbf{x}}_a + \mathbf{K}_{aa}\mathbf{x}_a = \mathbf{K}_{ab}\mathbf{x}_b. \quad (4)$$

Equation (4) can be extended to three components:

$$\mathbf{M}_{aa}\ddot{\mathbf{u}}_a + \mathbf{C}_{aa}\dot{\mathbf{u}}_a + \mathbf{K}_{aa}\mathbf{u}_a = \mathbf{K}_{ab}(\mathbf{x}_b + \mathbf{y}_b + \mathbf{z}_b), \quad (5)$$

where \mathbf{x}_b , \mathbf{y}_b , and \mathbf{z}_b are the input ground motion displacements in two horizontal directions and one vertical direction, respectively.

4. The Comparison of Frequencies of Different Systems

Based on finite element model of transmission tower-line system shown in Figures 2 and 3, the frequencies of the suspension type and tension type system are calculated using dynamic characteristic analysis, respectively. The primary modal frequencies of the transmission tower and line can be obtained, respectively [24].

4.1. The Comparison of Frequencies of the Suspension Type Model. The comparison of the fundamental frequencies of the suspension type model is shown in Table 3. In the longitudinal direction, the fundamental frequencies of the transmission line and tower of Model 2 are smaller than those of Model 1, but the differences could be ignored. In the transverse direction, the differences between the fundamental frequencies of the transmission line and tower of Model 1 and Model 2 are very small, and the maximum difference is only 1.15%, so the differences cannot be considered.

TABLE 3: Comparison of the fundamental frequencies of the suspension type model.

Frequency	Transmission line		
	Model 1 (Hz)	Model 2 (Hz)	Difference/%
Longitudinal	0.1510	0.1464	3.05
Transverse	0.1394	0.1387	1.15
Frequency	Transmission tower		
	Model 1 (Hz)	Model 2 (Hz)	Difference/%
Longitudinal	1.7830	1.7705	0.70
Transverse	1.7556	1.7332	1.05

TABLE 4: Comparison of the fundamental frequencies of the tension type model.

Frequency	Transmission line		
	Model 3 (Hz)	Model 4 (Hz)	Difference/%
Longitudinal	0.2835	0.2624	7.44
Transverse	0.1492	0.1594	-6.84
Frequency	Transmission tower		
	Model 3 (Hz)	Model 4 (Hz)	Difference/%
Longitudinal	1.4438	1.7098	-18.42
Transverse	1.6707	1.6748	-0.25

4.2. The Comparison of Frequencies of the Tension Type Model.

The comparison of the fundamental frequencies of the tension type model is shown in Table 4. In the longitudinal direction, the fundamental frequency of the transmission tower of Model 4 is larger than that of Model 3, and the increase of the frequency is 18.4%. However, the fundamental frequency of the transmission line of Model 4 is smaller than that of Model 3, and the decrease of the frequency is 7.4%. In the transverse direction, the differences between the fundamental frequencies of the transmission tower of Model 4 and Model 3 are small. The fundamental frequency of the transmission line of Model 4 is larger than that of Model 3, and the increase of the frequency is 6.8%.

The variations of the fundamental frequencies of the transmission tower and transmission line of the suspension type and tension type can be obtained based on the above analysis. For the suspension type, the differences between the fundamental frequencies of the transmission tower and line of the two models are very small, and the differences could be ignored. For the tension type, the differences between the fundamental frequencies of the transmission tower of the two models are obvious in the longitudinal direction, but the differences are small in the transverse direction. Therefore, in order to obtain accurate frequencies of the system, Model 1 or Model 2 could be adopted for the suspension type, but Model 4 should be used for the tension type.

5. Numerical Analysis and Discussion

The analyses of the suspension type and tension type shown in Figures 2 and 3 under multicomponent and multisupport seismic excitations are calculated using nonlinear time history analysis method, respectively. The damping ratio of

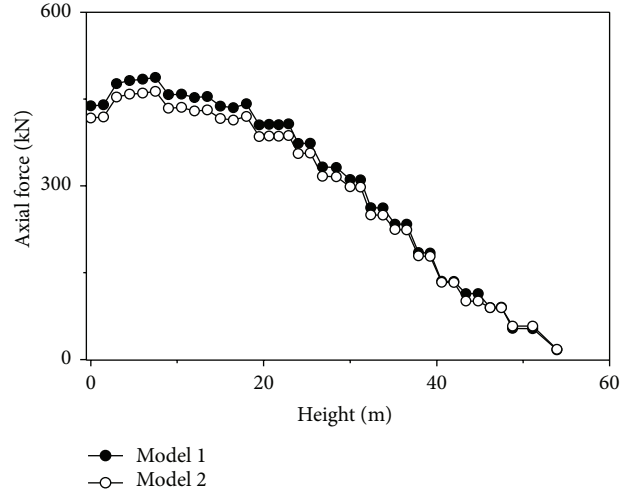


FIGURE 5: Comparison of the maximum axial forces of the transmission towers of the two models of the suspension type.

tower and line is assumed to be 2% and 1%, respectively. The step-by-step integration of the Hilber-Hughes-Taylor method is used in the dynamic analysis. The longitudinal, transverse, and vertical responses of the two models of the suspension type and tension type are compared, respectively. A reasonable model could be obtained according to the comparison of the responses of the transmission tower and line under nonuniform seismic excitations.

5.1. The Comparison of the Responses of the Suspension Type.

The comparison of the maximum axial forces of the transmission towers of the two models of the suspension type under nonuniform seismic excitations is shown in Figure 5. It can be seen from Figure 5 that the axial forces of the transmission tower of Model 1 are larger than those of Model 2, but the maximum increment is only 5%.

The comparisons of the displacement time histories on the top of the transmission towers of the two models of the suspension type under nonuniform seismic excitations are shown in Figure 6. It can be seen from Figure 6 that the longitudinal and transverse displacements of the transmission tower of Model 1 are larger than those of Model 2, but the differences between the displacement responses of two models are very little, and the shapes of time history curves of the two models are approximately consistent.

From the above analysis, the differences between the responses of the transmission towers of Model 1 and Model 2 of the suspension type under nonuniform seismic excitations are small, and the maximum difference is only 5%. Therefore, Model 1 or Model 2 could give satisfactory results.

The comparisons of the maximum displacements of the transmission lines of the two models of the suspension type are shown in Figure 7. It can be seen from Figure 7 that the differences of the transverse displacements of the transmission lines of the two models are small, and the displacement change slightly with the span varying. The vertical displacements of the transmission line of Model 1

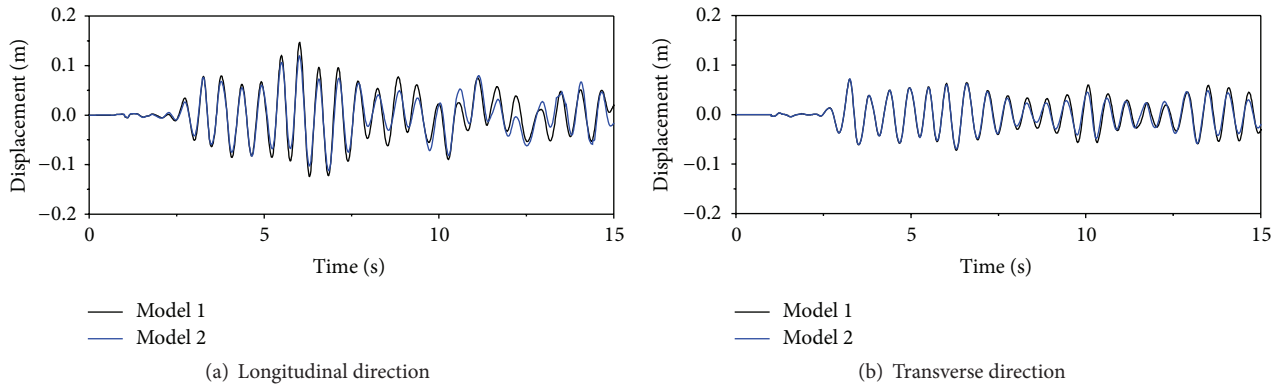


FIGURE 6: Comparison of the displacement time histories on the top of the transmission towers of the two models of the suspension type.

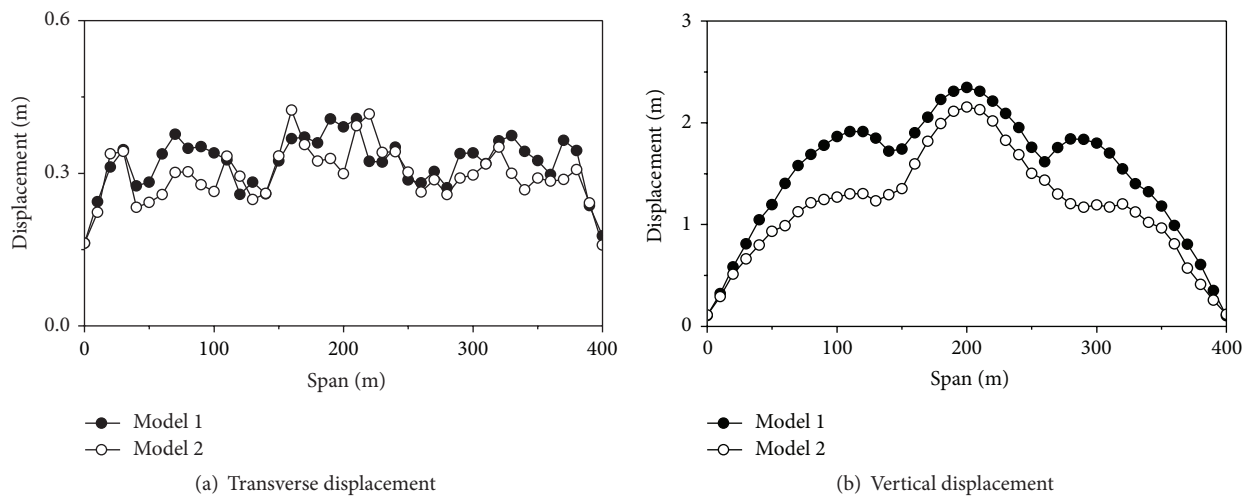


FIGURE 7: Comparison of the maximum displacements of the transmission lines of the two models of the suspension type.

are larger than those of Model 2, but the curves of vertical displacements of two models are similar. Because of the suspension type insulator, apparent velocity of seismic wave, and frequencies of the transmission lines, the vertical displacements of the transmission line are symmetrical, and the main reason is the frequency of the transmission lines. The vertical displacement of middle span of the transmission line is the largest in the span due to antisymmetric modes of the transmission lines.

According to the above analysis of Model 1 and Model 2 of the suspension type, Model 1 could meet the requirement because of the effect of two lateral springs. Therefore, Model 1 or Model 2 could be used for calculation model when the system is subjected to nonuniform seismic excitations.

5.2. The Comparison of the Responses of the Tension Type. The comparison of the maximum axial forces of the transmission towers of the two models of the tension type is shown in Figure 8. It can be seen from Figure 8 that the axial forces of the transmission tower of Model 3 are significantly smaller than those of Model 4, and the maximum decrease is 30%,

and the differences of the axial forces between the two models vary obviously at different height of the transmission tower.

Figure 9 shows the comparisons of the displacement time histories on the top of the transmission towers of the two models. It can be seen from Figure 9 that the differences between the longitudinal displacement time histories on the top of the tower of Model 3 and Model 4 are obvious, and the longitudinal displacements on the top of the tower of Model 4 are significantly larger than those of Model 3. Owing to the effect of outside transmission tower, the responses of two models have a phase difference. However, the differences between the transverse displacement time histories on the top of the tower of Model 3 and 4 are small.

According to the results of the transmission tower analysis, the differences between the responses of the transmission towers of Model 3 and Model 4 are significant, especially for the axial forces and longitudinal displacements on the top of the transmission tower. Therefore, in order to obtain accurate responses, Model 4 should be used for seismic analysis of system. Neglecting the effect of the boundary condition, the axial force and the longitudinal maximum displacement of

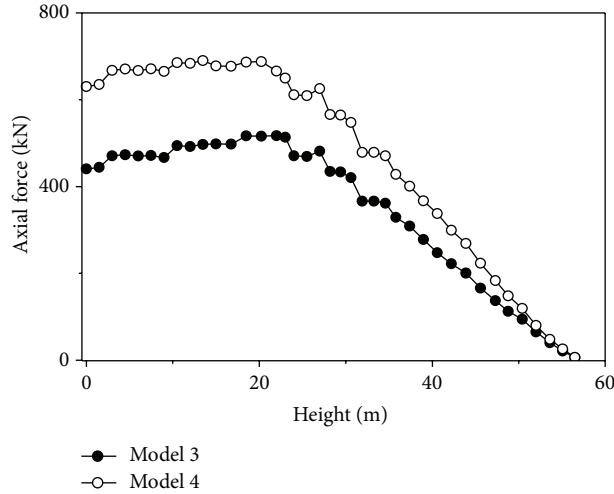


FIGURE 8: Comparison of the maximum axial forces of the transmission towers of the two models of the tension type.

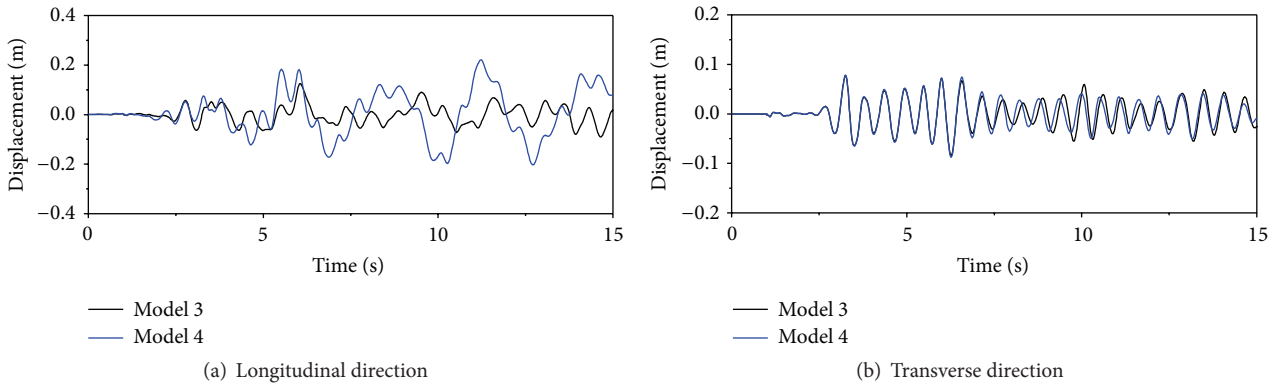


FIGURE 9: Comparison of the displacement time histories on the top of the transmission towers of the two models of the tension type.

the transmission tower could be underestimated by more than 30% and 45%, respectively.

The comparison of the maximum tension forces of the transmission lines of the two models is given in Table 5. It can be seen from Table 5 that the differences between the tension forces of the transmission lines of Model 3 and Model 4 are small, and the maximum difference is only 8%. The tension forces of the transmission line of Model 4 may be larger or smaller than those of Model 3. The effect of the boundary condition could be ignored for the seismic analysis of tension forces of the transmission line.

Figure 10 shows the comparison of the maximum displacements of the transmission lines of the two models of the tension type. It can be seen from Figure 10 that the differences of the transverse displacements of the transmission lines of the two models are small, but the differences of the vertical displacements of the transmission lines of the two models are significant. The maximum vertical displacement of the transmission line of Model 3 is almost two times larger than that of Model 4.

According to the results of the transmission line analysis, the differences between the responses of the transmission lines of Model 3 and Model 4 are obvious, especially for the

TABLE 5: Comparison of the maximum tension forces of the transmission lines of the two models of the tension type.

Layer	Model 3 (kN)	Model 4 (kN)	Difference (%)
1	29.73	29.46	0.92
2	81.10	88.38	-8.24
3	64.74	67.03	-3.42
4	64.15	63.08	1.70
5	45.72	43.89	4.17
6	48.36	45.30	6.75
7	50.40	47.46	6.19

vertical displacements of the transmission line. Both sides of the transmission tower would tilt easily due to missing the outside transmission line, and the large vertical displacement of transmission line would happen.

The above results demonstrate that the axial forces and longitudinal displacements on the top of the transmission tower of the tension type would be underestimated using Model 3, but the vertical displacements of the transmission line would be seriously overestimated. The seismic responses

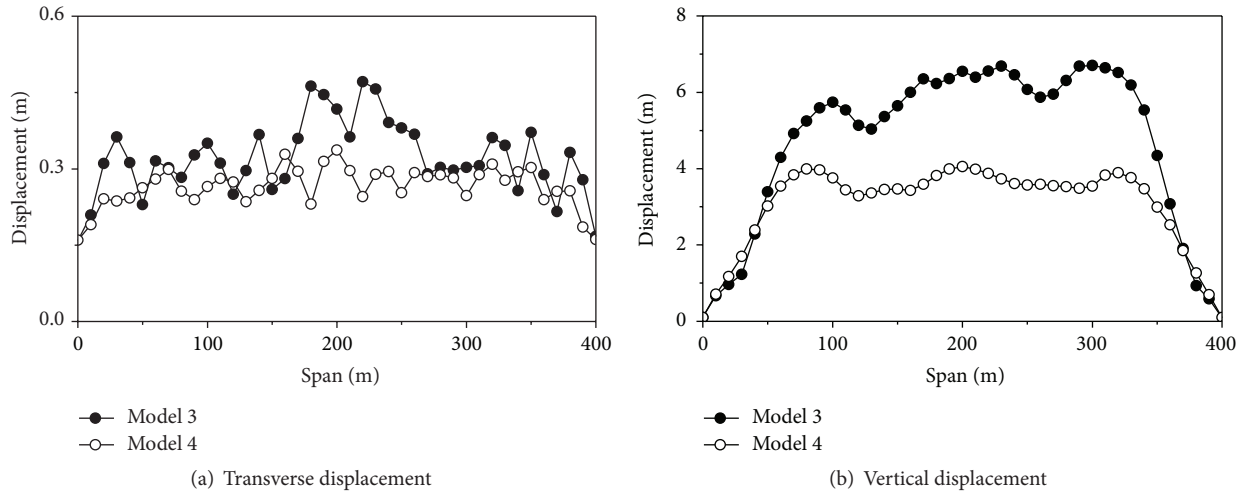


FIGURE 10: Comparison of the maximum displacements of the transmission lines of two models of the tension type.

of the transmission tower and the transmission line are not reasonable using Model 3. Therefore, Model 4 should be used for the seismic analysis of the system of the tension type under nonuniform seismic excitations.

6. Conclusion

Nonlinear seismic behaviors of different boundary conditions of transmission line systems under nonuniform seismic excitations are studied in this paper. The responses of the suspension type and tension type of the transmission tower-line system are investigated using nonlinear time history analysis method, respectively. Based on the numerical results, the following conclusions are drawn:

- (1) The frequencies of the two models of the suspension type are slightly different in the longitudinal and transverse directions, but the frequencies of the two models of the tension type are obviously different in the longitudinal direction due to the effect of boundary condition. To obtain an accurate frequency, Model 3 should not be adopted.
- (2) The differences between the responses of the transmission tower and transmission line of the two models of the suspension type are very little, so Model 1 can get accurate results and could be used for seismic analysis when the system is under nonuniform seismic excitations.
- (3) The responses of the transmission tower and transmission line of the two models of the tension type are significantly different. Neglecting the effect of the boundary condition, the responses of the transmission tower would be underestimated, but the responses of the transmission line would be overestimated. To obtain accurate results, Model 4 should be used for seismic analysis when the system is under nonuniform seismic excitations.

- (4) To obtain accurate responses of the system, Model 1 or Model 2 could be used for the seismic analysis of the suspension type transmission tower-line system, but Model 4 should be adopted for the seismic analysis of the tension type transmission tower-line system.

Conflict of Interests

The authors declare that there is no conflict of interests regarding the publication of this paper.

Acknowledgments

This research is supported by the National Natural Science Foundation of China under Grant nos. 51208285 and 51578325. The supports for this research are greatly appreciated.

References

- [1] H. Li and H. Bai, "High-voltage transmission tower-line system subjected to disaster loads," *Progress in Natural Science: Materials International*, vol. 16, no. 9, pp. 899–911, 2006.
- [2] M. Shinozuka, "The Hanshin-Awaji earthquake of January 17, 1995 performance of life lines," Tech. Rep. NCEER-95-0015, NCEER, 1995.
- [3] C. J. Wong and M. D. Miller, *Guidelines for Electrical Transmission Line Structural Loading*, American Society of Civil Engineers, New York, NY, USA, 2009.
- [4] American Society of Civil Engineers, *Design of Latticed Steel Transmission Structures*, American Society of Civil Engineers, Reston, Va, USA, 1997.
- [5] H. Li and Q. Wang, "Dynamic characteristics of long-span transmission lines and their supporting towers," *China Civil Engineering Journal*, vol. 30, no. 5, pp. 28–36, 1997.
- [6] J. F. Hall, W. T. Holmes, and P. Somers, *Northridge Earthquake of January 17, 1994*, Earthquake Engineering Research Institute, Oakland, Calif, USA, 1994.

- [7] NCREC, *Damage Report on 921 Chi-Chi Earthquake-Lifeline System*, NCREC, 1999.
- [8] P. Zhang, G. Song, H.-N. Li, and Y.-X. Lin, "Seismic control of power transmission tower using pounding TMD," *Journal of Engineering Mechanics*, vol. 139, no. 10, pp. 1395–1406, 2013.
- [9] J. Eidinger, "Wenchuan earthquake impact to power systems," in *Proceedings of the Lifeline Earthquake Engineering in a Multihazard Environment (TCLEE '09)*, pp. 1–12, Oakland, Calif, USA, June-July 2009.
- [10] H. Li, W. Shi, and L. Jia, "Limitations of effects of lines on in-plane vibration of transmission towers and simplified seismic calculation method," *Journal of Vibration and Shock*, vol. 23, no. 2, pp. 1–7, 2004.
- [11] H.-N. Li, W.-L. Shi, G.-X. Wang, and L.-G. Jia, "Simplified models and experimental verification for coupled transmission tower-line system to seismic excitations," *Journal of Sound and Vibration*, vol. 286, no. 3, pp. 569–585, 2005.
- [12] T. Suzuki, K. Tamamatsu, and T. Fukasawa, "Seismic response characteristics of transmission towers," in *Proceedings of the 10th World Conference on Earthquake Engineering*, pp. 4961–4967, Madrid, Spain, July 1992.
- [13] A. Ghobarah, T. S. Aziz, and M. El-Attar, "Response of transmission lines to multiple support excitation," *Engineering Structures*, vol. 18, no. 12, pp. 936–946, 1996.
- [14] H. Li, S. Xiao, and S. Wang, "Model of transmission tower-pile-soil dynamic interaction under earthquake: in-plane," in *Proceedings of the ASME Pressure Vessels and Piping Conference*, pp. 143–147, Vancouver, Canada, August 2002.
- [15] Y.-H. Lei and Y.-L. Chien, "Seismic analysis of transmission towers considering both geometric and material nonlinearities," *Tamkang Journal of Science and Engineering*, vol. 8, no. 1, pp. 29–42, 2005.
- [16] F.-L. Bai, H. Hao, K.-M. Bi, and H.-N. Li, "Seismic response analysis of transmission tower-line system on a heterogeneous site to multi-component spatial ground motions," *Advances in Structural Engineering*, vol. 14, no. 3, pp. 457–474, 2011.
- [17] W. M. Wang, H. N. Li, and L. Tian, "Progressive collapse analysis of transmission tower-line system under earthquake," *Advanced Steel Construction*, vol. 9, no. 2, pp. 161–174, 2013.
- [18] G. Wu, C.-H. Zhai, S. Li, and L.-L. Xie, "Seismic response of large crossing transmission tower-line system subjected to near-fault ground motions," *Engineering Mechanics*, vol. 30, no. 6, pp. 77–82, 2013.
- [19] L. Tian, H. Li, and G. Liu, "Seismic response of power transmission tower-line system subjected to spatially varying ground motions," *Mathematical Problems in Engineering*, vol. 2010, Article ID 587317, 20 pages, 2010.
- [20] H. Deng, X. Chen, H. Tu, X. Ma, and Z. Wang, "Experimental study on model of Jiangyin long span transmission tower," *Journal of Building Structures*, vol. 22, no. 6, pp. 31–35, 2001.
- [21] S. Shen, C. Xu, and C. Zhao, *Design of Suspension Structure*, China Architecture and Building Press, Beijing, China, 1997.
- [22] R. W. Clough and J. Penzien, *Dynamics of Structures*, McGraw-Hill, New York, NY, USA, 1975.
- [23] E. L. Wilson, *Three Dimensional Static and Dynamic Analysis of Structures: A Physical Approach with Emphasis on Earthquake Engineering*, Computer and Structures, Berkeley, Calif, USA, 2002.
- [24] H. Yasui, H. Marukawa, Y. Momomura, and T. Ohkuma, "Analytical study on wind-induced vibration of power transmission towers," *Journal of Wind Engineering and Industrial Aerodynamics*, vol. 83, no. 2, pp. 431–441, 1999.

Review Article

Recent Advances in Bidirectional Modeling and Structural Control

Satyam Paul, Wen Yu, and Xiaoou Li

Departamento de Control Automatico, CINVESTAV-IPN, 07360 Mexico City, DF, Mexico

Correspondence should be addressed to Wen Yu; yuw@ctrl.cinvestav.mx

Received 1 July 2015; Revised 22 September 2015; Accepted 29 September 2015

Academic Editor: Chia-Ming Chang

Copyright © 2016 Satyam Paul et al. This is an open access article distributed under the Creative Commons Attribution License, which permits unrestricted use, distribution, and reproduction in any medium, provided the original work is properly cited.

This paper provides an overview of building structure modeling and control under bidirectional seismic waves. It focuses on different types of bidirectional control devices, control strategies, and bidirectional sensors used in structural control systems. This paper also highlights the various issues like system identification techniques, the time-delay in the system, estimation of velocity and position from acceleration signals, and optimal placement of the sensors and control devices. The importance of control devices and its applications to minimize bidirectional vibrations has been illustrated. Finally, the applications of structural control systems in real buildings and their performance have been reviewed.

1. Introduction

Historic studies expose the fact that several earthquakes have caused severe damage in civil structures all over the world including 1985 Mexico City, 1994 Northridge, 1995 Kobe, 1999 Kocaeli, 2001 Bhuj, 2008 Sichuan, 2008 Chile, and 2012 Emilia. The process of modification or controlling the building structures from severe damage has become a salient topic in structural engineering. The control of building structures from the hazardous earthquake waves is an area of great interest for the researchers that is growing rapidly [1, 2]. The challenging part of the job lies on the protection of super structures in the whole of geographic locations from the seismic events, thus providing a means of safer environment for the human occupants. The extensive damage due to an earthquake can be noteworthy and so there is utter necessity to develop an effective method for protection.

The structural control methodology and its applications during earthquakes were first suggested by the researches more than a century ago. But major developments have been noticed during the last 25 years where the structures with preventive systems have been developed. Yao in 1972 [3] had proposed the idea of structural control that played a major role in the advancement of the field of structural engineering.

In the area of structural design and its control, the following points should be taken care of:

- (i) the pattern in which the ground vibrates during earthquake,
- (ii) the design techniques of buildings to withstand earthquakes,
- (iii) innovative strategies for the response control of building structures.

Passive and active control systems play an important role in the response reduction of civil engineering structures subjected to strong seismic vibrations. Passive, active, and semiactive control systems are the most important class of structural engineering. The two techniques that can be utilized for the control of structural vibrations are

- (i) implementation of smart materials in the construction of buildings [4],
- (ii) the use of control devices like actuators, dampers, and isolators in the building structures [5].

A worldwide popularity and high demand of structural control and its application had given rise to various researches leading to the publication of many textbooks, for example,

[6]. The authors [4] had suggested different types of passive, active, semiactive, and hybrid control systems in their review paper that highlights the importance of control theory in the vibration control of structures. In this paper, a detailed review on various passive, semiactive, and hybrid control system applied to control the translation-torsion coupled response of structure under bidirectional seismic events are portrayed in sequential manner. Reference [1] had focused on in-depth studies about active, semiactive, and hybrid control devices along with some control strategies. The main factors affecting the performance of structural control can be categorized as

- (i) excitation criteria (e.g., unidirectional or bidirectional earthquake and winds),
- (ii) structural characteristics (e.g., natural frequency, degree-of-freedom, and nonlinearity in structures),
- (iii) design of the control system (e.g., devices types and quantity, device placements, system models, and control algorithm) [7].

Although the most of research has been vested on the seismic analysis considering unidirectional seismic waves, very less researches have been detected on bidirectional seismic waves. The fact cannot be denied that the earthquake has indeed an arbitrary direction, represented by a bidirectional ground movement [8, 9]. The bidirectional seismic inputs in buildings will induce translation-torsion coupled vibrations in buildings which are more severe with severe structural damage and should be taken into consideration [10]. The investigation revealed the fact that one of the prime factors of building collapse in recent times is asymmetric building structures under the grip of bidirectional seismic ground motions [11]. So a detailed review of a detailed methodology on selection of control criteria, mathematical modeling techniques, and the effectiveness of control device to protect the building structures from bidirectional seismic waves is required to be presented in potential manner.

The aim of this review is to address all aspects involved in bidirectional structure control, taking into consideration modeling and vibration control of building structures under bidirectional seismic inputs. This paper also addresses the application of all possible devices for bidirectional vibration control. The foundation on the methodology of state estimation, system identification, optimal device placement, and the effect of the time delay on the stability is discussed in this review. We compare different control strategies for the bidirectional vibrations, such as PID control, H_∞ control, optimal control, sliding mode control, artificial neural network control, genetic control, and fuzzy control. The paper concludes with some of the observations noticed throughout the review.

2. Bidirectional Modeling of Building Structures

Structural mechanics involves the study of vibrations incorporated in structures. In order to control a structure effectively, it is important to have the knowledge about its dynamics. The control of structures is associated with

the safeguard of building structures from unidirectional or bidirectional seismic forces. One of the structural design objects is to model dynamic loadings and to produce innovative approach to curb vibration. The vibration control generates the required dynamics in the building structures within a stable range. This control design is decided by the structure of mathematical model [12, 13]. In [4], a compact relationship between the controller and the structure model is established.

All engineering structures are composed of intrinsic mass and elastic characteristics. The dynamic modeling has similar characteristics with the static analysis. However, the dynamic analysis is much complex than static analysis. For example, the mass modeling technique for the dynamic model requires an elastic model and a mass model minutely refined by discrete masses [6].

2.1. Bidirectional Excitation. Recent earthquakes show that the bidirectional effect is the main damage source of the structural damage. The seismic analysis should consider the bidirectional excitation. The normal method of building structure design regards the seismic response arising from the ground motion that acts separately in the two orthogonal directions. Generally, the earthquake exhibits arbitrary direction which is represented as bidirectional ground movement, and it could reduce the participation of the traverse frames to the structure torsional and lateral stiffness. A noteworthy change in the elastic torsional behavior of the building is observed considering a nonlinear behavior in the transverse frames.

The effect of the magnitude of the axial forces acting in the corner columns in case of bidirectional ground motion subjected to structures is different from that in case of unidirectional ground motion [8]. Reference [14] also suggested that, for a structure exposed to two simultaneous horizontal earthquake components, the transverse element behavior can be nonlinear and so the contribution to the real torsional stiffness is smaller. Reference [15] presents the analysis of one-story models with and without transverse elements subjected to unidirectional and bidirectional earthquakes. The study concluded that the addition of the transverse elements in the model significantly hampers the response of the border elements when the structure is subjected to the bidirectional seismic waves.

The analysis of real buildings suggests that it is asymmetric in nature to some degree with a formal symmetric plan. The asymmetric nature of building will induce lateral as well as torsional vibrations simultaneously and is termed as torsion coupling (TC) considering the case of pure translational excitations. Soil-structure interaction (SSI) effects are considered and can be significant in case of the building structures constructed on soft medium. The effects of SSI can critically modify the dynamic characteristics of a structure such as natural frequencies, damping ratios, and mode shapes [16].

The knowledge of behavior and impact of the excitation forces plays a significant role in the formulation of the building structures dynamic model. The movement of the portion of the earth crust is termed as earthquake which is

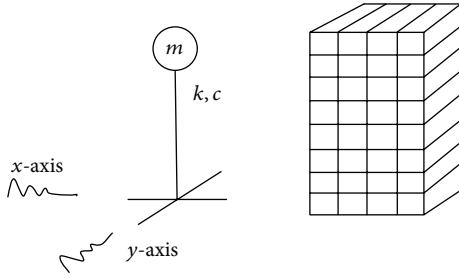


FIGURE 1: Bidirectional ground forces that are exerted on the building structures.

accompanied with the sudden release of stresses. Usually the epicenters for earthquake exist less than 25 miles below the earth's surface and are followed by series of vibrations. The bidirectional ground forces exerting on the building structure are shown in Figure 1. These forces result in series of structure vibrations.

The forces acting on the x -axis and y -axis can be illustrated by the following dynamic equations:

$$\begin{aligned} f_x &= -m\ddot{x}_g, \\ f_y &= -m\ddot{y}_g, \end{aligned} \quad (1)$$

where m is the mass and \ddot{x}_g and \ddot{y}_g are the ground accelerations, caused by the seismic waves.

The main factors of the seismic movement for the building are the amplitude (displacement, velocity, and acceleration) and the frequency of the ground motion. The ground motion is complex, and the vibration frequency is time-varying. The ground motion and the building vibration affect each other, depending on the distance between the natural frequency of the building structure and seismic motion frequency. When the seismic wave frequency is close to the natural frequency of the building, the damage becomes bigger. Structure analysis shows that the shorter the building, the higher the natural frequency. One of the prime concerns is controlling the structure vibrating with respect to low frequency, because the major part of the structure elastic energy is stored in low frequency zone [17].

2.2. Structure Model under Bidirectional Excitation. A controllable building structure can be regarded as a planar structure on a fixed base. The asymmetric characteristic of the building induces simultaneous lateral and torsional vibrations, known as torsion coupling (TC) [18], which are subjected to bidirectional seismic inputs. The schematic plan view of structure involving torsion coupled (TC) is shown in Figure 2. The impacts of seismic forces in x and y directions result in building oscillation as in Figure 3. It includes x oscillation, y oscillation, and the torsional oscillation defined as Φ .

The simplest structure is one-story under lateral translational motion at the roof level. It is a single degree-of-freedom system. The motion model is [19]

$$m\ddot{v} + c\dot{v} + kv = p(t), \quad (2)$$

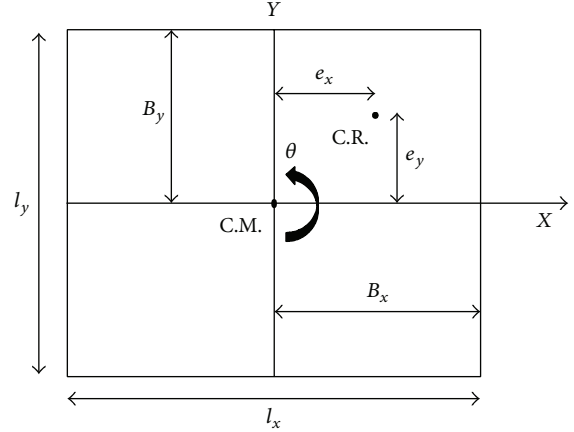


FIGURE 2: The torsion coupled force.

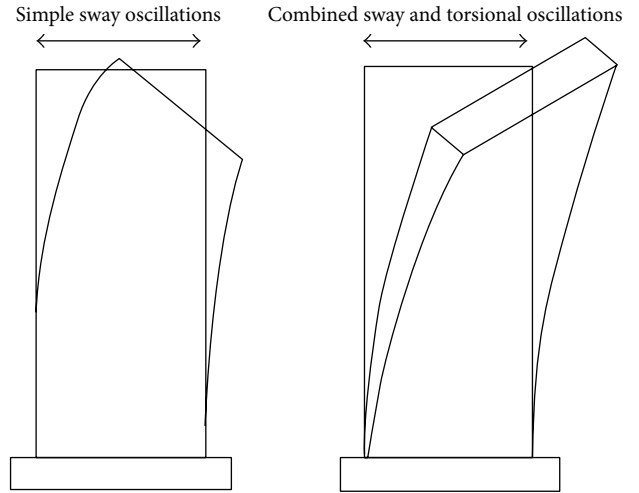


FIGURE 3: The seismic forces result in building oscillation.

where m is the mass, c is the damping, k is the stiffness, \ddot{v} is the acceleration of the mass, \dot{v} is the velocity of the mass relative to the base, v is the displacement, and $p(t)$ is the applied force; see Figure 4.

Similarly, the equation of motion of a linear structure with n -degree-of-freedom (n -DOF) can be expressed as

$$M\ddot{X} + C\dot{X} + KX = P(t), \quad (3)$$

where M , C , and $K \in \mathbb{R}^{n \times n}$ are the mass, damping, and stiffness matrices, respectively, \ddot{X} , \dot{X} , and $X \in \mathbb{R}^{n \times 1}$ are the relative acceleration, velocity, and displacement vectors, respectively, and $P(t) \in \mathbb{R}^{n \times 1}$ is the external force vector.

The technique of modeling the stiffness parameter K can be on the basis of either a linear (elastic) or a nonlinear (inelastic) component [20]. The linear case means that the relationship between the lateral force and the resulting deformation is linear [21].

When both ground translation and rotation are considered, the motion equation is [22]

$$M\ddot{X} + C\dot{X} + KX = F - MI_n\ddot{a}_g, \quad (4)$$

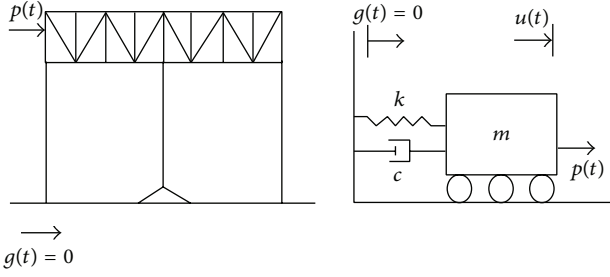


FIGURE 4: A single degree-of-freedom system for one-story building.

where \ddot{a}_g represents the earthquake acceleration component, I_n is the system influence coefficient vector, $X = [x^T, y^T, \theta^T]^T$, $x = [x_1, \dots, x_n]^T$, $y = [y_1, \dots, y_n]^T$, $\theta = [\theta_1, \dots, \theta_n]^T$, $I_n = [I_1 \ I_2 \ 0]^T$, and $\ddot{a}_g = [\ddot{x}_g \ \ddot{y}_g \ 0]$.

The mathematical analysis of the TC structure yields the following mass matrix, damping matrix, and stiffness matrix:

$$M = \begin{bmatrix} M_x & 0_{n \times n} & 0_{n \times n} \\ 0_{n \times n} & M_y & 0_{n \times n} \\ 0_{n \times n} & 0_{n \times n} & J_0 \end{bmatrix}, \quad (5)$$

$$K = \begin{bmatrix} K_{xx} & 0_{n \times n} & -K_{x\theta} \\ 0_{n \times n} & K_{yy} & K_{y\theta} \\ -K_{x\theta} & K_{y\theta} & K_{\theta\theta} \end{bmatrix},$$

where $J_0 = \text{diag}[m_1 r_1^2, \dots, m_n r_n^2]$, J_0 is the polar moment of inertia of the story, r is the radius of gyration of the floor, n is the number of stories of the building, and C is the damping matrix which is proportional to mass and stiffness matrix by the Rayleigh method [23].

For a simple case, the mass of each floor is concentrated at the floor plate (N -story shear model). Two seismic waves are in the x direction and the y direction. Here the torsional components are zero; see Figure 5. The left figure represents 3-dimensional building structures and the right figure exhibits the parameters of each floor. The motion equations show the relative displacements of the building structures with respect to the ground motions [10]:

$$\begin{aligned} m_j \ddot{x}_j + p_{j-1} - p_j &= -m_j \ddot{x}_g(t), \\ m_j \ddot{y}_j + q_{j-1} - q_j &= -m_j \ddot{y}_g(t), \\ J_j \ddot{\theta}_j + r_{j-1} - r_j &= 0, \end{aligned} \quad (6)$$

where x_j and y_j are the j th floor displacements in x direction and y direction, respectively, and θ_j is the j th floor torsion angle relative to the ground. p_{j-1} and q_{j-1} are the j th floor column shear forces in x direction and y direction, respectively, p_j and q_j are the $j+1$ th floor column shear forces in x direction and y direction, respectively, r_{j-1} is the j th floor torque generated by the shear forces, r_j is the $j+1$ th floor torque, m_j is the mass of the j th floor, and J_j is the rotational inertia. In the above motion equation, the $\ddot{x}_g(t)$ and $\ddot{y}_g(t)$ are the ground

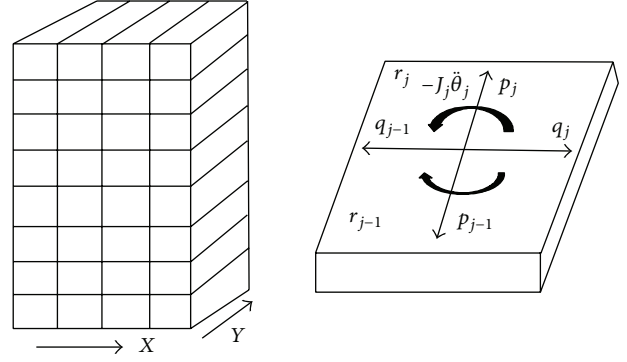


FIGURE 5: Three-dimensional building structures with parameters of each floor.

accelerations that strike the building structures due to an earthquake. The total forces exerted on each floor of the buildings in x and y directions are multiplied by the mass of the building at each floor. The torsional components of the ground acceleration are neglected and so the right hand side of the third equation is zero. The movement of the buildings in x and y directions, that is, the acceleration components, are \ddot{x}_j and \ddot{y}_j , respectively. Due to the bidirectional motion of the building, there will be coupling action on the building which gives rise to the torsional motion in the building which is denoted by the component $\ddot{\theta}_j$.

If we only consider x -axis seismic wave, the torsion effect on the building is in x -component [24]; see Figure 6. The motion equations are

$$\begin{aligned} p_{j-1} &= K_j (x_j - x_{j-1}) + C_j (\dot{x}_j - \dot{x}_{j-1}) \\ &\quad + B_j (\theta_j - \theta_{j-1}) + D_j (\dot{\theta}_j - \dot{\theta}_{j-1}), \\ r_{j-1} &= B_j (x_j - x_{j-1}) + D_j (\dot{x}_j - \dot{x}_{j-1}) \\ &\quad + E_j (\theta_j - \theta_{j-1}) + F_j (\dot{\theta}_j - \dot{\theta}_{j-1}), \\ r_j &= B_{j+1} (x_{j+1} - x_j) + D_{j+1} (\dot{x}_{j+1} - \dot{x}_j) \\ &\quad + E_{j+1} (\theta_{j+1} - \theta_j) + F_{j+1} (\dot{\theta}_{j+1} - \dot{\theta}_j), \end{aligned} \quad (7)$$

where $K_j = \sum_{i=1}^I K_{j,i}$, $C_j = \sum_{i=1}^I C_{j,i}$, $B_j = \sum_{i=1}^I K_{j,i} l_{j,i}$, $D_j = \sum_{i=1}^I C_{j,i} l_{j,i}$, $E_j = \sum_{i=1}^I K_{j,i} l_{j,i}^2$, $F_j = \sum_{i=1}^I C_{j,i} l_{j,i}^2$, $K_{j,i}$ and $C_{j,i}$ are the stiffness and viscous damping coefficient, respectively, of the i th plane frame at the j th floor, m_j is the mass of the j th floor, J_j is the moment of inertia of the j th floor, $l_{j,i}$ is the distance of mass centre of the j th floor to the i th plane frame, and I is total number of plane frames. $l_{j,i}$ is positive if the i th plane frame is located on the left of the mass centre; otherwise, it is negative.

3. Bidirectional Structural Control Devices

Vibration suppression in appropriate quantity can prevent the structures from fracture or collapse. Some devices play this suppression role to prevent the structure from damage. The

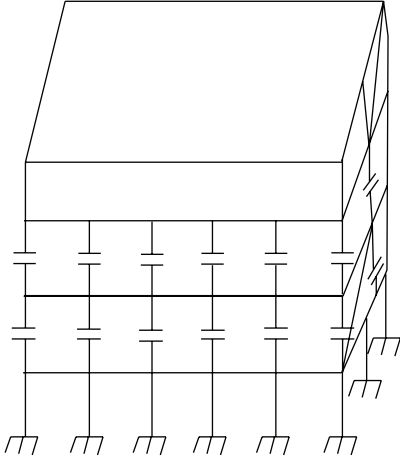


FIGURE 6: The torsion effect on the building is in x -component.

control devices, such as actuators, isolators, and dampers, are installed to suppress the external vibrations. These structural control devices are getting more popularity and attention along with their applications in building structures. The structural control devices for the seismic hazards can be categorized as passive, active, hybrid, and semiactive [25]. In the last two decades, the active, semiactive, and hybrid control are paid more attention compared to the passive devices [26]. The conception and characteristic of the structural control devices for bidirectional seismic waves are illustrated below.

3.1. Passive Devices. A passive control device is incorporated to a structure. It modifies the stiffness or the damping of the structure in an suitable way. The passive control system does not require an external power source for its operation. It generates control force opposite to the motion of controlled structured system [27]. The passive systems can be divided into two basic categories: (1) base isolation systems and (2) energy dissipation systems.

There are many passive control devices, for example, viscoelastic dampers, tuned mass dampers, frictional dampers, tuned liquid dampers, and base-isolation systems [28]. The principal function of a passive energy dissipation system is to reduce the inelastic energy dissipation demand on the framing system of a structure [29].

The forces of the passive control devices solely depend on the structural motion. They can be expressed as [7]

$$f_i(t) = -c_i \dot{x}_{di}(t), \quad (8)$$

where \dot{x}_{di} is relative velocity across i th device and c_i is the damping coefficient associated with the i th device.

We use the following sections to describe some famous dampers for the bidirectional control.

The tuned mass damper (TMD) is considered to be an energy dissipation system, although the primitive concept of this system is not to dissipate energy. It transfers the energy from the building structure to the tuned mass dampers (absorbers). The basic principle of TMD is to obtain optimal damping parameters, in order to control the displacement of an undamped system subjected to a harmonic force [30].

The coupled lateral-torsional motions under seismic excitations are exhibited by the building structures with intended eccentricities between their mass and stiffness centers. Reference [31] investigated tuned mass dampers in arrangements termed as coupled tuned mass dampers (CTMDs), where translational springs and viscous dampers are used to connect mass in an eccentric manner. The CTMD works in coupled mode that includes lateral and rotational vibration. This technology is utilized to control coupled lateral and torsional vibrations of asymmetric buildings. The results revealed that CTMDs are more effective and robust in controlling coupled lateral and torsional vibrations of asymmetric buildings. Reference [32] had proposed multiple tuned mass dampers (MTMDs) with distributed natural frequencies. Several researches had been carried out to establish the effectiveness of multiple tuned mass dampers and it had been verified that MTMDs had advantages over single TMD. A multiple tuned mass damper (MTMD) system is shown in Figure 7. It consists of a main system, which has n tuned mass dampers with different dynamic characteristics. The main system is subjected to a lateral force. The main system and each TMD vibrate in the lateral direction. Due to torsional coupling, the main system has torsional vibration. The total degrees-of-freedom of the combined system is $n+2$. Two uncoupled frequency parameters of the main system are defined by

$$\begin{aligned} \omega_{sxy} &= \sqrt{\frac{K_{sxy}}{m_{sxy}}}, \\ \omega_{\theta} &= \sqrt{\frac{K_{\theta}}{m_{sxy} r_S^2}}, \\ m_{sxy} &= \begin{bmatrix} M_x & 0 & 0 \\ 0 & M_y & 0 \\ 0 & 0 & J_0 \end{bmatrix}, \\ K_{sxy} &= \begin{bmatrix} K_{xx} & 0 & -K_{x\theta} \\ 0 & K_{yy} & K_{y\theta} \\ -K_{x\theta} & K_{y\theta} & K_{\theta\theta} \end{bmatrix}, \end{aligned} \quad (9)$$

where m_{sxy} is the mass of the main system, K_{sxy} is the main system lateral stiffness, K_{θ} and r_S are the torsional stiffness and radius of gyration, respectively, related to the main system about the center of mass, and J_0 is the polar moment of inertia related to the story.

Tuned liquid column damper (TLCD) has uniform cross-section with U shaped tube attached. The schematic view has been shown in Figure 8. The vibrational energy from the structure is transferred to the TLCD liquid via the movement of the rigid TLCD container, thus stimulating the TLCD liquid.

Reference [33] investigated the methodology of vibration control of eccentric structures using TLCD modeled as torsionally coupled multistory shear structures which is under the grip of multidimensional seismic excitations. For a multistory eccentric model with TLCD arrangements, O , S , and M

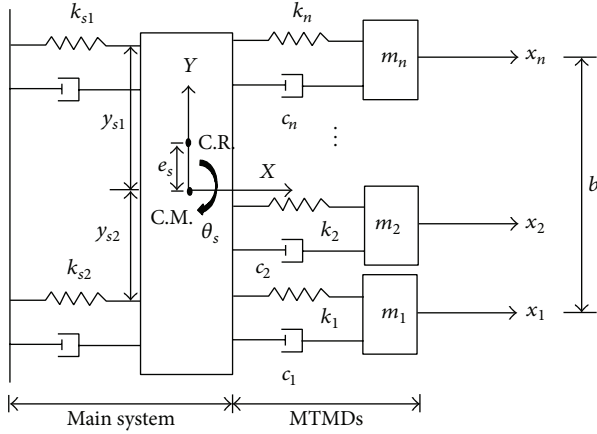


FIGURE 7: The multiple tuned mass damper (MTMD).

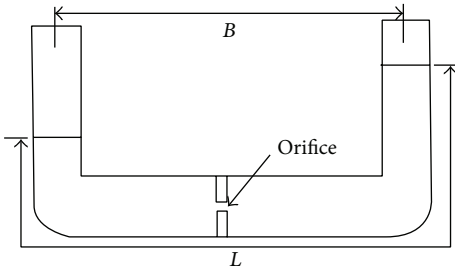


FIGURE 8: The tuned liquid column damper.

are the geometry, stiffness, and mass centers, respectively, with u , v denoting floor translational displacement along x -axis and y -axis, respectively, and θ denoting the rotational angle about vertical z -axis. The equation of motion along x and y directions is illustrated by

$$m_h \ddot{h} + c_h \dot{h} + k_h h = -\rho A_h B_h [\ddot{x}_l + \ddot{u}_g - l_{vh} (\ddot{\theta}_l + \ddot{\theta}_g)], \quad (10)$$

$$m_s \ddot{s} + c_s \dot{s} + k_s s = -\rho A_s B_s [\ddot{y}_l + \ddot{v}_g + l_{us} (\ddot{\theta}_l + \ddot{\theta}_g)],$$

where $m_h = \rho A_h L_h$, $m_s = \rho A_s L_s$, $c_h = (1/2)\rho A_h \xi_h |\dot{h}|$, $c_s = (1/2)\rho A_s \xi_s |\dot{s}|$, $k_h = 2\rho A_h g$, $k_s = 2\rho A_s g$. Natural frequencies are $\omega_h = \sqrt{k_h/m_h} = \sqrt{2g/L_h}$, $\omega_s = \sqrt{k_s/m_s} = \sqrt{2g/L_s}$, ρ = Liquid Density, ξ_h and ξ_s are damping ratios related to TLCD, and h and s are the displacements of liquid in the TLCD of u and v directions. L_h and L_s , B_h and B_s , and A_h and A_s are the notations for length, width, and cross sectional, respectively, of the liquid in two TLCDs. Coordinate positions of the TLCDs in x direction are represented by l_{uh} and l_{vh} . Coordinate positions of the TLCDs in y direction are represented by l_{us} and l_{vs} . \ddot{u}_g , \ddot{v}_g , and $\ddot{\theta}_g$ are the ground seismic acceleration along u , v , and θ directions. \ddot{x}_l , \ddot{y}_l , and $\ddot{\theta}_l$ are the accelerations of the i th floor along x , y , and θ directions.

The circular tuned liquid column damper (CTLCD) is shown in Figure 9. This advanced control device is highly responsive to the torsion. CTLCD can be applied for both torsional vibration and torsionally coupled vibration. The effectiveness of CTLCD for the structural torsional response

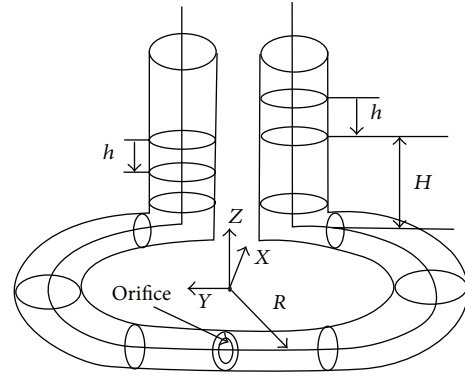


FIGURE 9: The circular tuned mass damper (CTLCD).

is studied by [34]. Stochastic vibration theory is applied to identify the optimal parameters of CTLCD in [35]. The motion equation of CTLCD is given by [36]

$$\rho A (2H + 2\pi R) \ddot{h} + \frac{1}{2} \rho A \xi |\dot{h}| \dot{h} + 2\rho A g h = -2\rho A \pi R^2 (\ddot{u}_\theta + \ddot{u}_{g\theta}), \quad (11)$$

where R is the radius of the horizontal circular column, \ddot{u}_θ is the structures torsional acceleration, and $\ddot{u}_{g\theta}$ is the torsional acceleration of ground motion.

Reference [9] presents a new type of control device termed as tuned liquid mass damper (TLMD), to control the torsional response of building structures subjected to bidirectional earthquake waves. The mass of TLMD includes both TLCD tank and the liquid in the tank. The stiffness is compensated by natural rubbers. The main working concept of TLMD is to operate a TLCD in one direction and run a TMD in the other orthogonal direction; see Figure 10.

The stiffness of TMD and the liquid high are determined as

$$k = m (2\pi f_m)^2,$$

$$L = \frac{2g}{(2\pi f_L)^2}, \quad (12)$$

where m and f_m are the mass and the tuned frequency in the TMD control direction and g and f_L are the gravity acceleration and the tuned frequency of TLCD.

Tuned liquid column dampers (TLCDs) are a special type of TLDs that depends on the motion of a column of liquid in a U-tube-like container to neutralize the forces acting on the structure. The introduction of the damping factor is done in the oscillating liquid column through an orifice in the liquid passage. The damping, however, unlike TMDs, is amplitude dependent, and thus the TLCD dynamics are associated with nonlinearity. On the other hand, circular tuned liquid column dampers (CTLCDs) are very much active when exposed to torsional response. As the earthquake is practically multidimensional, the torsionally coupled vibration factor cannot be ignored and so CTLCD is much favored in this case. Reference [37] had discussed

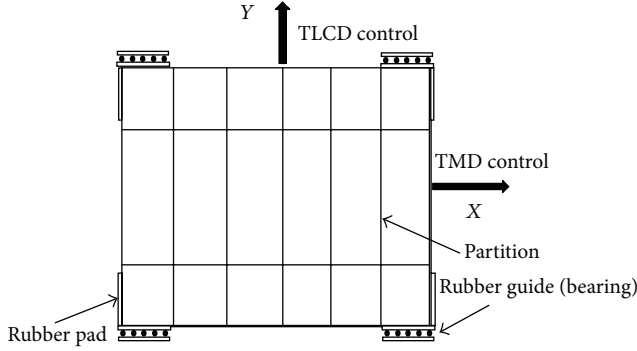


FIGURE 10: The tuned liquid mass damper.

the control performance of the novel sealed, torsional tuned liquid column gas damper (TTLCGD) in order to minimize the coupled flexural torsional response of plan-asymmetric buildings under the grip of seismic loads. The analysis of technique associated reveals that TTLCGD is an effective control device in suppressing the time-harmonic excitation and the earthquake response.

3.2. Active Devices. The main drawback of the passive control devices is that they cannot adapt the change of the natural frequency caused by the structural nonlinearities and huge seismic excitations, especially for multiple floor buildings [1], although multiple and tuned dampers can be applied for different frequencies.

Since 1970s, remarkable progress has been made in the field of active control of civil engineering structures subjected to natural forces such as winds and earthquakes [26]. The active structure control modifies the structural motion by some external forces. Topics covered on active structural control can be found in [38]. Compared with the passive devices, the active systems have the following advantages [28]:

- (1) Motion control can be achieved with greater effectiveness.
- (2) In account of ground motions, it is relatively insensitive.
- (3) It can be applied to the multihazard remission circumstances.
- (4) Control objectives can be selected flexibly.

In order to control actively, the external excitations and inner structural responses are needed. Measured information is sent to the control algorithm to generate desired control forces. So the active devices usually use displacement sensors.

The active tuned mass damper (ATMD) uses control strategy to improve the tuned mass damper (TMD). It improves the effectiveness in minimizing the structural response [39]. As the proof of [40], the qualities of TMD can be enhanced by introducing an active force between the structure and the TMD. ATMD methodology can be also regarded as a modification version of ATMD, robustness version of TMD.

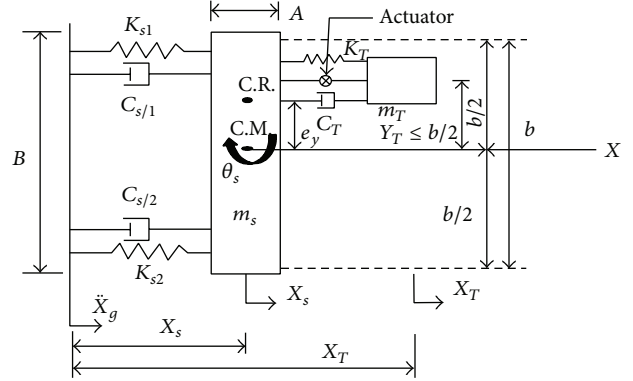


FIGURE 11: The active tuned mass damper for a 2-DoF structure.

The active controller should be able to absorb the translation-torsion coupled vibrations. Besides the translational vibrations, the torsional vibrations under the seismic waves also affect the performance of ATMD. An asymmetric structure under the coupled lateral-torsional responses is discussed in [41]. The lateral displacement of asymmetric structures and the optimum parameters incorporated in ATMD are shown by a two-degree-of-freedom (2-DoF) structure; see Figure 11. The mathematical expression of the ATMD active control force that is generated is

$$U(t) = -m_t \ddot{x}_s - c_t [\dot{x}_T - (\dot{x}_s + y_T \dot{\theta}_s)] - k_t [x_T - (x_s + y_T \theta_s)], \quad (13)$$

where m_t is the feedback gain of acceleration associated with asymmetric structure, c_t is the feedback gain of the velocity of the ATMD, and k_t is the feedback gain of the displacement of the ATMD. Reference [42] had proposed a new performance index for active vibration control of three-dimensional structures. To analytically proof the existence of the proposed performance index, a six-story three-dimensional structure is taken into consideration as an example with a fully active tendon controller system implemented in one direction of the building. The building under analysis is modeled as a structure made up of members joint by a rigid floor diaphragm in a manner so that it has three degrees of freedom at each floor, lateral displacements in two perpendicular directions, and a rotation with respect to a vertical axis for the third dimension.

3.3. Semiactive Devices. Semiactive control devices are regarded as controllable passive devices. The main objective of these devices is saving control resources. The actuators of the semiactive control do not add mechanical energy to the structure directly. The power break down semiactive control system offers some degrees of protection with the help of embedded passive components.

The semiactive devices take the advantages of the passive and the active control. It requires less power than the active control devices. They can even be operated by the battery in the case of power failure during the seismic event [26]. They perform significantly better than passive devices.

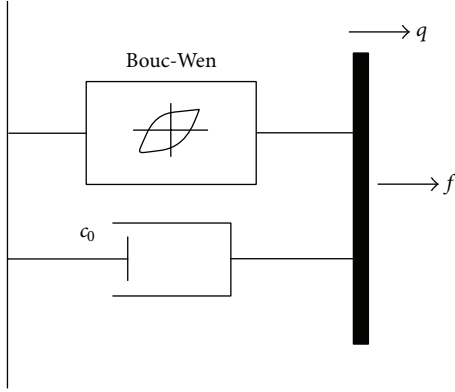


FIGURE 12: Simple mechanical model of MR.

An exhaustive review on the semiactive devices is proposed in [25].

The magnetorheological (MR) damper is the most popular semiactive damping device. It works on the magnetorheological fluid and is controlled by a magnetic field. Generally, the magnetic field is produced by electromagnet. It requires minimal power for its operation. The suspended minute iron particles in a base fluid are termed as MR fluids. This type of liquids has the capability of changing from free flowing linear viscous state to semisolid state with controllable yield strength under a magnetic field.

The result of uncovering the liquid to a magnetic field is the particles use the form of chains. These chains obstruct the flow and solidify the fluid in a span of milliseconds. The stress is directly proportional to the magnitude of the applied magnetic field [43]. The behavior of MR fluid can be simulated by the Bingham plastic model, which is an extension of the Newtonian flow. The other way of determining the behavior of MR fluid is to analyze the yield stress of the fluid. The total stress is given by [44]

$$\tau = \tau_y \operatorname{sgn}(\dot{\gamma}) + \eta \dot{\gamma}, \quad (14)$$

where τ_y is the yield stress induced by the magnetic field, $\dot{\gamma}$ is the shear rate, and η is the viscosity of the fluid.

The application of MR damper to control the torsional and torsionally coupled responses subjected to bidirectional seismic waves is investigated in [45]. The MR damper contributes significantly to the field of civil engineering. The simple mechanical model of MR is shown in Figure 12. In [46], a prototype shear-mode MR damper is proposed.

The governing force f generated by MR device is

$$\begin{aligned} f &= c_0 \dot{q} + \alpha z, \\ \dot{z} &= -\gamma |\dot{q}| |z| |z|^{n-1} - \beta \dot{q} |z|^n + A \dot{q}, \end{aligned} \quad (15)$$

where q is the device displacement, z is the evolutionary variables that keeps track of the response history dependence, and γ , β , n , and A can control the linearity in the unloading and the smoothness of the transition from the preyield to the postyield region.

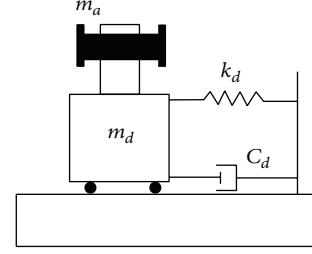


FIGURE 13: HMD system installed in n th floor.

3.4. Hybrid Devices. Hybrid base isolation (HBI) had been a matter of interest for a number of researchers due to its effectiveness and consists of a passive base isolation system combined with a control actuator to generate the effects of the base isolation system. Several research on base isolation system has been carried out and installed in several structural engineering projects due to its positive attributes like simplicity, reliability, and effectiveness. Reference [47] has proposed the application of HMD system consisting of tuned mass damper and active mass damper to control torsionally coupled building structures under bidirectional seismic force. In this context, the fuzzy logic controller is used to control the HMD system. The schematic view is shown in Figure 13.

The equation of motion for HMD system installed in N -story building is given by

$$M_h \ddot{u}_h + C_h \dot{u}_h + K_h u_h = -M_h P_h \ddot{u}_{aN} + K_h P_c u_c, \quad (16)$$

where the mass, damping, and stiffness matrices of the HMD system are M_h , C_h , and K_h , respectively. u_h is a vector of displacements of the HMD system relative to the N th floor. P_h and P_c are position vectors of the absolute acceleration of N th floor, \ddot{u}_{aN} , and control command vector u_c , respectively. Reference [48] had investigated hybrid damper-TLCD control system to control 3D coupled irregular buildings subjected to bidirectional seismic waves. Simulation results for control of two multistory moment resisting space steel structures with vertical and plan irregularities show clearly that the hybrid damper-TLCD control system significantly reduces responses of irregular buildings subjected to various earthquake ground motions and increases reliability and maximum operability during power failure. The comparison between uncontrolled, passive control, active control, semiactive control, and hybrid control devices are demonstrated by Figure 14.

4. Bidirectional Vibration Control

The appropriate design of a controller is utterly necessary so that it can send essential control signal to the control devices in order to reduce the structural responses. The main strategy involved within the control scheme to prevent the collapse of building structures under bidirectional seismic waves is to control the coupled translation-torsion response of the building structures [49–52]. In this section, various control strategies on the basis of various techniques are presented. The main object of the bidirectional control is to change

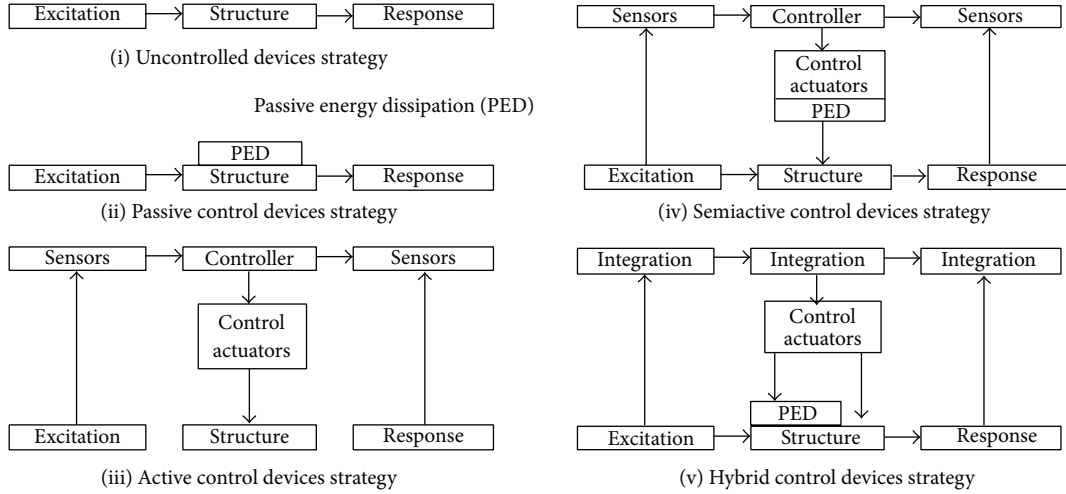


FIGURE 14: Comparison of control devices.

the coupled translation-torsion response of the building structure, in order to prevent the collapse of building under bidirectional seismic waves [53]. Robustness, fault tolerance, simplicity, and reliability criteria are considered [54].

4.1. Time Delay Problem in Vibration Control. Time delay from the measurement to the actuator is a limit for vibration control. The control loop includes vibration data measurement, data filtration, control algorithm, data transmission, and actuation. The control loop has also phase shift by time delay [55]. The time delay may cause instability in the closed-loop [56].

The motion equation of n -DoF structure with time delay t_d is

$$M\ddot{x}(t) + C\dot{x}(t) + Kx(t) = \Gamma u(t - t_d) - M\Lambda\ddot{x}_g(t). \quad (17)$$

If t_d is fixed, the Laplace form transformation is

$$F_d(s) = e^{-st_d} (g_1 s + g_2). \quad (18)$$

A review on time-delay compensation methods can be found in [57].

4.2. Optimal Placement. The proper placement of sensing and control devices is an important research field of structural control. It gives the measurement and control operation effectively. It also affects the controllability and observability of the controlled system [58, 59]. Reference [60] shows that the location performance index of the actuator and sensor can be computed by the Hankel singular values γ_{wz}^2 and γ_{uy}^2 :

$$k^2 = \frac{(\gamma_{wz}^2)^T \gamma_{uy}^2}{\|\gamma_{wz}^2\|_z \|\gamma_{uy}^2\|_z}, \quad (19)$$

where k is the nonnegative correlation coefficient, γ_{wz}^2 and γ_{uy}^2 denote the Hankel singular values of the transfer functions G_{wz} and G_{uy} , u and w represent the input to the system,

and y and z represent the output of the system. Reference [61] suggests that the sensor is placed at the center of mass. Reference [61] shows that the center of mass may not be good for the sensor position. Arbitrary arrangement of sensors is better subjected to bidirectional seismic motion. Reference [2] presents a detail survey on the optimal placement of control devices. Reference [24] uses energy dissipation to analyze the position of the controller, in order to minimize translation-torsion coupling effects. It suggests that the locations which are nearby to the geometric centre of the structure can minimize the torsional effect.

4.3. Linear Controllers. The working principle of PID controller is based on the feedback error $e(t)$ which is otherwise used to calculate the required control force. In case of structural applications if the desired state is in the equilibrium position then the reference signal is considered to be taken as zero. The principle of PID control is to use the feedback error $e(t)$, which is the difference between the output signal $y(t)$ and the reference signal $r(t)$. Once the error is calculated, the main aim of the controller is to minimize the error for the next iteration process by carefully manipulating the inputs. It has the following form:

$$u(t) = K \left[e(t) + \frac{1}{T_i} \int e(t) dt + T_d \frac{de(t)}{dt} \right], \quad (20)$$

where K is the proportional gain, T_i is the integral time, and T_d is the derivative time, $e(t) = r(t) - y(t)$. PID control is a negative feedback algorithm. It can force $e(t)$ to zero. It is the most popular industrial controller. Reference [42] uses MR damper with the MR-MD scheme for PID to control a three-dimensional structure with bidirectional seismic excitations. The aim of the controller is to calculate the essential forces to control the structural vibrations. Reference [62] investigates the effectiveness of active tendon PID control implemented in a single-story torsionally coupled structure. A comparison between a sliding mode control and PID control for the structural system is investigated by [63]. Reference [64] had

investigated the effects of measuring seismic waves on a six-story asymmetric structural model compiled with frictional dampers. The methodology deals with the control of torsional response of asymmetric structures and to obtain a lower level of torsional balance by arranging empirical centre of balance (ECB) of the structure at same distance from the edges of the building plan. The axial displacement of each actuator is controlled using a conventional PID controller. In this research, frictional dampers proved their effectiveness of controlling lateral-torsional coupling of torsionally flexible as well as stiff structures.

The most important optimal controllers are the linear quadratic regulator (LQR) and linear quadratic Gaussian (LQG) control. The equation of motion can be exhibited in the form mentioned below:

$$\dot{X} = Ax + Bu, \quad (21)$$

where the state and input system matrices are A and B , respectively. The LQR algorithm calculates a control law u in the form of criteria of performance or cost function:

$$J = \int_0^{\infty} (x_{\text{ref}} - x(t))^T Q (x_{\text{ref}} - x(t)) + u(t)^T R u(t) dt \quad (22)$$

is minimal. The design matrices Q and R take back the compensation on the deviations of state variables from their set-point and the control actions, respectively.

The increase in elements of Q results in the increase of cost function, the compensation associated with any track change from the desired set-point of that state variable, and thus the specific control gain will be larger. The increase in R matrix results in a larger penalty that is applied to the audacity of the control action, and the control gains are uniformly decreased. The feedback gain of the optimal control is computed by minimizing a cost function $J = J(z, t, u(t))$ [55]:

$$J = \lim_{\tau \rightarrow \lambda} \frac{1}{\tau} E \left[\int_0^{\tau} \{y_r^T Q y_r + f^T R f\} dt \right]. \quad (23)$$

Reference [65] presents a semiactive control to the coupled translational and torsional vibration of a 2-story asymmetric building subjected to seismic excitations. A LQG controller is involved as a nominal linear controller, considering the ground acceleration with white noise. The LQG controller is given by

$$\begin{aligned} \dot{\hat{z}} &= (A - LC)\hat{z} + Ly_m + (B - LD)f_m, \\ f_c &= -K\hat{z}, \end{aligned} \quad (24)$$

where L is the state estimator gain matrix and K is the LQR gain matrix. The authors [66] in their research implemented active isolation and conducted experiments in order to verify the behavior of seismically excited buildings under multidirectional earthquake force. Active isolation technique works in combination with base isolation system and controllable

actuators. The base isolation methodology offers effective approach in reducing interstory drifts and floor accelerations that works in phase with the adaptive nature of the active system in order to generate higher level performance against wide range of earthquakes. In this methodology, LQG control steps are obtained using LQR and Kalman estimator. The optimal control gain is achieved using the following:

$$u(t) = -K\bar{x}(t), \quad (25)$$

where K is optimal control gain with respect to the states of the augmented system. The authors [48] had researched the control of 3D coupled irregular buildings subjected to bidirectional seismic waves. To find the optimal control forces, a wavelet based algorithm involving optimal control is utilized. It has been suggested in their work that LQR or LQG algorithm can be used as a control algorithm for the feedback controller as per the investigation mentioned [28, 67, 68]. The authors [69] in their study suggested a sequential optimal control for serially connected isolated structure subjected to bidirectional earthquake. Sequential control algorithm has inherent capabilities to construct control objective function under bidirectional earthquake situations. The objective function which is in quadratic form can be illustrated as in (41)

$$J = \int_{t_0}^{t_f} \left[\frac{1}{2} \{X(t)\}^T [Q] \{X(t)\} + \{f_c(t)\}^T [R] \{f_c(t)\} \right], \quad (26)$$

where weighted matrices Q and R represent structure response and control force. x , y structural response is contained in $X(t)$, t_0 is control starting time, and t_f is control conclusion time. The mathematical expression of sequential optimal control is depicted by the following equations:

$$\begin{aligned} \{f_c(t_A)\} &= -[R]^{-1} [B]^T \{\lambda(t_A)\}, \\ \{\dot{\lambda}\} &= -[A]^T \{\lambda\} - [Q] \{X\}, \\ \{\lambda(t_f)\} &= 0, \\ \{\dot{X}\} &= [A] \{X\} + [B] \{f\}_c + \{E\} \ddot{U}_g^T, \end{aligned} \quad (27)$$

where t_A is current time, the domain is expressed in $[t_A, t_f]$, and the value of λ can be computed directly.

The result of the entire analysis was in the favour of the algorithm not only being an effective measure to control the bidirectional horizontal response of earthquake but also reducing the isolation layer movement by large extent. Reference [70] investigated the lateral-torsional earthquake response control of two single-story asymmetric plan buildings associated with multiple magnetorheological (MR) dampers. The desired control forces are generated using LQR technique. The damper forces are extracted using the method of least square minimization. Reference [71] investigates the response related to seismic and harmonic waves for a true free-plan tall building equipped with two tuned inertial

masses (TMs) and magnetorheological (MR) dampers. The technique of LQR strategy is hold as a benchmark in order to compare the performance with the proposed physical controller. A 21-story R/C structure building is investigated of typical story height of 3.6 m with total height of 90 m. In the y direction, the building being more flexible, there is existence of lateral torsional coupling. As a result, two TMs, one along the flexible edge and one along the stiff edge of the building, were designed and built on the 21st story. The controller used in this investigation is quite similar to the LQR controller which was implemented to control TM-MR damper.

H^∞ control methodology has been relied as an effective approach in structural vibration control which is classified as linear robust control. This scheme is unresponsive to the disturbances and parametric differences and so it is most preferred for multiple input multiple output (MIMO) type structural control systems [72]. Design method of H^∞ control system and its effectiveness was presented by [73]. The analysis was carried out on actual 23-story building in Tokyo using a pair of hybrid mass dampers. Bidirectional seismic excitations were considered during the investigation. The control technique was established by taking into consideration x direction and y direction separately. The bending component of the vibration was controlled along x direction only while along the y direction, control of bending and torsion are considered. The scheme of the control system is shown in Figures 15 and 16.

H^∞ control theory was applied to design the controller on the basis of reduced order model depicted in

$$\begin{aligned} \dot{x}_r &= A_r x_r + B_r u + D_r w, \\ y &= [\xi_1 + l\xi_3 z]^T = C_r x_r. \end{aligned} \quad (28)$$

The designed controller should follow the following inequality:

$$\left\| \begin{array}{c} W_1(s) N(s) \\ W_2(s) M(s) \end{array} \right\|_\infty < 1, \quad (29)$$

where $N(s)$ and $M(s)$ mean the transfer function from external input to control input and from external force to output, respectively.

The controller was installed and then the vibration tests are performed. These test results suggested that the control action generated was effective and as per the design. Reference [74] has elaborated the use of a robust optimal H^∞ control for the two AMD systems. The AMD system was placed on the top of the irregular building for the vibration control. The building was subjected to bidirectional seismic excitations. The H^∞ control uses the technique of LMI-based solution blended with robustness specifications. For an uncertain structural system, the efficient and necessary control forces are determined and then optimized using H^∞ control via LMI as illustrated in

$$\begin{aligned} (M + \Delta M) \ddot{v} + (C + \Delta C) \dot{v} + (K + \Delta K) v \\ = (M + \Delta M) E w(t) + B_s u(t), \end{aligned} \quad (30)$$

where ΔM , ΔK , ΔC , and ΔB_s are corresponding disturbances. The bound condition satisfied by ΔM is given by $\|\Delta M M^{-1}\| \leq \|\delta\| \leq 1$.

Then using the above criteria, the state space equation can be written as

$$\dot{Z}(t) = (A + \Delta A) Z(t) + (B + \Delta B) u(t) + H w(t). \quad (31)$$

Considering linear time invariant criteria for the above state space equation, the performance index is given by

$$J = \int_0^\infty (Z^T(t) Q Z(t) + u^T(t) R u(t)) dt, \quad (32)$$

where $Q \geq 0$ and $R > 0$ are weighted matrix. H^∞ direct output feedback control of buildings under bidirectional acceleration considering the effects of soil-structure interaction was investigated by [18]. In the investigation, the tendon displacement vector of feedback control with direct approach was found to be as depicted by

$$U(t) = G Y(t), \quad (33)$$

where G is a time-invariant feedback gain matrix of $4 \times s$. H^∞ control algorithm was used to find the entries of G matrix.

4.4. Nonlinear Controllers

4.4.1. Sliding Mode Control. The sliding mode control (SMC) is designed for uncertain nonlinear systems [72]. It is very much effective in terms of robustness against the changes in the parameters and external disturbances. It has been successfully applied for structural control [75].

The control force of sliding mode control is

$$u(\hat{v}_c, t) = u_{eq}(\hat{v}_c, t) - \rho \operatorname{sgn}(\sigma(\hat{v}_c)), \quad (34)$$

where u_{eq} is the linear part of control force, $\sigma(\hat{v}_c)$ is the sliding surface, and ρ is the control gain.

In [76], SMC is used to control bending and torsional vibration of a six-story flexible structure. The controller takes into accounts two conditions as follows.

(1) Controller design considering only nonlinear control inputs: the dynamic system and the switching function are given by

$$\begin{aligned} \dot{x}(t) &= Ax(t) + Bu(t), \\ y(t) &= Cx(t), \\ \sigma(t) &= Sy(t), \end{aligned} \quad (35)$$

where S is switching hyperplane. The controller has the following nonlinear form:

$$u(t) = -K_{nt} (SCB)^{-1} \frac{\sigma(t)}{\|\sigma(t)\|}, \quad (36)$$

where K_{nt} is the scalar coefficient, SCB is the multiplication factor of the matrices S , C , and B .

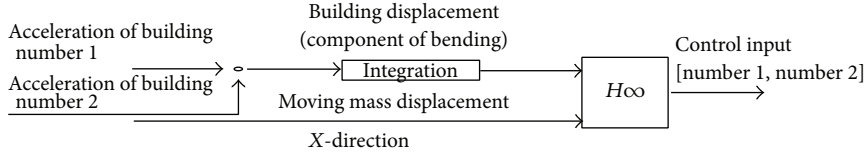


FIGURE 15: X direction.

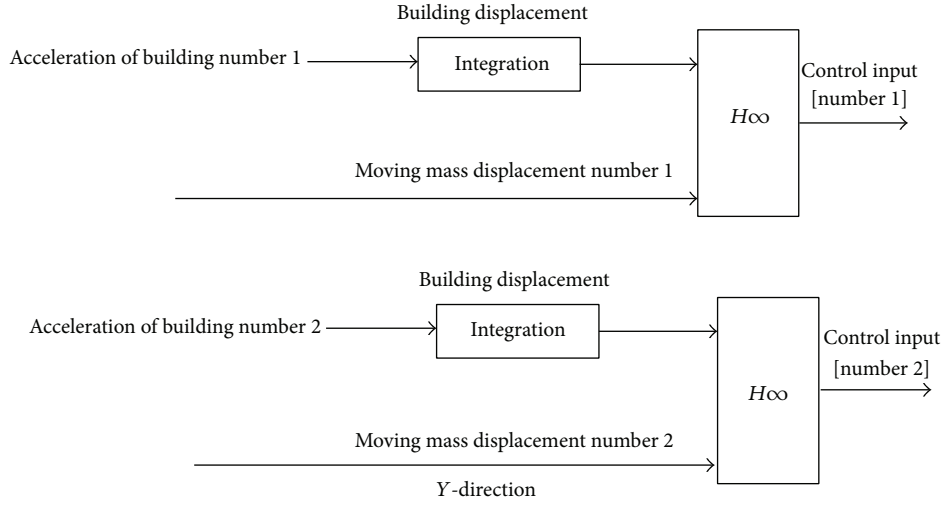


FIGURE 16: Y direction.

(2) Controller design considering nonlinear and subequivalent control inputs: the controller has the following nonlinear form:

$$u_{nt}(t) = -K_{nt} (SCB)^{-1} \frac{\sigma}{\|\sigma\|}. \quad (37)$$

Also,

$$u = u_t + u_{nt}. \quad (38)$$

The inputs of sliding mode control are designed as the sum-up of linear and nonlinear inputs. Subequivalent control inputs can be generated from the solo measured outputs as given in

$$u_t = u_{eq} = -k_{eq}y, \quad (39)$$

where k_{eq} is the scalar equivalent. The important feature of SMC is robustness under the uncertainties and disturbances. Lyapunov stability theory is implemented to prove the system stability in [75].

4.4.2. Neural Network Based Structure Control. A neural network (NN) is characterized by (1) an area which consists of number of neurons along with their interconnections and layers and (2) its technique of evaluating the weights on the connections which is termed as learning algorithm. In [77], a neural network based emulator computes the response of a 2D frame structure involving 3-story building. The feedforward multilayer perceptron with the backpropagation

algorithm is used in [54] for structure control. Reference [78] presents a wavelet neural network (WNN) based active nonlinear controller for 3D buildings subjected to seismic excitation in both x and y directions.

The combination of NN with the classical control theory yields better control results [79, 80]. The hybrid intelligent control algorithm applied to semiactive control of the magnetorheological (MR) damper is presented in [74]. It is subjected to bidirectional seismic wave. The training data for structure usually need to be normalized into $[0, 1]$

$$\bar{N}_i = \frac{2(N_i - N_{i,\min})}{N_{i,\max} - N_{i,\min}} - 1, \quad (40)$$

where N_i is the input component and its domain is $(N_{i,\min}, N_{i,\max})$. Reference [81] presents a direct adaptive neural controller subjected to bidirectional earthquake inputs. Both the system parameters and the nonlinear estimation of force have uncertainties, which can be canceled by the adaptive controller. The control law is

$$F_c^*(k) = \bar{G}(z(k-1), \dots, z(k-n_1), A_g(k), \dots, A_g(k-n_1)) = \bar{G}(V), \quad (41)$$

where $n_1 \geq n$, \bar{G} is the mapping function, and $F_c^*(k)$ is the desired control force. NN is used to model \bar{G} . References [82, 83] use NN for the structural reliability analysis. Reference [84] proposes a NN based prediction scheme for the dynamic behavior of structural systems under

multiple seismic excitations. The NN prediction includes two different ways: (1) a nonadaptive scheme that uses multiple accelerometers in training NN and utilizes for the prediction of the structural seismic response; (2) an adaptive that scheme uses multiple accelerometers in the training.

4.4.3. Fuzzy Control. Linguistic criteria are an effective feature of fuzzy control rules that can be easily modified and understood clearly [85]. The application of fuzzy logic in structural control has been studied by [17]. Reference [47] proposes a fuzzy logic controller with multipurpose optimal design to drive hybrid mass damper (HMD) for the response control of the torsionally coupled seismically excited buildings. HMD system consists of four HMDs arranged in such a way that this system can control the torsional mode of vibration effectively in addition to the texture modes of vibration. The design of the fuzzy logic controller (fLC) is based on the selection procedure that includes five membership functions for each of input variable and seven membership functions for the output variable. The input and output variables includes acceleration and velocity in x , y , and θ directions and control command u_c , respectively.

In their study, bell shaped membership functions have been used and are represented by

$$\mu_x = \frac{1}{1 + |(x - c)/a|^{2b}}, \quad (42)$$

where a is the half-width of the membership function at 0.5 membership grade, b is the membership function slope, and c is the central position of the membership function.

The minimization of structural torsion responses using semiactive dampers has been presented by [86]. In their investigation, the MR damper is employed for the real time control of the response of structures under seismic excitations. The methodology of fuzzy modeling of MR dampers has been shown in [87]. Reference [88] presents a numerical study to show the effectiveness of a supervisory fuzzy logic controller for seismic response control of an eight-story base isolated structure effected by translation-torsional motion. Reference [88] applies supervisory fuzzy controller to control two lower level fuzzy controllers. The weight is determined by

$$V_d = \frac{W_N V_N + W_F V_F}{W_N + W_F}, \quad (43)$$

where W_N and W_F are the weighting factors and V_N and V_F are the command voltages. Reference [89] shows that the dynamic fuzzy wavelet NN can precisely forecast structural displacements. Reference [78] had presented wavelet neural network (WNN) model based active nonlinear controller for the response control of 3D buildings subjected to seismic excitation in both x and y directions. The main aim is to control the torsional and lateral motions of 3D irregular structures. The structural responses are predicted using a dynamic fuzzy WNN which is a fuzzy wavelet neuroemulator. Estimation of future time steps is utterly necessary to control the structural responses effectively. This method is essential in determining the magnitude of the required control forces.

4.4.4. Structure Control with Genetic Algorithm. Holland, 1975, was the first to propose the general scheme of genetic algorithm (GA) and uses natural genetic theory to build an optimal search algorithm [90]. A GA can be divided into three parts [91]:

- (1) Code and decode the variables into the strings form.
- (2) Fit each solution string.
- (3) Evaluate strings of the next generation by applying genetic operators.

The aim of the optimization problem is to evaluate the minimum of the performance index:

$$\text{Adaptality} = \begin{cases} J_{\max} - J & \text{if } J < J_{\max} \\ 0 & \text{otherwise.} \end{cases} \quad (44)$$

The applications of the GA method to structural control are published by various researchers. Reference [92] used GA to MR dampers in the reduction of translation-torsion coupled responses of an asymmetric structure. The experiment was carried out at the State Key Lab of Coastal and Off-shore Engineering in Dalian University of Technology. The parameters of the multistate control strategy (MSC) which utilizes the velocity response as the state-switch parameter are optimized by genetic algorithm (GA) method. This MSC is developed in the intention to control torsional seismic response of an asymmetric structure. In their research, also the threshold vector of the MR damper is optimized using genetic algorithm. The parameters from the velocity response and the threshold vector of the MR damper are optimized by the GA method. Reference [93] presents a new neurogenetic algorithm to evaluate the optimal control forces for active control of 3D building structures. It includes geometrical and material nonlinearities, coupling action between lateral and torsional motions, and actuator dynamics. In this case a floating-point GA was used. The methodology used can be categorized as follows: (i) representation of chromosomes, (ii) initial population, (iii) function related to fitness, (iv) selection function, (v) genetic operator, and (vi) termination scheme.

In the investigation mentioned, a nonuniform mutation operator is applied as the genetic operator to evaluate better solution for the new generation. It is expressed by

$$F'_j = \begin{cases} F_j + (F_{\max} - F_j) h(g), & \text{if } r_1 \geq 0.5 \\ F_j & \text{otherwise,} \end{cases} \quad (45)$$

where $j = 1, 2, \dots, N_p$, F_j is j th variable value in the chromosomes related to current population, F'_j is improved value of the same variable related to the new generation, and $h(g)$ is robability function of mutation.

The study results suggest that the new control technique efficiently reduces the response of two irregular 3D building structures under seismic inputs including structures with plan and irregular elevation. The study results suggest that the new control technique efficiently reduces the response

of two irregular 3D building structures under seismic inputs including structures with plan and irregular elevation. Reference [78] develops a new nonlinear control model for the active control of a 3D building structure. The optimal control forces are computed with the floating-point GA. GA can help to decide the positions of the control devices [45]. The coupled torsional-lateral response is attenuated by a semiactive control under bidirectional seismic input. Reference [94] gives a technique of reducing the seismic effects of the spatial structures by the installation of magnetorheological (MR) dampers. It uses small populations to solve the optimization problem embedded in the semiactive control. GA is used to optimize dampers passive parameters and controller gain in [95].

The concept of absorber system with multiobjective optimal design for torsionally coupled earthquake excited structures is presented by [47]. It uses a multiobjective version of GA to extract the design parameters of absorber system. The two branch tournament genetic algorithm as mentioned by [96] extend two-branch tournament GA to three-branch tournament GA and applies to the multiple bjective optimization of the TMD system.

5. Conclusions and Remarks

In this review, the modeling and structural control techniques of building structures subjected to bidirectional earthquake are considered. The main difference with normal structure controllers is the lateral-torsional coupled response. We discuss recent new techniques, methodology, and concepts in this areas. We focus all important results in last two decades in the field of structural engineering with respect to the bidirectional earthquakes.

From the analysis of the above paper, we have the following important observations:

- (1) Most of existing reviews only consider the structure control under unidirectional seismic wave. This review explores the effects of bidirectional seismic waves, which are normal for the real earthquake.
- (2) Real buildings are generally asymmetric in nature to some extent. These criteria induce lateral and torsional vibrations in combination.
- (3) The reduction of translational and torsional response of structures often involves the usage of multiple dampers [97].
- (4) Hybrid control devices are more popular due to their abilities for the seismic vibration along 3-DoF. The authors [47, 98] in their investigation have used hybrid mass damper to control vibration along 3-DoF. The proposed HMD system consists of four HMDs arranged in such a way that this system can control the torsional mode of vibration effectively in addition to the flexure modes of vibration.
- (5) Few papers use sliding mode control to reduce translation-torsion coupled vibration with bidirectional seismic inputs.
- (6) Finding placement of control devices is a challenging task especially for coupled lateral and torsional responses.
- (7) In case of building structures subjected to multiple excitations, the use of online identification technique is better.
- (8) The intelligent control is favored for the structural control, because it does not require system information.

Conflict of Interests

The authors declare that there is no conflict of interests regarding the publication of this paper.

References

- [1] N. R. Fisco and H. Adeli, "Smart structures: part I—active and semi-active control," *Scientia Iranica*, vol. 18, no. 3, pp. 275–284, 2011.
- [2] N. R. Fisco and H. Adeli, "Smart structures: part II—hybrid control systems and control strategies," *Scientia Iranica*, vol. 18, no. 3, pp. 285–295, 2011.
- [3] J. T. P. Yao, "Concept of structural control," *Journal of the Structural Division*, vol. 98, no. 7, pp. 1567–1574, 1972.
- [4] G. W. Housner, L. A. Bergman, T. K. Caughey et al., "Structural control: past, present, and future," *Journal of Engineering Mechanics*, vol. 123, no. 9, pp. 897–971, 1997.
- [5] R. J. McNamara, "Tuned mass dampers for buildings," *Journal of the Structural Division*, vol. 103, no. 9, pp. 1785–1798, 1977.
- [6] B. Donaldson, *Introduction to Structural Dynamics*, Cambridge University Press, Cambridge, UK, 2006.
- [7] F. Yi and S. J. Dyke, "Structural control systems: performance assessment," in *Proceedings of the American Control Conference*, vol. 1, pp. 14–18, IEEE, Chicago, Ill, USA, September 2000.
- [8] E. Cruz and S. Cominetti, "Three-dimensional buildings subjected to bi-directional earthquakes. Validity of analysis considering unidirectional earthquakes," in *Proceedings of the 12th World Conference on Earthquake Engineering*, Auckland, New Zealand, January-Friday 2000.
- [9] J.-S. Heo, S.-K. Lee, E. Park et al., "Performance test of a tuned liquid mass damper for reducing bidirectional responses of building structures," *The Structural Design of Tall and Special Buildings*, vol. 18, no. 7, pp. 789–805, 2009.
- [10] J. Zhang, K. Zeng, and J. Jiang, "An optimal design of bi-directional TMD for three dimensional structure," in *Computational Structural Engineering*, pp. 935–941, Springer, Dordrecht, The Netherlands, 2009.
- [11] J.-L. Lin and K.-C. Tsai, "Seismic analysis of two-way asymmetric building systems under bi-directional seismic ground motions," *Earthquake Engineering and Structural Dynamics*, vol. 37, no. 2, pp. 305–328, 2008.
- [12] A. Forrai, S. Hashimoto, H. Funato, and K. Kamiyama, "Structural control technology: system identification and control of flexible structures," *Computing and Control Engineering Journal*, vol. 12, no. 6, pp. 257–262, 2001.
- [13] J. Zhang and P. N. Roschke, "Active control of a tall structure excited by wind," *Journal of Wind Engineering and Industrial Aerodynamics*, vol. 83, no. 1–3, pp. 209–223, 1999.

- [14] W. K. Tso and T. J. Zhu, "Design of torsionally unbalanced structural systems based on code provisions I: ductility demand," *Earthquake Engineering and Structural Dynamics*, vol. 21, no. 7, pp. 609–627, 1992.
- [15] J. C. Correnza, G. L. Hutchinson, and A. M. Chandler, "Effect of transverse load-resisting elements on inelastic earthquake response of eccentric-plan buildings," *Earthquake Engineering & Structural Dynamics*, vol. 23, no. 1, pp. 75–89, 1994.
- [16] W.-H. Wu, J.-F. Wang, and C.-C. Lin, "Systematic assessment of irregular building–soil interaction using efficient modal analysis," *Earthquake Engineering & Structural Dynamics*, vol. 30, no. 4, pp. 573–594, 2001.
- [17] K.-M. Choi, S.-W. Cho, D.-O. Kim, and I.-W. Lee, "Active control for seismic response reduction using modal-fuzzy approach," *International Journal of Solids and Structures*, vol. 42, no. 16-17, pp. 4779–4794, 2005.
- [18] C.-C. Lin, C.-C. Chang, and J.-F. Wang, "Active control of irregular buildings considering soil-structure interaction effects," *Soil Dynamics and Earthquake Engineering*, vol. 30, no. 3, pp. 98–109, 2010.
- [19] J. C. Anderson and F. Naeim, *Basic Structural Dynamics*, Wiley, Los Angeles, Calif, USA, 2012.
- [20] A. C. Nerves and R. Krishnan, "Active control strategies for tall civil structures," in *Proceedings of the International Conference on Industrial Electronics, Control, and Instrumentation*, vol. 2, pp. 962–967, Orlando, Fla, USA, November 1995.
- [21] A. K. Chopra, *Dynamics of Structures*, Prentice-Hall International Series, Prentice Hall, 2011.
- [22] F. Y. Cheng, *Matrix Analysis of Structural Dynamics: Applications and Earthquake Engineering*, CRC Press, New York, NY, USA, 2000.
- [23] G. C. Hart and K. Wong, *Structural Dynamics for Structural Engineers*, Wiley, 1999.
- [24] B. Wu, J.-P. Ou, and T. T. Soong, "Optimal placement of energy dissipation devices for three-dimensional structures," *Engineering Structures*, vol. 19, no. 2, pp. 113–125, 1997.
- [25] B. F. Spencer Jr. and S. Nagarajaiah, "State of the art of structural control," *Journal of Structural Engineering*, vol. 129, no. 7, pp. 845–856, 2003.
- [26] T. T. Soong and B. F. Spencer Jr., "Supplemental energy dissipation: state-of-the-art and state-of-the-practice," *Engineering Structures*, vol. 24, no. 3, pp. 243–259, 2002.
- [27] S. G. Luca, F. Chira, and V. O. Rosca, "Passive active and semi-active control systems in civil engineering," *Constructiv Arhitectura*, vol. 3-4, pp. 23–32, 2005.
- [28] T. T. Soong, *Active Structural Control: Theory and Practice*, Addison-Wesley, New York, NY, USA, 1999.
- [29] M. C. Constantinou and M. D. Symans, "Seismic response of structures with supplemental damping," *The Structural Design of Tall Buildings*, vol. 2, no. 2, pp. 77–92, 1993.
- [30] J. P. Hartog, *Mechanical Vibrations*, McGraw-Hill, New York, NY, USA, 1956.
- [31] N. B. Desu, S. K. Deb, and A. Dutta, "Coupled tuned mass dampers for control of coupled vibrations in asymmetric buildings," *Structural Control and Health Monitoring*, vol. 13, no. 5, pp. 897–916, 2006.
- [32] K. Xu and T. Igusa, "Dynamic characteristics of multiple substructures with closely spaced frequencies," *Earthquake Engineering & Structural Dynamics*, vol. 21, no. 12, pp. 1059–1070, 1992.
- [33] H.-N. Li and L.-S. Huo, "Seismic response reduction of eccentric structures using tuned liquid column damper (TLCD)," in *Vibration Analysis and Control -New Trends and Development*, InTech, 2011.
- [34] M. J. Hochrainer, C. Adam, and F. Ziegler, "Application of tuned liquid column dampers for passive structural control," in *Proceedings of the 7th International Congress on Sound and Vibration (ICSV '00)*, Garmisch-Partenkirchen, Germany, 2000.
- [35] S. G. Liang, "Experiment study of torsionally structural vibration control using circular tuned liquid column dampers," *Special Structures*, vol. 13, no. 3, pp. 33–35, 1996.
- [36] L. Huo and H. Li, "Torsionally coupled vibration control of eccentric buildings using liquid dampers," in *Active and Passive Smart Structures and Integrated Systems*, vol. 7288 of *Proceedings of SPIE*, 2009.
- [37] C. Fu, "Application of torsional tuned liquid column gas damper for plan-asymmetric buildings," *Structural Control and Health Monitoring*, vol. 18, no. 5, pp. 492–509, 2011.
- [38] T. K. Datta, "A state-of-the-art review on active control of structures," *ISET Journal of Earthquake Technology*, vol. 40, no. 1, pp. 1–17, 2003.
- [39] R. Collins, B. Basu, and B. Broderick, "Control strategy using bang–bang and minimax principle for FRF with ATMDs," *Engineering Structures*, vol. 28, no. 3, pp. 349–356, 2006.
- [40] J. C. H. Chang and T. T. Soong, "Structural control using active tuned mass damper," *Journal of Engineering Mechanics*, vol. 106, no. 6, pp. 1091–1098, 1980.
- [41] C. Li, J. Li, and Y. Qu, "An optimum design methodology of active tuned mass damper for asymmetric structures," *Mechanical Systems and Signal Processing*, vol. 24, no. 3, pp. 746–765, 2010.
- [42] A. Yanik, J. P. Pinelli, and H. Gutierrez, "Control of a three-dimensional structure with magneto-rheological dampers," in *Proceedings of the 11th International Conference on Vibration Problems*, Z. Dimitrovova, J. Almeida, and R. Goncalves, Eds., Lisbon, Portugal, 2013.
- [43] M. R. Jolly, J. W. Bender, and J. D. Carlson, "Properties and applications of commercial magnetorheological fluids," in *Smart Structures and Materials 1998: Passive Damping and Isolation*, vol. 3327 of *Proceedings of SPIE*, pp. 262–275, San Diego, Calif, USA, March 1998.
- [44] J. Yang, J. B. Li, and G. Lin, "A simple approach to integration of acceleration data for dynamic soil-structure interaction analysis," *Soil Dynamics and Earthquake Engineering*, vol. 26, no. 8, pp. 725–734, 2006.
- [45] O. Yoshida and S. J. Dyke, "Response control of full-scale irregular buildings using magnetorheological dampers," *Journal of Structural Engineering*, vol. 131, no. 5, pp. 734–742, 2005.
- [46] F. Yi, S. J. Dyke, J. M. Caicedo, and J. D. Carlson, "Experimental verification of multiinput seismic control strategies for smart dampers," *Journal of Engineering Mechanics*, vol. 127, no. 11, pp. 1152–1164, 2001.
- [47] A. S. Ahlawat and A. Ramaswamy, "Multiobjective optimal FLC driven hybrid mass damper system for torsionally coupled, seismically excited structures," *Earthquake Engineering & Structural Dynamics*, vol. 31, no. 12, pp. 2121–2139, 2002.
- [48] H. Kim and H. Adeli, "Hybrid control of irregular steel highrise building structures under seismic excitations," *International Journal for Numerical Methods in Engineering*, vol. 63, no. 12, pp. 1757–1774, 2005.

- [49] J. M. Angeles-Cervantes and L. Alvarez-Icaza, "3D Identification of buildings seismically excited," in *Proceedings of the 16th IFAC World Congress*, vol. 16, Prague, Czech Republic, 2005.
- [50] V. Gattulli, M. Lepidi, and F. Potenza, "Seismic protection of frame structures via semi-active control: modeling and implementation issues," *Earthquake Engineering and Engineering Vibration*, vol. 8, no. 4, pp. 627–645, 2009.
- [51] J.-L. Lin, K.-C. Tsai, and Y.-J. Yu, "Bi-directional coupled tuned mass dampers for the seismic response control of two-way asymmetric-plan buildings," *Earthquake Engineering & Structural Dynamics*, vol. 40, no. 6, pp. 675–690, 2011.
- [52] B. Zhao and H. Gao, "Torsional vibration control of high-rise building with large local space by using tuned mass damper," *Advanced Materials Research*, vol. 446–449, pp. 3066–3071, 2012.
- [53] M. P. Singh, S. Singh, and L. M. Moreschi, "Tuned mass dampers for response control of torsional buildings," *Earthquake Engineering and Structural Dynamics*, vol. 31, no. 4, pp. 749–769, 2002.
- [54] Y. Tang, "Active control of SDF systems using artificial neural networks," *Computers and Structures*, vol. 60, no. 5, pp. 695–703, 1996.
- [55] R. Alkhatib and M. F. Golnaraghi, "Active structural vibration control: a review," *The Shock and Vibration Digest*, vol. 35, no. 5, pp. 367–383, 2003.
- [56] M. D. Symans and M. C. Constantinou, "Semi-active control of earthquake induced vibration," in *Proceedings of the 11th World Conference on Earthquake Engineering*, Acapulco, Mexico, June 1996.
- [57] A. K. Agrawal and J. N. Yang, "Compensation of time-delay for control of civil engineering structures," *Earthquake Engineering & Structural Dynamics*, vol. 29, no. 1, pp. 37–62, 2000.
- [58] F. Amini and M. R. Tavassoli, "Optimal structural active control force, number and placement of controllers," *Engineering Structures*, vol. 27, no. 9, pp. 1306–1316, 2005.
- [59] O. Ibadapo-Obe, "Optimal actuators placements for the active control of flexible structures," *Journal of Mathematical Analysis and Applications*, vol. 105, no. 1, pp. 12–25, 1985.
- [60] W. Gawronski, "Actuator and sensor placement for structural testing and control," *Journal of Sound and Vibration*, vol. 208, no. 1, pp. 101–109, 1997.
- [61] J. M. Angeles-Cervantes and L. Alvarez-Icaza, "3D identification of seismically excited buildings with sensors arbitrarily placed," in *Proceedings of the American Control Conference*, pp. 3807–3812, Minneapolis, Minn, USA, June 2006.
- [62] S. M. Nigdeli and M. H. Boduroglu, "Active tendon control of torsionally irregular structures under near-fault ground motion excitation," *Computer-Aided Civil and Infrastructure Engineering*, vol. 28, no. 9, pp. 718–736, 2013.
- [63] R. Guclu, "Sliding mode and PID control of a structural system against earthquake," *Mathematical and Computer Modelling*, vol. 44, no. 1-2, pp. 210–217, 2006.
- [64] I. J. Vial, J. C. de la Llera, J. L. Almazán, and V. Ceballos, "Torsional balance of plan-asymmetric structures with frictional dampers: experimental results," *Earthquake Engineering and Structural Dynamics*, vol. 35, no. 15, pp. 1875–1898, 2006.
- [65] O. Yoshida, S. J. Dyke, L. M. Giacosa, and K. Z. Truman, "Experimental verification of torsional response control of asymmetric buildings using MR dampers," *Earthquake Engineering and Structural Dynamics*, vol. 32, no. 13, pp. 2085–2105, 2003.
- [66] C.-M. Chang, B. F. Spencer Jr., and P. Shi, "Multiaxial active isolation for seismic protection of buildings," *Structural Control and Health Monitoring*, vol. 21, no. 4, pp. 484–502, 2014.
- [67] H. Adeli and A. Saleh, "Optimal control of adaptive/smart bridge structures," *Journal of Structural Engineering*, vol. 123, no. 2, pp. 218–226, 1997.
- [68] R. E. Christenson, B. F. Spencer Jr., N. Hori, and K. Seto, "Coupled building control using acceleration feedback," *Computer-Aided Civil and Infrastructure Engineering*, vol. 18, no. 1, pp. 4–18, 2003.
- [69] Y. Du and Z. Lin, "Sequential optimal control for serially connected isolated structures subject to two-directional horizontal earthquake," in *Proceedings of the 8th IEEE International Conference on Control and Automation (ICCA '10)*, pp. 1508–1511, Xiamen, China, June 2010.
- [70] N. K. Chandiramani and G. B. Motra, "Lateral-torsional response control of MR damper connected buildings," in *Proceedings of the International Mechanical Engineering Congress and Exposition (IMECE '13)*, vol. 4, ASME, San Diego, Calif, USA, November 2013.
- [71] R. Zemp, J. C. De La Llera, and J. L. Almazán, "Tall building vibration control using a TM-MR damper assembly," *Earthquake Engineering and Structural Dynamics*, vol. 40, no. 3, pp. 339–354, 2011.
- [72] V. I. Utkin, *Sliding Modes in Control and Optimization*, Springer, Berlin, Germany, 1992.
- [73] T. Fujinami, Y. Saito, M. Morishita, Y. Koike, and K. Tanida, "A hybrid mass damper system controlled by H^∞ control theory for reducing bending-torsion vibration of an actual building," *Earthquake Engineering and Structural Dynamics*, vol. 30, no. 11, pp. 1639–1653, 2001.
- [74] Z. Li and S. Wang, "Robust optimal H_∞ control for irregular buildings with AMD via LMI approach," *Nonlinear Analysis: Modelling and Control*, vol. 19, no. 2, pp. 256–271, 2014.
- [75] T. H. Nguyen, N. M. Kwok, Q. P. Ha, J. Li, and B. Samali, "Adaptive sliding mode control for civil structures using magnetorheological dampers," in *Proceedings of the 23rd International Symposium on Automation and Robotics in Construction*, pp. 636–641, Tokyo, Japan, 2006.
- [76] K. Iwamoto, Y. Koike, K. Nonami, K. Tanida, and I. Iwasaki, "Output feedback sliding mode control for bending and torsional vibration control of 6-story flexible structure," *JSME International Journal, Series C: Mechanical Systems, Machine Elements and Manufacturing*, vol. 45, no. 1, pp. 150–158, 2002.
- [77] J. Ghaboussi and A. Joghataie, "Active control of structures using neural networks," *Journal of Engineering Mechanics*, vol. 121, no. 4, pp. 555–567, 1995.
- [78] X. Jiang and H. Adeli, "Pseudospectra, MUSIC, and dynamic wavelet neural network for damage detection of highrise buildings," *International Journal for Numerical Methods in Engineering*, vol. 71, no. 5, pp. 606–629, 2007.
- [79] K. Bani-Hani and J. Ghaboussi, "Nonlinear structural control using neural networks," *Journal of Engineering Mechanics*, vol. 124, no. 3, pp. 319–327, 1998.
- [80] J.-T. Kim, H.-J. Jung, and I.-W. Lee, "Optimal structural control using neural networks," *Journal of Engineering Mechanics*, vol. 126, no. 2, pp. 201–205, 2000.
- [81] S. Suresh, S. Narasimhan, and S. Nagarajaiah, "Direct adaptive neural controller for the active control of earthquake-excited nonlinear base-isolated buildings," *Structural Control and Health Monitoring*, vol. 19, no. 3, pp. 370–384, 2012.

- [82] N. D. Lagaros, V. Plevris, and M. Papadrakakis, "Neurocomputing strategies for solving reliability-robust design optimization problems," *Engineering Computations*, vol. 27, no. 7, pp. 819–840, 2010.
- [83] N. D. Lagaros and M. Fragiadakis, "Fragility assessment of steel frames using neural networks," *Earthquake Spectra*, vol. 23, no. 4, pp. 735–752, 2007.
- [84] N. D. Lagaros and M. Papadrakakis, "Neural network based prediction schemes of the non-linear seismic response of 3D buildings," *Advances in Engineering Software*, vol. 44, no. 1, pp. 92–115, 2012.
- [85] L. A. Zadeh, "Fuzzy sets," *Information and Control*, vol. 8, no. 3, pp. 338–353, 1965.
- [86] D. A. Shook, P. N. Roschke, P.-Y. Lin, and C.-H. Loh, "Semi-active control of a torsionally-responsive structure," *Engineering Structures*, vol. 31, no. 1, pp. 57–68, 2009.
- [87] D. A. Shook, P. N. Roschke, P.-Y. Lin, and C.-H. Loh, "GA-optimized fuzzy logic control of a large-scale building for seismic loads," *Engineering Structures*, vol. 30, no. 2, pp. 436–449, 2008.
- [88] D. G. Reigles and M. D. Symans, "Supervisory fuzzy control of a base-isolated benchmark building utilizing a neuro-fuzzy model of controllable fluid viscous dampers," *Structural Control and Health Monitoring*, vol. 13, no. 2-3, pp. 724–747, 2006.
- [89] H. Adeli and X. Jiang, "Dynamic fuzzy wavelet neural network model for structural system identification," *Journal of Structural Engineering*, vol. 132, no. 1, pp. 102–111, 2006.
- [90] J. H. Holland, *Adaptation in Natural and Artificial Systems*, MIT Press, 1975.
- [91] C. Camp, S. Pezeshk, and G. Cao, "Optimized design of two-dimensional structures using a genetic algorithm," *Journal of Structural Engineering*, vol. 124, no. 5, pp. 551–559, 1998.
- [92] H.-N. Li and X.-L. Li, "Experiment and analysis of torsional seismic responses for asymmetric structures with semi-active control by MR dampers," *Smart Materials and Structures*, vol. 18, no. 7, Article ID 075007, 2009.
- [93] X. Jiang and H. Adeli, "Neuro-genetic algorithm for non-linear active control of structures," *International Journal for Numerical Methods in Engineering*, vol. 75, no. 7, pp. 770–786, 2008.
- [94] H.-N. Li, Z.-G. Chang, G.-B. Song, and D.-S. Li, "Studies on structural vibration control with MR dampers using μ GA," in *Proceedings of the American Control Conference (AAC '04)*, vol. 6, pp. 5478–5482, Boston, Mass, USA, July 2004.
- [95] Y. Arfiadi and M. N. S. Hadi, "Passive and active control of three-dimensional buildings," *Earthquake Engineering and Structural Dynamics*, vol. 29, no. 3, pp. 377–396, 2000.
- [96] W. A. Crossley, A. M. Cook, D. W. Fanjoy, and V. B. Venkayya, "Using the two branch tournament genetic algorithm for multiobjective design," *AIAA Journal*, vol. 37, no. 2, pp. 261–267, 1999.
- [97] H.-N. Li and L.-S. Huo, "Optimal design of liquid dampers for torsionally coupled vibration of structures," *Intelligent Control and Automation*, vol. 5, pp. 4535–4538, 2004.
- [98] L.-S. Fur, H. T. Y. Yang, and S. Ankireddi, "Vibration control of tall buildings under seismic and wind loads," *Journal of Structural Engineering*, vol. 122, no. 8, pp. 948–957, 1996.

Research Article

Modeling and Simulation of Flexible Transmission Mechanism with Multiclearance Joints for Ultrahigh Voltage Circuit Breakers

Fangang Meng, Shijing Wu, Fan Zhang, Zenglei Zhang, Jicai Hu, and Xiaoyong Li

School of Power and Mechanical Engineering, Wuhan University, Wuhan 430072, China

Correspondence should be addressed to Shijing Wu; 76811886@qq.com

Received 20 April 2015; Accepted 3 August 2015

Academic Editor: Salvatore Strano

Copyright © 2015 Fangang Meng et al. This is an open access article distributed under the Creative Commons Attribution License, which permits unrestricted use, distribution, and reproduction in any medium, provided the original work is properly cited.

The transmission mechanism, of which the dynamic characteristics determine the reliability of the circuit breaker, is the principal component of the ultrahigh voltage (UHV) circuit breaker. The characteristics of transmission mechanism are quick motion, high sensibility, and high reliability. The transmission mechanism with multiclearance joints present strong non-linear vibration feature which strongly affects the reliability of the UHV circuit breaker. In this investigation, a planar rigid-flexible coupling model of the transmission mechanism considering the clearance joints and the flexibility of components is established by using ADAMS software. The dynamic contact model in clearance joints is performed, based on clearance vector model of clearance joint. Then, the reliability of the model is proved by means of comparing the results of experiments. The simulation results show that the dynamic response of the mechanism is greatly influenced by the clearance and the flexibility of components has a role of suspension for the mechanism. Moreover, the influence of the clearance size, input speed, and number of clearance joints on the dynamic characteristics of the mechanism are also investigated.

1. Introduction

The ultrahigh voltage (UHV) circuit breaker is a device for protecting and controlling UHV transmission and distribution network. The main function of the UHV circuit breaker is that, when the signal of opening or closing is received, it disconnects or connects circuit with accuracy, efficiency, and stability in order to control and protect the grid. The transmission mechanism, of which the dynamic characteristics determine the reliability of the circuit breaker, is the principal component of the UHV circuit breaker. Compared with the driving mechanism of a low voltage circuit breaker, the transmission mechanism has a more complicated process, suffers heavier loads, and has a higher speed of moving contact. According to statistics, the mechanical failure of transmission mechanism accounted for 63.8% of all high voltage circuit breaker failures [1]. Therefore, the operation stability and reliability of UHV circuit breaker are directly determined by the performances of the transmission mechanism.

Lots of research works have been done on the circuit breaker by many domestic and foreign scholars, mainly focusing on the broken arc, the power source (hydraulic system and spring system), and the simulation research of the control circuit [2–6], while little attention had been paid to the dynamic characteristics of the transmission mechanism. The components of the transmission mechanism are mostly connected by hinges, while the clearance of the articulated kinematic pair is inevitable due to the assembling, manufacturing error and wear, and so forth [7–9]. The impact and collision caused by the clearance can result in vibration and noise of the mechanism, exacerbating mechanism wear and reducing mechanism kinematic accuracy, efficiency, and service life especially for high speed heavy haul mechanism [10].

Dynamic characteristic of mechanism is becoming one key concern of domestic and abroad mechanical engineering [11, 12]. Over the last few decades, there are many scholars who have done a great deal of researches on the dynamic analysis of slider-crank or four-bar mechanisms with imperfect

joints by using theoretical and experimental approaches. Flores et al. studied the influence of different contact force laws in the revolute joint with clearance on the dynamic responses of mechanism [12, 13]. Khemili and Romdhane were interested in the study of the dynamic behavior of a planar flexible slider-crank mechanism with clearance; simulation and experimental tests were carried out for this goal [14]. The simulation and experimental result show that, in the presence of clearance, the coupler flexibility has role of suspension for the mechanism. Muvengei et al. numerically investigated the parametric effects of differently located frictionless revolute clearance joints on the overall dynamic characteristics of a typical slider-crank mechanism [15]. The simulation results reveal that the dynamic behavior of one clearance revolute joint cannot be used as a general case for a mechanical system. Megahed and Haroun established a model for a slider-crank mechanism considering multiple clearance joints, which was incorporated into ADAMS for conducting the dynamic simulation [16]. Bauchau and Rodriguez investigated the dynamic characteristics of clearance and flexibility on the dynamic response of the mechanism by establishing the dynamic equations based on the nonlinear dynamic theory [17]. Tian et al. studied the elasticity of the connecting links in mechanisms with clearance using all absolute nodal coordinate formulation based on Lankarani and Nikravesh's continuous force law and Coulomb's friction law [18, 19].

In most of previous works, the research object was only a simple slider-crank mechanism or four-bar mechanism. Also, the dynamic model of a mechanism with clearance has always considered one revolute clearance joint and neglected the flexibility of components, because considering more than one clearance joint and the flexibility of mechanism will make the dynamic analysis more complex. In this work, a planar rigid-flexible coupling dynamic model of high speed multilink transmission mechanisms with clearance for ultrahigh voltage circuit breaker (1100 kv) is proposed using ADAMS software, based on the nonlinear continuous contact theory and the modified Coulomb friction model. Moreover, the elastic behavior of the collided bodies also is considered.

After an introduction, this paper is organized as follows. The physical structure and principle of the transmission mechanism with multiclearence joint for UHV are described briefly in Section 2. A contact force model based on clearance vector model of clearance joint is established in Section 3. The dynamic model of the transmission mechanism with multiclearence joint is established, and the reliability of the model under ADAMS is validated by experimental test in Section 4. Numerical simulations of the dynamic model are described and detailed discussion of the obtained results is presented in Section 5. Finally, the rigid-flexible model for the transmission mechanism of UHV is summarized and the conclusions are also outlined in Section 6.

2. Description of the Transmission Mechanism

As shown in Figure 1, the transmission mechanism of the UHV circuit breaker which completes on/off action is a multilink combination mechanism used to transmit force and motion. Driving link 1 is directly used to input the driving

TABLE 1: Parameters of the components in the mechanism.

Body	Length L_i (m)	Mass M_i (kg)	Moment of inertia I_i (kg·m ²)
1	0.250	3.670	0.044
2	0.248	3.720	0.015
3	0.230	56.92	0.200
4	0.210	4.760	0.010
5	0.492	12.06	0.090
6	0.900	81.54	0.051
7	0.480	25.66	0.120
8	0.280	13.25	0.027
9	0.714	5.420	0.038

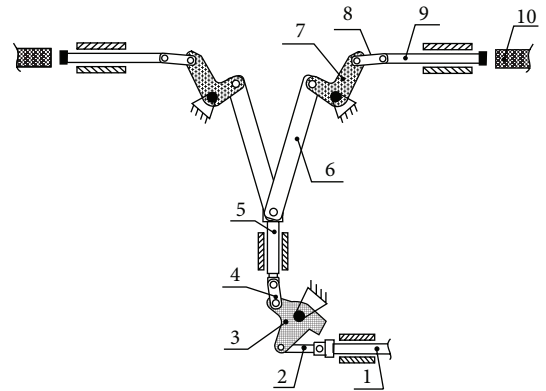


FIGURE 1: Transmission mechanism of the ultrahigh voltage circuit breaker. 1: driving link, 2: lower linkage, 3: lower turn arm, 4: lower linking board, 5: seal pole, 6: insulating pole, 7: upper turn arm, 8: upper linking board, 9: moving contact, and 10: static contact.

force. Insulation pole 6 is used to cut off the current. The transmission components between insulation pole 6 and moving contact 9 are located in the arc quenching chamber of the UHV circuit breaker. The horizontal stroke (input displacement) of driving link 1 is 230 mm while the horizontal stroke (output displacement) of the moving contact is 280 mm. The closing time is 85 ms and the opening time is 40 ms during the opening and closing process of the UHV circuit breaker; thus the velocity of the transmission mechanism is so high that the instantaneous velocity can even reach up to 20 m/s. The components of the transmission mechanism above seal pole 5 have some symmetry. The right side of the mechanism is a 9-linkage planar mechanism with one degree of freedom that has three shifting pairs and ten revolute pairs. The characteristics parameters of each component of the mechanism are listed in Table 1 and the schematic diagram of the transmission mechanism with multiclearence joints is shown as in Figure 2.

3. Contact Force Model of Clearance Joint

3.1. Definition of Clearance Joints. It is assumed that the positional tolerance of the revolute joint is neglected. A revolute joint with clearance is shown in Figure 3. The difference in

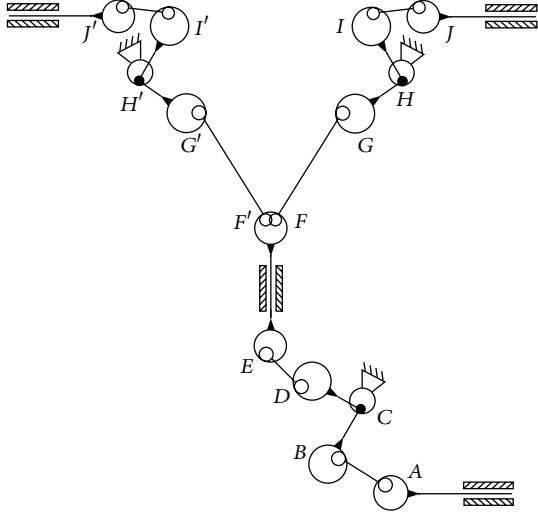


FIGURE 2: Schematic diagram of the transmission mechanism with multiclearance joints.

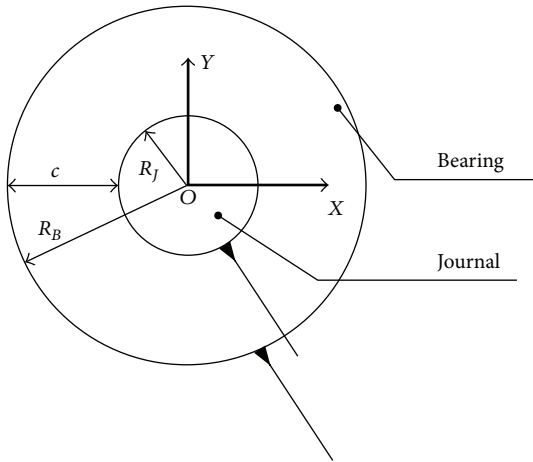


FIGURE 3: Schematic diagram of revolute joint with clearance.

radius between the bearing and the journal represents the size of the radial clearance.

Although a revolute joint with clearance does not constrain any degree of freedom from the mechanism, it introduces some kinematic constraints. This limits the journal to move within the bearing boundaries. Therefore, two kinematic constraints are removed and two extra degrees of freedom are introduced instead in a revolute clearance joint.

The difference in radius between the bearing and the journal is as follows:

$$c = R_B - R_J, \quad (1)$$

where R_B and R_J represent the radius of bearing and journal.

Figure 4 depicts the three different types of motion between the bearing and journal during dynamics of the realistic revolute joint with clearance: (a) free flight mode,

in which the journal and bearing are not in contact and the journal moves freely within the bearing boundaries, (b) impact mode, which presents at the end of the free flight mode, and (c) continuous contact mode; that is, contact is always maintained, despite the relative penetration depth between the bearing and journal.

Where O_i and O_j are the centers of bearing and journal, \mathbf{r}_i and \mathbf{r}_j represent the position vectors of bearing and journal in the global inertia coordinate. Thus, clearance vector can be given by

$$\mathbf{e}_{ij} = \mathbf{r}_i - \mathbf{r}_j, \quad (2)$$

where \mathbf{e}_{ij} represents the eccentric vector of journal relative to bearing. So the eccentricity of bearing and journal can be described as

$$e_{ij} = \sqrt{e_x^2 + e_y^2}. \quad (3)$$

The unit normal vector at the contact point of the bearing and journal is represented as

$$\mathbf{n} = \frac{\mathbf{e}_{ij}}{e_{ij}}. \quad (4)$$

Figure 4(c) describes the relative penetration depth between the bearing and journal, which are represented in global coordinate system. The penetration depth caused by collision between bearing and journal can be stated as follows:

$$\delta = e_{ij} - c. \quad (5)$$

3.2. Normal Force Model of Clearance Joint. For the modeling of the contact, the contact method based on the INPACT function is used to model. In this method, the contact force from the INPACT function is calculated by the ADAMS function library. The contact force is essentially modeled as a non-linear spring-damper. From the simulations, ADAMS/Solver can give a continuous flow of responses, including accelerations, velocities, positions, and forces from all the elements and points of contact. This continuous contact force model is widely used for contact-impact process of mechanism system with joint clearance [10, 14].

It is clear that the normal contact model in ADAMS can be expressed as

$$F_n = \begin{cases} 0 & \delta \leq 0 \\ K\delta^n + D\dot{\delta} & \delta > 0, \end{cases} \quad (6)$$

where $K\delta^n$ represents the elastic deformation force, $D(\delta)\dot{\delta}$ represents the energy dissipation, δ is the penetration depth, and $\dot{\delta}$ is the relative impact velocity. The exponent of the force deformation characteristic, n , depends on the material of the contact surfaces (n is set to 1.5 for metallic material) [20]. $D(\delta)$

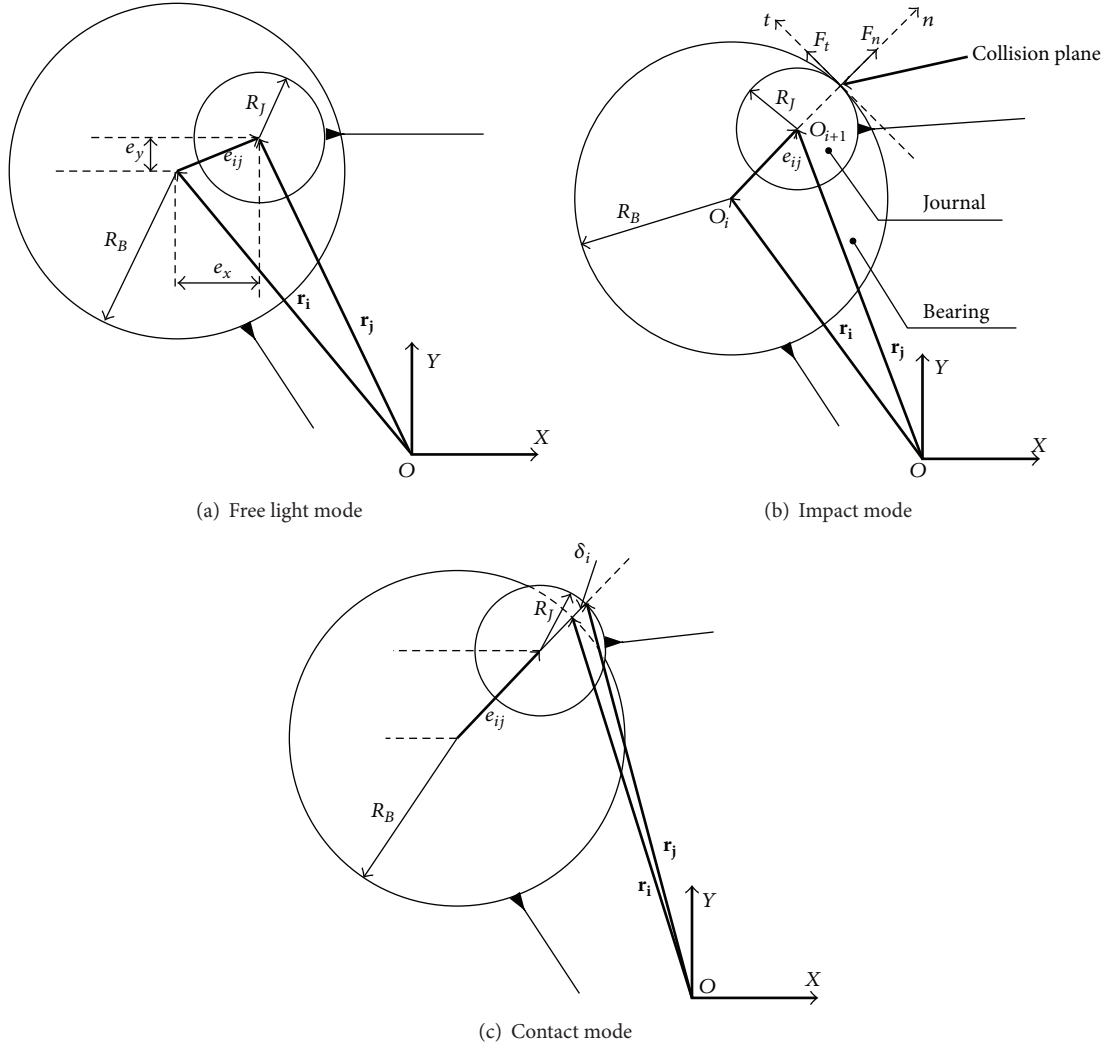


FIGURE 4: Realistic revolute joint with clearance.

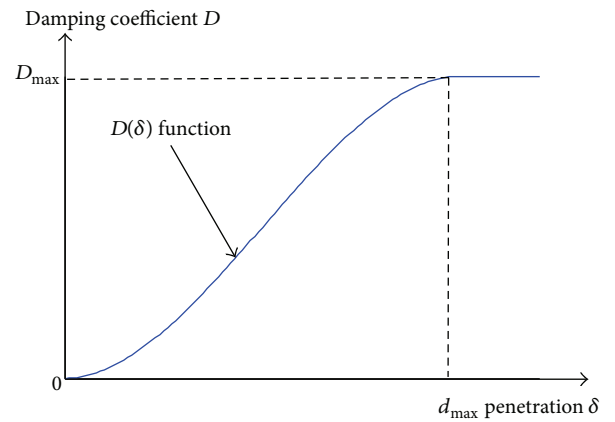
is the instantaneous damping coefficient, which can be given by

$$D(\delta) = \begin{cases} 0 & \delta \leq 0 \\ D_{\max} \left(\frac{\delta}{d_{\max}} \right)^2 \left(3 - 2 \frac{\delta}{d_{\max}} \right) & 0 < \delta \leq d_{\max} \\ D_{\max} & \delta > d_{\max} \end{cases} \quad (7)$$

where D_{\max} is the maximum value of the damping coefficient, d_{\max} is the maximum value of penetration depth, and $D(\delta)$ is a function with respect to D_{\max} , δ , and d_{\max} , as shown in Figure 5. One has

$$H_{\text{avg}} = \frac{2K(1-r^2)}{4\delta^*}, \quad (8)$$

$$D_{\max} = H_{\text{avg}} d_{\max}^n.$$

FIGURE 5: $D(\delta)$ function.

The maximum damping coefficient D_{\max} is calculated using (8), and more accurate values of D_{\max} can be obtained by updating the values of D_{\max} and δ^* using numerical iteration till the value of D_{\max} is stabilized.

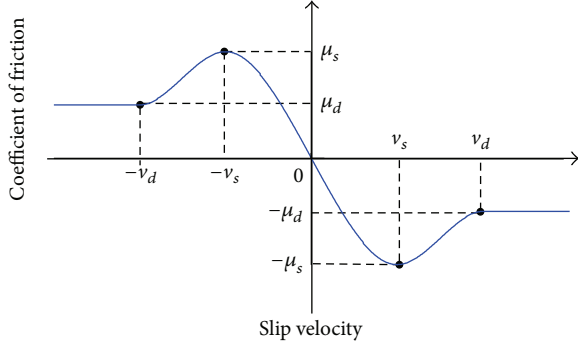


FIGURE 6: Coefficient of friction versus slip velocity.

The stiffness parameter K can be calculated as follows:

$$K = \frac{4}{3(\sigma_1 + \sigma_2)} \left[\frac{R_1 R_2}{R_1 + R_2} \right]^{1/2},$$

$$\sigma_i = \frac{(1 - \nu_i^2)}{E_i} \quad (i = 1, 2), \quad (9)$$

$$\frac{1}{E^*} = \frac{(1 - \nu_1^2)}{E_1} + \frac{(1 - \nu_2^2)}{E_2},$$

where R_1 and R_2 represent, respectively, the radii of bearing and journal, ν_i is Poisson's ratio, and E_i is Yong's modulus for element i .

$$\mu(v_t) = \begin{cases} -\mu_d \operatorname{sign}(v_t) & \text{for } |v_t| > v_d \\ -\left\{ \mu_d + (\mu_s - \mu_d) \left(\frac{|v_t| - v_s}{v_d - v_s} \right)^2 \left[3 - 2 \left(\frac{|v_t| - v_s}{v_d - v_s} \right) \right] \right\} \operatorname{sign}(v_t) & \text{for } v_s < |v_t| < v_d \\ -\mu_s - 2\mu_s \left(\frac{v_t + v_s}{2v_s} \right)^2 \left(3 - \frac{v_t + v_s}{v_s} \right) & \text{for } |v_t| < v_s, \end{cases} \quad (12)$$

where v_d is maximum critical velocity of the kinetic friction, v_s is critical velocity of static friction, μ_d is kinetic friction coefficient, and μ_s is static friction coefficient. The function curve of kinetic friction coefficient can be described as in Figure 6.

4. Modeling of the Mechanism with Clearance and Experimental Verification

4.1. Dynamic Model of Transmission Mechanism of UHV with Clearance. The high speed multilink transmission mechanism of UHV with multiclearence joint was established under ADAMS, as shown in Figure 7. During the dynamic simulation of ADAMS, it is assumed that the revolute joints with clearance are studied under the condition of dry lubrication, and no wear occurs at the joints. The insulating pole, upper turn arm, upper linking board, and t moving contact

The expression of nonlinear continuous contact force model is expressed as follows:

$$F_n = \begin{cases} 0 & \delta \leq 0 \\ K\delta^n + D\dot{\delta} & \delta > 0. \end{cases} \quad (10)$$

3.3. Friction Force Model of Clearance Joint. In this paper, the tangential contact force of clearance is calculated using the modified Coulomb friction model [21]. Friction coefficient of the modified Coulomb friction model is function of tangential sliding velocity, which can avoid the abrupt change of friction in the course of numerical calculating as the change of velocity direction. And, also, the modified Coulomb friction induces the viscous and microslip phenomenon in relative motion more accurately.

The tangential contact forces model can be represented by

$$F_t = -\mu(v_t) F_n \frac{v_t}{|v_t|}, \quad (11)$$

where v_t is sliding velocity in tangential direction at the collision point of journal and bearing, that is, the velocity component in tangential direction.

$\mu(v_t)$ is friction coefficient, which can be expressed as

are flexible, which are established under the finite element software HYPERMESH for obtaining their eigenfrequencies and eigenmodes (Figure 8). The material properties of the flexible components are presented in Table 2. Moreover, the first twelve modes with corresponding natural frequencies are chosen for the simulation of dynamics of the rigid-flexible coupling mechanism with clearance. The modal neutral files (.mnf) of flexible components are exported into the ADAMS to connect with other rigid components of the mechanism. The rigid-flexible coupling model of transmission mechanism with multiclearence joints under ADAMS can obtain more accurate dynamic responses of the mechanism.

In order to obtain the best numerical results, the Gear Stiff (GSTIFF) integrator is chosen, which uses a backwards differentiation formula (BDF) to integrate differential and algebraic standard index-three equations. It provides good solutions for simulations of stiff models (models with a mix of high and low frequencies) using modified Newton-Raphson

The transmission mechanism of UHV with multiclearance joint modeled under ADAMS

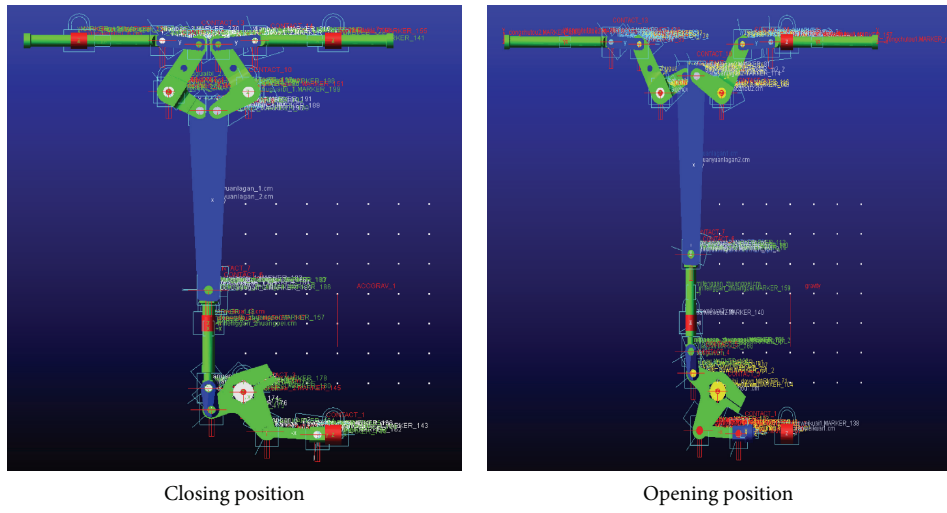


FIGURE 7: Transmission mechanism modeled in ADAMS.

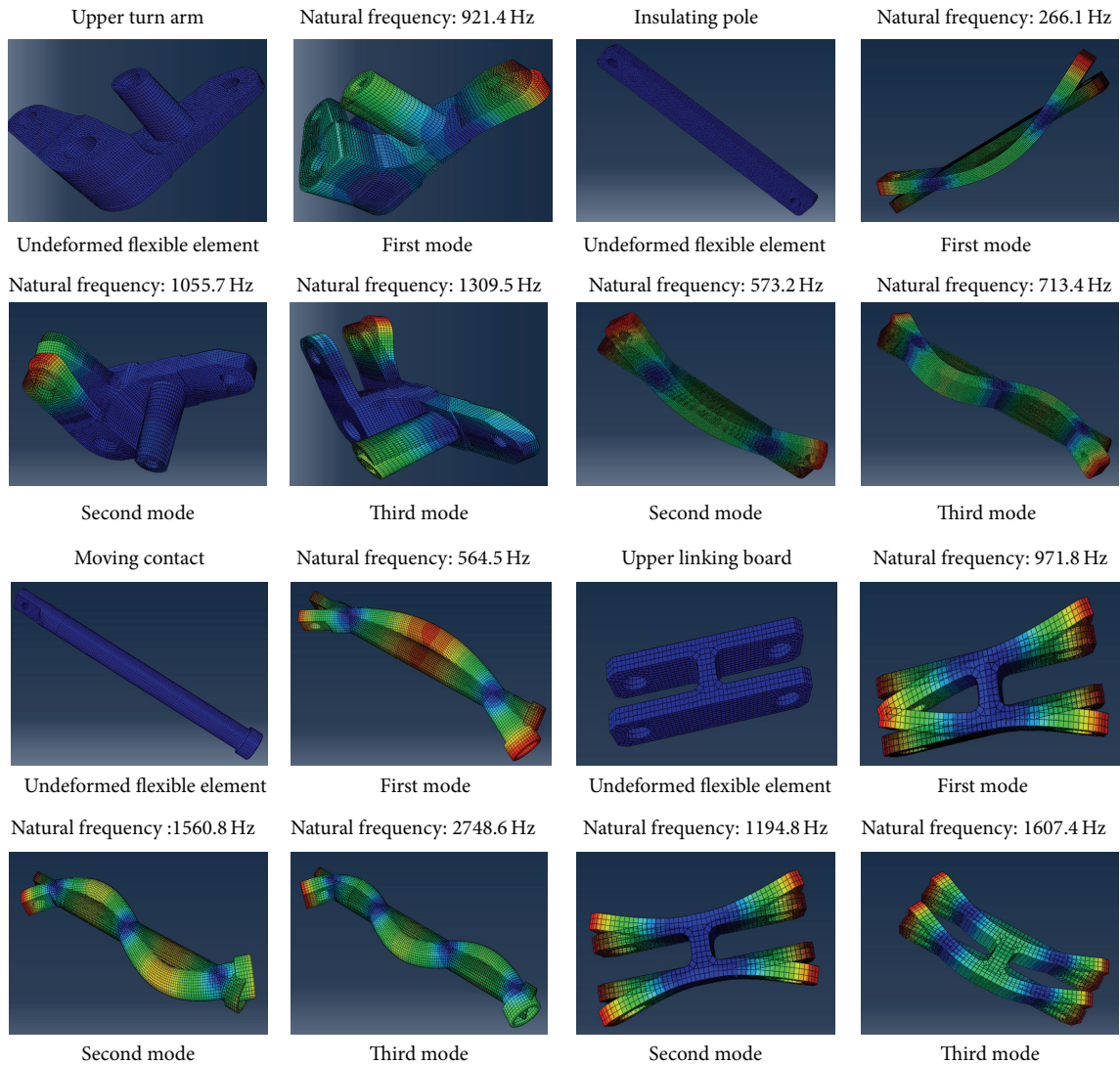


FIGURE 8: Flexible coupler: eigenfrequencies and eigenmodes computation.

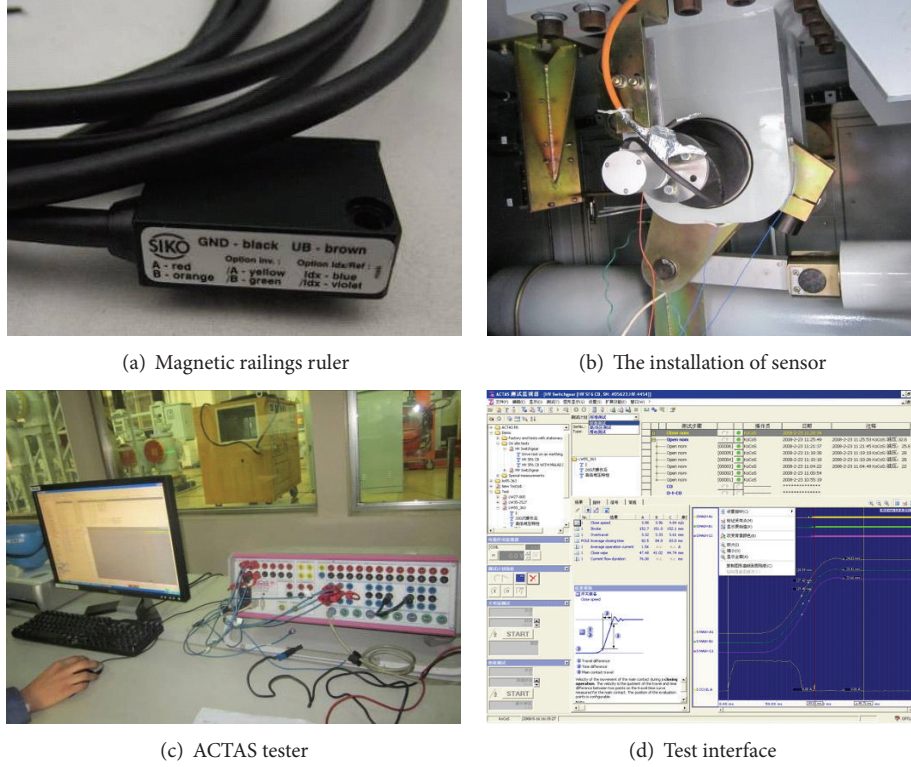


FIGURE 9: Experimental test system.

TABLE 2: The material properties of the flexible components.

Flexible components	Modulus of elasticity (Pa)	Poisson's ration	Density (kg/m^3)
Insulating pole	1.03×10^{12}	0.3	7600
Upper turn arm	2.11×10^{12}	0.25	7850
Upper linking board	2.11×10^{12}	0.277	7850
Moving contact	2.13×10^{12}	0.286	7870

iterative algorithm in the numerical integrating of the difference equation [22]. The maximum number of the iterations allowed for the solution of the nonlinear equations using Newton-Raphson method to converge is ten. The integrator formulation (SII) has been chosen for the selected integration method (GSTIFF) since it takes the constraint derivatives into account when solving the equations of motion and monitors the integration error on the impulse of the Lagrange Multipliers in the system. The contact model of Section 3 is incorporated into ADAMS, which is used to simulate the clearance joint. The simulation characteristics are listed in Table 3.

4.2. Experimental Verification. The experimental test system is shown in Figure 9. The displacement of seal pole is measured by using magnetic railings ruler, which can reduce the negative impact of mechanical vibration on the experimental test. The rotational angular velocity of lower turn arm is measured by using ROS Photoelectric Rotating-Speed Sensor, which can avoid the influence of extra load on

TABLE 3: Simulation characteristics.

Stiffness coefficients K (N/m)	3.81×10^7
Force exponent n	1.5
Damping coefficient D (N·s/m)	3.81×10^5
Normal maximum penetration δ_{\max} (m)	1.0×10^{-5}
Static friction coefficient μ_s	0.2
Dynamic friction coefficient μ_d	0.16
Stiction translation velocity v_s (m/s)	1.0×10^{-4}
Friction translation velocity v_d (m/s)	1.0×10^{-2}
Radius of the solids in contact R (m)	0.05
Modulus of elasticity E (Pa)	2.07×10^{11}
Poisson's ratio μ	0.3
Density ρ (kg/m^3)	7.8×10^3
Max. number of iteration	100
Initial time step	1.0×10^{-7}
Max. time step	1.0×10^{-3}
Min. time step	1.0×10^{-9}
Accuracy	1.0×10^{-7}
Jacobian pattern	100%

the experimental test. Then German's ACTAS tester was used for treatment of experimental data, which can confirm high accuracy and reliability on the treatment of experimental data for its high accuracy and linear frequency responses under various complex electromagnetic environments.

Figure 11 shows a comparison between the experimental and the simulation results. During the dynamic simulation,

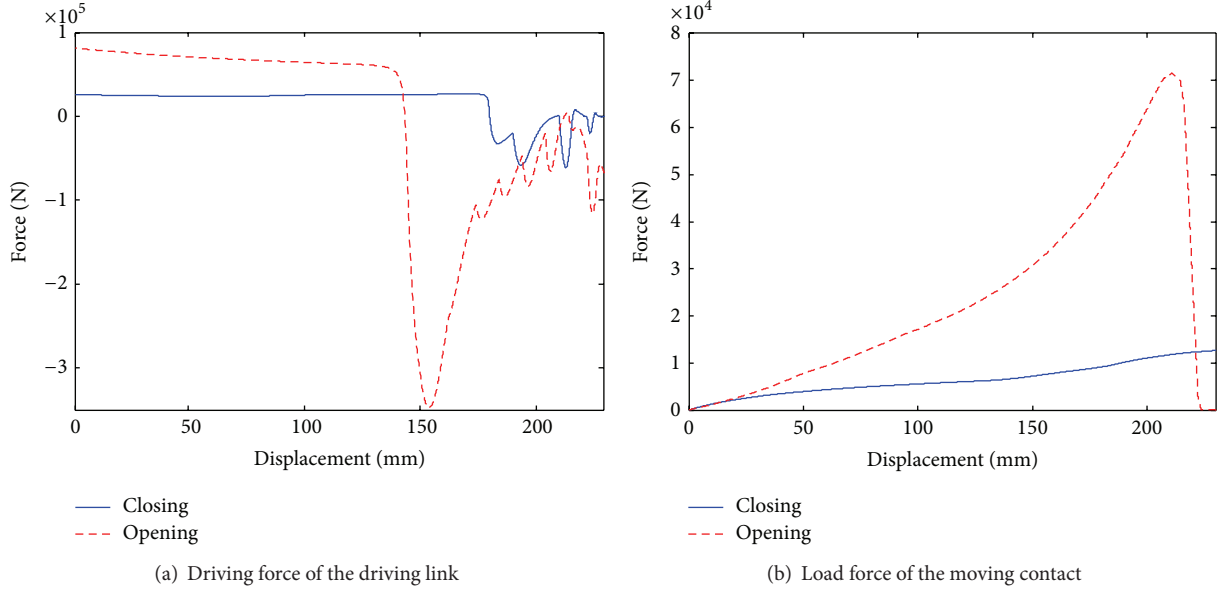


FIGURE 10: Driving force and load force.

the driving force of the driving link and the load force of the moving contact can be expressed as in Figure 10. The revolute joints *A* and *B* (Figure 2) of the rigid-flexible coupling model were modeled as clearance joints and others are ideal revolute joints. The clearance size of the revolute joint is set to be 0.1 mm for the present work, which is supported by manufacturing error and assemblage. It is shown that the simulation and experimental results are in good agreement.

5. Result and Discussion

In order to study the dynamic characteristics of transmission mechanism with multclearance joints, the STEP5 function in ADAMS is selected as input function of motion. The STEP5 function provides approximation to the Heaviside step function with a quintic polynomial, which can meet the requirements for input displacement and closing time of transmission mechanism.

The format defining the STEP5 function is

$$\text{STEP5}(x, x_0, h_0, x_1, h_1), \quad (13)$$

where x is the independent variable, x_0 and x_1 are real variables that specify the x value at which the STEP5 function begins and ends, respectively, and h_0 and h_1 are the initial and final value of the step.

The equation defining the STEP5 function is

$$\alpha = h_1 - h_0,$$

$$\Delta = \frac{(x - x_0)}{(x_1 - x_0)},$$

STEP5

$$= \begin{cases} h_0 & x \leq x_0 \\ h_0 + \alpha \Delta^3 [10 - 15\Delta + 6\Delta^2] & x_0 < x \leq x_1 \\ h_1 & x > x_1. \end{cases} \quad (14)$$

During the dynamic simulation, the motion time of the mechanism is 0.085 s and the input stroke is 230 mm; therefore, the input function STEP5 can be set as

$$\text{STEP5}(\text{time}, 0, 0, 0.085, 230). \quad (15)$$

The input displacement of motion and corresponding input velocity can be described as in Figure 12.

5.1. Dynamic Responses Based on the Rigid Model of the Transmission Mechanism with Clearance. During the dynamic simulation, the revolute joints *A* and *J* (Figure 2) of the rigid-flexible coupling model are modeled as clearance joints and others are ideal revolute joints. The clearance size of the revolute joint is set to 0.1 mm, while the simulation time duration is 0.085 s. The displacement, velocity, and acceleration of the moving contact for rigid model are shown in Figure 13.

As can be observed from Figure 13, the effects of clearance on acceleration of transmission mechanism are severer than the effects of clearance on displacement and velocity. The displacement and velocity of the transmission mechanism with clearance are generally consistent with those without clearance. The deviation value of the output stroke of the moving contact is 0.1 mm. The existence of clearance leads to oscillating and time delay of the velocity. Remarkably, the existence of clearance induces the high-frequency shake of

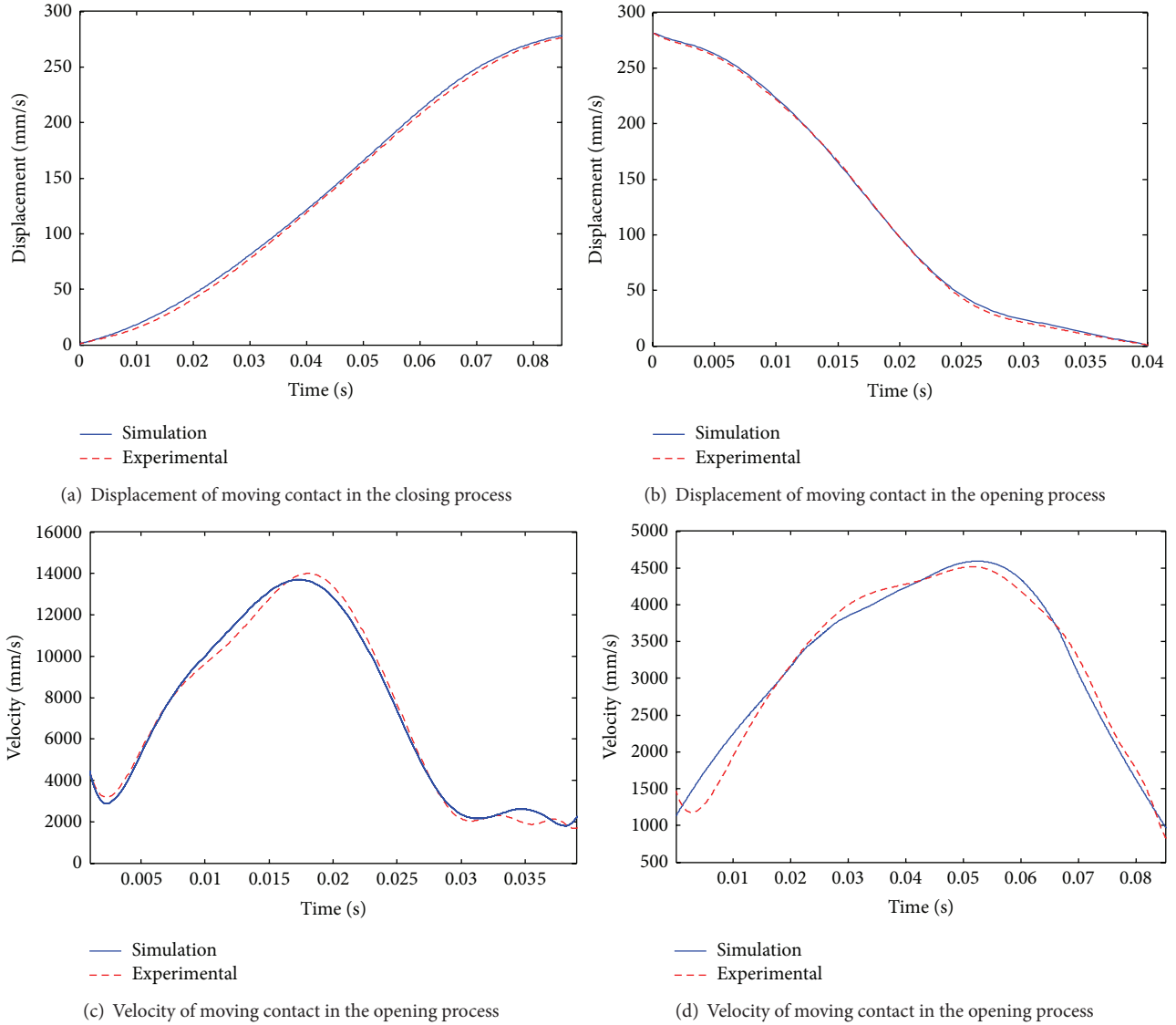


FIGURE 11: Simulation and experimental results.

acceleration, and the maximum value of acceleration of the mechanism is 2.29 times more than that of the mechanism without clearance. It is clear that the existence of the clearance joint has an important effect on the dynamic response of the mechanism, and the clearance joint must be considered for reliable analysis of the mechanisms.

5.2. *Dynamic Responses Based on the Rigid-Flexible Coupling Model of Transmission Mechanism with Clearance.* In order to highlight the effect of flexibility, the same simulation characteristics as in the case of the rigid transmission mechanism are chosen. The displacement, velocity, and acceleration of the moving contact for rigid-flexible coupling model are shown in Figure 14.

As can be seen from Figure 14, the displacement and velocity of the transmission mechanism with clearance are

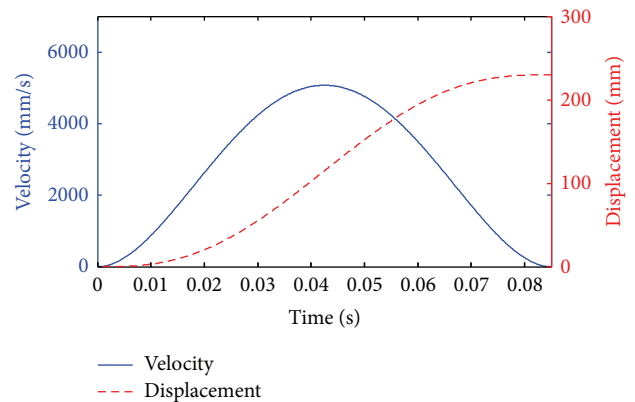


FIGURE 12: Characteristics of the input displacement and velocity (STEP5).

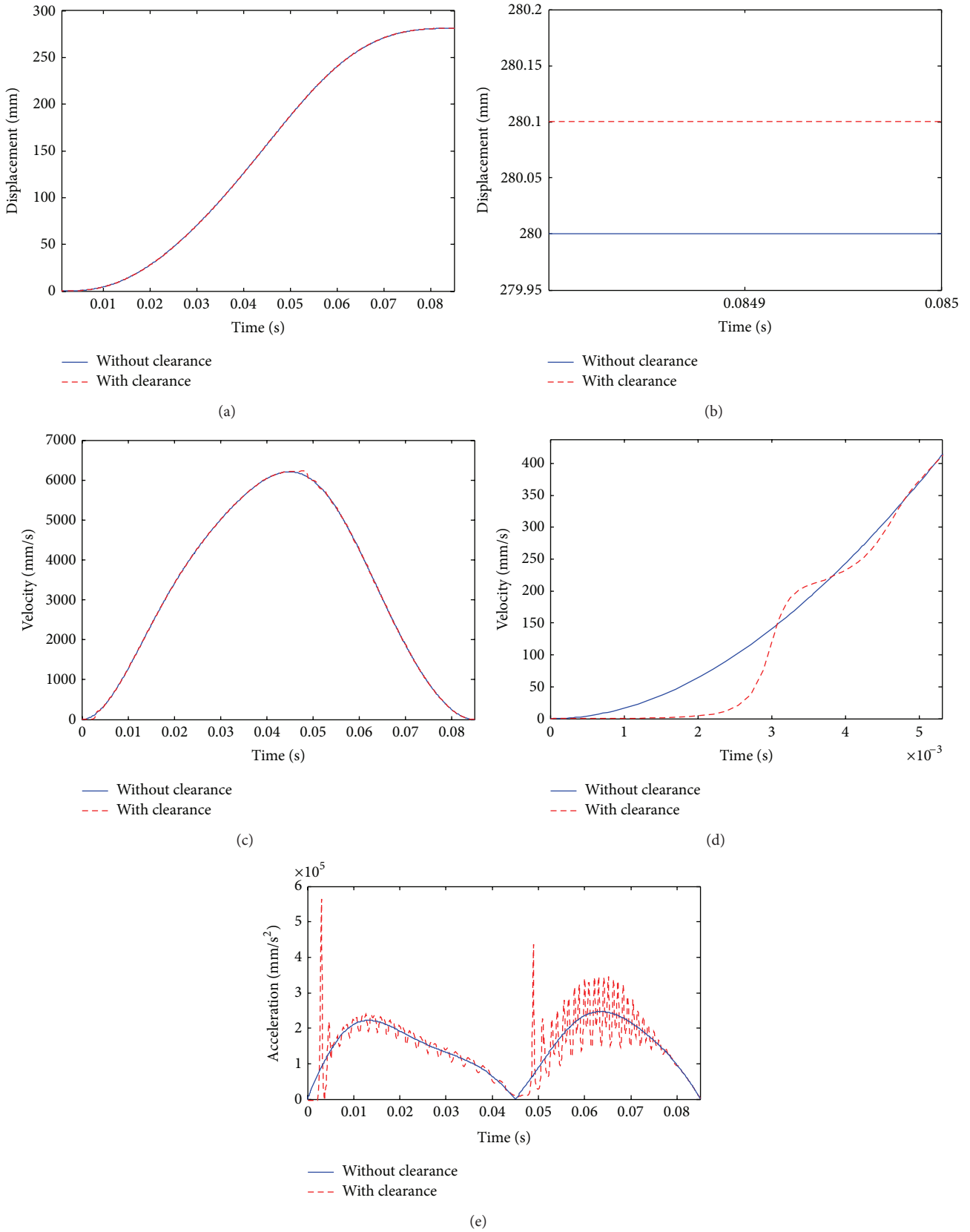


FIGURE 13: Responses based on the rigid model with clearance: (a) displacement, (b) enlarged drawing of displacement, (c) velocity, (d) enlarged drawing of velocity, and (e) acceleration.

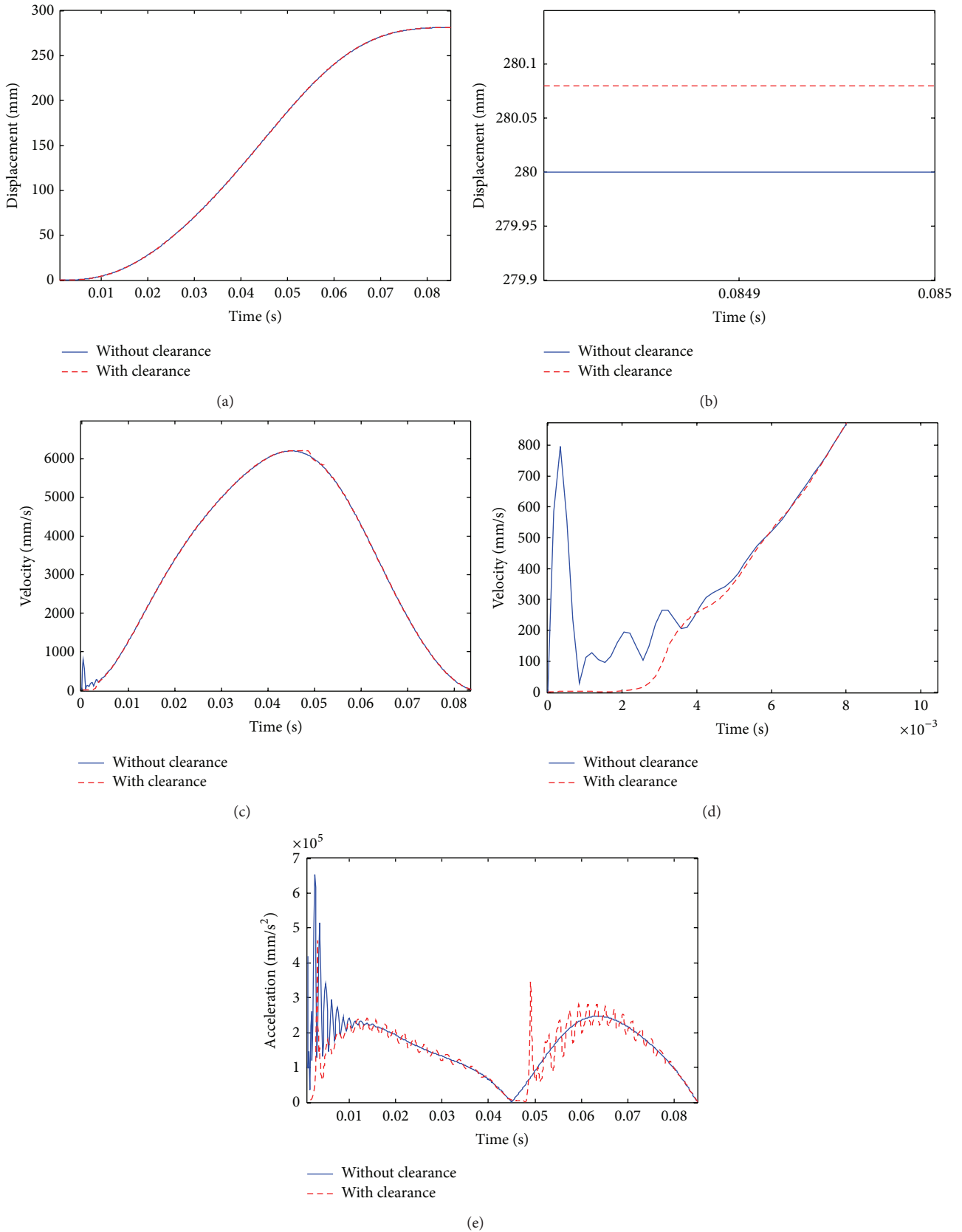


FIGURE 14: Responses based on the rigid-flexible coupling model with clearance: (a) displacement, (b) enlarged drawing of displacement, (c) velocity, (d) enlarged drawing of velocity, and (e) acceleration.

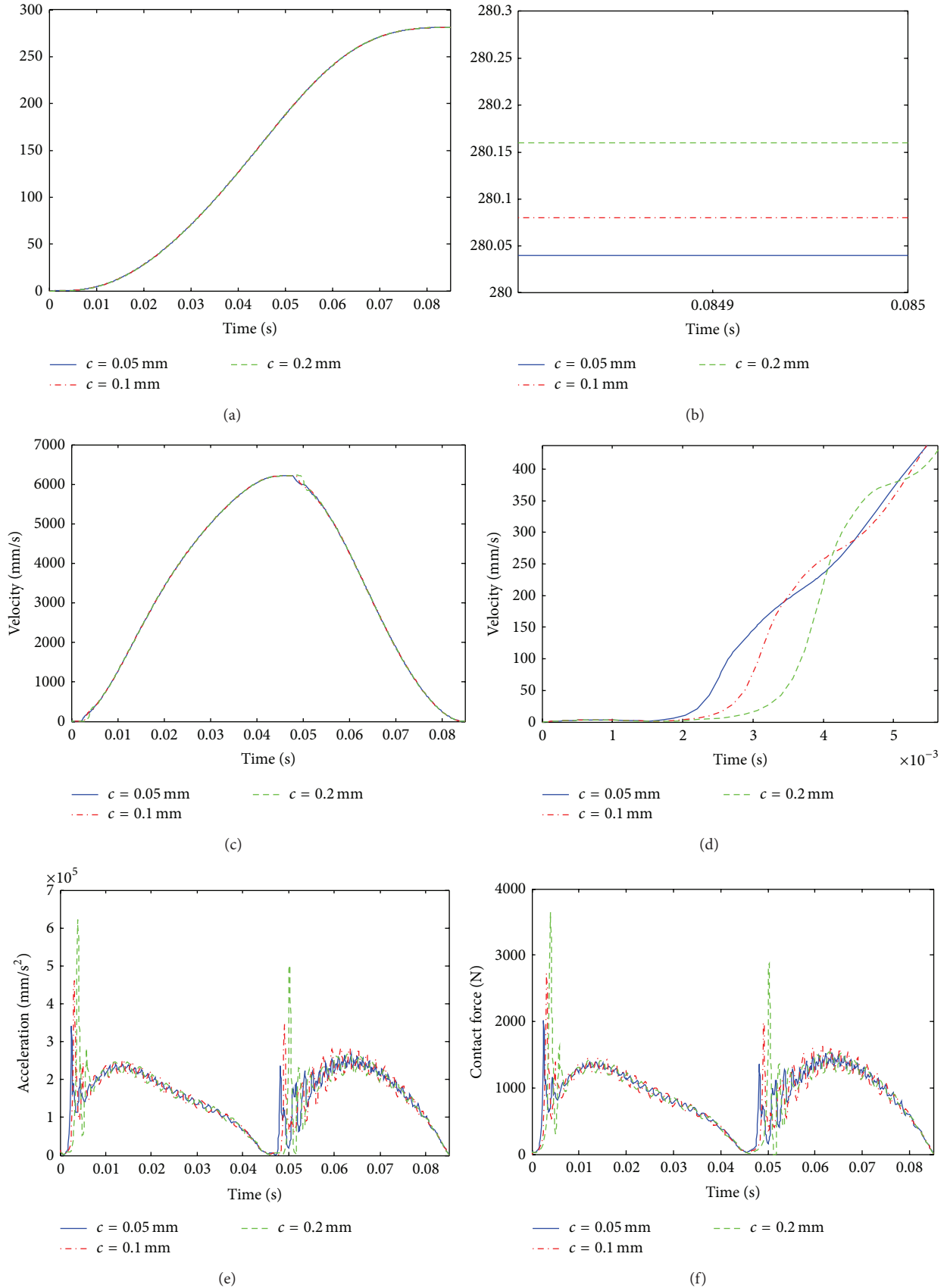


FIGURE 15: Responses for different clearance sizes: (a) displacement, (b) enlarged drawing of displacement, (c) velocity, (d) enlarged drawing of velocity, (e) acceleration, and (f) contact force.

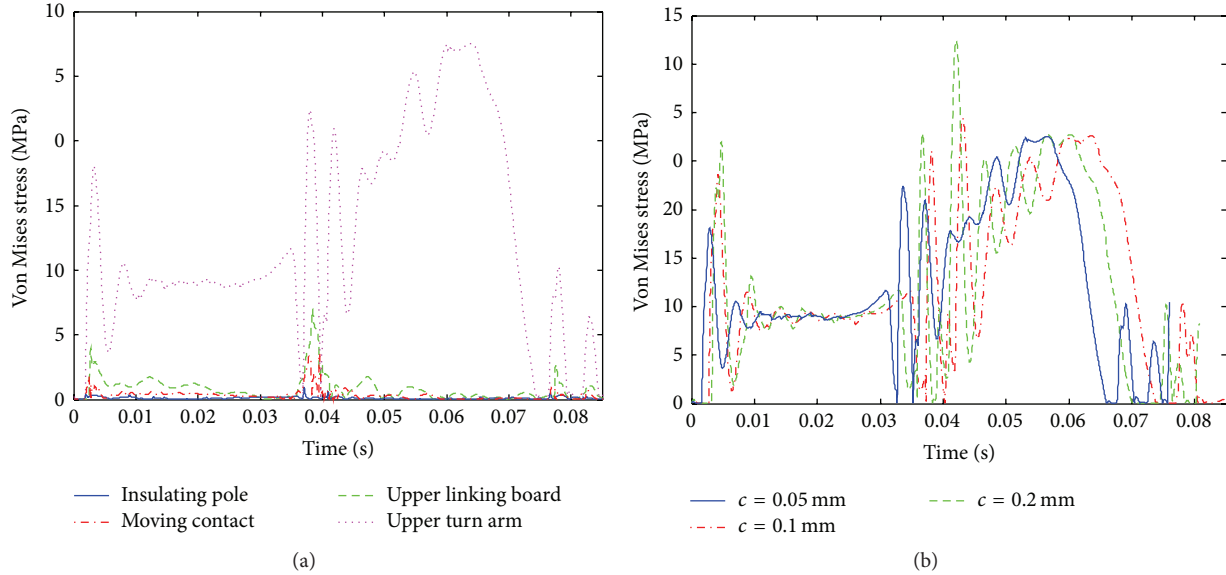


FIGURE 16: Dynamic stress for different clearance sizes: (a) Von Mises stress of the components and (b) Von Mises stress of upper turn arm.

generally consistent with those without clearance. The deviation value of the output stroke is 0.08 mm. Compared with the rigid model without clearance, velocity and acceleration of the rigid-flexible coupling model without clearance produce large amplitude vibration in the starting stage of motion; the reason is that the high speed moving of transmission mechanism causes the excessive deformation of the flexible components, especially for the moving contact restricted by shifting pairs, which leads to clamping stagnation in the transmission motion. As can be seen from Figure 14(e), the existence of clearance can highly reduce the impact and vibration of the transmission mechanism. That is, the existence of clearance acts as the suspension for the rigid-flexible coupling model.

Compared with the acceleration of rigid model with clearance, the maximum value of acceleration of rigid-flexible coupling model with clearance is reduced from 563.5 m/s^2 to 460.2 m/s^2 . Therefore, for the case of the rigid-flexible coupling model, the maximum value of acceleration and impacts are dramatically reduced and the elastic components act as a suspension for the mechanism.

5.3. Influence of the Clearance Size. The effect of the clearance size on the dynamic responses of the rigid-flexible coupling model of the mechanism is investigated. During the dynamic simulation, the revolute joints A and J (Figure 2) are modeled as clearance joints. Three case studies are implemented for the different clearance sizes of 0.05 mm, 0.1 mm, and 0.2 mm. The displacement, vibration displacement, velocity, and acceleration of the moving contact for different clearance sizes are shown in Figure 15.

It is clear that the effects of the clearance sizes for revolute joint on the displacement and velocity of moving contact are slight, since the displacement and the velocity of moving contact without clearance are generally consistent with those of moving contact with different clearance sizes. However,

with the increase in clearance size, the deviation value of the output stroke, the fluctuation frequency, and the hysteretic nature of velocity in time domain are more obvious. When the clearance size increases from 0.05 mm to 0.2 mm, the corresponding deviation value of the output stroke increases from 0.04 mm to 0.17 mm. Particularly, the time delay of velocity in the starting stage of motion increases from 0.0015 s to 0.0044 s. Although the time is very short, it will lead to a kinematic error of about 7.8 percent for the transmission mechanism with characteristics of high speed and heavy haul, which causes a huge negative effect for transmission motion, even a serious Power Grid Accident.

The simulation results also verify that the effects of clearance size on contact force at the joint and acceleration of transmission mechanism are severer than those on displacement and velocity, especially for the high speed mechanism. Remarkably, the maximum value of acceleration increases from 345.5 m/s^2 to 612.2 m/s^2 ; the maximum value of contact force in joint (J) increases from 2032.4 N to 3680.6 N. The excessive contact force of the joints will greatly reduce the lifespan and dynamic performance of the mechanism.

As can be seen from Figure 16, during the simulation, the maximum dynamic stress of transmission mechanism occurs at the chamfer of upper turn arm. The reason is that it is constrained to the fixed axis rotation and has thin-walled structure in chamfer zone, which leads to bending moments and stress concentration. It can be seen that, with the increase in the clearance size, the maximum dynamic stress of upper turn arm increases from 13.63 MPa to 18.71 MPa. The simulation results indicate that the increase of the clearance size increases the level of dynamic stress of mechanism obviously.

In addition, the simulation results are compared to other studies from previous literature [23–25], in which the research results also revealed that clearance size played important roles in the dynamic performance of mechanical

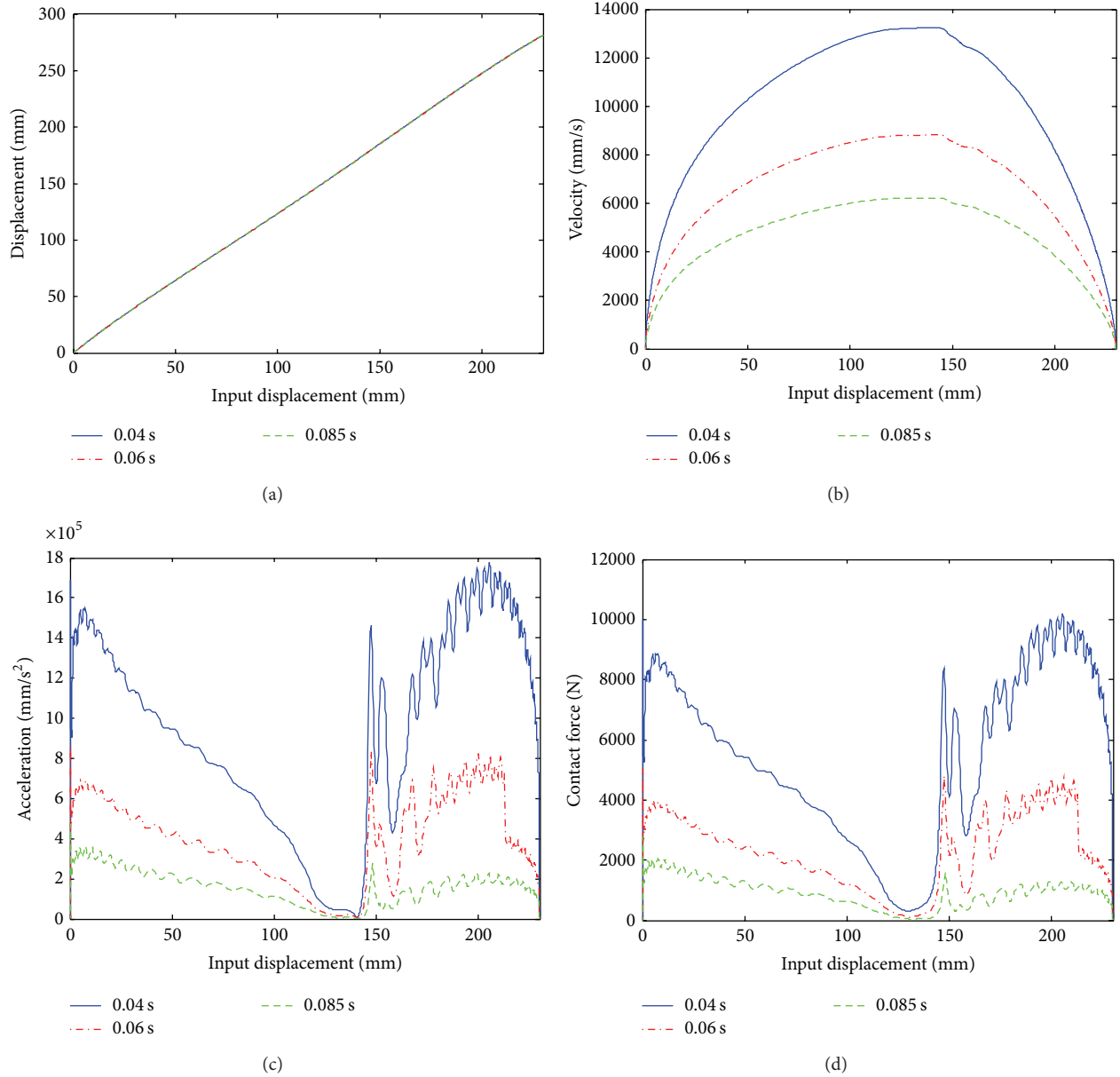


FIGURE 17: Responses for different input speeds: (a) displacement, (b) velocity, (c) acceleration, and (d) contact force.

system. It also represented that clearance leads to oscillations of mechanism, and higher size of clearance leads to larger amplitude of the acceleration of mechanism. So the simulation results are validated by other data published on the field on dynamics of mechanism with clearance joints.

5.4. Influence of the Input Speed. The influence of the input speed of driving link on the dynamic responses of the rigid-flexible coupling transmission mechanism is investigated in this section. Again, in the simulation of transmission mechanism, the revolute joints *A* and *J* (Figure 2) are modeled as clearance joints. The clearance size of the revolute joints is set to 0.1 mm.

When driving link's stroke is 230 mm, the time duration of the simulation of transmission mechanism was 0.04 s,

0.06 s, and 0.085 s, respectively. That is, the input function of motion is, respectively, $\text{step5}(\text{time}, 0, 0, 0.04, 230)$, $\text{step5}(\text{time}, 0, 0, 0.06, 230)$, and $\text{step5}(\text{time}, 0, 0, 0.085, 230)$. The displacement, velocity, acceleration, and contact force of the rigid-flexible coupling transmission mechanism with clearance are shown in Figure 17.

As can be seen from Figure 17, the different input speeds of driving link do not affect the displacement of moving contact in a significant way. In sharp contrast, the velocity, acceleration, and contact force of moving contact are strongly affected by input speed of driving link. With the increase in input speed of driving link, the maximum value of velocity of moving contact increases from 6.21 m/s to 13.31 m/s, the value of contact force in clearance joint (*J*) increases from 3820 N to 9754 N, and that of acceleration increases from 460.2 mm/s²

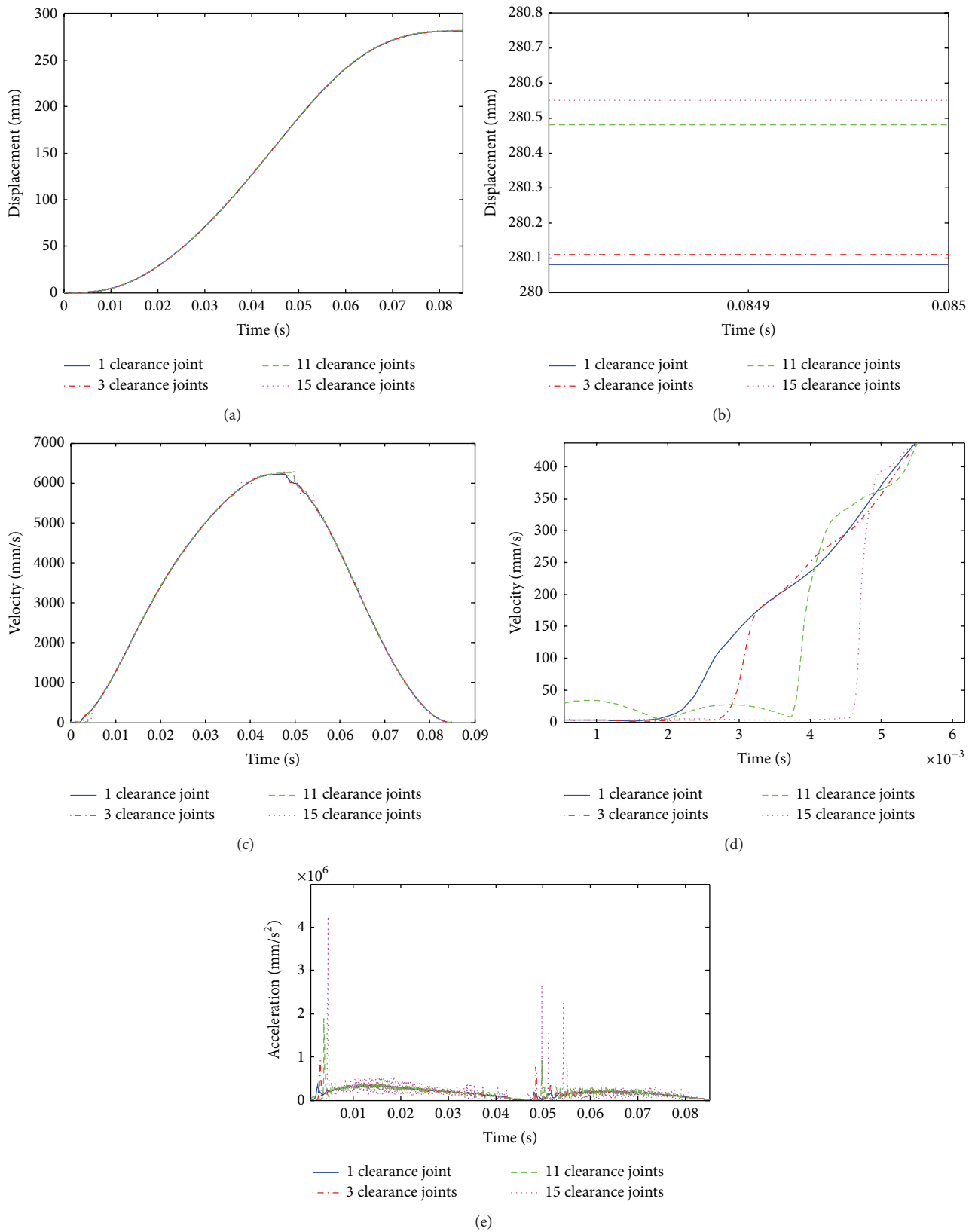


FIGURE 18: Responses for different number of clearance joints: (a) displacement, (b) enlarged drawing of displacement, (c) velocity, (d) enlarged drawing of velocity, and (e) acceleration.

to 1625.6 m/s^2 . It indicates the higher input speed, the higher acceleration, and contact force. Therefore, as the input speed increases, the effects of clearance on dynamic response of the mechanism are more obvious.

5.5. Influence of the Number of Clearance Joints. The simulation of transmission mechanism is performed with one, four, eleven, and fifteen clearance joints. In the simulation, the clearance size of revolute joint is set to be 0.1 mm and the simulation time duration is 0.085 s; the displacement, velocity, and acceleration of the moving contact for different number of clearance joints are shown in Figure 18.

As can be seen from Figure 18, an increase in number of clearance joints causes the enhancement of the dynamic response of transmission mechanism. When the number of clearance joints increases from 1 to 15, the corresponding deviation value of the output stroke increases from 0.08 mm to 0.54 mm, the time delay of velocity in the starting stage of motion increases from 0.0015 s to 0.0044 s, and the maximum value of acceleration increases from 331.5 m/s^2 to 4260.6 m/s^2 . With the increase of the number of clearance joints, the impact strength and vibration frequency will be stronger and higher. Therefore, the dynamic responses of transmission mechanism are affected tremendously by the number of clearance joints. As the number of clearance joints increases, the dynamic responses of the mechanism are more severe.

6. Conclusion

In this work, a planar rigid-flexible coupling model of the transmission mechanism of (UHV) with multiclearance joints is established using ADAMS software. The dynamic contact model in clearance joints is performed, in which the normal force is considered using nonlinear continuous contact force model and tangential force is considered using modified Coulomb's friction model. The reliability of the model is proved by means of comparing the results of experiments. Moreover, drawing into calculator simulation method for supplement because of the limitations on experiment, it has greater applicable scope.

The simulation results show that the dynamic response of the mechanism is influenced greatly by the clearance and components flexibility. Compared with the rigid model, in the case of flexible model, the maximum value of acceleration is highly reduced to about 1.5 times, and flexible components act as a suspension for the mechanism. Furthermore, the influences of clearance size, input speed, and number of clearance joints on the dynamic response of the mechanism are also investigated. It can be included that the increased clearance size, number of clearance joints, and input speed make the dynamic responses of mechanism worse, which leads to the destruction and failure of components and performs as more obvious motion lag and impact. In addition, this work provides a practical method to analyze the dynamics characteristics of transmission mechanism with clearance joints and can predict the effects of clearance on transmission mechanism preferably, which is the basis for precision analysis, optimization design of transmission mechanism, and reliability operation of breaker circuit.

Conflict of Interests

The authors declare that there is no conflict of interests regarding the publication of this paper.

Acknowledgment

The authors would like to express sincere gratitude to the Pinggao Technology for the financial and technological support given to this study through the project "High Voltage Circuit Breaker Hydraulic Operating Mechanism Characteristic Research" (Project no. 208239881).

References

- [1] G. Song, J. Cui, and D. Yuan, "Operating analysis of high voltage circuit breaker in 1999–2003," *Electrical Equipment*, vol. 6, no. 2, pp. 6–13, 2005.
- [2] A. Ziani and H. Moulai, "Hybrid model of electric arcs in high voltage circuit breakers," *Electric Power Systems Research*, vol. 92, pp. 37–42, 2012.
- [3] W. Liu and B. Xu, "Characteristic analysis of high voltage circuit breaker with hydraulic operating mechanism," *Journal of Mechanical Engineering*, vol. 46, no. 10, pp. 148–155, 2010.
- [4] F.-C. Chen and Y.-F. Tzeng, "On the dynamics of spring-type operating mechanism for 69 KV SF6 gas insulated circuit breaker in open operation," *Computers and Structures*, vol. 80, no. 22, pp. 1715–1723, 2002.
- [5] F.-C. Chen, "Dynamic response of spring-type operating mechanism for 69 kV SF6 gas insulated circuit breaker," *Mechanism and Machine Theory*, vol. 38, no. 2, pp. 119–134, 2003.
- [6] T.-M. Lyu and J.-P. Tao, "Calculation and improvement of spring operating mine-used device for vacuum circuit breaker," *Coal Mine Machinery*, vol. 35, no. 9, pp. 34–36, 2012.
- [7] P. Flores, "A parametric study on the dynamic response of planar multibody systems with multiple clearance joints," *Nonlinear Dynamics*, vol. 61, no. 4, pp. 633–653, 2010.
- [8] S. Erkaya and I. Uzmay, "A neural-genetic (NN-GA) approach for optimising mechanisms having joints with clearance," *Multibody System Dynamics*, vol. 20, no. 1, pp. 69–83, 2008.
- [9] Q. Tian, Y. Zhang, L. Chen, and P. Flores, "Dynamics of spatial flexible multibody systems with clearance and lubricated spherical joints," *Computers and Structures*, vol. 87, no. 13-14, pp. 913–929, 2009.
- [10] E. Zheng and X. Zhou, "Modeling and simulation of flexible slider-crank mechanism with clearance for a closed high speed press system," *Mechanism and Machine Theory*, vol. 74, pp. 10–30, 2014.
- [11] Z.-F. Bai, Y. Zhao, and H. Tian, "Dynamics simulation of deployment for solar panels with hinge clearance," *Journal of Harbin Institute of Technology*, vol. 41, no. 3, pp. 11–14, 2009.
- [12] P. Flores, J. Ambrósio, and J. P. Claro, "Dynamic analysis for planar multibody mechanical systems with lubricated joints," *Multibody System Dynamics*, vol. 12, no. 1, pp. 47–74, 2004.
- [13] P. Flores, J. Ambrósio, J. C. P. Claro, and H. M. Lankarani, "Influence of the contact-impact force model on the dynamic response of multi-body systems," *Proceedings of the Institution of Mechanical Engineers, Part K*, vol. 220, no. 1, pp. 21–34, 2006.
- [14] I. Khemili and L. Romdhane, "Dynamic analysis of a flexible slider-crank mechanism with clearance," *European Journal of Mechanics—A/Solids*, vol. 27, no. 5, pp. 882–898, 2008.

- [15] O. Muvengei, J. Kihui, and B. Ikua, "Numerical study of parametric effects on the dynamic response of planar multi-body systems with differently located frictionless revolute clearance joints," *Mechanism and Machine Theory*, vol. 53, pp. 30–49, 2012.
- [16] S. M. Megahed and A. F. Haroun, "Analysis of the dynamic behavioral performance of mechanical systems with multi-clearance joints," *Journal of Computational and Nonlinear Dynamics*, vol. 7, no. 1, Article ID 011002, 11 pages, 2012.
- [17] O. A. Bauchau and J. Rodriguez, "Modeling of joint clearances and joint flexibility effects in multibody systems dynamics," *International Journal of Solids and Structures*, no. 39, pp. 41–63, 2002.
- [18] Q. Tian, Y. Zhang, L. Chen, and J. Yang, "Simulation of planar flexible multibody systems with clearance and lubricated revolute joints," *Nonlinear Dynamics*, vol. 60, no. 4, pp. 489–511, 2010.
- [19] Q. Tian, C. Liu, M. MacHado, and P. Flores, "A new model for dry and lubricated cylindrical joints with clearance in spatial flexible multibody systems," *Nonlinear Dynamics*, vol. 64, no. 1–2, pp. 25–47, 2011.
- [20] A. L. Schwab, J. P. Meijaard, and P. Meijers, "A comparison of revolute joint clearance models in the dynamic analysis of rigid and elastic mechanical systems," *Mechanism and Machine Theory*, vol. 37, no. 9, pp. 895–913, 2002.
- [21] Z. F. Bai and Y. Zhao, "A hybrid contact force model of revolute joint with clearance for planar mechanical systems," *International Journal of Non-Linear Mechanics*, vol. 48, pp. 15–36, 2013.
- [22] D.-Y. Yu and Y.-J. Qian, "Parameter-settings for the dynamic simulation based on ADAMS," *Computer Simulation*, no. 9, pp. 103–107, 2006.
- [23] S. Erkaya, "Investigation of joint clearance effects on welding robot manipulators," *Robotics and Computer-Integrated Manufacturing*, vol. 28, no. 4, pp. 449–457, 2012.
- [24] K.-L. Ting, J. Zhu, and D. Watkins, "The effects of joint clearance on position and orientation deviation of linkages and manipulators," *Mechanism and Machine Theory*, vol. 35, no. 3, pp. 391–401, 2000.
- [25] A. Kote, K. Balaji, B. S. Nataraju, and V. C. Aralimatti, "Effect of solar array deployment on spacecraft attitude," *Journal of Spacecraft Technology*, vol. 17, no. 2, pp. 1–8, 2007.

Research Article

Optimal Trajectory Planning and Linear Velocity Feedback Control of a Flexible Piezoelectric Manipulator for Vibration Suppression

Junqiang Lou,¹ Yanding Wei,² Guoping Li,¹ Yiling Yang,² and Fengran Xie²

¹Zhejiang Provincial Key Lab of Part Rolling Technology, College of Mechanical Engineering and Mechanics, Ningbo University, Ningbo 315211, China

²China Key Laboratory of Advanced Manufacturing Technology of Zhejiang Province, School of Mechanical Engineering, Zhejiang University, Hangzhou 310027, China

Correspondence should be addressed to Junqiang Lou; loujunqiang@nbu.edu.cn

Received 26 June 2015; Revised 4 August 2015; Accepted 5 August 2015

Academic Editor: Mario Terzo

Copyright © 2015 Junqiang Lou et al. This is an open access article distributed under the Creative Commons Attribution License, which permits unrestricted use, distribution, and reproduction in any medium, provided the original work is properly cited.

Trajectory planning is an effective feed-forward control technology for vibration suppression of flexible manipulators. However, the inherent drawback makes this strategy inefficient when dealing with modeling errors and disturbances. An optimal trajectory planning approach is proposed and applied to a flexible piezoelectric manipulator system in this paper, which is a combination of feed-forward trajectory planning method and feedback control of piezoelectric actuators. Specifically, the joint controller is responsible for the trajectory tracking and gross vibration suppression of the link during motion, while the active controller of actuators is expected to deal with the link vibrations after joint motion. In the procedure of trajectory planning, the joint angle of the link is expressed as a quintic polynomial function. And the sum of the link vibration energy is chosen as the objective function. Then, genetic algorithm is used to determine the optimal trajectory. The effectiveness of the proposed method is validated by simulation and experiments. Both the settling time and peak value of the link vibrations along the optimal trajectory reduce significantly, with the active control of the piezoelectric actuators.

1. Introduction

Flexible manipulators have been used in various applications including field inspection, space exploration, medical application, and hazardous environment. Compared with their rigid counterparts, flexible manipulators exhibit many advantages such as higher manipulation speed, greater payload to weight ratio, and lower energy consumption. Moreover, they can be quickly adapted to changing situations and product design variations [1]. However, the conflicting requirements between high speed and high positioning accuracy have made the control of flexible manipulators a real challenging problem. Structural flexibility leads to the appearance of undesirable vibrations during motion. So flexible manipulator system exhibits combined behaviors of rigid body motions

and vibrations [2]. These oscillations lead to deterioration of positioning accuracy and efficiency, making the control of such system extremely difficult.

To address these problems, quite a lot of researches have been conducted on the vibration control of flexible manipulators. The existing vibration control techniques can be broadly classified into two categories, namely, feedback control and feed-forward control. The advantage of feed-forward control is that it does not require any additional sensors or actuators. Hence, the control system can be manufactured at low costs, thus being more economical. One special feed-forward control strategy, known as input command shaping, has been studied widely since its first appearance [3]. Mohamed et al. [4] presented investigations into vibration control of a flexible manipulator using input shaping techniques with

positive and negative input shapers. Alam and Tokhi [5] developed the design of a command shaping controller for vibration suppression of a flexible manipulator, using multi-objective genetic optimization process. More recently, Cole and Wongratanaphisan [6] described an adaptive FIR input command shaping methodology to achieve zero residual vibration control of a rigid-flexible manipulator system. The input command shaping method is effective to ensure that the input does not excite vibrations of the manipulator. But it usually costs a large amount of computation when dealing with multiple vibration modes. And it cannot suppress the induced and existing vibrations.

An alternative feed-forward control strategy to achieve vibration control of flexible manipulators is the trajectory planning approach. Wu et al. [7] proposed an optimal trajectory planning method for vibration reduction of a dual arm space robot with front flexible links, in which the trajectory was described using a fourth-order quasi-uniform B-spline. Heidari et al. [8] considered the problem on the rest-to-rest motion of a flexible manipulator and formulated the trajectory planning problem as a Pontryagin optimal problem. Springer et al. [9] focused on time-optimal trajectory planning for robots with flexible links and determined the minimum time trajectory for avoiding elastic vibration of the link. Choi et al. [10] described a new trajectory planning method for output tracking of linear flexible system using exact equilibrium manifolds. However, the trajectory planning technique is a feed-forward control strategy; vibration modes of the flexible manipulator are still controlled in open loop [11]. When dealing with various disturbances and parameters variations, there would still be large residual vibrations that need to be controlled [12].

To overcome the drawbacks of feed-forward control schemes, many researchers have tried to solve the problems of link vibration suppression using feedback control techniques. Among them, some researchers concentrated on reducing the link vibrations using joint motor [13]. However, the existence of nonminimum phase dynamics between the tip position and the input torque applied at the joint motor makes the system difficult to stabilize [14]. A rather different approach for feedback control of link vibrations has been developed in recent years, relying on the use of smart materials [15]. Among those smart materials, piezoelectric (PZT) materials have been found extensive applications in structure vibration control, due to their lightweight, fast response, large bandwidth, and so on [16]. Sun et al. [17] realized the rigid motion control and vibration damping of a flexible manipulator, using a combined scheme of a PD controller for the joint motor and a linear velocity feedback (L-type) controller for the piezoelectric actuators. Gurses et al. [18] extended the previous work studied and introduced a serial array of fiber optic sensors to the control of flexible manipulators which allowed simultaneous linear (L-type) and angular (A-type) velocity feedback. Li et al. [19] presented a study on vibration suppression of a flexible piezoelectric manipulator using adaptive fuzzy sliding mode control. Choi et al. [20] studied the position control of a single-link flexible manipulator and designed a hysteresis compensator for the piezoelectric actuators.

However, in most studies on active control of flexible manipulator, attention seems to be focused on how to improve the performance of the piezoelectric controller. The contributions of the feed-forward torque or the required trajectory planning are rarely considered. A more reasonable and efficient approach seems to emerge if a combined strategy is considered. Specifically, the joint motor is responsible for the gross vibrationless motion of the structure through trajectory planning approach, while the PZT actuators are used to deal with vibrations that may arise from modeling errors and external disturbances after joint motion, by means of active control. The remainder of this paper is organized as follows. In Section 2, the flexible piezoelectric manipulator system is introduced and the governing equations of the system are derived. Section 3 proposes the optimal trajectory planning approach. The joint angle of the link is expressed as a quintic polynomial function. The constraint conditions, the initial and final conditions of the joint angle, angular velocity, and angular acceleration are applied. The sum of the link vibration energy is chosen as the objective function. Then, the optimal trajectory planning algorithm is constructed by the use of genetic algorithm. In Section 4, numerical analysis and simulations are conducted. The optimal trajectory of the flexible piezoelectric manipulator in a point-to-point motion is obtained. Section 5 describes an experimental apparatus of the flexible manipulator system, together with the experimental results, before concluding in Section 6.

2. Dynamic Modeling

The schematic diagram of the flexible piezoelectric manipulator system is shown in Figure 1. It is composed of a rotary joint, a single-link flexible manipulator with a rectangular cross section and a pair of collocated piezoelectric (PZT) actuators. The manipulator is attached to the hub in such a way that it rotates in the horizontal plane only. The effect of gravity can be ignored, so the link can be modeled as an Euler-Bernoulli beam. The axis ox_o is the inertial reference line. The axis ox is the tangential line to the neutral axis of the beam at the hub. For the sake of simplicity, the same assumptions are made as [17].

It is assumed that the dynamic behavior of the flexible manipulator during a point-to-point motion is dominated by the first several vibration modes, so the contributions of the higher vibration modes are negligible. Using assumed mode method, the deflection $w(x, t)$ of the link can be represented as

$$w(x, t) = \sum_{i=1}^m \varphi_i(x) q_i(t) = \mathbf{\Phi}(x) \mathbf{q}(t), \quad (1)$$

where $\varphi_i(x)$ and $q_i(t)$ devote the i th mode shape function and corresponding generalized coordinate, respectively. $\mathbf{\Phi}(x) = [\varphi_1 \cdots \varphi_i \cdots \varphi_m]$ and $\mathbf{q}(t) = [q_1 \cdots q_i \cdots q_m]$ represent the mode shape function and generalized coordinate index, respectively. m is the mode number.

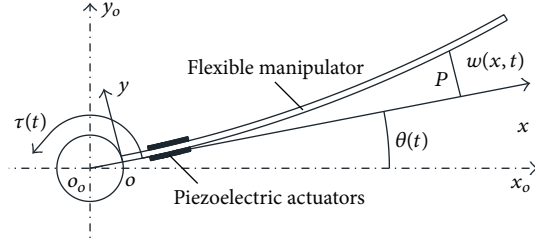


FIGURE 1: Schematic diagram of the flexible manipulator system.

Extended Hamilton's principle is used to derive the system equation. The derivation process and parameter expressions are explicitly presented in Appendix. The governing equations of the system can be derived as

$$I_{\theta\theta}\ddot{\theta} + \mathbf{q}^T \mathbf{m}_{qq} \mathbf{q}\ddot{\theta} + 2\mathbf{q}^T \mathbf{m}_{q\dot{q}} \mathbf{q}\dot{\theta} + \mathbf{m}_{\theta q} \ddot{\mathbf{q}} = \tau(t), \quad (2)$$

$$\mathbf{m}_{qq} \ddot{\mathbf{q}} + \mathbf{m}_{\theta q}^T \ddot{\theta} + \mathbf{K}_q \mathbf{q} - \mathbf{m}_{qq} \mathbf{q}\dot{\theta}^2 = cV(t) \left[\widehat{\Phi}' \right]^T (x_s). \quad (3)$$

It should be noticed that (2) represents the rigid motion of the piezoelectric manipulator, while (3) describes the dynamic behavior of the flexible link with the control of PZT actuators. If the desired trajectory can be realized by means of tracking control, for example, trajectory control can be realized when the servo motor works in the speed control mode. In the case that tracking control is possible, only (3) is used for planning a trajectory where the elastic vibration of the link is eliminated or minimum. Augmenting the proportional damping, the dynamic equation of the flexible manipulator system can be expressed as

$$\begin{aligned} & \mathbf{m}_{qq} \ddot{\mathbf{q}} + \mathbf{m}_{\theta q}^T \ddot{\theta} + \mathbf{C}_q \dot{\mathbf{q}} + \mathbf{K}_q \mathbf{q} - \mathbf{m}_{qq} \mathbf{q}\dot{\theta}^2 \\ & = cV(t) \left[\widehat{\Phi}' \right]^T (x_s). \end{aligned} \quad (4)$$

It is known that it is feasible to use linear velocity feedback in the controller formulation. Thus, the linear velocity feedback (L-type) approach is readily implementable. Furthermore, the stability of the close-loop system including the L-type controller has been confirmed by Sun et al. in [17], as well as the effectiveness of the controller. Therefore, the linear velocity feedback (L-type) approach is employed to design the applied voltage of the PZT actuators in this study. In the L-type control strategy, the control voltage of the actuators is defined as

$$V(t) = -k_L \left[\dot{w}(x_s + l_p) - \dot{w}(x_s) \right] = -k_L \widehat{\Phi}(x_s) \dot{\mathbf{q}}, \quad (5)$$

where k_L is a positive control gain. Then, substituting (5) into (4) leads to

$$\begin{aligned} & \mathbf{m}_{qq} \ddot{\mathbf{q}} + \mathbf{m}_{\theta q}^T \ddot{\theta} + \mathbf{C}_q \dot{\mathbf{q}} + ck_L \left[\widehat{\Phi}' \right]^T (x_s) \widehat{\Phi}(x_s) \dot{\mathbf{q}} + \mathbf{K}_q \mathbf{q} \\ & - \mathbf{m}_{qq} \mathbf{q}\dot{\theta}^2 = 0. \end{aligned} \quad (6)$$

It can be observed from (6) that the rigid motion of the joint, elastic vibration of the link, and active control of

the PZT actuators are all considered in the procedure of trajectory planning. However, it is known that the piezoelectric parameters are very small numbers, which means that the contribution assured by the PZT control is relatively less than that of the feed-forward trajectory planning during joint motion. Therefore, the essence of the optimal trajectory planning approach is that the feed-forward trajectory planning is responsible for the gross vibrationless motion of the structure during joint motion, while the PZT actuators are used to deal with vibrations after joint motion, by means of L-type control strategy.

3. Optimal Trajectory Planning

This study focuses on the problem related to a point-to-point (PTP) motion of the flexible manipulator system rotating from the initial joint angle θ_0 to the final joint angle θ_f over a fixed traveling time t_f [21]. In practice, elastic vibrations of the flexible link are unavoidable due to the flexible-rigid coupled dynamics. Considering the presence of parameter uncertainties and external disturbances, the residual vibrations of the link are still exciting at the end of PTP motion, in spite of active control of PZT actuators. For a given PTP maneuver in joint space, the objective is to find an optimal joint trajectory that minimizes link vibrations during and after joint motion. The total vibration energy of a trajectory is adopted as the performance index, which is defined as

$$PI(x) = \lambda_1 \int_{t_0}^{t_f} \mathbf{q}^T(t) \mathbf{q}(t) dt + \lambda_2 \int_{t_f}^{t_d} \mathbf{q}^T(t) \mathbf{q}(t) dt, \quad (7)$$

where t_d is the settling time of the link vibrations with piezoelectric control. The first part in (7) represents vibration energy of the link during joint motion, while the second part represents residual vibration energy after joint motion. λ_1 and λ_2 are the weighting indexes of the two parts, respectively.

To realize a smooth motion, smooth and continuous functions are typically adopted to plan the joint trajectory. Moreover, the first and second derivatives of the trajectory are also expected to be smooth and continuous. Among those common trajectory functions, the quintic polynomial function has the advantages of being accurate, precise, and easy to design and control. Moreover, it has the extra advantage of controlling the acceleration at the initial point and goal [22]. So the quintic polynomial function is selected to interpolate the optimal trajectory curves, which can be written as

$$\theta(t) = C_0 + C_1 t + C_2 t^2 + C_3 t^3 + C_4 t^4 + C_5 t^5, \quad (8)$$

where $C_0, C_1, C_2, C_3, C_4,$ and C_5 are the coefficients to be determined from the initial and final boundary conditions. To get a smooth motion, the initial angle, angular velocity, and angular acceleration are set to be zero. Meanwhile, the final angular velocity and angular acceleration are also set to be zero.

To get the optimal trajectory that minimizes the performance index in (7), the travelling time t_f is divided into n divisions, each of which has an equal time interval.

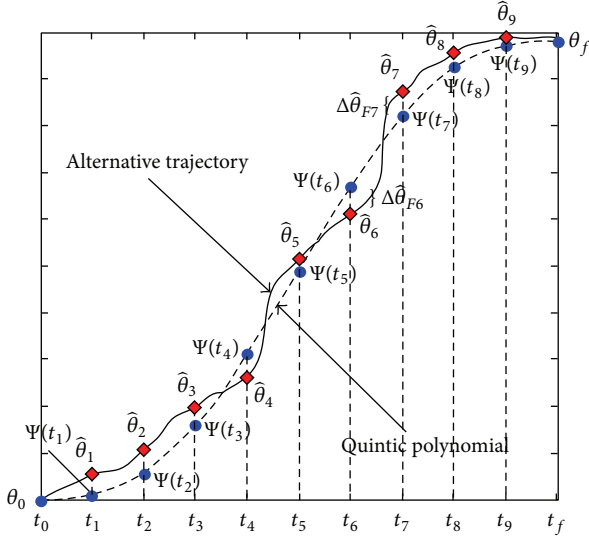


FIGURE 2: Discrete joint angle of the flexible manipulator system $\hat{\theta}_i$ ($n = 10$).

If the times at divided knots can be denoted by $t_0 (= 0)$, $t_1, \dots, t_i, \dots, t_{n-1}, t_f$, the joint angle at t_i is denoted by $\hat{\theta}_i$. To construct the optimal trajectory, the quintic polynomial function is employed to interpolate the discrete angles. The angular velocity and angular acceleration are obtained by differentiating the quintic polynomial curves with respect to time. Finally, the discrete angles of the link are defined by introducing parameters $\Delta\hat{\theta}_{Fi}$ as

$$\hat{\theta}_i = \Psi(t_i) + \Delta\hat{\theta}_{Fi}, \quad (9)$$

where $\Psi(t)$ represents the quintic polynomial motion with the above boundary conditions.

Consequently, the parameter $\Delta\hat{\theta}_{Fi}$ denotes the deviation from the trajectory for the quintic polynomial motion. The discrete joint angles of the flexible link are shown in Figure 2.

Genetic algorithm (GA) approach is gaining popularity for solving complex problems in robotics. It is a population-based stochastic and global search method. Its performance is superior to that revealed by classical optimization techniques and has been successfully used in robot trajectory planning technique [23]. As the procedure discussed above, it is possible to express the optimal trajectory $\hat{\theta}_i$ by using the parameter $\Delta\hat{\theta}_{Fi}$, whose number is $n-1$ for the n divisions of t_f . The trajectory planning procedures of the link using GA are carried out as follows. The parameters $\Delta\hat{\theta}_{Fi}$ ($i = 1, 2, \dots, n-1$) are considered to be optimized. First, the angular velocity $\dot{\hat{\theta}}(t)$ and angular acceleration $\ddot{\hat{\theta}}(t)$ are obtained from the quintic polynomial interpolation of the discrete joint angles $\hat{\theta}_i$. Then, the dynamic response of the flexible piezoelectric manipulator is calculated through numerical integration of (6). Finally, the optimal trajectory can be derived through minimizing the performance index in (7), using genetic algorithm. The main steps are summarized as below.

Step 1. Division number n is determined; the discrete angles of the quintic polynomial motion $[\psi(t_1), \psi(t_2), \dots, \psi(t_i), \dots, \psi(t_{n-1})]$ are calculated. Meanwhile, the parameters of the GA are also determined.

Step 2. The initial population for the first generation is generated through a random generator. Every individual includes $n-1$ genes corresponding to the interior points to be selected, which is defined as $\mathbf{x}_k = [x_{k1}, x_{k2}, \dots, x_{ki}, \dots, x_{k(n-1)}]$. The gene of the individual x_{ki} represents the optimized parameter $\Delta\hat{\theta}_{Fi}$, and the dimension of the search space is $n-1$.

Step 3. The trajectory of the link is generated through the quintic polynomial interpolation, and the vibration response of the link is derived through numerical simulations. The fitness values $PI(x)$ of all the individuals in (7) are evaluated.

Step 4. A set of genetic operators, which are selection, crossover, and mutation, are used in succession to create a new population of chromosomes for the next generation.

Step 5. The process of evaluation and creation of new successive generations is repeated until the termination condition is satisfied. And the optimal trajectory for vibration suppression is finally decided where the fitness value $PI(x)$ is minimum.

4. Simulation Studies

Numerical simulations are carried out to evaluate the performance of the proposed trajectory planning approach using MATLAB. The parameters of the proposed flexible manipulator system are shown in Table 1. In simulation, the actuator pairs are chosen to lie near the root of the link, where the strain energy of the structure is the highest [24]. For simplicity, only the first vibration mode is taken into account, which is found to be at $\omega_1 = 24.5$ rad/s (3.9 Hz), with modal damping $\zeta_1 = 0.02$. And the parameters of the GA are given in Table 2. The weighting indexes of the vibration energy during and after joint motion are set to $\lambda_1 = 0.25$, $\lambda_2 = 0.75$.

A fast motion case is considered, here. The traveling time t_f is set to be 0.5 seconds. The initial and final angles of the joint are set to be 0 rad and $\pi/2$ rad, respectively. And the number of trajectory partitions n is set to be 10. Meanwhile, to speed up the convergence of GA search, the search space of the optimized parameters $\Delta\hat{\theta}_{Fi}$ is taken to be

$$\Delta\hat{\theta}_{Fi} \in [-0.5 |\psi(t_i) - \theta_f| \quad 0.5 |\psi(t_i) - \theta_f|]. \quad (10)$$

For a real flexible manipulator system, the joint acceleration, the torque of the motor, and control voltage of the PZT actuator should have constraint values [25]. The constraint conditions of the flexible manipulator system are defined as

$$\begin{aligned} 0 < \hat{\theta}_i < \theta_f \quad (i = 1, 2, \dots, n-1), \\ \ddot{\theta} &\leq \ddot{\theta}_{\max}, \\ V &\leq V_{\max}, \end{aligned} \quad (11)$$

where the parameter V_{\max} is set to be 150 V and the maximum of the joint acceleration $\ddot{\theta}_{\max}$ is assumed to be 80 rad/s².

TABLE 1: Parameters of the flexible manipulator system.

Parameter	Flexible link	PZT actuator
Material	Epoxy	PZT-5
Length (mm)	620.0	40.0
Width (mm)	30.0	10.0
Thickness (mm)	3.0	0.8
Young's modulus (Gpa)	34.6	117.0
Density (Kg/m ³)	1840.0	7500.0
PZT coefficient d_{31} (C/N)	N/A	187×10^{-12}

TABLE 2: Parameters of genetic algorithm.

Parameter	Value
Population type	Binary string
Number of genes	48 bits
Population size	25
Crossover ratio	0.6
Mutation ratio	0.05
Generations	100

The evolution history of the GA search is shown in Figure 3. It can be seen that the fitness reduces with an increasing value of the generation number. And the optimal trajectory can be approximately obtained at the 40th generation. The results of numerical calculations and simulations are presented in Figure 4. The angular displacement, velocity, and acceleration of the obtained optimal trajectory are depicted in Figures 4(a)–4(c), respectively. The tip vibration response of the flexible link along the optimal trajectory is illustrated in Figure 4(d). For comparison, the simulation results along the quintic polynomial trajectory are also presented, correspondingly.

As seen in Figure 4(d), dynamic response of the link along the optimal trajectory shows nearly no trace of oscillations after joint motion. That is to say, there is nearly no residual vibration in the flexible link (i.e., the modal displacement after 0.5 s), while the dynamic response of the link along the quintic polynomial trajectory owns large oscillations all through the simulation interval. The presence of residual vibrations after joint motion is clearly visible, even after a period of 3-fold traveling time t_f .

5. Experimental Results

A photograph of the experimental setup is shown in Figure 5. The flexible piezoelectric manipulator is driven by an AC servo motor (Yaskawa SGMAH01A1A2S) with a reduction gear (Harmonic Drive CSF-17-50-2A) 50:1. A built-in 16-bit incremental encoder is installed within the motor to measure the rotation angle. The link is clamped at the shaft of the reduction gear through a coupling and is limited to rotate only in the horizontal plane. Meanwhile, a pair of strain gauges assembled in half-bridge configuration (resistance 120 Ω , sensitivity 2.08) are placed at the base of the link to

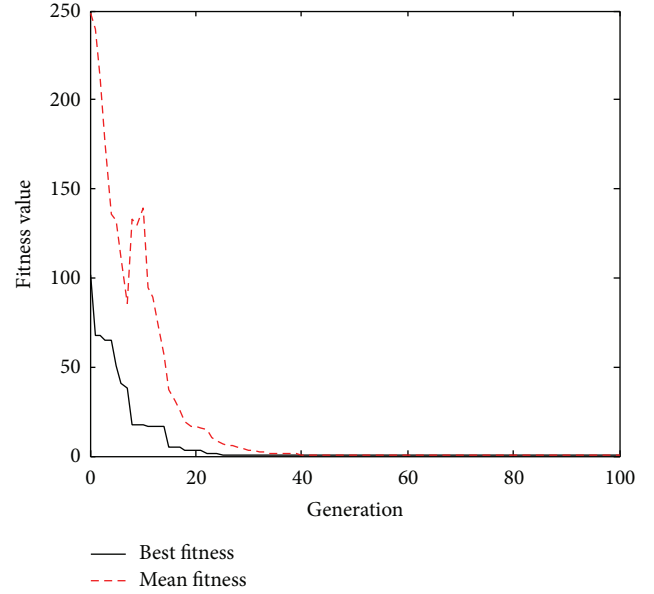


FIGURE 3: Evolution history of the genetic algorithm.

measure the vibrations. A pair of piezoelectric patches (PZT-5A) are attached to the link for the vibration suppression, located close to the strain sensor to get the best control effect.

The control system is realized with an industrial computer. A DAQ device (Advantech PCI-1742U) is used, providing multichannel D/A, A/D, and counter modules for data acquisition and control output. For joint motion control, the AC servomotor is operated in the speed control mode. The output signal of the encoder is fed back to the industrial computer through the counter module of the DAQ. And the input torque determined from the PD controller is applied to the motor through the D/A converter and servo driver (Yaskawa SGDH01AE). Meanwhile, the vibration signal of the flexible manipulator is low-pass filtered and amplified through a strain amplifier, which can amplify the signal to a voltage range of -10 V to 10 V, and then fed into the industrial computer through an A/D converter. To suppress the link vibrations actively, the input voltage determined from the controller, amplified 15 times with a power amplifier, is supplied to the PZT actuators through a D/A converter. The schematic diagram of the experimental setup is shown in Figure 6.

The first experiment was conducted to rotate the link from 0 rad to $\pi/2$ rad in 0.5 seconds along the quintic polynomial trajectory. But the active control of PZT actuators was not applied. Experimental results are presented in Figure 7. The angular displacement, velocity, and acceleration of the quintic polynomial trajectory are depicted in Figures 7(a)–7(c), respectively. The measured vibration response of the link by the strain gauges is shown in Figure 7(d).

As seen in Figures 7(a) and 7(b), the experimental results of joint angle and angular velocity are in perfect agreement with the reference curves. Thus, it can be inferred that the joint reference trajectory of the quintic polynomial was

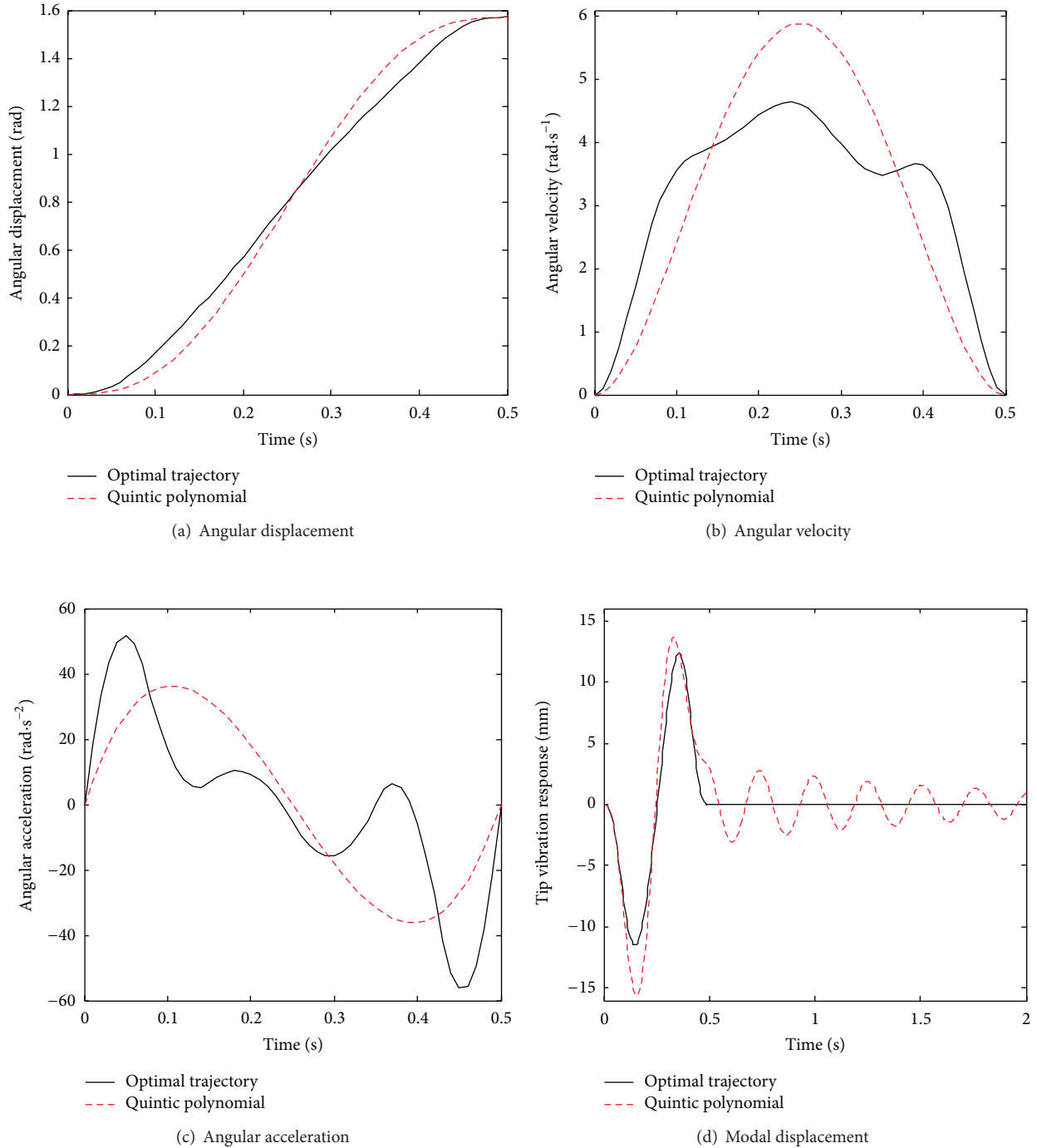


FIGURE 4: Comparison of simulation results between the optimal trajectory and quintic polynomial trajectory.

closely followed. However, unwanted oscillations with large amplitude both during and after the joint motion were clearly observed. As shown in Figure 7(d), the peak value of the measured vibration response exceeds the range of the A/D converter, even after the joint motor has stopped for a period of 1 s. Furthermore, the settling time of the uncontrolled link

vibrations, which is defined as the damping period when the peak value of the sensor voltage does not exceed 0.1 V, is found to be nearly 20 times longer than that of the motor motion (0.5 s), reaching 9.5 s. Thus, vibration suppression of the link is necessary to attain a high positioning accuracy and efficiency.

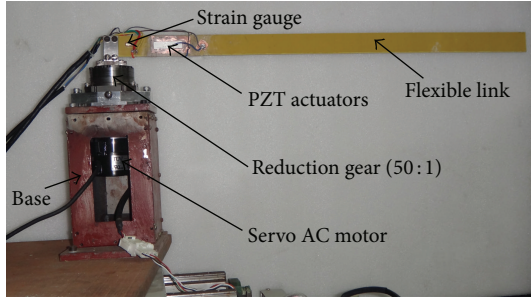


FIGURE 5: Photograph of the experimental setup.

The following experiment was the implementation of the optimal trajectory approach. But vibration control of the PZT actuators was still not applied. Figures 8(a)–8(d) show the angular displacement, velocity, acceleration, and measured vibration response of the link along the optimal trajectory, respectively. The link vibrations obtained from the quintic polynomial trajectory are compared with those obtained from the optimal trajectory strategy, as depicted in Figure 8(d). It can be observed from Figures 8(a) and 8(b) that experimental results of the angular displacement and velocity fairly coincide with the desired curves. Therefore, it can be confirmed that the trajectory tracking control of the flexible manipulator system is realized. Although the peak value of the link vibrations still exceeds the range of the A/D converter during the joint motion, residual vibrations corresponding to the optimal trajectory are significantly less than those caused by the quintic polynomial trajectory. The settling time of the link vibrations reduces to 4.3 s, as shown in Figure 8(d). However, residual vibrations of the link are not perfectly suppressed as the simulation results plotted in Figure 4(d). Unwanted residual vibrations occur after joint motion. This is because the joint motor is not capable of absolutely tracking the given reference trajectory as assumed and tracking error is unavoidable. In addition, modeling error also exists in simulation.

The last experiment was the combination of optimal trajectory and feedback control of the PZT actuators. Those experimental results are presented in Figure 9. As the joint trajectory, velocity, and acceleration were not significantly changed, these results were not given. The vibration response of the link is presented in Figure 9(a). It can be seen that the peak value of the link vibrations still exceeds the range of the A/D converter during joint motion, but the residual vibrations, which can be explained by the tracking error and unmodelled high frequency characteristics of the link, are significantly suppressed by the combined effect of the optimal trajectory and active control of PZT actuators. Moreover, the results obtained from the last experiment are compared with those obtained from the above two experiments. Both the peak value and settling time of the measured vibration response after joint motion are given in Table 3.

TABLE 3: Comparison of the experimental results.

	Peak value after joint motion (V)	Settling time after joint motion (s)
Quintic polynomial trajectory	>10	9
Optimal trajectory without PZT control	1.28	3.8
Optimal trajectory with PZT control	0.72	2.3

As shown in Table 3, it can be observed that residual vibration of the link obtained from the proposed approach is only 0.72 V, less than 10 percent of those obtained by assuming that the trajectory corresponds to the quintic polynomial motion. Meanwhile, compared with the results along the quintic polynomial trajectory, the settling time of the residual vibrations along the optimal trajectory descends approximately 75 percent with the active control of the PZT actuators, reducing to 2.3 s from 9 s. As a conclusion, the proposed optimal trajectory planning approach is effective for vibration suppression of the flexible manipulator system.

6. Conclusions

The above sections have presented an optimal trajectory planning approach for vibration suppression of a flexible piezoelectric manipulator system with bonded PZT actuators. The proposed approach is a combination of the feed-forward trajectory planning method and L-type velocity feedback control of piezoelectric actuators based on the Lyapunov approach. The dynamic equations of the link are derived using Hamilton's principle and assumed mode method. In the procedure of trajectory planning, the flexible piezoelectric manipulator system is taken as a whole; rigid motion of the joint, elastic vibration of the link, and active control of the PZT actuators are all considered. Specifically, the joint controller is responsible for trajectory tracking and gross vibration suppression of the link during motion, while the active controller of actuators is expected to deal with residual vibrations after joint motion. The joint angle of the link is expressed as a quintic polynomial function. And the sum of the link vibration energy is chosen as the objective function. Then, the optimal trajectory planning approach is constructed using genetic algorithm. Simulation and experimental results validate the effectiveness of the proposed method. Both the settling time and peak value of the link vibrations along the optimal trajectory descend significantly, with the active control of the PZT actuators. As a conclusion, the proposed optimal trajectory planning approach is effective for vibration suppression of the flexible piezoelectric manipulator system.

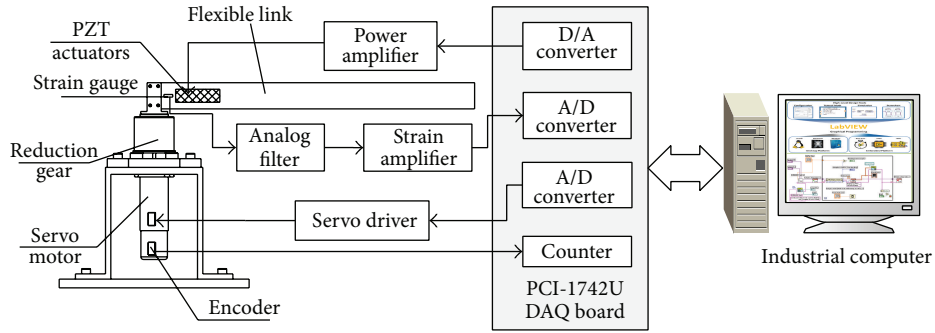


FIGURE 6: Schematic diagram of the experimental setup.

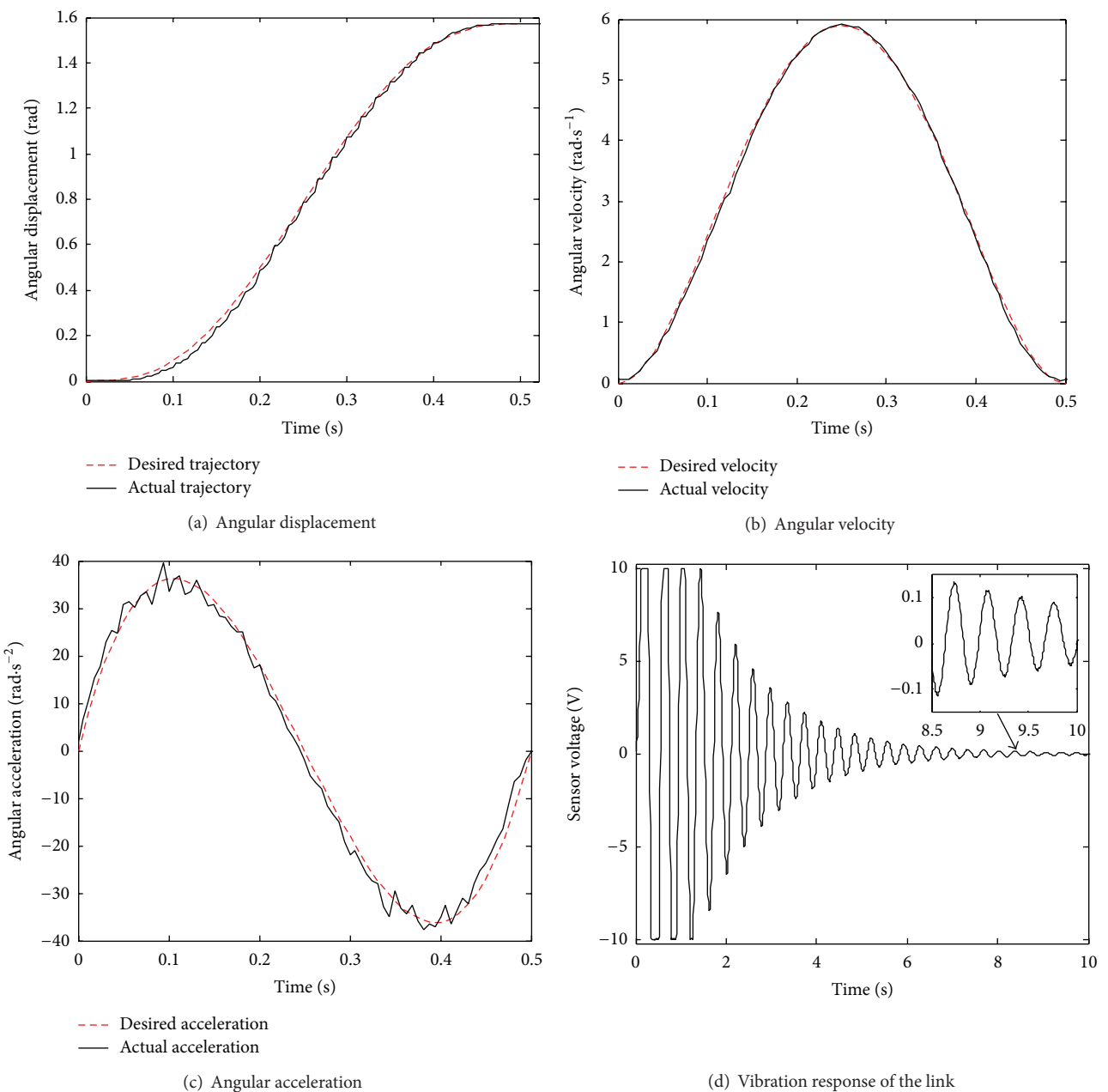


FIGURE 7: Experimental results of the link along the quintic polynomial trajectory.

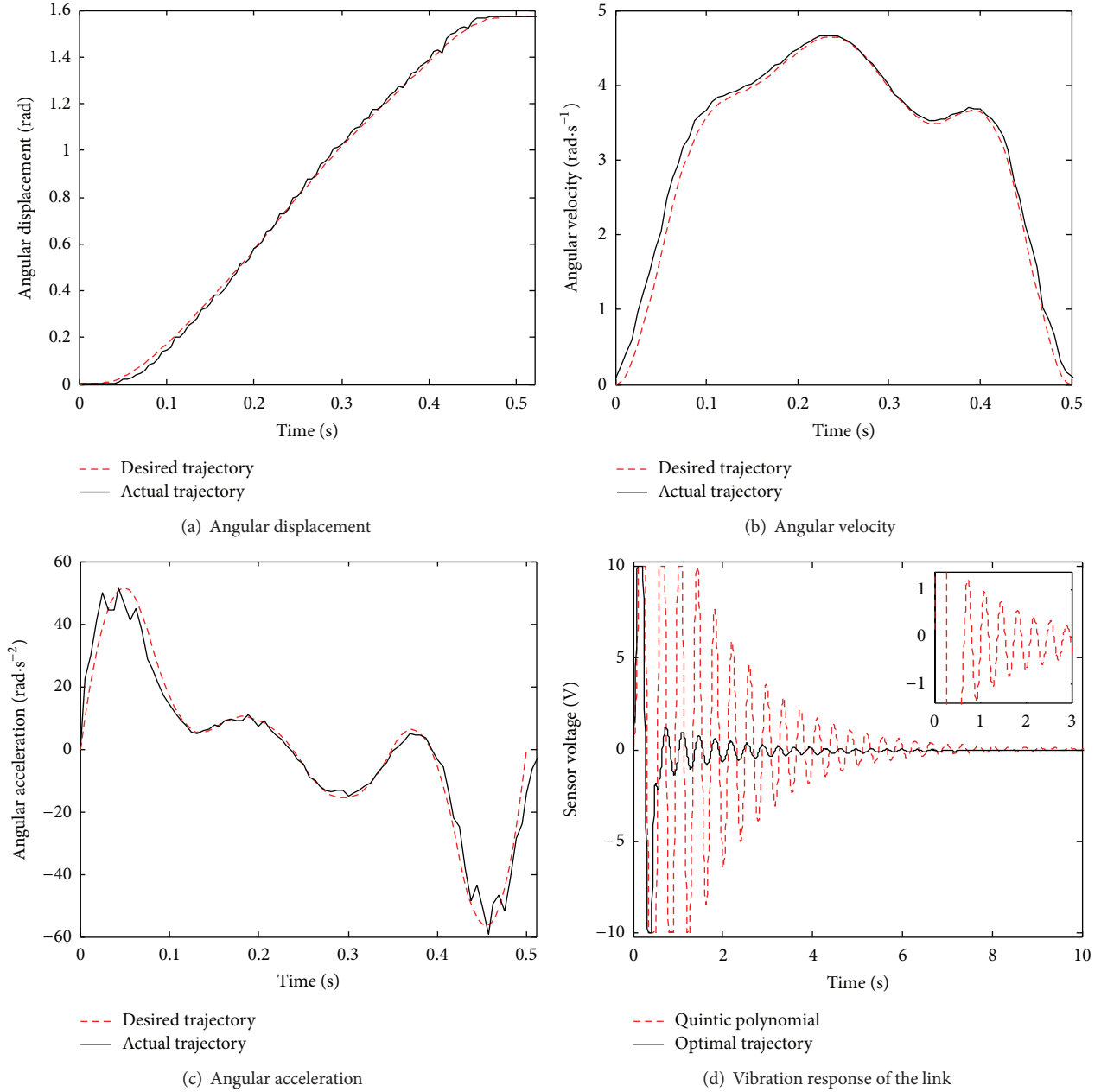


FIGURE 8: Experimental results of the link along the optimal trajectory.

Appendix

The position vector \mathbf{p} of the link relative to the inertial frame at an arbitrary location x can be expressed as

$$\mathbf{p} = \begin{bmatrix} p_x \\ p_y \end{bmatrix} = \begin{bmatrix} (r+x) \cos \theta(t) - w(x,t) \sin \theta(t) \\ (r+x) \sin \theta(t) + w(x,t) \cos \theta(t) \end{bmatrix}, \quad (\text{A.1})$$

where r is the radius of the rigid hub, $\theta(t)$ is the joint angle, and $w(x,t)$ is the elastic deflection of the link.

The kinetic energy and the potential energy of the flexible manipulator system can be written as

$$\begin{aligned} T &= \frac{1}{2} \int_0^{l_b} \rho_b A_b(x) (\dot{p}_x^2 + \dot{p}_y^2) dx \\ &\quad + \frac{1}{2} \int_{x_s}^{x_s+l_p} 2\rho_p A_p (\dot{p}_x^2 + \dot{p}_y^2) dx, \\ V_p &= \frac{1}{2} \int_0^{l_b} E_b I_b \{w''(x,t)\}^2 dx \\ &\quad + \frac{1}{2} \int_{x_s}^{x_s+l_p} E_p I_p \{w''(x,t)\}^2 dx. \end{aligned} \quad (\text{A.2})$$

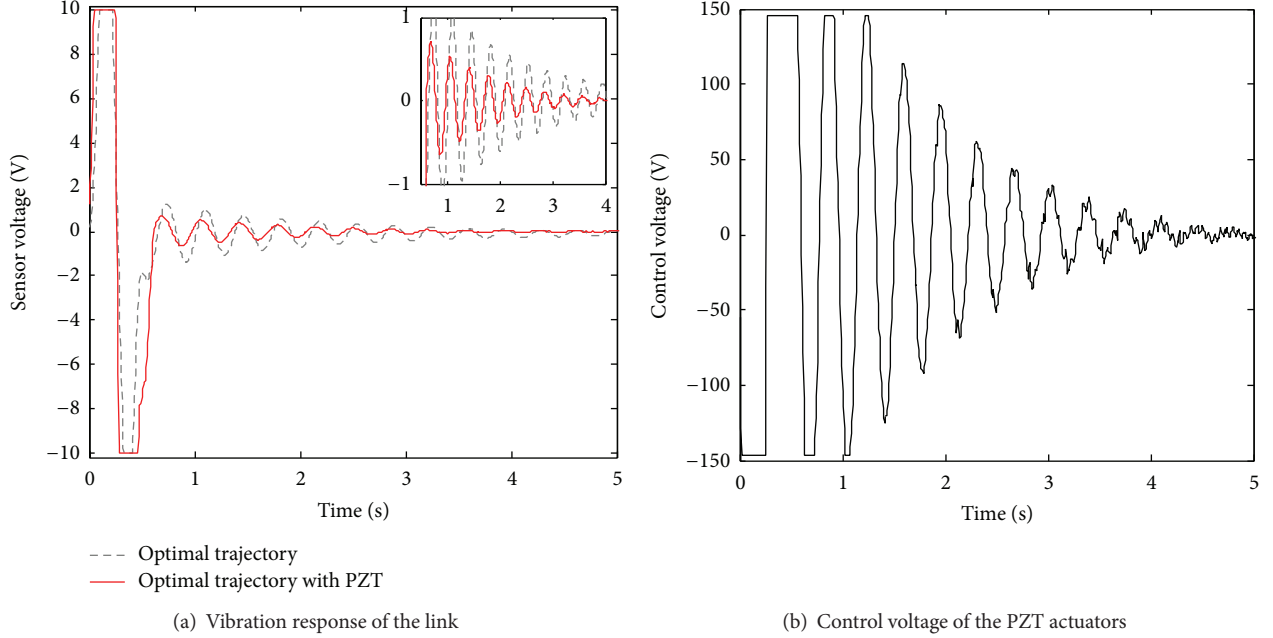


FIGURE 9: Experimental results of the link along the optimal trajectory with PZT control.

Here, ρA is the effective mass per unit length of the structure. ρ_b , A_b , l_b and ρ_p , A_p , l_p denote the density, cross-sectional area, and length of the link and PZT actuators, respectively. x_s is the start coordinate of the PZT actuators to the clamped side. And EI is the equivalent flexural rigidity of the link with PZT actuators. E_b , I_b and E_p , I_p denote the modulus of elasticity, the moment of inertia of the link, and PZT actuators, respectively.

The virtual work carried out by the moment $M(t)$ of PZT actuators and the input torque acting on the hub $\tau(t)$ can be evaluated as

$$\delta W = \tau(t) \delta \theta(t) + M(t) \delta w'(x_s, t). \quad (\text{A.3})$$

As each PZT actuator is bonded to each side of the link, the bending moment $M(t)$ resulting from the voltage applied to the PZT actuators is given by

$$M(t) = -2E_p d_{31} b_p h_p V(t) = cV(t), \quad (\text{A.4})$$

where d_{31} is the piezoelectric constant, b_p and h_p are the width and thickness of the PZT actuators respectively, and $V(t)$ is a uniform control voltage applied to the PZT actuators.

Extended Hamilton's principle is used to derive the system equation. Hamilton's principle is given by the following variational statement:

$$\int_{t_1}^{t_2} (\delta T - \delta V + \delta W) dt = 0. \quad (\text{A.5})$$

Substituting (A.1)~(A.3), incorporating (1) into (A.5), the governing equations of the system can be derived as

$$\begin{aligned} I_{\theta\theta} \ddot{\theta} + \mathbf{q}^T \mathbf{m}_{qq} \mathbf{q} \ddot{\theta} + 2\dot{\mathbf{q}}^T \mathbf{m}_{q\theta} \dot{\theta} + \mathbf{m}_{\theta q} \ddot{\mathbf{q}} &= \tau(t), \\ \mathbf{m}_{qq} \ddot{\mathbf{q}} + \mathbf{m}_{\theta q}^T \ddot{\theta} + \mathbf{K}_q \mathbf{q} - \mathbf{m}_{q\theta} \mathbf{q} \dot{\theta}^2 &= cV(t) \left[\widehat{\Phi}' \right]^T(x_s), \end{aligned} \quad (\text{A.6})$$

where the corresponding coefficients are defined as

$$\begin{aligned} I_{\theta\theta} &= \frac{1}{3} \rho_b A_b [(r + l_b)^3 - r^3] \\ &\quad + \frac{1}{3} 2\rho_p A_p [(r + x_s + l_p)^3 - (r + x_s)^3], \\ \mathbf{m}_{q\theta} &= \int_0^{l_b} \rho_b A_b \Phi^T(x) \Phi(x) dx \\ &\quad + \int_{x_s}^{x_s+l_p} \rho_p A_p \Phi^T(x) \Phi(x) dx, \\ \mathbf{m}_{\theta q} &= \int_0^{l_b} \rho_b A_b (x + r) \Phi(x) dx \\ &\quad + \int_{x_s}^{x_s+l_p} \rho_p A_p (x + r) \Phi(x) dx, \\ \mathbf{K}_q &= \int_0^{l_b} E_b I_b [\Phi'']^T(x) \Phi''(x) dx \\ &\quad + \int_{x_s}^{x_s+l_p} E_p I_p [\Phi'']^T(x) \Phi''(x) dx, \\ \widehat{\Phi}(x_s) &= \Phi(x_s + l_p) - \Phi(x_s). \end{aligned} \quad (\text{A.7})$$

Conflict of Interests

The authors declare that there is no conflict of interests regarding the publication of this paper.

Acknowledgments

This work was supported by the National Natural Science Foundation of China (no. 51375433) and Zhejiang Provincial Natural Science Foundation of China (Grant nos. LY13E050008 and LQ15E050002). The authors would also like to thank the K. C. Wong Magna Fund in Ningbo University for its support.

References

- [1] C. T. Kiang, A. Spowage, and C. K. Yoong, "Review of control and sensor system of flexible manipulator," *Journal of Intelligent and Robotic Systems: Theory and Applications*, vol. 77, no. 1, pp. 187–213, 2014.
- [2] M. Chu, G. Chen, Q.-X. Jia, X. Gao, and H.-X. Sun, "Simultaneous positioning and non-minimum phase vibration suppression of slewing flexible-link manipulator using only joint actuator," *Journal of Vibration and Control*, vol. 20, no. 10, pp. 1488–1497, 2013.
- [3] W. Singhose, "Command shaping for flexible systems: a review of the first 50 years," *International Journal of Precision Engineering and Manufacturing*, vol. 10, no. 4, pp. 153–168, 2009.
- [4] Z. Mohamed, A. K. Chee, A. W. I. Mohd Hashim, M. O. Tokhi, S. H. M. Amin, and R. Mamat, "Techniques for vibration control of a flexible robot manipulator," *Robotica*, vol. 24, no. 4, pp. 499–511, 2006.
- [5] M. S. Alam and M. O. Tokhi, "Designing feedforward command shapers with multi-objective genetic optimisation for vibration control of a single-link flexible manipulator," *Engineering Applications of Artificial Intelligence*, vol. 21, no. 2, pp. 229–246, 2008.
- [6] M. O. T. Cole and T. Wongratanaphisan, "A direct method of adaptive FIR input shaping for motion control with zero residual vibration," *IEEE/ASME Transactions on Mechatronics*, vol. 18, no. 1, pp. 316–327, 2013.
- [7] H. Wu, F. C. Sun, Z. Q. Sun, and L. C. Wu, "Optimal trajectory planning of a flexible dual-arm space robot with vibration reduction," *Journal of Intelligent and Robotic Systems*, vol. 40, no. 2, pp. 147–163, 2004.
- [8] H. R. Heidari, M. H. Korayem, M. Haghpanahi, and V. F. Batlle, "Optimal trajectory planning for flexible link manipulators with large deflection using a new displacements approach," *Journal of Intelligent and Robotic Systems: Theory and Applications*, vol. 72, no. 3-4, pp. 287–300, 2013.
- [9] K. Springer, H. Gattringer, and P. Stauffer, "On time-optimal trajectory planning for a flexible link robot," *Proceedings of the Institution of Mechanical Engineers, Part I: Journal of Systems and Control Engineering*, vol. 227, no. 10, pp. 752–763, 2013.
- [10] Y. Choi, J. Cheong, and H. Moon, "A trajectory planning method for output tracking of linear flexible systems using exact equilibrium manifolds," *IEEE/ASME Transactions on Mechatronics*, vol. 15, no. 5, pp. 819–826, 2010.
- [11] J. Lessard, P. Bigras, Z. Liu, and B. Hazel, "Characterization, modeling and vibration control of a flexible joint for a robotic system," *Journal of Vibration and Control*, vol. 20, no. 6, pp. 943–960, 2014.
- [12] M. Moallem, M. R. Kermani, R. V. Patel, and M. Ostojic, "Flexure control of a positioning system using piezoelectric transducers," *IEEE Transactions on Control Systems Technology*, vol. 12, no. 5, pp. 757–762, 2004.
- [13] V. B. Nguyen and A. S. Morris, "Genetic algorithm tuned fuzzy logic controller for a robot arm with two-link flexibility and two-joint elasticity," *Journal of Intelligent and Robotic Systems: Theory and Applications*, vol. 49, no. 1, pp. 3–18, 2007.
- [14] J. Das and N. Sarkar, "Passivity-based target manipulation inside a deformable object by a robotic system with non-collocated feedback," *Advanced Robotics*, vol. 27, no. 11, pp. 861–875, 2013.
- [15] C.-Y. Lin and C.-M. Chang, "Hybrid proportional derivative/repetitive control for active vibration control of smart piezoelectric structures," *Journal of Vibration and Control*, vol. 19, no. 7, pp. 992–1003, 2013.
- [16] J.-J. Wei, Z.-C. Qiu, J.-D. Han, and Y.-C. Wang, "Experimental comparison research on active vibration control for flexible piezoelectric manipulator using fuzzy controller," *Journal of Intelligent and Robotic Systems: Theory and Applications*, vol. 59, no. 1, pp. 31–56, 2010.
- [17] D. Sun, J. K. Mills, J. J. Shan, and S. K. Tso, "A PZT actuator control of a single-link flexible manipulator based on linear velocity feedback and actuator placement," *Mechatronics*, vol. 14, no. 4, pp. 381–401, 2004.
- [18] K. Gurses, B. J. Buckham, and E. J. Park, "Vibration control of a single-link flexible manipulator using an array of fiber optic curvature sensors and PZT actuators," *Mechatronics*, vol. 19, no. 2, pp. 167–177, 2009.
- [19] L. Y. Li, G. B. Song, and J. P. Ou, "Adaptive fuzzy sliding mode based active vibration control of a smart beam with mass uncertainty," *Structural Control and Health Monitoring*, vol. 18, no. 1, pp. 40–52, 2011.
- [20] S.-B. Choi, M.-S. Seong, and S. H. Ha, "Accurate position control of a flexible arm using a piezoactuator associated with a hysteresis compensator," *Smart Materials and Structures*, vol. 22, no. 4, Article ID 045009, 2013.
- [21] Y. S. Bian and Z. H. Gao, "Impact vibration attenuation for a flexible robotic manipulator through transfer and dissipation of energy," *Shock and Vibration*, vol. 20, no. 4, pp. 665–680, 2013.
- [22] A. A. Ata, "Inverse dynamic analysis and trajectory planning for flexible manipulator," *Inverse Problems in Science and Engineering*, vol. 18, no. 4, pp. 549–566, 2010.
- [23] M. D. G. Marcos, J. A. Tenreiro Machado, and T.-P. Azevedo-Perdicoulis, "A multi-objective approach for the motion planning of redundant manipulators," *Applied Soft Computing Journal*, vol. 12, no. 2, pp. 589–599, 2012.
- [24] T. Nestorović and M. Trajkov, "Optimal actuator and sensor placement based on balanced reduced models," *Mechanical Systems and Signal Processing*, vol. 36, no. 2, pp. 271–289, 2013.
- [25] W. C. Sun, H. J. Gao, and O. Kaynak, "Adaptive backstepping control for active suspension systems with hard constraints," *IEEE/ASME Transactions on Mechatronics*, vol. 18, no. 3, pp. 1072–1079, 2013.

Research Article

Experimental and Theoretical Study on Influence of Different Charging Structures on Blasting Vibration Energy

Wenbin Gu, Zhenxiong Wang, Jianghai Chen, Jianqing Liu, and Ming Lu

College of Field Engineering, PLA University of Science and Technology, Nanjing, Jiangsu 210007, China

Correspondence should be addressed to Zhenxiong Wang; wangzhenxiong70310@126.com

Received 20 April 2015; Revised 1 July 2015; Accepted 2 July 2015

Academic Editor: Mario Terzo

Copyright © 2015 Wenbin Gu et al. This is an open access article distributed under the Creative Commons Attribution License, which permits unrestricted use, distribution, and reproduction in any medium, provided the original work is properly cited.

As an important parameter in blasting design, charging structure directly influences blasting effect. Due to complex conditions of this blasting and excavating engineering in Jiangsu, China, the authors carried out comparative researches with coupling structure, air-decoupling structure, and water-decoupling structure. After collecting, comparing, and analyzing produced signals on blasting vibration, the authors summarized that when proportional distances are the same, water-decoupling structure can reduce instantaneous energy of blasting vibration more effectively with more average rock fragmentation and less harm of dust. From the perspective of impedance matching, the present paper analyzed influence of charging structure on blasting vibration energy, demonstrating that impedance matching relationship between explosive and rock changes because of different charging structures. Through deducing relationship equation that meets the impedance matching of explosive and rock under different charging structures, the research concludes that when blasting rocks with high impedance, explosive with high impedance can better transmit blasting energy. Besides, when employing decoupling charging, there exists a reasonable decoupling coefficient helping realize impedance matching of explosive and rock.

1. Introduction

In rock blasting of engineering, energy that can be effectively used through explosion approximately accounts for 60~70 percent of the total explosive energy. The rest may be used in exploding surrounding medium or produce harmful effects, such as blasting vibration, blasting shock wave, blasting flying blasting, blasting soot, blasting noise, and blasting harmful gas [1, 2]; thus, it is of great significance to improve effective use of blasting vibration energy. According to damage characteristics of rock blasting, with explosion as the center, there are crushed zone, fracture zone, and vibration zone [3], from the center to distant area, and how to apply more explosive energy to fracture zone is key to engineering on rock blasting and excavating. Parameters affecting geotechnical blasting results are mainly on characteristics of rock and characteristics of explosive and blasting parameters and specific parameters are over 20 categories. When blasting environment and explosive are determined, charging structure plays a pivotal role in influencing blasting energy transmission. With decoupling charging, decoupling way between blasting hole

and blasting charging, decoupling coefficient, compressible degree of decoupling medium (air or water), and initiating position of charging will largely affect transmitting process of blasting energy. Aimed at investigating charging structure's influence on blasting energy and effect, scholars both at home and abroad have carried out numerous researches on experiment and numerical simulation. Day examined distribution of explosive's pressure on rock hole wall of air-decoupling, water-decoupling and coupling charging structures with the same distance explosive conditions [4]. Zong and Meng analyzed effects of different charging structures of blasting hole on blasting energy and concluded that decoupling charging structure is beneficial under certain conditions [5]. Chen et al. conducted experiments on charging structure's influence on blasting seismic effects and concluded attenuation law of particle vibration velocity and vibration frequency [6]. Wang and Li carried out comparative numerical calculation on different radial coupling coefficient of water-decoupling charging structure in infinite concrete medium and then comprehensively analyzed relationships between damage zone distribution and pore wall pressure and acceleration as

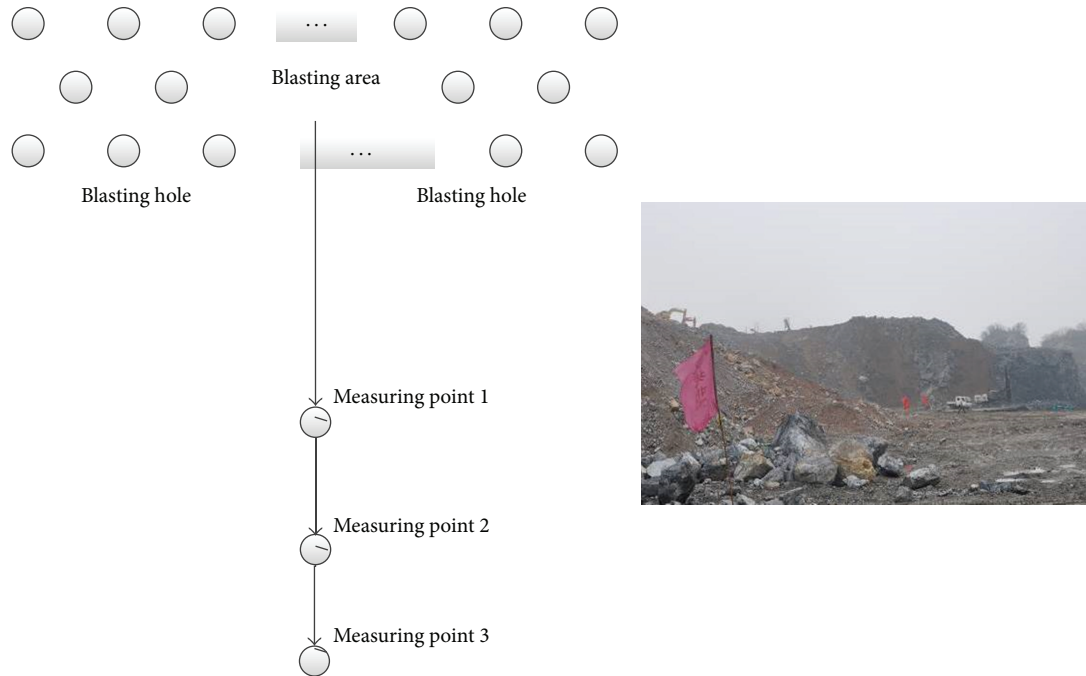


FIGURE 1: Schematic diagram and site layout of measuring points and blasting region.

well as velocity and radial decoupling coefficient [7]. Pape et al. carried out finite-element analysis methods, studied the explosion phenomena and effects of explosions on structures systematically, and predicted the harmful effects of blasting with different criterions [8, 9]. By evaluating charging structure's influence on blasting effect and blasting vibration of near area, a large number of engineering practices, tests, and numerical simulations on charging structure indicate that decoupling charging structure can enhance utilization rate of explosive energy and improve blasting effect. However, in practical engineering, different construction environment requires different charging structures, yet there are not enough studies about analysis of energy transmission and blasting effects of different charging structures as well as carried energy of blasting vibration of far region of blasting. Hence, the present paper intends to explore relevant factors to provide an insightful reference for further investigations.

During rock excavation of engineering scene in Jiangsu province, researchers adopted rock drilling blasting method, which is widely applied in geotechnical engineering. Because of complexity of test scene and condition, the test accordingly selected different blasting charging structures. Through collecting blasting vibration signals, vibration speed was obtained, and so was instantaneous explosion vibration energy, and it was concluded that different charging structures' attenuation law of blasting vibration is different [10]. After explosion, observation on rock fragmentation of blasting area revealed that distribution of rock fragmentation produced by different blasting charging structures is obviously different. Based on the test, this research theoretically analyzed energy transmission of different charging structures from the perspective of impedance matching. The present study was designed to deduce the law of different charging

structures' influence on blasting vibration energy of far region of blasting and provide reference for controlling side-effects of blasting vibration and designing parameters of charging structure.

2. Experimental Research

2.1. Set of Tests. To determine the influence of different charging structures on blasting vibration energy, the present paper took a blasting engineering in Jiangsu, China, as the example, carrying out experimental researches on the transmission of seismic wave of coupling charging, water-decoupling charging, and air-decoupling charging structures. Through test and analysis on vibration velocity of three charging structures in far region of blasting, blasting vibration energy was calculated.

Blasting network employed in experiment was multiple row hole blasting with differential time of 25 ms and two holes were blasted together; consequently, dosage of the two holes should be counted together to get the single detonation quantity in fitting calculating formula. The hole diameter was 0.09 m, and, in experiments of decoupling charging, charging diameter was 0.07 m, hole depth was 10 m, and charging length was 7 m. Schematic diagram as well as site layout of blasting region and measuring points are clarified in Figure 1.

Tests monitored vibration velocity with blasting vibration tester TC-4850 produced by Zhongke Measurement and Control Company. The tester has three parallel channels for monitoring vibration velocity in three directions; sampling rate is 1~50 KHz, with frequency response range 0~10 KHz. TC-4850 is widely used in engineering and its stability as well as accuracy can meet test requirements. In order to better gather blasting vibration signals, the test fixed collecting part

TABLE 1: Peak vibration velocity of different charging structures at measuring points (cm/s).

Charging structure	Proportional distance r	v_{\max}^x	v_{\max}^y	v_{\max}^z	v_{sum}	v_{formula}
Coupling charging	4.281	14.361	11.769	19.666	20.180	6.614~25.986
	8.561	4.136	0.003	7.652	7.936	2.339~10.554
	12.842	3.143	3.244	3.430	4.748	1.273~6.230
Air-decoupling charging	13.922	1.305	2.155	1.814	2.561	0.962~4.888
	14.228	1.753	1.003	1.108	2.481	0.932~4.754
	18.573	0.667	0.003	1.924	1.991	0.625~3.363
	21.341	1.360	0.757	0.888	1.792	0.507~2.806
	23.208	1.210	1.242	0.962	1.671	0.447~2.516
	30.826	1.096	0.677	0.767	1.237	0.292~1.740
Water-decoupling charging	12.747	1.103	1.952	2.483	2.654	1.099~5.484
	16.995	0.574	1.320	0.943	1.618	0.714~3.773
	25.493	0.534	0.003	1.119	1.170	0.388~2.227



FIGURE 2: Site layout of blasting vibration tester.

of TC-4850 on the ground with gypsum and the site set is apparent in Figure 2.

2.2. Test Results. Prediction of blasting vibration is usually judged by peak vibration velocity of the particle, and the most commonly used one is Steve Sadove formula, where relationship between peak vibration velocity and proportional distance is [11]

$$v = kr^{-\alpha}. \quad (1)$$

Here, r is for proportional distance, and its calculating formula is $r = R/\sqrt[3]{Q}$, where R is the distance from blasting hole with m as the unit; k and α are coefficients associated with explosive conditions and rock properties. Q is for the total dosage of one time with kg as the unit. Rock in test area is limestone that belongs to middle-hard rock, according to whose characteristics, k 's value range in the formula is 50~150, and α 's value range is 1.3~1.5 [12].

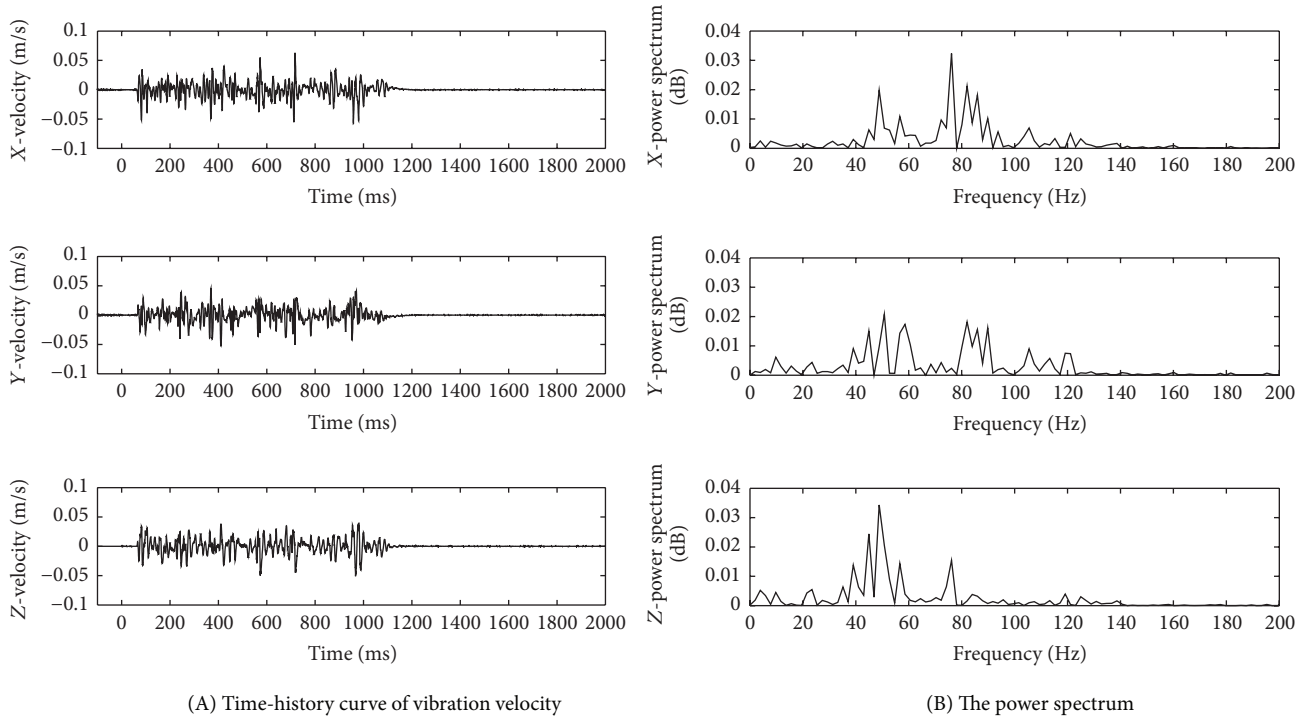
Figure 3 is time-history curve of vibration velocity and power spectrum of different charging structures. The main frequency of blasting vibration is about 0~200 Hz, and, to reduce high frequency's influence on blasting vibration signals, those high frequency components are processed by software in data analysis to get the table of peak vibration velocity, as is demonstrated in Table 1. The superscript stands for direction. In Table 1, v_{sum} 's are in the data range deduced and calculated from experience formula (1), so the test data

are reliable. From those data, it can be seen that particle velocity of measuring points in three directions varies numerically, and peak value of the single component will also vary under different blasting environments, time, and frequency. So it is reasonable to choose square root from the square sum of three portions' peak speed as the particle's peak vibration velocity. The value of peak vibration velocity of the particle is [13]

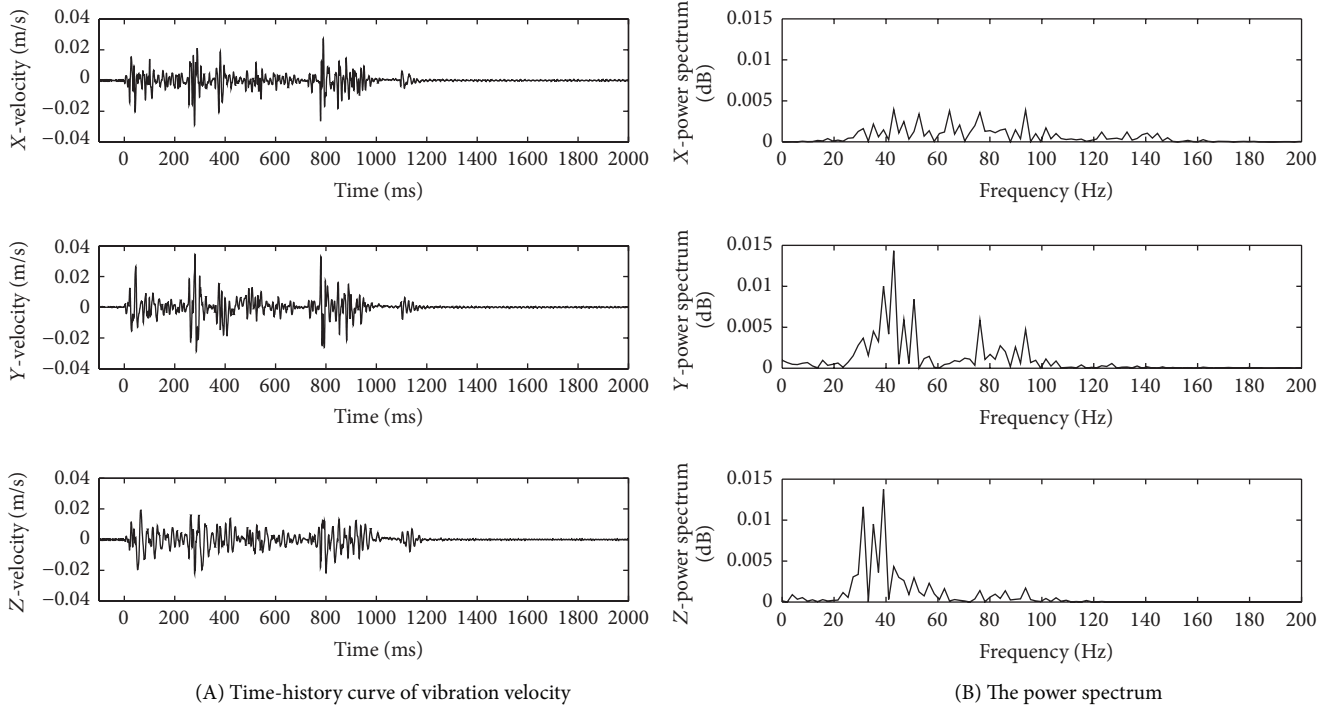
$$|v_{\text{sum}}| = \sqrt{(v_x)^2 + (v_y)^2 + (v_z)^2}. \quad (2)$$

Therefore, to better predict blasting vibration, it may be most reasonable to evaluate it with module of the total vibration velocity vector (like formula (2)) [14]. With analysis of test data through least square method [15], it is indicated that, for different charging structures, values of k and α in vibration velocity formula are demonstrated in Table 2. And Figure 4 displays data fitting curve of different charging structures.

Table 2 clearly indicates that there exist huge distinctions among coefficients in vibration predicting formula fitted for different charging structures. To better compare and analyze three charging structures' influence on blasting vibration, α can be supposed as 1.3; then the analysis can be realized with comparison of k 's values. Through calculating and data fitting, when $\alpha = 1.3$ and proportional distance r are



(a) Coupling charging structure $r = 12.842$



(b) Air-decoupling charging structure $r = 13.922$

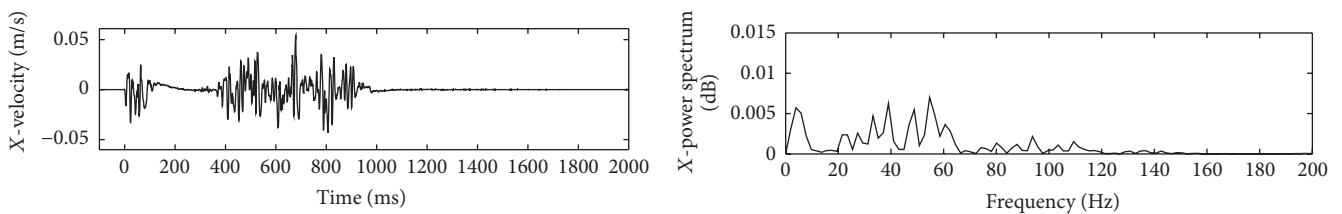


FIGURE 3: Continued.

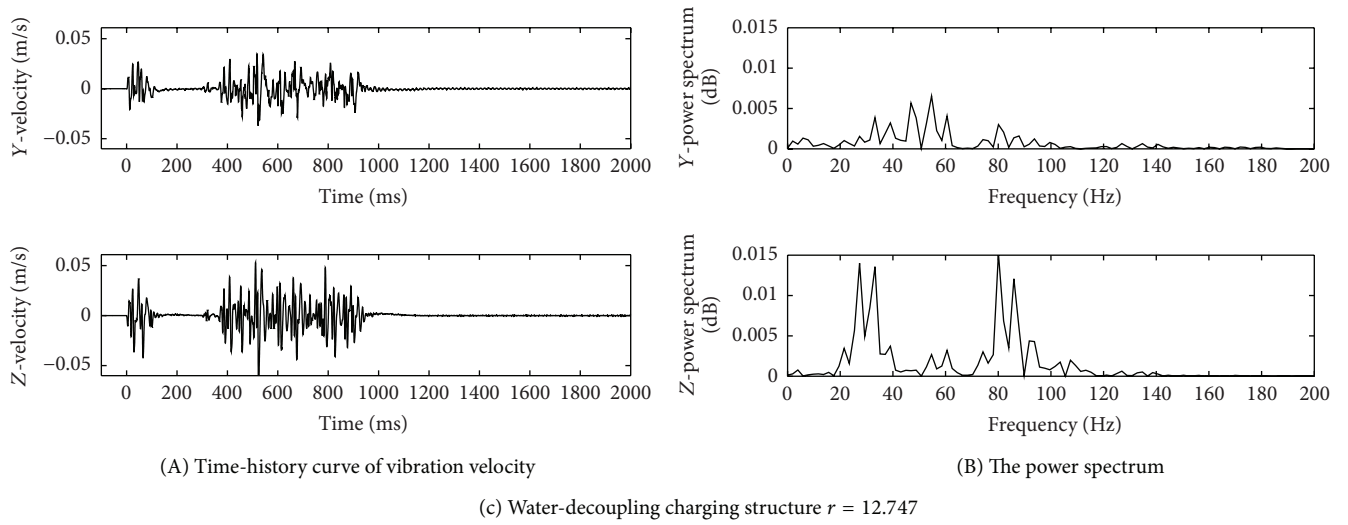


FIGURE 3: Schedule chart of different charging structures' vibration velocity and power spectrum in three directions.

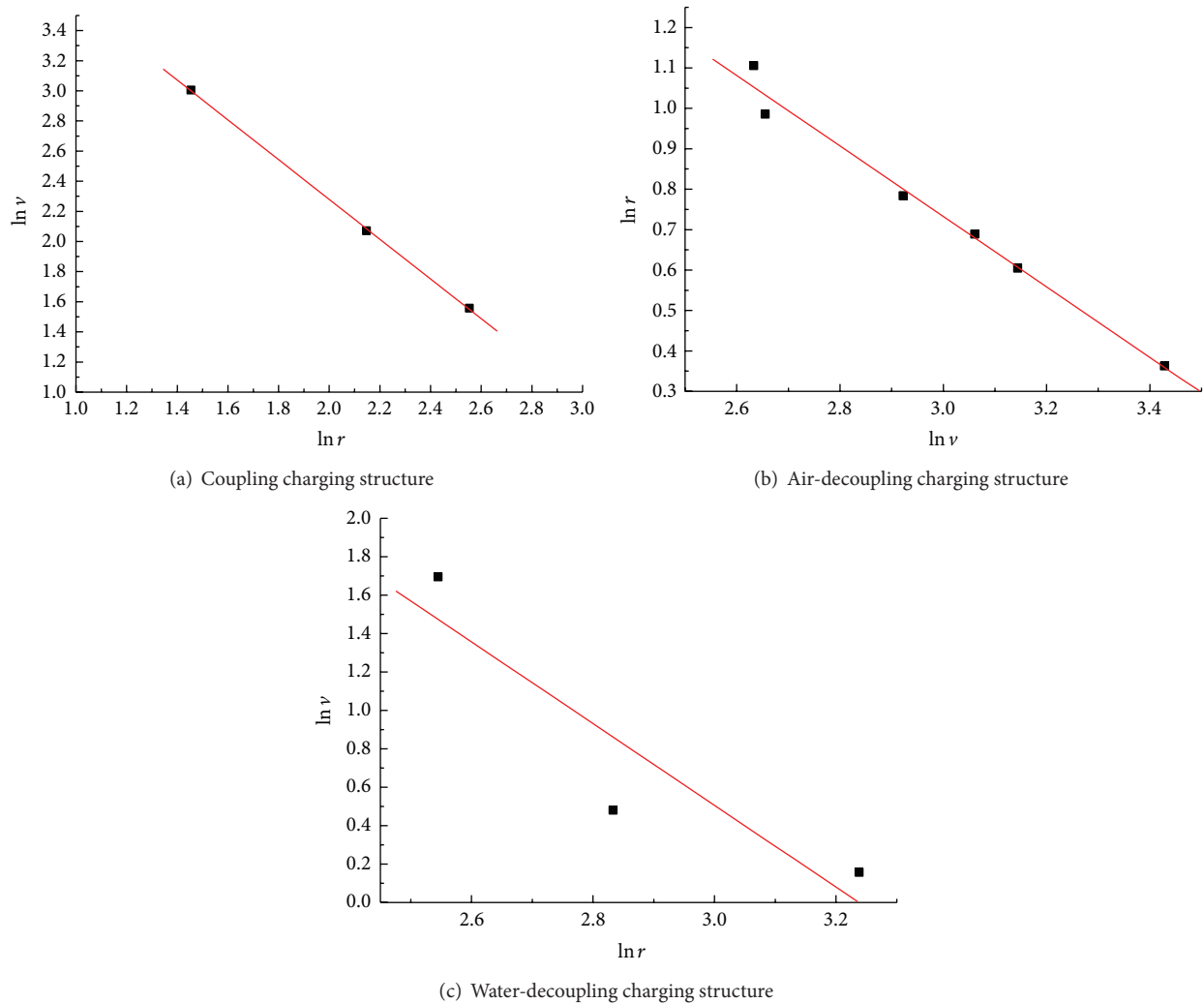


FIGURE 4: Fitting curve of three charging structures.

TABLE 2: Value of k and α in fitting vibration formula of different charging structures.

Charging structure	k	α	Correlation coefficient	k 's value with $\alpha = 1.3$
Coupling	136.866	1.320	-0.99986	131.368
Air-decoupling	28.479	0.872	-0.99231	101.646
Water-decoupling	47.500	1.157	-0.97652	71.586

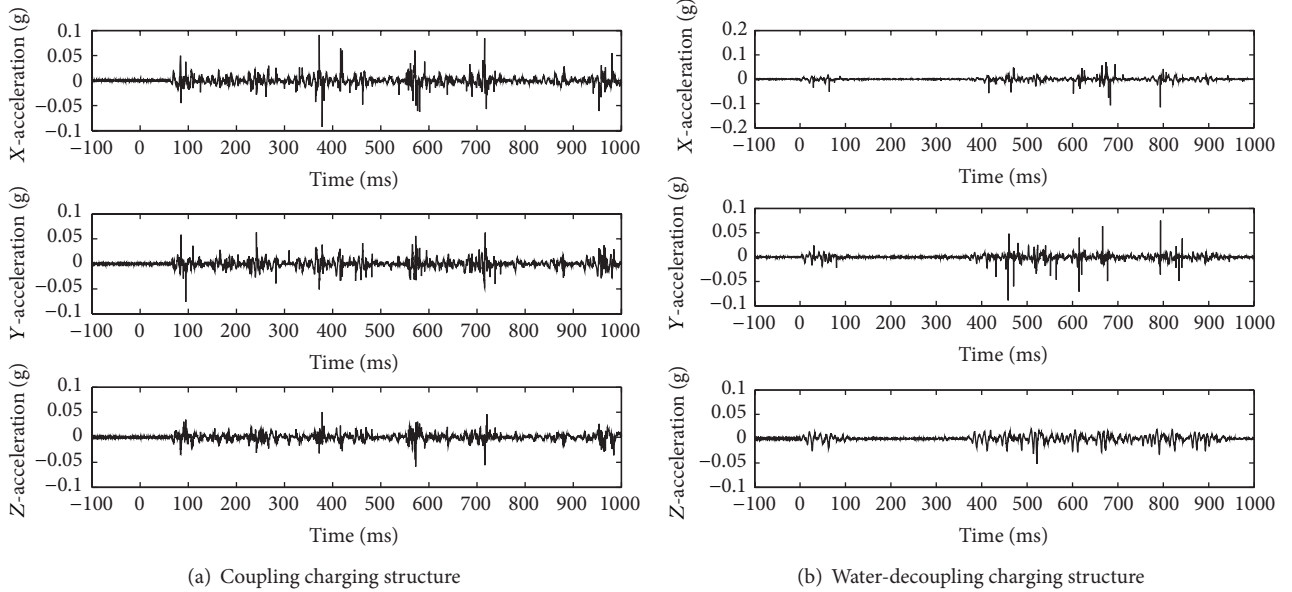


FIGURE 5: Schedule chart of different charging structures' vibration acceleration in three directions.

determined, vibration velocity formula of three charging structures can be compared as follows:

$$\begin{aligned}
 v_{\text{coupling}} &= 131.368r^{-1.3} > v_{\text{air-decoupling}} = 101.646r^{-1.3} \\
 &> v_{\text{water-decoupling}} = 71.586r^{-1.3}.
 \end{aligned}
 \quad (3)$$

In blasting rocks, instantaneous energy E of blasting vibration at a moment is proportional to v^2 ; that is, instantaneous energy of blasting vibration is proportional to vibration velocity's quadratic [16]; hence, instantaneous energy of blasting vibration carried by seismic wave of measuring points can be reflected by vibration velocity. With formula (3), relationship between instantaneous energy of blasting vibration of three charging structures is

$$E_{\text{coupling}} > E_{\text{air-decoupling}} > E_{\text{water-decoupling}}. \quad (4)$$

At measuring points with close rational distance, that is, $r = 12.842$ in coupling charging and $r = 12.747$ in water-decoupling charging, when charging structures are different, time-history curves of acceleration in three directions are shown in Figure 5, and peak value of vibration acceleration at that rational distance is about 0.1 g. If there exist structural buildings near the blasting area, a series of protective actions should be taken [17, 18]. Comparative relationship of vibration acceleration intensity of blasting with different charging structures is in accordance with conclusions in (3) on comparative relationship of vibration velocity intensity as well as (4) on comparative relationship of energy intensity.

3. Theoretical Research

Explosion produces detonation wave in the hole and when transmitting between different media, there may be refraction and reflection at the interface due to different wave impedance; thus, energy transmitted in wave may change. Test data suggest that, with different charging structures, detonation products have different effects on hole wall, distribution pressure produced on hole wall is different, and so is vibration energy at the measuring points of far region of blasting. According to speed fitting formula (3), vibration energy transmitted in coupling charging structure is the largest and that of water-decoupling charging is the smallest. From the perspective of impedance matching, when detonation products equal rock impedance, detonation products of coupling charging directly affect hole wall; explosive of air-decoupling charging structure explodes in the air, and detonation products inflate and fill the blasting hole and then affect hole wall; explosive of water-decoupling charging structure explodes in the water, and detonation products compress the medium water and then transmit blasting energy to rock. To sum up, when rock impedance is determined, detonation products of different charging structures have different impedance on the hole wall, so impedance matching relationships are different, suggesting that charging structure will have influence on blasting vibration energy.

No matter which kind of charging structure is adopted, detonation products will keep touching rock at the interface.

And, according to continuous conditions and Newton's third law, after reflection and transmission, velocity and stress of the particle on interface's both sides are equal; therefore, the following equation group can be deduced [3, 19]:

$$\begin{aligned} v_I + v_R &= v_T, \\ \sigma_I + \sigma_R &= \sigma_T. \end{aligned} \quad (5)$$

Here, v stands for particle's velocity, σ is particle's stress, and subscripts I , R , and T , respectively, refer to relevant elements disturbed by incident, reflection, and transmission. As momentum of wave-front conserves

$$\frac{\sigma_I}{\rho_b C_b} - \frac{\sigma_R}{\rho_b C_b} = \frac{\sigma_T}{\rho_y C_y}, \quad (6)$$

combine (5)~(6) as follows:

$$\begin{aligned} \sigma_R &= F\sigma_I, \\ v_R &= -Fv_I, \\ \sigma_T &= T\sigma_I, \\ v_T &= nTv_I, \\ n &= \frac{(\rho_b C_b)}{(\rho_y C_y)}. \end{aligned} \quad (7)$$

Here, $\rho_b C_b$ and $\rho_y C_y$, respectively, stand for denotation products of the explosive and rock's impedance, with n as impedance ratio. Combine the equations, and then transmission coefficient $T = 2/(1+n)$ and reflection coefficient $F = (1-n)/(1+n)$ can be calculated. Therefore, T and F depend on impedance ratio of denotation products and the rock. When $n = 1$, $\rho_b C_b = \rho_y C_y$, $T = 1$, and $F = 0$, the largest amount of energy can be transmitted from denotation products to the rock.

3.1. Coupling Charging. Coupling charging means that explosive fills hole in direct contact with the hole wall. When explosive blows up, explosion products of denotation directly affect the hole wall, transmitting blasting energy to the rock to make it broken with cracks; then some energy can be transmitted in the form of seismic wave to far region of blasting. The transmission of blasting energy is relatively easy and according to the denotation theory of denotation explosive [13, 17], due to high denotation pressure, explosive's initial pressure can be negligible, and then denotation products' acoustic velocity and density can be

$$D_b = \frac{\gamma}{\gamma + 1} D_z, \quad (8)$$

$$\rho_b = \frac{\gamma + 1}{\gamma} \rho_z. \quad (9)$$

Here, ρ and D , respectively, are density and velocity, subscripts z and b stand for explosive and denotation products, and γ stands for adiabatic index. When denotation products'

wave impedance equals that of the explosive (i.e., impedance ratio $n = 1$), the largest amount of energy from explosion can get transmitted into the rock. Though it is generally difficult to realize impedance matching, according to relevant theories, explosives with high impedance can better help transmit explosive energy to rocks with high impedance.

3.2. Air-Decoupling Charging. When air-decoupling charging structure was adopted, charging diameter d_z is different from that of blasting hole d_0 and decoupling coefficient of charging is k_d :

$$k_d = \frac{d_0}{d_z}. \quad (10)$$

After explosive blasting, detonation products firstly transmitted in air cushion, forming air shock wave and acting on the hole wall. Detonation products expand adiabatically in the hole. Ignore quality of the air and then relationship between decoupling coefficient and density of the denotation products ρ_k is

$$\frac{\rho_b}{\rho_k} = \frac{d_0^2}{d_z^2} = k_d^2. \quad (11)$$

Subscript k stands for correlative of detonation products in the air after explosion (same as below). Combine (9)~(11):

$$\rho_k = \frac{\gamma + 1}{\gamma} k_d^{-2} \rho_z. \quad (12)$$

Regardless of other factors' influence, detonation products in the hole follow adiabatic expansion; then

$$\begin{aligned} \frac{P_k}{P_b} &= \left(\frac{\rho_k}{\rho_b} \right)^\gamma, \\ P_b &= \frac{1}{8} \rho_z D_z^2. \end{aligned} \quad (13)$$

Here, P_k refers to detonation products' pressure that fills the hole and P_b is detonation products' initial pressure upon explosive's blasting. Combine (13):

$$P_k = \frac{1}{8} k_d^{-2\gamma} \rho_z D_z^2. \quad (14)$$

Relationship between detonation products' acoustic velocity D_k and pressure in the hole P_k is

$$D_k = \left(\frac{\gamma P_k}{\rho_k} \right)^{1/2} = \frac{\sqrt{2(\gamma + 1)}}{4(\gamma + 1)} \gamma k_d^{1-\gamma} D_z. \quad (15)$$

Combine (12) and (15); it can be seen that, in air-decoupling charging structure, impedance of detonation products operating on the wall of borehole after explosion is

$$\rho_k D_k = \frac{\sqrt{2(\gamma + 1)}}{4} k_d^{-\gamma-1} \rho_z D_z. \quad (16)$$

Supposing adiabatic exponent γ is determined, in air-decoupling charging structure, relationship between detonation products' impedance and explosive's impedance is relevant to decoupling coefficient. According to impedance matching theory, when impedance of detonation products equals that of the rock, energy produced by explosion can be transmitted to the rock more effectively; that is

$$\rho_k D_k = \frac{\sqrt{2(\gamma+1)}}{4} k_d^{-\gamma-1} \rho_z D_z = \rho_y D_y. \quad (17)$$

As decoupling coefficient k_d is larger than 1, $\rho_k D_k$ decreases with the increase of k_d . From the perspective of impedance matching, to better transmit blasting energy, it is necessary to synthetically analyze relationship between the rock's impedance of blasting area, explosive's categories, and decoupling coefficient of the charging. When rock and explosive are determined, if air-decoupling charging structure is selected, decoupling coefficient in (17) should be adopted to advance the transmission of blasting energy.

3.3. Water-Decoupling Charging. When adopting water-decoupling charging structure to blast, detonation products expand and compress the water, resulting in changes of water's density and wave velocity. Based on adiabatic expansion rule and the theory of fluid mechanics [20], the following equations can be concluded:

$$\begin{aligned} \frac{\rho_s}{\rho_{s0}} &= \frac{d_0^2 - d_z^2}{d_0^2 - (d_z + \omega)^2} \\ D_s &= \left(\frac{k_w}{\rho_s} \right)^{1/2} \\ dP &= \frac{k_w}{V} dV. \end{aligned} \quad (18)$$

Here, ρ_s is water's density under the influence of the detonation, ρ_{s0} is water's original density, ω refers to water's radial compression in the expanding and compressing process, D_s stands for water's acoustic velocity after compression, and k_w stands for water's bulk modulus; P and V , respectively, refer to pressure and water's volume in the compressing process.

Combine (18) and reorganize it to get

$$\rho_s = \rho_{s0} e^{(\rho_z D^2 / 8k_w)(d_z / (d_z + \omega))^6}. \quad (19)$$

Combine (18)~(19) and then water's impedance after detonation products' compression is

$$\rho_s D_s = \left[k_w \rho_{s0} e^{(\rho_z D^2 / 8k_w)(d_z / (d_z + \omega))^6} \right]^{1/2}. \quad (20)$$

Equation (20) shows that impedance matching relationship of water charging is different from that of coupling structure or air-decoupling charging structure. With water-decoupling charging structure, relationship between impedance detonation products acting on the hole wall and explosive's impedance turns into exponential relationship.

To realize impedance matching between detonation products and the rock, not only charging radius but also bulk modulus of the water should be taken into consideration. Consequently, impedance matching can be achieved through adjusting the decoupling coefficient. And when rock and explosive are determined, explosive's utilization can be further improved with adjustment on decoupling coefficient.

With analysis of explosion energy's transmission of three charging structures from the perspective of impedance matching [21, 22], it can be summarized that impedance of explosive and rock directly influences explosive energy's transmission. No matter which charging structure to take, the rock with high impedance requires explosive with high impedance to better utilize explosion energy. When both explosive and rock are determined, different decoupling media result in different influences of decoupling coefficients; nevertheless, formulas can be employed to calculate and get a decoupling coefficient realizing impedance matching of detonation products and the rock.

4. Discussions

Intensity of shock wave of explosion inside the rock quickly decreases with the increase of transmitting distance. According to damage characteristics of rock blasting, with explosion as the center, there are crushed zone, fracture zone, and vibration zone [15], from the blasting center to distant area. Analysis on test data suggests that charging structure has a significant influence on blasting vibration energy. Under the geological condition of present test, comparison of three charging structures confirms that when proportional distance of the measuring point is determined, coupling charging generates blasting larger vibration energy, blasting vibration energy of decoupling charging is relatively small, and blasting vibration energy of water-decoupling charging is smaller than that of air-decoupling charging. The present paper identified influence of different charging structures on explosion energy's transmission from the perspective of impedance matching, suggesting that advanced charging structure can better transmit explosion energy. Combining test and theory, charging structure apparently plays a significant role in transmission and distribution of blasting energy; thus, adjusting charging structure in blasting excavation engineering can help enlarge rock's fracture zone and reduce explosion energy's distribution in crushed zone and vibration zone.

Explosive of coupling charging structure directly operates on the hole wall; hence the instant the explosive blasts (regarding the explosive as completely detonating) detonation products operate on hole wall and directly transmit explosion energy to rock. On the basis of theoretical analysis in Section 3, when impedance of explosive matches that of rock, explosion energy can be completely transmitted to rock and a large amount of explosion energy is consumed around the explosive for rock smashing. Energy consumption occurs before shock wave as well as behind wave-front; part of the energy is transformed into left elastic deformation energy and another part of the energy is sent out in the form of elastic wave (seismic wave) [23]. According to (4), when analyzed

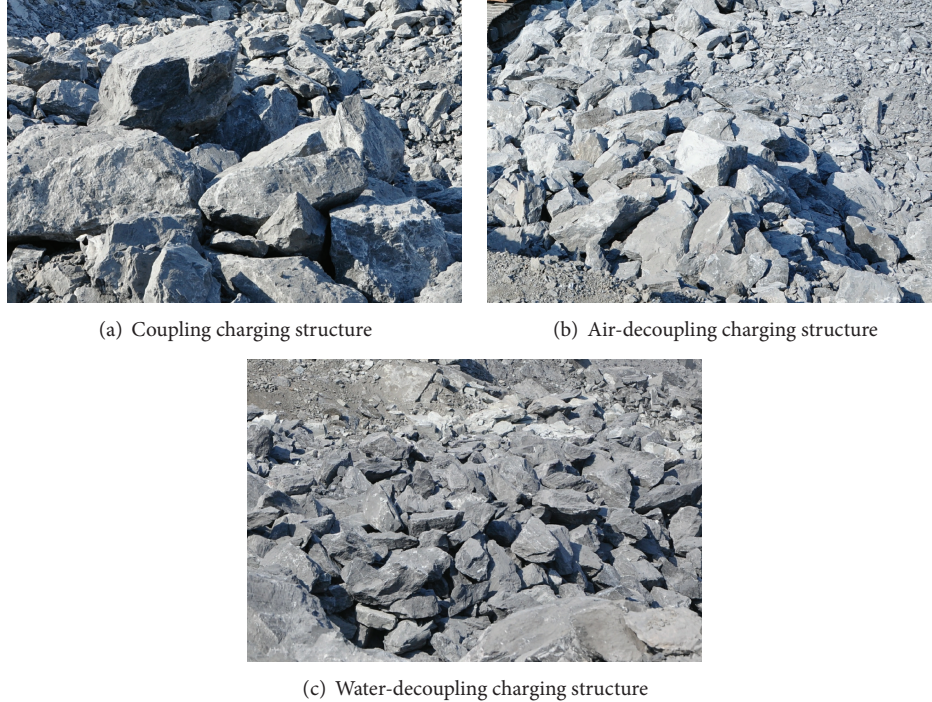


FIGURE 6: The effect diagram of blasting of different charge structures.

energy is carried by seismic wave, coupling charging generates the largest amount of blasting vibration energy; in other words, energy is transformed into elastic wave to the largest extent, but the energy is unavailable and increases damaging effects of blasting vibration. Thus, the less ratio energy accounts for, the more effective utilization of explosive can be achieved. In addition, when coupling charging explodes, explosion energy acts on hole wall and then the intensity shock wave generated is far more than rock's dynamic compressive strength. As produced explosion energy will enlarge rock's crushed area, more explosion energy can be applied to rock smashing. Besides, blasting rocks requires appropriate rock size for convenient transportation and reuse; therefore, to reduce explosion energy on smashing rocks and enlarge rock's fracture zone, better charging structure is essential for the engineering.

When decoupling charging structure is adopted, detonation products firstly operate on decoupling medium and then transmit explosive energy to the hole wall. When air is selected as decoupling medium, explosive explodes in the air and detonation products act on hole wall after filling the hole. According to impedance matching theory, when explosive and rock are determined, decoupling coefficient decides impedance relationship between detonation products operating on hole wall and the rock. Impedance of explosive adopted in the test is smaller than that of the rock, so, based on (17), with the increase of decoupling coefficient, ratio of detonation energy transmitted to rock decreases. And it can also get demonstrated for the test suggests that, at measuring points with the same proportional distance, explosion vibration energy generated by air-decoupling charging is smaller than that of coupling charging.

Water and air have different physical properties; thus, water has more apparent incompressibility, while water is compressible for rock. When explosion's detonation products are transmitted in water, energy of detonation shock wave may decrease; however, detonation energy acting on hole wall can be more evenly distributed.

Test data confirm that, at measuring points with the same proportional distance, explosion vibration velocity generated by water-decoupling charging structure is the smallest in three charging structures. Equation (20) is based on theoretical derivation, stating that impedance relationship between detonation products produced by water-decoupling charging and rock is relatively complex and it is not only related to decoupling coefficient, but also influenced by water's radial compression in the hole. At the test scene, when water-decoupling charging structure is adopted, rock dust is obviously produced rarely in blasting area, which reveals blasting dust can be effectively reduced by water-decoupling charging structure.

Through observation on rock fragmentation after blasting and analysis of pictures (like Figure 6), whether from the perspective of impedance matching theory or actual situations in tests, it turns out that charging structures have influence on blasting effects, especially water-decoupling charging for it can enhance the utilization of explosive energy and distribution of explosion rock fragmentation. According to tests and theoretical analysis, when explosive and rock are fixed, the closer their impedance matching is, the more the explosion energy can be transmitted to the rock. And, for coupling charging structures, without transmission through decoupling media, explosion energy cannot be evenly operated on rocks; thus, crushing zone's scope will be larger than that

of decoupling charging structure. With different decoupling media, impedance matching relationships between explosives and rocks may change. And, in tests, when used as decoupling medium, water can help operate explosion energy on rocks and can generate the least crushing zone in blasting.

Hence, decoupling charging is beneficial to utilization of explosive crushing [24, 25]. When coupling charging structure is adopted, operating time of explosive's blasting is short and its instantaneous energy carried when transmitting to the rock is larger than that of decoupling charging, so more energy is consumed on rock smashing. Consequently, decoupling charging can effectively reduce the initial shock pressure acting on hole wall and prolong operating time to make detonation energy slowly act on the rock; therefore, instantaneous energy can be reduced, and it can be ensured to use more detonation energy on enlarging fracture zone and reduce detonation energy in crushed zone and vibration zone. In summary, vibration velocity of coupling charging structure in far region of blasting is larger than that of decoupling charging.

5. Conclusions

With test and theoretical analysis, this research presented the influence of charging structure on blasting vibrating energy and the following conclusions can be obtained:

- (1) Charging structure greatly influences instantaneous energy of blasting vibration and blasting effects: decoupling charging structure can prolong detonation products' operating time, distribute explosion energy more evenly, reduce instantaneous energy of blasting vibration, and apply more explosions to fracture zone. Furthermore, water-decoupling charging structure has the best effects on reducing vibration and generating the most even rock fragmentation.
- (2) Analyzed from the perspective of impedance matching, impedance of explosive and rock has a pivotal impact on transmission of explosion energy: explosive with high impedance can help better transmit energy of high-impedance rock blasting. No matter which charging structure to choose, matching relationship determines energy projection; therefore, different engineering requirements need comprehensive analysis and selection of appropriate charging structures.
- (3) Decoupling charging structure's medium and coefficient can influence blasting vibration energy and effects to some extent. For different engineering requirements, different charging structures should be adopted and appropriate decoupling coefficient should be selected to help improve explosion utilization and achieve better blasting effects.

Conflict of Interests

The authors declare that there is no conflict of interests regarding the publication of this paper.

Acknowledgments

This work was supported by a grant from Department of Infrastructure Barracks, Grant no. KYGYZXJK0914. Their contribution to bringing this project to fruition is much appreciated. In addition, the authors would like to express their gratitude to Blasting Technology Service Department of College of Field Engineering for their invaluable support and considerable help. Meanwhile, sincere thanks go to graduated students Wang Zheng, Qin Ruping, and Chen Xueping of the laboratory, who have offered selfless devotion and profound concern in completion of the research. And high tribute will be paid to Liang Ting, who has provided insightful comment on editing and translating for this thesis. The authors would like to express their appreciation to the referees for making valuable advice in contributing to this paper.

References

- [1] J. R. Brickman, "Crushing mechanism separation shock wave and gas expansion effects," in *Proceedings of the 2nd International Symposium on Rock Blasting*, pp. 1–8, Yangtze River Scientific Research, Wuhan, China, 1990.
- [2] X. Xie, *Precision Blasting*, Huazhong University of Science and Technology Press, Wuhan, China, 2010.
- [3] J. Ning, C. Wang, and T. Ma, *Explosion and Shock Dynamics*, National Defense Industry Press, Beijing, China, 2010.
- [4] P. R. Day, "Controlled blasting to minimize over break with big boreholes underground," in *Proceedings of the 8th Conference on Explosives and Blasting Techniques*, pp. 262–274, Louisiana State University, New Orleans, La, USA, January–February 1982.
- [5] Q. Zong and D. Meng, "Influence of different kinds of hole charging structure on explosive energy transmission," *Chinese Journal of Rock Mechanics and Engineering*, vol. 22, no. 4, pp. 641–645, 2003.
- [6] J. Chen, C. Bai, Y. Zeng, Z. Wang, and J. Li, "Experiment study of charging constriction influence on explosion seismic effect," in *Proceedings of the National Security Emergency and Hazardous Substances Technical Symposium*, pp. 1098–1103, 2013.
- [7] Z.-L. Wang and Y.-C. Li, "Numerical simulation on effects of radial water-decoupling coefficient in engineering blast," *Rock and Soil Mechanics*, vol. 26, no. 12, pp. 1926–1930, 2005.
- [8] R. Pape, K. R. Mniszewski, and A. Longinow, "Explosion phenomena and effects of explosion on structures. I–III," *Practice Periodical on Structural Design and Construction*, vol. 15, no. 2, pp. 135–169, 2010.
- [9] A. Longinow and K. R. Mniszewski, "Protecting buildings against vehicle bomb attacks," *Practice Periodical on Structural Design and Construction*, vol. 1, no. 1, pp. 51–54, 1996.
- [10] W. M. Yan and K.-V. Yuen, "On the proper estimation of the confidence interval for the design formula of blast-induced vibrations with site records," *Rock Mechanics and Rock Engineering*, vol. 48, no. 1, pp. 361–374, 2015.
- [11] P. Segarra, J. A. Sanchidrián, R. Castedo, L. M. López, and I. del Castillo, "Performance of some coupling methods for blast vibration monitoring," *Journal of Applied Geophysics*, vol. 112, pp. 129–135, 2015.
- [12] Y. Nianhua, *Theory of Blasting Vibration and Testing Technology*, China Railway Publishing House, Beijing, China, 2014.
- [13] C. H. Dowing, *Blast Vibration Monitoring and Control*, vol. 3, Prentice Hall, Englewood Cliffs, NJ, USA, 1985.

- [14] L. P. Orlenko, *Explosion Physics*, Science Press, Beijing, China, 2011.
- [15] D. Zhang, *MATLAB Numerical Analysis*, China Machine Press, Beijing, China, 2012.
- [16] H. Li, W. Lu, D. Shu, X. Yang, and C. Yi, "Study of energy attenuation law of blast-induced seismic wave," *Chinese Journal of Rock Mechanics and Engineering*, vol. 29, supplement 1, pp. 3364–3369, 2010.
- [17] A. Longinow, "Blast protection of buildings," *Practice Periodical on Structural Design and Construction*, vol. 18, no. 4, pp. 194–195, 2013.
- [18] G. F. Revey, "Managing rock blasting work in urban environments," *Practice Periodical on Structural Design and Construction*, vol. 11, no. 2, pp. 86–92, 2006.
- [19] L. Wang, *Foundation of Stress Waves*, National Defense Industry Press, Beijing, China, 2005.
- [20] J. Ye, Z. Liu, and S. Xu, *Fluid Mechanics*, Fudan University Press, Shanghai, China, 1989.
- [21] Q. Zhang, "Explosion and impedance matching between explosive and rock," *Coal Science and Technology*, vol. 18, no. 7, 1990.
- [22] X. Li, "The energy study of impedance matching between rock and explosive," *Journal of Mid-South Mining Industry Academy*, vol. 23, no. 1, 1992.
- [23] Q. Qian and M. Wang, *Impact and Explosion Effects in Rock and Soil*, National Defense Industry Press, Beijing, China, 2010.
- [24] W. Liang, H. Liu, and F. Zhou, "Influence of air-decoupling charge on rock blasting," *Transactions of Beijing Institute of Technology*, vol. 32, no. 12, pp. 1215–1218, 2012.
- [25] W. Wang, X.-C. Li, L. Shi, and Z.-M. Fang, "Discussion on decoupled charge loosening blasting in deep rock mass," *Rock and Soil Mechanics*, vol. 29, no. 10, pp. 2837–2842, 2008.

Research Article

Nonlinear Dynamics Analysis of the Semiactive Suspension System with Magneto-Rheological Damper

Hailong Zhang,^{1,2} Enrong Wang,² Fuhong Min,² Ning Zhang,¹
Chunyi Su,³ and Subhash Rakheja³

¹Magneto-Electronic Lab, School of Physics and Technology, Nanjing Normal University, Nanjing 210046, China

²Vibration Control Lab, School of Electrical and Automation Engineering, Nanjing Normal University, Nanjing 210042, China

³Center for Advanced Vehicle Engineering, Department of Mechanical Engineering, Concordia University, Montreal, Canada H3G 1M8

Correspondence should be addressed to Ning Zhang; zhangning@njnu.edu.cn

Received 4 February 2015; Accepted 24 May 2015

Academic Editor: Salvatore Strano

Copyright © 2015 Hailong Zhang et al. This is an open access article distributed under the Creative Commons Attribution License, which permits unrestricted use, distribution, and reproduction in any medium, provided the original work is properly cited.

This paper examines dynamical behavior of a nonlinear oscillator which models a quarter-car forced by the road profile. The magneto-rheological (MR) suspension system has been established, by employing the modified Bouc-Wen force-velocity ($F-v$) model of magneto-rheological damper (MRD). The possibility of chaotic motions in MR suspension is discovered by employing the method of nonlinear stability analysis. With the bifurcation diagrams and corresponding Lyapunov exponent (LE) spectrum diagrams detected through numerical calculation, we can observe the complex dynamical behaviors and oscillating mechanism of alternating periodic oscillations, quasiperiodic oscillations, and chaotic oscillations with different profiles of road excitation, as well as the dynamical evolutions to chaos through period-doubling bifurcations, saddle-node bifurcations, and reverse period-doubling bifurcations.

1. Introduction

Magneto-rheological fluid (MRF) is a suspension of micron-sized, magnetic particles in a carrier fluid. When exposed to a magnetic field, the rheology of MRF reversibly and consecutive changes from a free-flowing Newton liquid to a semisolid Bingham with controllable yield strength, which is known as magneto-rheological effect [1–3]. Magneto-rheological damper (MRD) based on MRF has significant promise for effective vibration damping in many applications, such as MRD-based semiactive suspension system, which has attracted much attention to improve the ride comfort and handling safety of the vehicle [4–6]. Nevertheless, there are still numerous challenges in controlling a MRD to get the superior performances, because it has highly nonlinear characteristics and chaotic motion due to typical hysteretic characteristics.

In the past decades, many studies of MR suspension focused on the semiactive control algorithms. Many new

ideas were proposed, such as “Skyhook” control or artificial intelligence based control, and had been implemented in a practical vehicle. However, chaotic behavior may exist due to the nonlinearities in MR suspension, which was not studied well yet. Li et al. [7] investigated the chaotic motion in nonlinear suspension system with hysteretic characteristics and verified the path from quasiperiodic to chaos by deriving Melnikov method. Siewe Siewe [8] applied the method of multiple scales to analyze local bifurcation in the quarter-car system with periodically excited road profile, and a variety of nonlinear behaviors were found, such as resonance and antiresonance phenomena and saddle-node bifurcation. Litak et al. [9] used the analytical Melnikov theory and predicted the lowest critical amplitude that a single degree of freedom (DoF) vehicle model may transit to a chaotic motion, under a road surface profile consisting of harmonic and noisy components. Luo and Rajendran [10] carried out the periodic motion and stability of a single DoF semiactive suspension model by developing a mapping structure, and

the model of MRD was formulated with piecewise linear equations. However, all of above models are simple as single DoF model which is very different from the practical situation owing to the neglect of wheel movement, and this may explain that the vibrations appear for impossible amplitude of 0.4 m in [9]. Consequently, Borowiec and Litak [11] studied a 2-DoF quarter-car and find out the transition to chaos, by applying Melnikov theory and recurrence approach. In earlier studies, the suspension system was mostly considered as single DoF system for its simplicity. What is more, calculation models of MRD were mostly made employing polynomials or piecewise linear model in [9], while the Bouc-Wen model is considered appropriate to describe well the dynamic performance of MRD [12–14]. So far, there are no systematic nonlinear dynamics of the Bouc-Wen model based MR suspension system, owing to the complex structure of model.

In this paper, from the experimental results, such a commercial MRD is modeled using a modified Bouc-Wen model proposed by the author. A 2-DoF model is established to express the MR suspension system, by employing the identification results. The stability of the system is analyzed according to the stability criterion, and all possible motions of the MR suspension system are determined by plotting the frequency response, bifurcation diagrams, and phase portraits under different road profiles. The Lyapunov exponent (LE) is calculated to detect chaotic motion. Time series with combination of power spectrum density is used as assisted means for the special system parameters.

The paper is organized as follows. In Section 2, the dynamic model of 2-DoF MR suspension system is formulated, employing the modified Bouc-Wen calculation model of MRD. In Section 3, the stability of the system is analyzed by calculating the eigenvalue of the Jacobian matrix of fixed point. Next, the numerical calculation is conducted to determine the dynamic behavior and to confirm the stability analysis as well. Comprehensive numerical results include frequency response, bifurcation diagrams, phase plane portraits, Poincare map, and time series; thus, the process of the transition to chaotic motion is revealed. Finally, the conclusions of the research are presented in Section 4.

2. Dynamic Model of Quarter-Car Semiactive Suspension System

2.1. Mechanical Model and Formulation. In Figure 1, a classic dynamic model of a quarter MR suspension system [15] is presented, which involves main vehicle components such as the car body, suspension spring, MRD, and wheel. Amongst, only the MRD has strong force hysteresis and saturation nonlinearities. The other components have been addressed in linearization. m_s and m_u are defined as the sprung and unsprung masses. k_s , i_d , and F_d represent the suspension stiffness, direct drive current, and the yielded damping force of the MRD. k_t and c_t denote equivalent stiffness and damping coefficient of the tire, and x_i , x_s , and x_u are defined as the road excitation and vertical displacements of the sprung

and unsprung masses, respectively. Following the principle of Newton's second law of motion, the dynamic equation is formulated as

$$\begin{aligned} m_s \ddot{x}_s + k_s (x_s - x_u) + F_d &= 0, \\ m_u \ddot{x}_u + k_t (x_u - x_i) + c_t (\dot{x}_u - \dot{x}_i) - k_s (x_s - x_u) - F_d &= 0. \end{aligned} \quad (1)$$

2.2. Modified Bouc-Wen Calculation Model of MRD. The accurate and practical MRD dynamic model is crucial for application. Nevertheless, there is no recognized MRD dynamic model yet. Amongst, relative effective models include Bouc-Wen model by Spencer and the phenomenon model based on Bouc-Wen [14]. Figure 2 shows the structure of typical Bouc-Wen phenomenon model, and it accurately describes the MRD inherent hysteresis nonlinear properties. However, it cannot describe nonlinear response and saturation characteristics of the magnetic field, because the linear output item in the model is just to represent the relationship between the damping force and the control current. Therefore, the author has imported the sigmoid function to improve the conventional Bouc-Wen phenomenon model [16]. The issue is effectively solved by decoupling the hysteretic characteristics with the current modulation separation:

$$F_d = f(i_d) = c(i_d) F_h(x_r, v_r), \quad 0 \leq i_d \leq I_m, \quad (2)$$

$$c(i_d) = 1 + \frac{k_2}{1 + \exp(-a_0(i_d + I_0))} - \frac{k_2}{1 + \exp(-a_0 I_0)}, \quad (3)$$

$$F_h(x_r, v_r) = c_1 \dot{y} + k_1 (x_r - x_0), \quad (4)$$

$$x_r = x_s - x_u,$$

$$\dot{y} = \frac{1}{c_0 + c_1} [\alpha z + c_0 \dot{x}_r + k_0 (x_r - y)],$$

$$\begin{aligned} \dot{z} = -\gamma |\dot{x}_r - \dot{y}| z |z|^{n-1} - \beta (\dot{x}_r - \dot{y}) |z|^n \\ + A (\dot{x}_r - \dot{y}), \end{aligned} \quad (5)$$

where i_d and I_m express the direct current and its maximum value for driving the MRD, respectively, and $0 \leq i_d \leq I_m$. $c(i_d)$ denotes the saturated nonlinear direct current control function proposed by the authors and $c(i_d) \geq 1$, $c(i_d) = 1$, for $i_d = 0$. $F_h(v_r)$ denotes yielded passive damping force with hysteresis depending on the piston relative displacement velocity (v_r) of the MRD for $i_d = 0$. x_r is the piston travel of the MRD, y and z are inner variables without units, and k_0 , k_1 , k_2 , a_0 , I_0 , α , β , γ , c_0 , c_1 , n , A , and x_0 are constants, respectively.

As is shown in Figure 3(a), a CARRERA MagneShock MRD of the vehicle suspension is further employed from [16], which permits maximum control direct current 0.5 A at 12 V [16]. On the basis of the actual measured characteristic data of MRD, the model parameters are identified as $k_0 = 184.1$,

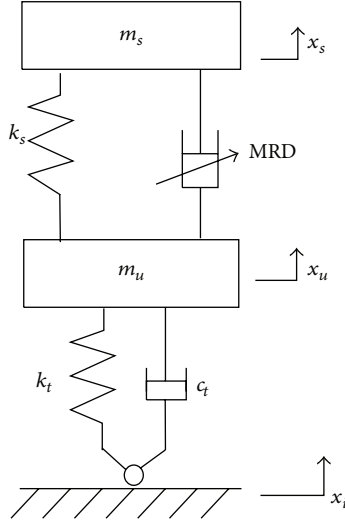


FIGURE 1: Schematic diagram of 2-DoF MR suspension system.

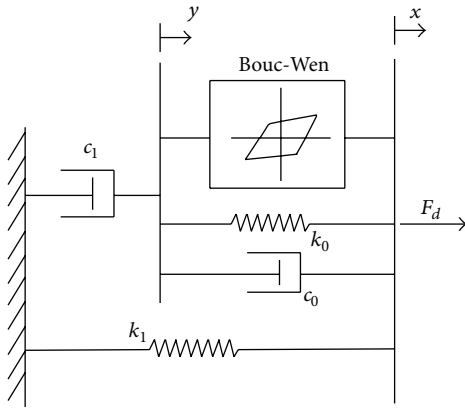


FIGURE 2: Bouc-Wen mechanical model.

$k_1 = 1528.1$, $k_2 = 10.092$, $a_0 = 7.526$, $I_0 = 0.069$, $\alpha = 20373.7$, $\beta = 233849.1$, $\gamma = 8816.9$, $c_0 = 1368.7$, $c_1 = 6222.7$, $n = 2$, $A = 20.6$, and $x_0 = -0.004$. Figure 3(b) shows the comparison of the modified Bouc-Wen hysteresis F - v model and the tested data of employed candidate MRD, under the harmonic excitation with amplitude 12.5 mm at 1.5 Hz and different direct drive current (0–0.4 A), which exhibits ideal coordination.

MRD has clear strong nonlinear property from the above results. Due to the damping force dependency on driven current and excitation frequency, the F - v curve varies evidently under different driven and excitation profiles [17]. As a result, nonlinear behavior caused by hysteresis cannot be ignored in engineering application.

3. Nonlinear Dynamics Characteristics of MR Suspension

Stability is undoubtedly the key requirements in the field of vehicle suspension control. In previous studies, comprehensive performances of the MR suspension were more

highly valued, by comparing the transmissibility of vibration and vibration amplitude with the traditional passive one. Here, the nonlinear dynamic response and the mechanism of the instability process are the problem to be solved.

In this section, the stability analysis of the MR suspension is conducted in view of modern control theory and nonlinear dynamics theory. Stability of the MR suspension system is examined at the equilibrium of the dimensionless nonlinear model. Further, the bifurcation analysis, combining LE assessment, is carried out to describe nonlinear dynamical evolution process and to find out the route to chaos. In addition, the phase portrait and Poincare map diagrams are plotted to give the more intuitive response of the system under different excitation conditions.

3.1. Stability Analysis. For definition of time coefficient $\tau = \omega \cdot t$, in which $\omega^2 = k_s/m_s$, the corresponding dimensionless equation of the motion is written as [7, 10]

$$\begin{aligned} \ddot{x}_s + \frac{k_s}{m_s \omega^2} (x_s - x_u) + \frac{1}{m_s \omega} F_d &= 0, \\ \ddot{x}_u - \frac{k_s}{m_u \omega^2} (x_s - x_u) - \frac{1}{m_u \omega} F_d + \frac{k_t}{m_u \omega^2} (x_u - X_i) &= 0, \\ + \frac{c_t}{m_u \omega} (\dot{x}_u - X_i') &= 0, \end{aligned} \quad (6)$$

where X_i denotes dimensionless form of road profile. The state space is defined as $x = [x_1, x_2, x_3, x_4, x_5, x_6]$, where $x_1 = x_s$, $x_2 = \dot{x}_s$, $x_3 = x_u$, $x_4 = \dot{x}_u$, $x_5 = y$, and $x_6 = z$. The state space is divided into four sections from (5), which are

$$\begin{aligned} D_0 &= \{(x_1, x_2, x_3, x_4, x_5, x_6) \mid \alpha x_6 + c_0 (x_2 - x_4) \\ &\quad + k_0 (x_1 - x_3 - x_5) < 0 \cap x_6 < 0\}, \\ D_1 &= \{(x_1, x_2, x_3, x_4, x_5, x_6) \mid \alpha x_6 + c_0 (x_2 - x_4) \\ &\quad + k_0 (x_1 - x_3 - x_5) > 0 \cap x_6 > 0\}, \\ D_2 &= \{(x_1, x_2, x_3, x_4, x_5, x_6) \mid \alpha x_6 + c_0 (x_2 - x_4) \\ &\quad + k_0 (x_1 - x_3 - x_5) > 0 \cap x_6 < 0\}, \\ D_3 &= \{(x_1, x_2, x_3, x_4, x_5, x_6) \mid \alpha x_6 + c_0 (x_2 - x_4) \\ &\quad + k_0 (x_1 - x_3 - x_5) < 0 \cap x_6 > 0\}, \end{aligned} \quad (7)$$

respectively.

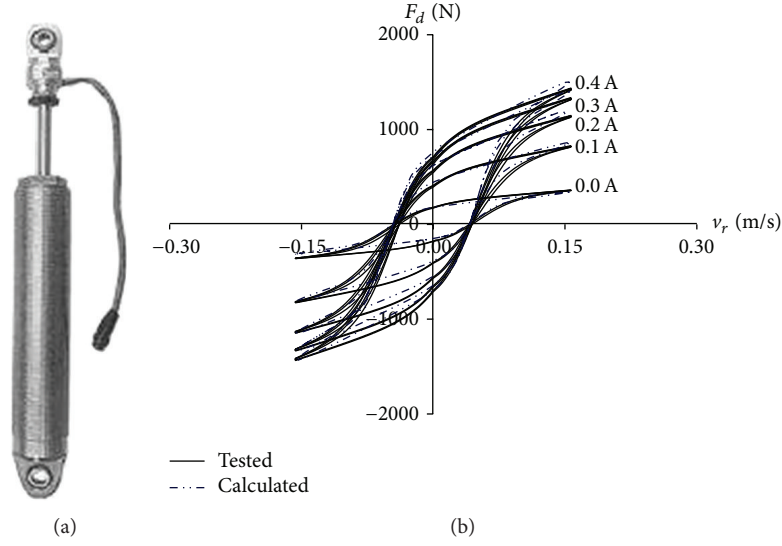


FIGURE 3: (a) A pictorial view of the candidate MRD. (b) Comparison of tested and calculated results.

Considering no excitation input, we get the state equation of the system further as follows from (1) to (7):

$$\begin{aligned}
 \dot{x}_1 &= x_2, \\
 \dot{x}_2 &= a_{21}x_1 + a_{22}x_2 + a_{23}x_3 + a_{24}x_4 + a_{25}x_5 + a_{26}x_6, \\
 \dot{x}_3 &= x_4, \\
 \dot{x}_4 &= a_{41}x_1 + a_{42}x_2 + a_{43}x_3 + a_{44}x_4 + a_{45}x_5 + a_{46}x_6, \\
 \dot{x}_5 &= a_{51}x_1 + a_{52}x_2 + a_{53}x_3 + a_{54}x_4 + a_{55}x_5 + a_{56}x_6, \\
 \dot{x}_6 &= (A + Bx_6^2) \\
 &\quad \cdot (a_{61}x_1 + a_{62}x_2 + a_{63}x_3 + a_{64}x_4 + a_{65}x_5 + a_{66}x_6),
 \end{aligned} \tag{8}$$

where

$$\begin{aligned}
 a_{21} &= -\frac{k_s}{m_s \omega^2} - \frac{c(i_d)}{m_s \omega} \frac{k_0 c_1}{c_0 + c_1} - \frac{c(i_d) k_1}{m_s \omega}, \\
 a_{22} &= -\frac{c(i_d)}{m_s \omega} \frac{c_0 c_1}{c_0 + c_1}, \\
 a_{23} &= \frac{k_s}{m_s \omega^2} + \frac{c(i_d)}{m_s \omega} \frac{k_0 c_1}{c_0 + c_1} + \frac{c(i_d) k_1}{m_s \omega}, \\
 a_{24} &= \frac{c(i_d)}{m_s \omega} \frac{k_0 c_1}{c_0 + c_1}, \\
 a_{25} &= \frac{c(i_d)}{m_s \omega} \frac{k_0 c_1}{c_0 + c_1},
 \end{aligned}$$

$$\begin{aligned}
 a_{26} &= -\frac{c(i_d)}{m_s \omega} \frac{\alpha c_1}{c_0 + c_1}, \\
 a_{41} &= \frac{k_s}{m_u \omega^2} + \frac{c(i_d)}{m_u \omega} \frac{k_0 c_1}{c_0 + c_1} + \frac{c(i_d) k_1}{m_u \omega}, \\
 a_{42} &= \frac{c(i_d)}{m_u \omega} \frac{c_0 c_1}{c_0 + c_1}, \\
 a_{43} &= -\frac{k_s}{m_u \omega^2} - \frac{c(i_d)}{m_u \omega} \frac{k_0 c_1}{c_0 + c_1} - \frac{c(i_d) k_1}{m_u \omega} - \frac{k_t}{m_u \omega^2}, \\
 a_{44} &= -\left(\frac{c(i_d)}{m_s \omega} \frac{k_0 c_1}{c_0 + c_1} + \frac{c_t}{m_u \omega} \right), \\
 a_{45} &= -\frac{c(i_d)}{m_u \omega} \frac{k_0 c_1}{c_0 + c_1}, \\
 a_{46} &= \frac{c(i_d)}{m_u \omega} \frac{\alpha c_1}{c_0 + c_1}, \\
 a_{51} &= \frac{k_0}{c_0 + c_1}, \\
 a_{52} &= \frac{c_0}{c_0 + c_1}, \\
 a_{53} &= -\frac{k_0}{c_0 + c_1}, \\
 a_{54} &= -\frac{c_0}{c_0 + c_1}, \\
 a_{55} &= -\frac{1}{c_0 + c_1},
 \end{aligned}$$

$$\begin{aligned}
a_{56} &= \frac{\alpha}{c_0 + c_1}, \\
a_{61} &= -\frac{k_0}{c_0 + c_1}, \\
a_{62} &= \frac{c_1}{c_0 + c_1}, \\
a_{63} &= \frac{k_0}{c_0 + c_1}, \\
a_{64} &= -\frac{c_1}{c_0 + c_1}, \\
a_{65} &= \frac{k_0}{c_0 + c_1}, \\
a_{66} &= -\frac{\alpha}{c_0 + c_1},
\end{aligned}$$

$$B = -\beta - \gamma \quad \text{for } x \in D_0 \cup D_1,$$

$$B = -\beta + \gamma \quad \text{for } x \in D_2 \cup D_3.$$

(9)

The parameters of the system are selected based on actual vehicle [15]: $m_s = 562.5$ kg, $m_u = 90$ kg, $k_s = 57000$ N/m, $k_t = 285000$ N/m, and $c_t = 100$ N/m·s⁻¹. Regardless of semiactive control of MRD, the driven current is constant $i_d = 0.5$ A, and other model parameters are as mentioned above. By setting the left side of (8) to zero, the equilibrium is obtained. Obviously, the system has a fixed point $X_0(0, 0, 0, 0, 0, 0)$, the stability of which is determined by the characteristic equation of the Jacobian matrix (10) at X_0 :

$$\begin{aligned}
&J \\
&= \begin{bmatrix} 0 - \lambda & 1 & 0 & 0 & 0 & 0 \\ a_{21} & a_{22} - \lambda & a_{23} & a_{24} & a_{25} & a_{26} \\ 0 & 0 & 0 - \lambda & 1 & 0 & 0 \\ a_{41} & a_{42} & a_{43} & a_{44} - \lambda & a_{45} & a_{46} \\ a_{51} & a_{52} & a_{53} & a_{54} & a_{55} - \lambda & a_{56} \\ Aa_{61} & Aa_{62} & Aa_{63} & Aa_{64} & Aa_{65} & Aa_{66} - \lambda \end{bmatrix}. \quad (10)
\end{aligned}$$

The eigenvalues of matrix (10) are calculated as $\lambda_1 = -1.5176 + 2.3913i$, $\lambda_2 = -1.5176 - 2.3913i$, $\lambda_3 = -0.0099 + 0.2057i$, $\lambda_4 = -0.0099 - 0.2057i$, $\lambda_5 = 0.0052$, and $\lambda_6 = 0$. Note that $\lambda_{1,2}$ and $\lambda_{3,4}$ are two couples of conjugate complex roots, while λ_5 is positive and λ_6 is zero, and therefore the system is instable at X_0 .

Furthermore, due to quadratic and absolute terms in the above six dimensions system, analytical solution is scarcely to obtain. Therefore, the numerical methods are usually employed to analyze such a system. Considering the application background, the range of frequencies and amplitudes of the road profile during vehicle running is certain, which are normally below 15 Hz and 10 cm, respectively [4–6]. We use the common harmonic excitation as the road surface. It is expressed as $x_i = A_m \sin(\Omega \cdot t)$, in which A_m represents

roughness of the road surface and Ω is angular frequency $\Omega = 2\pi f$. The dimensionless form of road excitation is $X_i = \Omega^2 A \sin(\Omega/\omega \cdot \tau)$. The following analysis methods of nonlinear dynamics are applied to such a special complex system:

- (1) By obtaining the frequency band response, we find out the area that the system is sensitive to the corresponding road profiles.
- (2) By drawing the bifurcation diagrams, we study the nonlinear dynamics of the system under different road parameters. Combing the calculated LE spectrum, we can further determine the chaotic motion of the system under the corresponding road profiles.
- (3) Based on the above analysis, the dynamics evolution process is vividly portrayed using phase plane portraits, time series, and power spectrum of the system response at critical parameters.

3.2. Numerical Results. It is known that the dynamics of a vibration system may be analyzed through the frequency response diagram [18]. Therefore, for the studied system, the frequency response is obtained by plotting the vibration amplitude of sprung mass m_s expressed by v_s . In addition, the LE spectrum [19] is used to reveal the detail of the system frequency response. Figure 4(a) shows the frequency response of the model, which covers pass-band of the road, and Figure 4(b) presents the LE spectrum as well. The road frequency f is slowly increased by increment of 0.001 Hz. As is illustrated in Figure 4(a) there exists a critical jump of the system response for $f = 1.752$ Hz [20] near the resonance point. The phenomenon of the jump causes the motion to change, but the system remains stable, as is shown in gray shadow. However, the diagram exhibits a more complicated and different behavior while f is increased to 2.71 Hz, with that restoration of stability in a short time. With f being increased, it is shown that the system falls into instability area as 2.75 Hz–4 Hz, which indicates that the chaotic motion may appear when f is within or near this area, as is shown in red shadow. This is confirmed by the LE spectrum showed in Figure 4(b). The diagram illustrates that there exist positive LE among the LE spectra in instable area shaded in red, which indicates the existence of the chaos. Next, the frequency response goes back to normal and all the LEs are less than zero, which indicates that the system remains stable up to 15 Hz.

The bifurcation and max LE diagrams under parameter variations are efficient methods for analyzing the nonlinear dynamic behavior. Figure 5 shows the bifurcation diagram and the corresponding LE diagram, with f varying in the above-mentioned instable area. The bifurcation diagram is obtained by plotting the stroboscopic point of the displacement x_s , because x_s is important for the safety of the vehicle. As is shown in Figure 5(a), when $f = 2.08$ Hz, the system loses period-1 stability, bifurcating from period-1 into period-2 motion. For $f \in (2.08\text{--}2.74)$ Hz, the period-2 motion of the system develops into period-8 through the period-doubling bifurcation. Moreover, it is interesting that complex motion occurs at $f \in (2.439\text{--}2.488)$ from the bifurcation

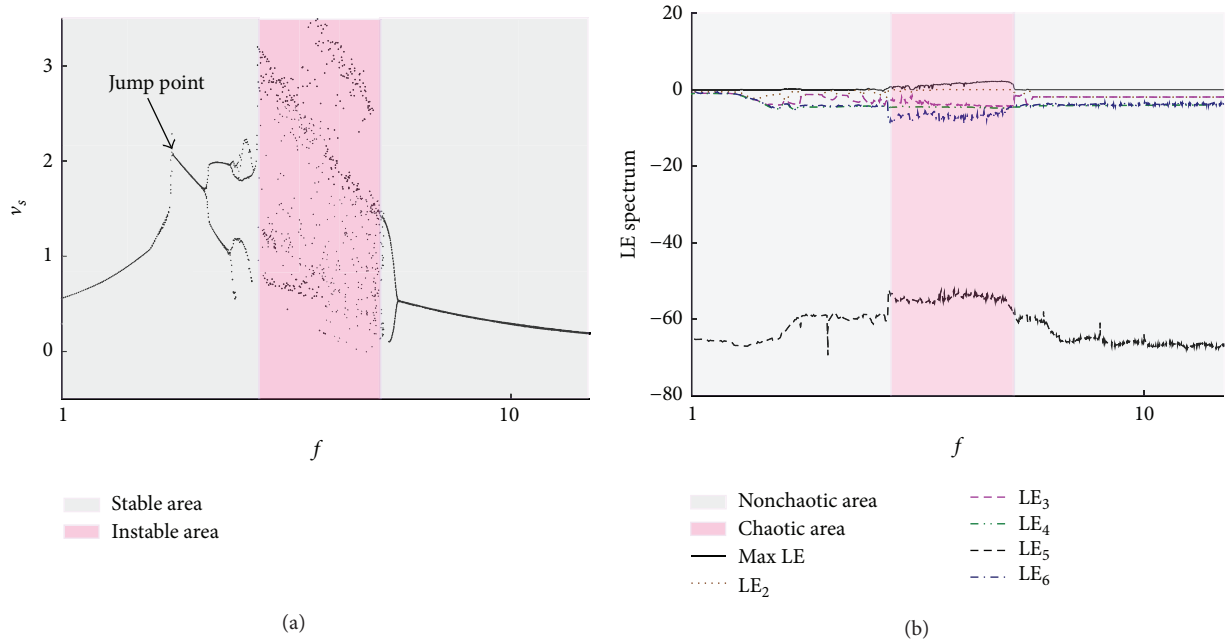


FIGURE 4: Frequency response diagram and LE spectrum diagram.

diagram, and the max LEs are positive. At the same time, note that the points in the bifurcation diagram are limited in enveloping curve, not wide distribution. Consequently, the exact dynamic behavior in this area will be identified later. Next, after short stay in the strange area, the system gets back to periodic motion until $f = 2.719$ Hz, through series of inverse period-doubling bifurcation from period-8 to period-2. Nevertheless, the system directly enters the chaotic state after period-2 motion, as is shown in Figure 5(b), and the max LE turns positive. When $f \in (2.78-4)$ Hz, periodic motion, period-doubling bifurcation, and chaotic motions appear alternately and the system suffers the saddle-node bifurcation. Beyond the threshold for the onset of chaotic motion, there are some “periodic windows,” which could be the feature of the transient chaos. The max LEs before and after the saddle-node bifurcation point are opposite in sign. Then, for larger frequency over 3.73 Hz, there are no longer “periodic windows” presented up to the cutoff value of f in simulation. In Figure 5(c), we can observe that the system escapes from chaos to periodic motions through reverse period-doubling bifurcation.

In order to give a rather clear presentation of the dynamical behavior, we depict phase portraits (with lines) and Poincare maps (with points) [21]. Figures 6(a)–6(h) show results for the following road frequency f : (a) $f = 1.5$ Hz; (b) $f = 2.2$ Hz; (c) $f = 2.39$ Hz; (d) $f = 2.245$ Hz; (e) $f = 2.471$ Hz; (f) $f = 2.8$ Hz; (g) $f = 3.071$ Hz; (h) $f = 3.2$ Hz; (i) $f = 3.75$ Hz, and amplitude A_m is fixed at 0.08 m. The displacement x_s and velocity v_s are adopted. A periodic dynamic response is exhibited, including period-1, period-2, period-4, and period-8. In Figure 6(a), the period-1 motion is presented, according to the one loop circle as well as a single point of the Poincare map. The period-1 motion is replaced

by period-2, period-4, and period-8 in turn, which confirms the analysis of process of bifurcating. Figure 6(e) shows the phase plane at $f = 2.471$ Hz in the above-mentioned strange area. Note that the phase plane is keeping regular even consist of amount of closed curves, and the Poincare map contains limited points. In order to verify the dynamic behavior, in the above strange area, we plot the timing diagram and calculate the power spectrum density (PSD) diagram of x_s for $f = 2.4617$ Hz. It is indicated that periodic and chaotic coexisting state exists when the system falls in the strange area [22], as is shown in Figure 7. Figure 6(f) reveals the chaotic attractor, because both of the phase plane and Poincare map distribute irregularly throughout the phase space. In the chaotic area, the saddle-node bifurcation is confirmed by phase plane portraits and Poincare maps, as is shown in Figures 6(g), 6(h), and 6(i). Note, as shown in Figure 6(i), a new chaotic attractor exists as f is increased, which covers a larger area compared with Figure 6(f). It means that the vibration amplitude rapidly increases with a small increase of road excitation frequency, which is harmful to driving safety.

The road surface amplitude is also essential in vehicle dynamics analysis. Figure 8 illustrates the influence of road amplitude on the system dynamics, of the global bifurcation graph and LE spectrum under different amplitude of road excitation. The amplitude varies from 0.005 m to the max 0.1 m, containing the normal road condition, and frequency f is fixed at 5 Hz. It is observed that the displacement x_s and velocity v_s exhibit a periodic response, including period-1, period-2, and period-4 motion, until the road amplitude is increased to $A_m = 0.0315$ m. Figure 9 expresses the phase portraits and Poincare map corresponding to $A_m = 0.01$ m, 0.02316 m, 0.02720 m, and 0.06 m, respectively.

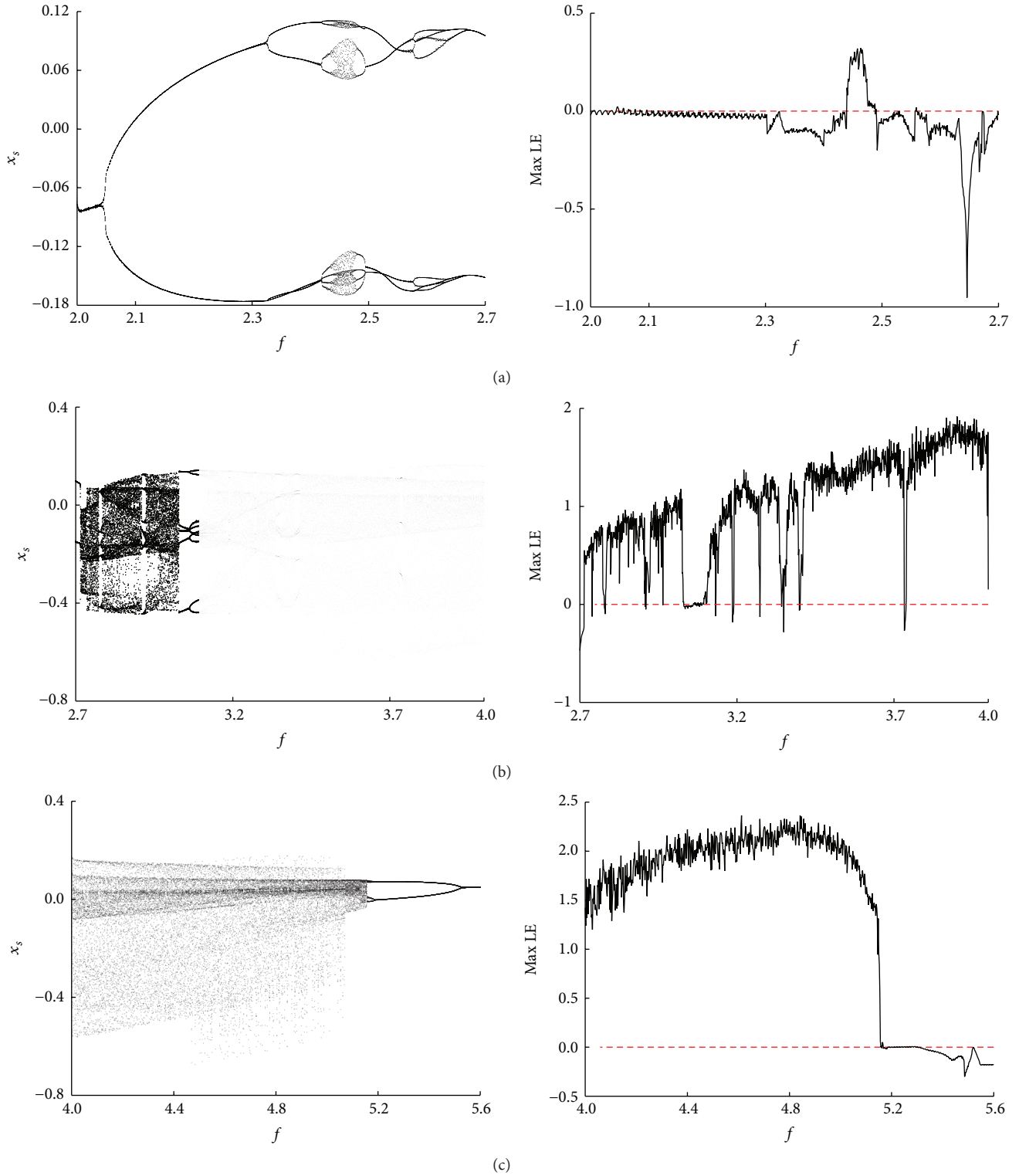


FIGURE 5: Bifurcation diagram and max LEs diagram of x_s by varying f : (a) $f \in (2.0-2.7)$ Hz; (b) $f \in (2.7-4.0)$ Hz; (c) $f \in (4.0-5.6)$ Hz.

The phase plane and Poincare map is plotted in Figures 9(a), 9(b), and 9(c), which confirms the process of period-doubling bifurcation shown in Figure 8(a). Note, for $A_m = 0.02720$ m, a limit circle occurs, which corresponds to the phenomenon of jump in the process of period-2 shown

in Figure 8(a). When the amplitude of road excitation is increased larger than $A_m = 0.0315$ m, the system enters the chaotic region from Figure 8 because the max LE turns positive. In addition, just as is shown in Figure 9(d), the phase plane and Poincare map of $A_m = 0.06$ m become irregular.

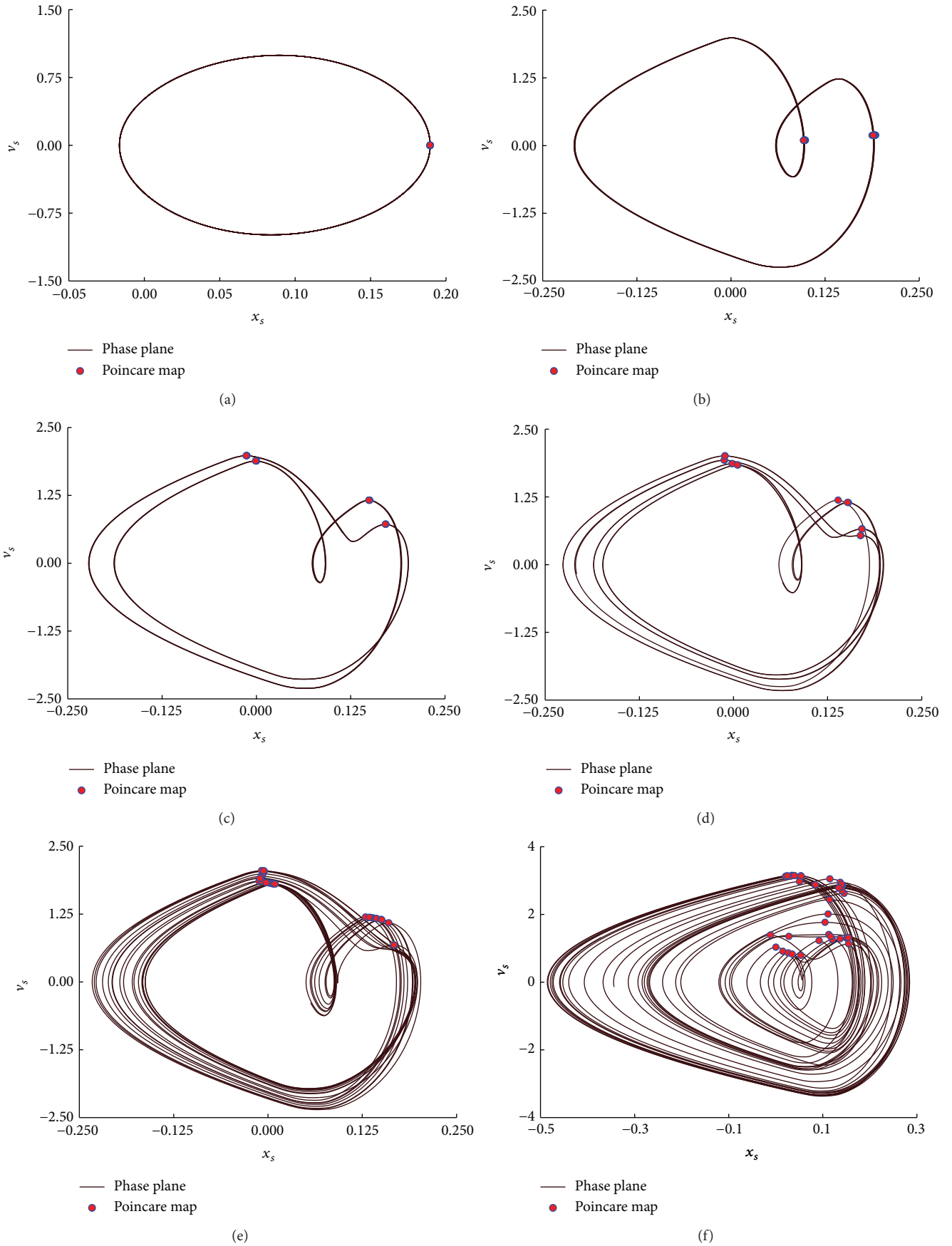


FIGURE 6: Continued.

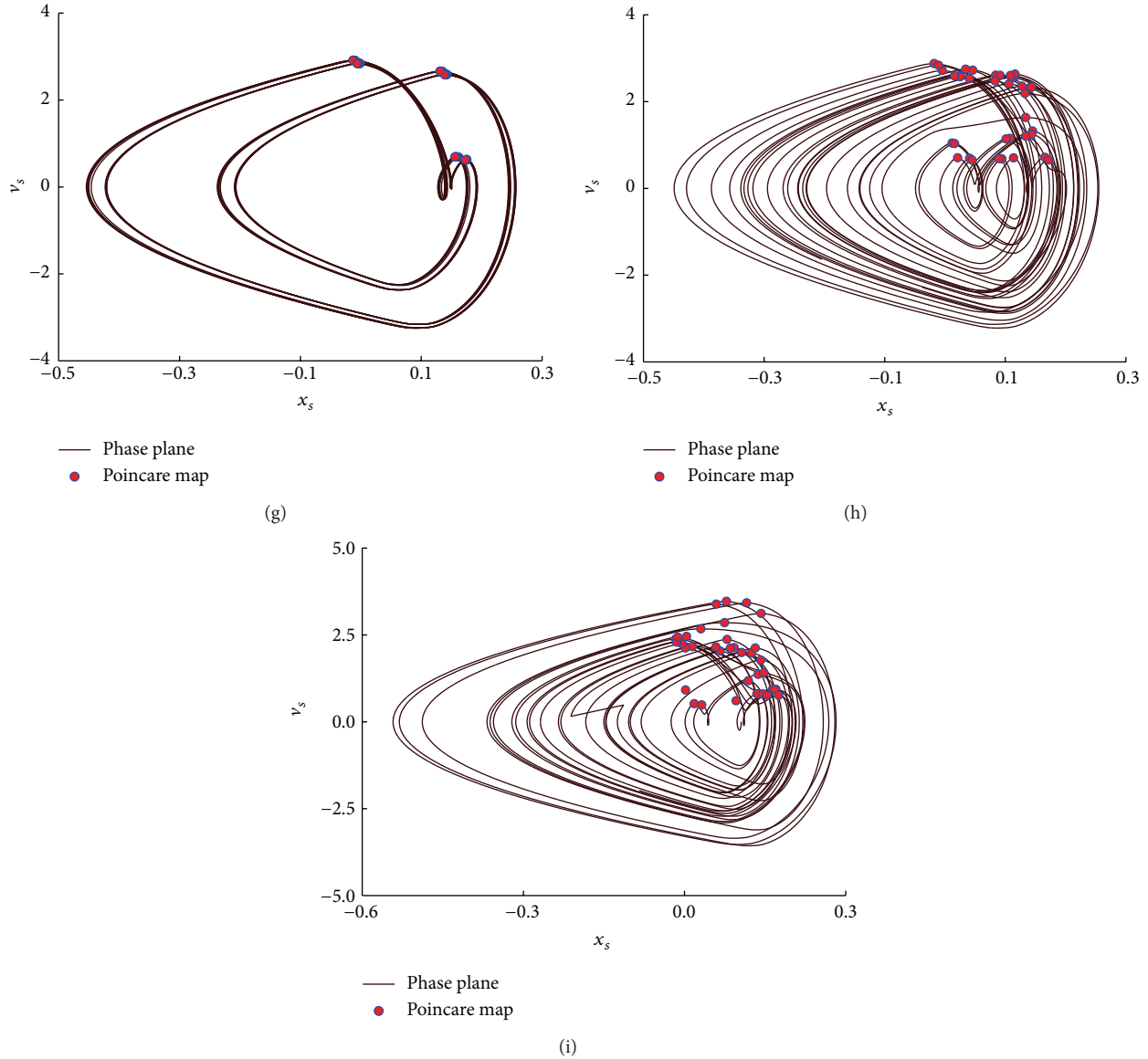


FIGURE 6: Phase portraits and corresponding Poincaré maps (velocity v_s versus displacement x_s) for different f : (a) $f = 1.5$ Hz; (b) $f = 2.2$ Hz; (c) $f = 2.39$ Hz; (d) $f = 2.245$ Hz; (e) $f = 2.471$ Hz; (f) $f = 2.8$ Hz; (g) $f = 3.071$ Hz; (h) $f = 3.2$ Hz; (i) $f = 3.75$ Hz.

The system maintains chaotic motion and vibration amplitude of suspension is getting far larger than the sustainable limit, which seriously threatens the handling safety of the vehicle.

The results of analysis above are complete descriptions of the set of parameters where chaos occurs under road profiles. The proposed analytical method is useful for estimating the suspension parameters so that chaos does not occur as desired, and thus avoiding the unexpected dangers in the running process of the vehicle.

4. Conclusions

This paper studies the nonlinear dynamics problems in the practical application of MRD. The 2-DoF MR vehicle

suspension was set up based on the identified data of a commercial MRD. By calculating the eigenvalues of the Jacobian matrix at fixed point, the possibility of chaotic movement in the system was discovered. The theoretical analysis was then confirmed by numerical simulations. Under the single frequency harmonic excitation, the nonlinear dynamic evolution process was analyzed with frequency varying. The main conclusion would be that the loss of stability of the system appears near the midfrequency band and high amplitude of road surface, through the dynamical evolution to chaos by period-doubling bifurcations, saddle-node bifurcations, and reverse period-doubling bifurcations. These show the importance of parametric excitation in the control of vibrations in a MR suspension system. The research

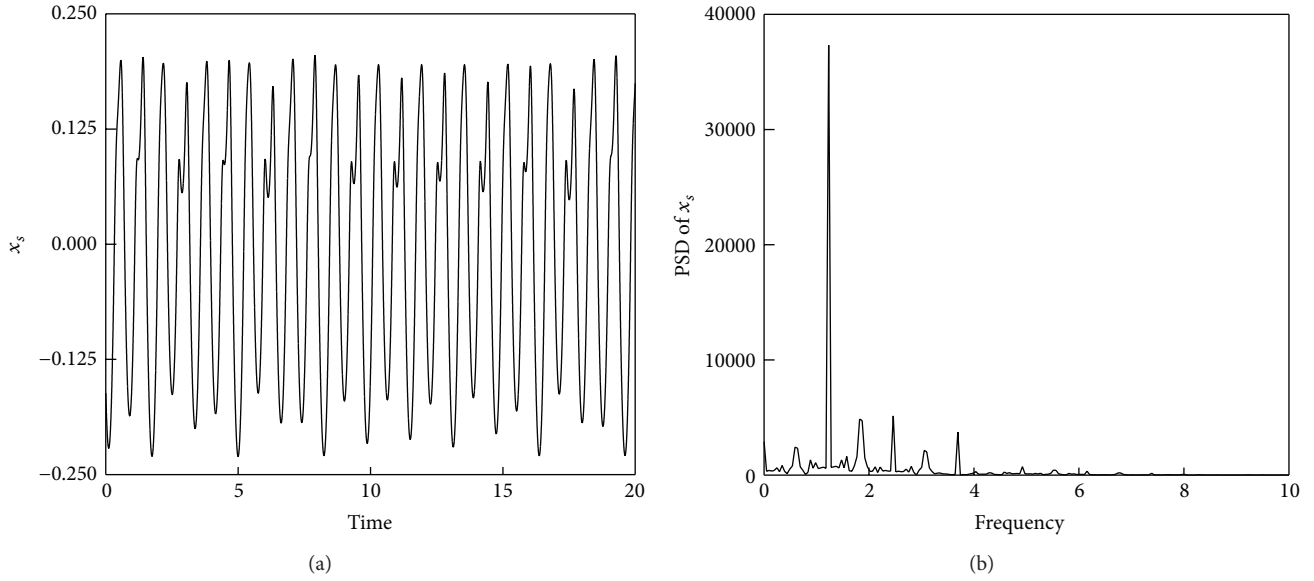


FIGURE 7: Timing history and PSD of x_s for $f = 2.4617$ Hz, $A_m = 0.08$ m.

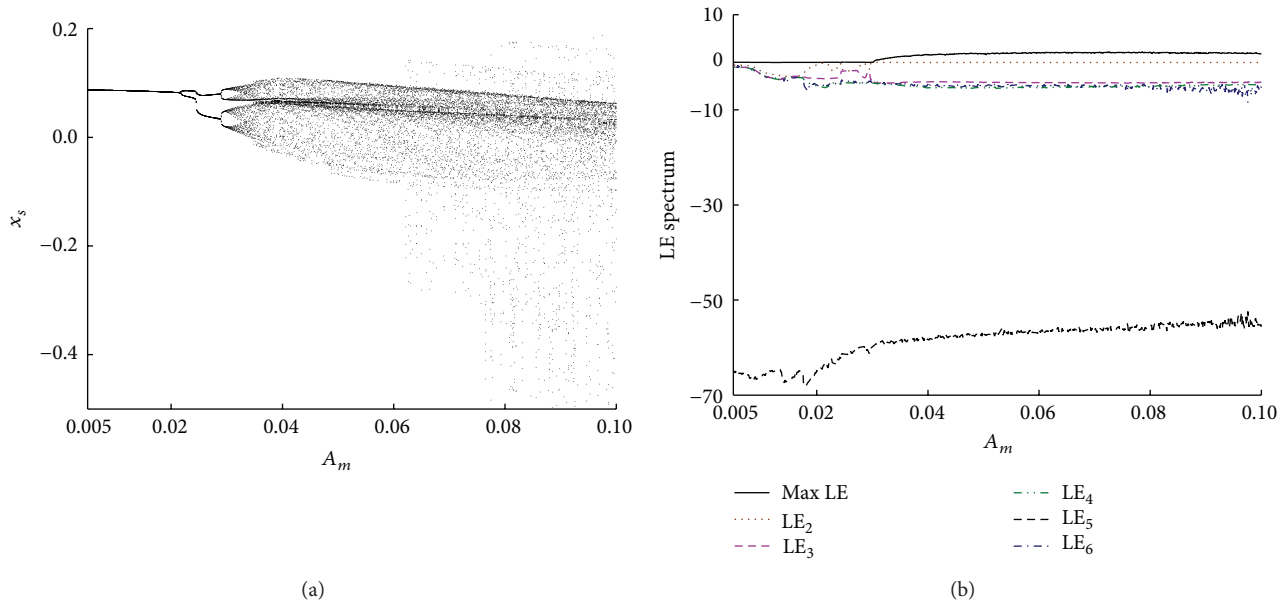


FIGURE 8: Bifurcation diagram and LE spectrum diagram of x_s by varying $A_m \in (0.005-0.1)$ m.

provides the reference for nonlinear dynamic analysis and control method in engineering application.

Conflict of Interests

The authors declare that there is no conflict of interests regarding the publication of this paper.

Acknowledgments

The research leading to these results has received funding from the National Science Foundation of China (Grants nos. 51475246, 51277098, and 51075215) and the Natural Science Foundation of Jiangsu Province of China (Grant no. BK20131402).

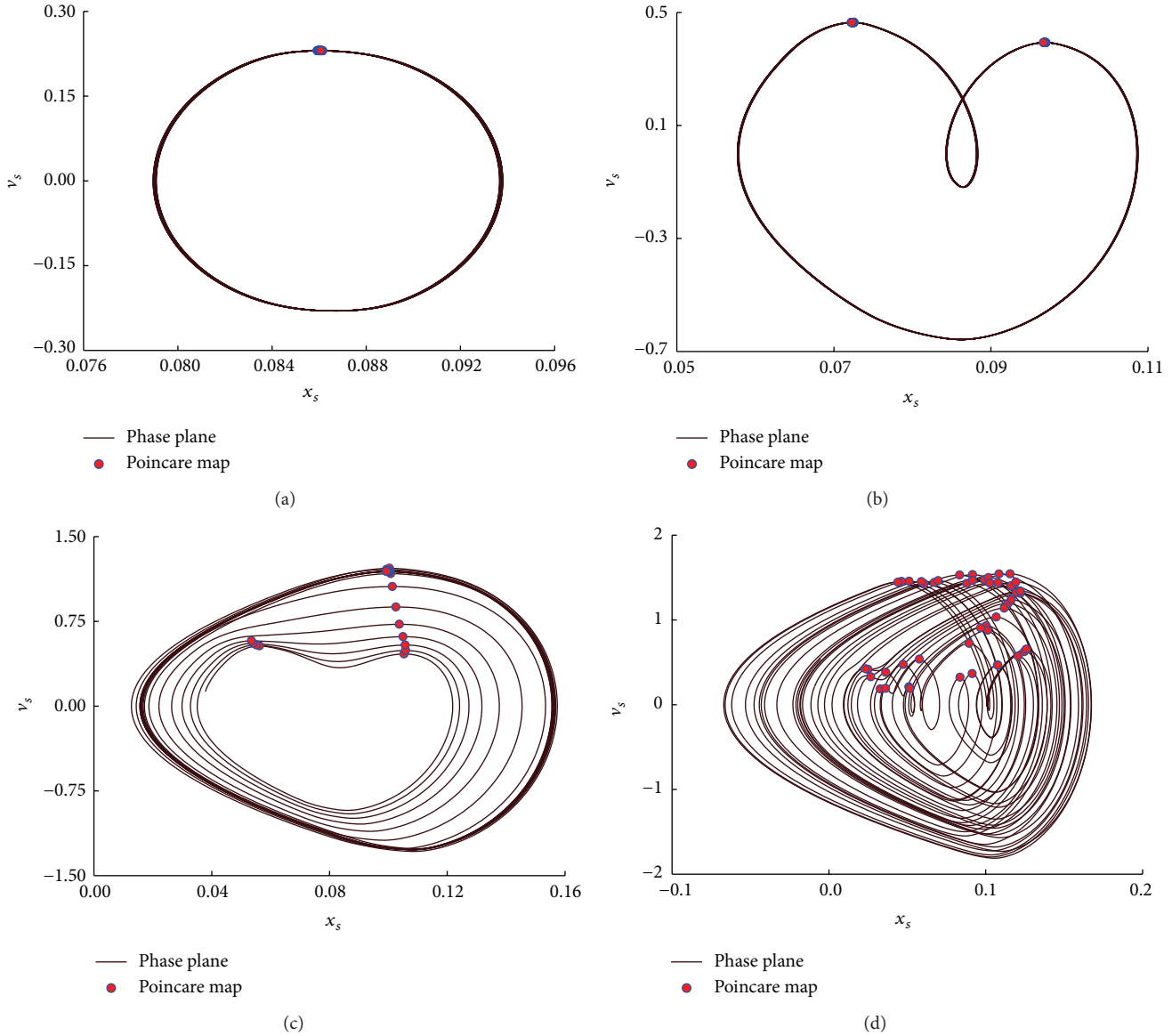


FIGURE 9: Phase plane portraits and corresponding Poincare maps (velocity v_s versus displacement x_s) for different A_m : (a) $A_m = 0.01$ m; (b) $A_m = 0.02316$ m; (c) $A_m = 0.02720$ m; (d) $A_m = 0.06$ m.

References

- [1] J. D. Carlson and K. D. Weiss, "A growing attraction to magnetic fluids," *Machine Design*, vol. 8, pp. 61–64, 1994.
- [2] D. Ivers and D. LeRoy, "Improving vehicle performance and operator ergonomics: commercial application of smart materials and systems," *Journal of Intelligent Material Systems and Structures*, vol. 24, no. 8, pp. 903–907, 2013.
- [3] M. Ahmadian and J. C. Poynor, "An evaluation of magneto rheological dampers for controlling gun recoil dynamics," *Shock and Vibration*, vol. 8, no. 3-4, pp. 147–155, 2001.
- [4] M. M. Rashid, N. A. Rahim, M. A. Hussain, and M. A. Rahman, "Analysis and experimental study of magnetorheological-based damper for semiactive suspension system using fuzzy hybrids," *IEEE Transactions on Industry Applications*, vol. 47, no. 2, pp. 1051–1059, 2011.
- [5] H.-H. Chiang and L.-W. Lee, "Optimized virtual model reference control for ride and handling performance-oriented semiactive suspension systems," *IEEE Transactions on Vehicular Technology*, vol. 64, no. 5, Article ID 2336878, pp. 1679–1690, 2014.
- [6] H. L. Zhang, E. R. Wang, N. Zhang, F. Min, R. Subash, and C. Su, "Semi-active sliding mode control of vehicle suspension with magneto-rheological damper," *Chinese Journal of Mechanical Engineering*, vol. 28, no. 1, pp. 63–75, 2015.
- [7] S. Li, S. Yang, and W. Guo, "Investigation on chaotic motion in hysteretic non-linear suspension system with multi-frequency excitations," *Mechanics Research Communications*, vol. 31, no. 2, pp. 229–236, 2004.
- [8] M. Siewe Siewe, "Resonance, stability and period-doubling bifurcation of a quarter-car model excited by the road surface profile," *Physics Letters A*, vol. 374, no. 13-14, pp. 1469–1476, 2010.

- [9] G. Litak, M. Borowiec, M. I. Friswell, and W. Przystupa, "Chaotic response of a quarter car model forced by a road profile with a stochastic component," *Chaos, Solitons and Fractals*, vol. 39, no. 5, pp. 2448–2456, 2009.
- [10] A. C. J. Luo and A. Rajendran, "Periodic motions and stability in a semi-active suspension system with MR damping," *Journal of Vibration and Control*, vol. 13, no. 5, pp. 687–709, 2007.
- [11] M. Borowiec and G. Litak, "Transition to chaos and escape phenomenon in two-degrees-of-freedom oscillator with a kinematic excitation," *Nonlinear Dynamics*, vol. 70, no. 2, pp. 1125–1133, 2012.
- [12] M. Ismail, F. Ikhoulane, and J. Rodellar, "The hysteresis Bouc-Wen model, a survey," *Archives of Computational Methods in Engineering*, vol. 16, no. 2, pp. 161–188, 2009.
- [13] M. J. L. Boada, J. A. Calvo, B. L. Boada, and V. Díaz, "Modeling of a magnetorheological damper by recursive lazy learning," *International Journal of Non-Linear Mechanics*, vol. 46, no. 3, pp. 479–485, 2011.
- [14] D. H. Wang and W. H. Liao, "Magnetorheological fluid dampers: a review of parametric modelling," *Smart Materials and Structures*, vol. 20, no. 2, Article ID 023001, 2011.
- [15] H. Zhang, E. Wang, F. Min, R. Subash, and C. Su, "Skyhook-based semi-active control of full-vehicle suspension with magneto-rheological dampers," *Chinese Journal of Mechanical Engineering*, vol. 26, no. 3, pp. 498–505, 2013.
- [16] W. J. Wang, L. Ying, and E. R. Wang, "Comparison on hysteresis models of controllable magneto-rheological damper," *Journal of Mechanical Engineering*, vol. 45, no. 9, pp. 100–108, 2009 (Chinese).
- [17] G. R. Iglesias, S. Ahualli, J. Echávarri Otero, L. F. Ruiz-Morón, and J. D. G. Durán, "Theoretical and experimental evaluation of the flow behavior of a magnetorheological damper using an extremely bimodal magnetic fluid," *Smart Materials and Structures*, vol. 23, no. 8, Article ID 085028, 2014.
- [18] Q. Zhu and M. Ishitobi, "Chaotic vibration of a nonlinear full-vehicle model," *International Journal of Solids and Structures*, vol. 43, no. 3-4, pp. 747–759, 2006.
- [19] J. Wang, Q. Zhang, Z. Chen, and H. Li, "Local bifurcation analysis and ultimate bound of a novel 4D hyper-chaotic system," *Nonlinear Dynamics*, vol. 78, no. 4, pp. 2517–2531, 2014.
- [20] D. Belato, H. I. Weber, J. M. Balthazar, and D. T. Mook, "Chaotic vibrations of a nonideal electro-mechanical system," *International Journal of Solids and Structures*, vol. 38, no. 10–13, pp. 1699–1706, 2001.
- [21] C. C. Wang and C. C. Liu, "Chaotic dynamic analysis of aquatic phytoplankton system," *Mathematical Problems in Engineering*, vol. 2014, Article ID 586262, 8 pages, 2014.
- [22] A. Farshidianfar and A. Saghafi, "Bifurcation and chaos prediction in nonlinear gear systems," *Shock and Vibration*, vol. 2014, Article ID 809739, 8 pages, 2014.